NASA/CR—2001-210974

Progressive Fracture of Composite Structures

Levon Minnetyan
Clarkson University, Potsdam, New York

Prepared under Grant NAG3–1101

National Aeronautics and
Space Administration

Glenn Research Center

July 2001

Note that at the time of research, the NASA Lewis Research Center was undergoing a name change to the NASA John H. Glenn Research Center at Lewis Field. Both names may appear in this report.

Contents were reproduced from the best available copy as provided by the author.

Available from

NASA Center for Aerospace Information
7121 Standard Drive
Hanover, MD 21076

National Technical Information Service
5285 Port Royal Road
Springfield, VA 22100

Available electronically at http://gltrs.grc.nasa.gov/GLTRS

CONTENTS

SUMMARY

This report includes the results of a research in which the COmposite Durability STRuctural ANalysis (CODSTRAN) computational simulation capabilities were augmented and applied to various structures for demonstration of the new features and verification. The first chapter of this report provides an introduction to the computational simulation or virtual laboratory approach for the assessment of damage and fracture progression characteristics in composite structures. The second chapter outlines the details of the overall methodology used; including the failure criteria and the incremental/iterative loading procedure with the definitions of damage, fracture, and equilibrium states. The subsequent chapters each contain an augmented feature of the code and/or demonstration examples. All but one of the presented examples contain laminated composite structures with various fiber/matrix constituents. For each structure simulated, damage initiation and progression mechanisms are identified and the structural damage tolerance is quantified at various degradation stages. Many chapters contain the simulation of defective and defect free structures to evaluate the effects of existing defects on structural durability.

Nomenclature

$\sigma_{\ell 11}$ - ply longitudinal stress
$\sigma_{\ell 22}$ - ply transverse stress
$\sigma_{\ell 33}$ - ply normal stress
$\sigma_{\ell 12}$ - ply in-plane shear stress
$\sigma_{\ell 23}$ - ply out-of-plane shear stress
$\sigma_{\ell 13}$ - ply out-of-plane shear stress
$\sigma_{\ell 11T}$ - ply longitudinal tensile stress
$\sigma_{\ell 11C}$ - ply longitudinal compressive stress
$\sigma_{\ell 22T}$ - ply transverse tensile stress
MDE - modified distortion energy failure criterion
R - radius of cylindrical shell
RR - delamination due to relative rotation

Chapter 1

Introduction

The behavior of fiber composite laminates during progressive damage and fracture has become of increasing interest in recent years due to the multitude of benefits that composites offer in practical engineering applications such as lightweight airframes, engine structures, space structures, marine and other transportation structures, high-precision machinery, and structural members in robotic manipulators. Composite structures lend themselves to tailoring to achieve desirable characteristics such as a high strength to weight ratio, dimensional stability under extreme thermal and hygral fluctuations, and the capability to allow controlled detectability such as in the Stealth technology. Because of the numerous possibilities with material combinations, composite geometry, ply orientations, and loading conditions, it is essential to have a reliable computational capability to predict the behavior of composites under any loading, geometry, composite material combinations, and boundary conditions. A computational capability is also essential to design effective experiments for the further development of composite micromechanics theories, and to utilize existing experimental results in the most productive manner. In summary, the development of reliable computational simulation methods is necessary for the commercial maturation of composite technology.

The behavior of composites during progressive fracture has been investigated both experimentally and by computational simulation [1], [2]. Recent additions to the computational simulation have enabled monitoring the variations in structural properties such as natural frequencies, vibration mode shapes, and buckling modes during progressive fracture [22].

1.1 Background

Existing computational capabilities in the simulation of structural damage and fracture of composite laminates have been implemented in the CODSTRAN (COmposite Durability STRuctural ANalyzer) computer program [3]. The ICAN (Integrated Composites ANalyzer) and MHOST computer codes [6], [5], [7] are coupled to form CODSTRAN.

Computational simulation methods relating the constitutive properties of materials to the overall structural behavior and damage resistance of polymer matrix and hybrid laminated

composites are based upon micromechanics relationships that are consolidated in the ICAN computer code. The ICAN computer code incorporates the cumulative result of composites research at NASA-Lewis Research Center on polymer matrix multi-layer angle-plied composites. ICAN is capable of determining the ability of the composite to endure stresses and deformations caused by applied loading and environmental effects such as temperatures and humidity. ICAN predicts all possible internal damage and fracture in the composite laminate. Fourteen distinct failure modes are checked by ICAN at each load increment during a CODSTRAN analysis stage. The failure modes that are monitored include the failure criteria associated with the positive and negative limits of the stress components, a modified distortion energy failure criterion, and delamination due to relative rotation. Another important capability of ICAN is to compute anisotropic elastic constants from the physical information on the composite laminate for the definition of nodal finite element properties for a piecewise linear incremental analysis of progressive fracture. ICAN utilizes a resident databank that contains the properties of typical fiber and matrix constituent materials, with provisions to add new constituents as they become available.

The influences of most loading and environmental conditions on material properties are interrelated. Micromechanics constitutive relationships implemented in ICAN are based on interaction equations that include the combined effects of all relevant conditions on the material behavior. Composite analysis carried out by ICAN has been demonstrated, tested, and verified from many perspectives. Computational composite mechanics provided by ICAN is a fundamental resource in the development of design evaluation methodologies for the structural response and integrity of polymer-matrix composites.

The constituent micromechanics relationships quantify degradation of matrix strength and moduli with increasing temperature and moisture. The effect of the reduction in matrix strength and moduli on the overall composite properties, strength, and durability is not easily predictable. The effect of matrix degradation on the overall composite depends upon the fiber properties and orientation of the plies, as well as matrix properties.

The integration of ICAN with a general purpose structural analysis code results in a piecewise linear incremental loading analyzer with equilibrium checks at each local iteration for each load increment. The current version of CODSTRAN uses MHOST as the structural analysis module due to the ability of the MHOST quadrilateral shell element to accept the composite laminate force-deformation relations predicted by ICAN. As an example, the load-displacement relationship computed by CODSTRAN for a typical composite plate structure is presented in Figure 1.1. This structure is loaded by a uniform static tensile loading applied in the longitudinal direction in the plane of the composite.

The CODSTRAN incremental loading procedure uses an accuracy criterion based on the allowable maximum number of damaged nodes during the application of a load increment. If too many nodes are damaged or fractured during a load increment, incremental loads are reduced and the analysis is repeated. Otherwise, if there is an acceptable amount of incremental damage, the load increment is kept constant but the constitutive properties and the structural geometry are updated to account for the damage and deformations in the

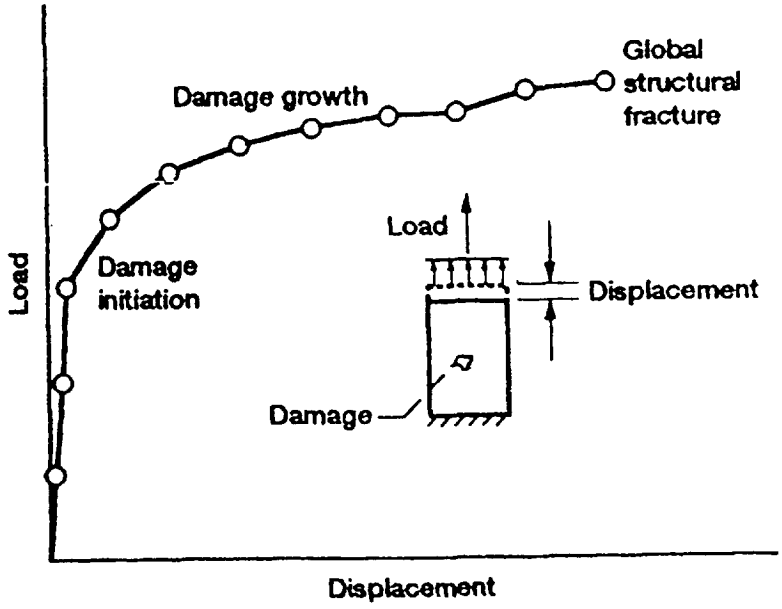

Figure 1.1: Incremental Loading Simulation

previous increment. The structure is then reanalyzed for further damage and deformation. If, after an incremental analysis step, there is no damage as determined by ICAN, the structure is considered to be in equilibrium and an additional load increment is applied. Analysis is stopped when global structural fracture is imminent.

During the computational simulation of progressive fracture, CODSTRAN also keeps track of degradation of structural integrity such as natural frequencies, vibration modes, buckling loads and buckling modes of the structure. CODSTRAN has been experimentally verified for the simulation of progressive fracture and failure under monotonically increasing static loading [2], [4].

The ICAN code [6] is used as the micromechanics module that is combined with a finite element analysis code [7] and an executive module for durability and degradation analysis, to form the COmposite Durability STRuctural ANalyzer (CODSTRAN) computer code. CODSTRAN is able to simulate composite damage initiation and growth under various loading and hygrothermal conditions. The concept and foundations of the computational simulation of composite structural durability were first laid out by the original implementation of the CODSTRAN code [3]. The simulation of progressive fracture by CODSTRAN was verified to be in reasonable agreement with experimental data from tensile tests [4].

The CODSTRAN code is able to predict the amount of internal damage as well as the fracture stability and safety of the damaged composite. The relationship between internal damage and structural properties such as natural frequencies and vibration mode shapes is useful for the in-service evaluation of safety and reliability. In this way composite structural behavior can be evaluated under any loading condition, geometry, or boundary conditions.

In general, overall structural damage may include individual ply damage and also through-the-thickness fracture of the composite laminate. CODSTRAN is able to simulate varied and complex composite damage mechanisms via evaluation of the individual ply failure modes and associated degradation of laminate properties. The type of damage growth and the sequence of damage progression depend on the composite structure, loading, material properties, and hygrothermal conditions. A scalar damage variable, derived from the total volume of the composite material affected by the various damage mechanisms is also evaluated as an indicator of the level of overall damage induced by loading. This scalar damage variable is useful for assessing the overall degradation of a given structure under a prescribed loading condition. The rate of increase in the overall damage during composite degradation may be used as a measure of structural propensity for fracture. Computation of the overall damage variable has no interactive feedback on the detailed simulation of composite degradation. The procedure by which the overall damage variable is computed is given in Chapter 5.

Damage progression characteristics may be better distinguished by quantifying a measure of structural resistance against damage propagation. The global Strain Energy Release Rate (SERR) also called the Damage Energy Release Rate (DERR) is defined as the rate of work done by external forces during structural degradation, with respect to the produced damage. SERR or DERR can be used to evaluate structural resistance against damage

propagation at different stages of loading. If the SERR for damage initiation is relatively small, low resistance to damage initiation is indicated. However, if after the damage initiation stage, SERR steadily increases, greater structural resistance against damage propagation is indicated prior to global fracture.

Chapter 2

Methodology

The behavior of fiber composite structures under loading is rather complex, especially when possible degradation with preexisting damage and damage propagation to structural fracture is to be considered. Because of the numerous possibilities with material combinations, laminate configuration, and loading conditions, it is essential to have an integrated and effective computational capability to predict the behavior of composite structures for any loading, geometry, composite material combinations, and boundary conditions. The predictions of damage initiation, growth, accumulation, and propagation to fracture are important in evaluating the load carrying capacity and reliability of composite structures. The CODSTRAN (COmposite Durability STRuctural ANalysis) computer code [3] has been developed for this purpose. CODSTRAN is able to simulate damage initiation, damage growth, and fracture in composites under various loading and environmental conditions. The simulation of progressive fracture by CODSTRAN has been verified to be in reasonable agreement with experimental data from tensile coupon tests on graphite/epoxy laminates [4]. Recent additions to CODSTRAN have enabled investigation of the effects of composite degradation on structural response [22], composite damage induced by dynamic loading [9], composite structures global fracture toughness [13], effect of hygrothermal environment on durability [23], damage progression in composite shells subjected to internal pressure [21], an overall evaluation of progressive fracture in polymer matrix composite structures [29], the durability of stiffened composite shell panels under combined loading [27], and damage progression in composite shell structures for expeditious and efficient structural design [30]. In all CODSTRAN simulations progressive fracture in fiber composite specimens is taken into account by tracking the damage initiation/propagation mechanisms.

CODSTRAN is an integrated, open-ended, stand alone computer code consisting of three modules: composite mechanics, finite element analysis, and damage progression modelling. The overall evaluation of composite structural durability is carried out in the damage progression module [3] that keeps track of composite degradation for the entire structure. The damage progression module relies on ICAN [6] for composite micromechanics, macromechanics and laminate analysis, and calls a finite element analysis module that uses anisotropic thick shell elements to model laminated composites [7].

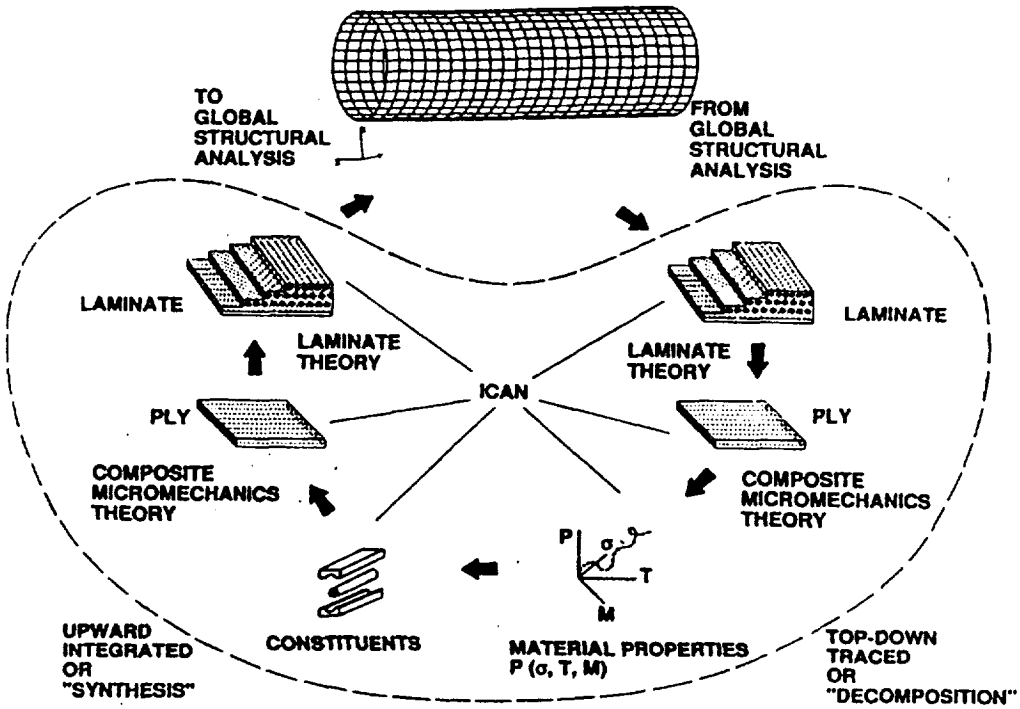

Figure 2.1: CODSTRAN Simulation Cycle

Figure 2.1 shows a schematic of the computational simulation cycle in CODSTRAN. The ICAN composite mechanics module is called before and after each finite element analysis. Prior to each finite element analysis, the ICAN module computes the composite properties from the fiber and matrix constituent characteristics and the composite layup. The finite element analysis module accepts the composite properties that are computed by the ICAN module at each node and performs the analysis at each load increment. After an incremental finite element analysis, the computed generalized nodal force resultants and deformations are supplied to the ICAN module that evaluates the nature and amount of local damage, if any, in the plies of the composite laminate. Individual ply failure modes are assessed by ICAN using failure criteria associated with the negative and positive limits of the six ply-stress components in the material directions as follows:

$$S_{\ell 11C} < \sigma_{\ell 11} < S_{\ell 11T} \tag{2.1}$$

$$S_{\ell 22C} < \sigma_{\ell 22} < S_{\ell 22T} \tag{2.2}$$

$$S_{\ell 33C} < \sigma_{\ell 33} < S_{\ell 33T} \tag{2.3}$$

$$S_{\ell 12(-)} < \sigma_{\ell 12} < S_{\ell 12(+)} \tag{2.4}$$

$$S_{\ell 23(-)} < \sigma_{\ell 23} < S_{\ell 23(+)} \tag{2.5}$$

$$S_{\ell 13(-)} < \sigma_{\ell 13} < S_{\ell 13(+)} \tag{2.6}$$

The stress limits in Equations (2.1-2.6) are computed by the micromechanics equations in ICAN, based on constituent stiffness, strength, and fabrication process parameters. The equations used for ply stress limits are given in reference [11]. If ply damage is predicted by Eq. (2.1), ply stiffness is reduced to zero at the damaged node. On the other hand, if ply damage is predicted by Eqs. (2.2-2.6), only the matrix stiffness is degraded and the longitudinal tensile stiffness of fibers is retained. In addition to the failure criteria based on the stress limits, interply delamination due to relative rotation of the plies, and a modified distortion energy (MDE) failure criterion that takes into account combined stresses is considered. The MDE failure criterion is expressed as:

$$F = 1 - \left[\left(\frac{\sigma_{\ell 11\alpha}}{S_{\ell 11\alpha}} \right)^2 + \left(\frac{\sigma_{\ell 22\beta}}{S_{\ell 22\beta}} \right)^2 - K_{\ell 12\alpha\beta} \frac{\sigma_{\ell 11\alpha}}{S_{\ell 11\alpha}} \frac{\sigma_{\ell 22}}{S_{\ell 22}} + \left(\frac{\sigma_{\ell 12S}}{S_{\ell 12S}} \right)^2 \right] \tag{2.7}$$

where α and β indicate tensile or compressive stress, $S_{\ell 11\alpha}$ is the local longitudinal strength in tension or compression, $S_{\ell 22\alpha}$ is the transverse strength in tension or compression, and

$$K_{\ell 12\alpha\beta} = \frac{(1 + 4\nu_{\ell 12} - \nu_{\ell 13})E_{\ell 22} + \quad (1 - \nu_{\ell 23})E_{\ell 11}}{[E_{\ell 11}E_{\ell 22}(2 + \nu_{\ell 12} + \nu_{\ell 13})(2 + \nu_{\ell 21} + \nu_{\ell 23})]^{1/2}} \tag{2.8}$$

The MDE failure criterion is obtained by modifying the usual distortion energy failure criterion that predicts combined stress failure in isotropic materials. The modification takes into account the significant differences in the stress limits of the longitudinal and transverse directions of an orthotropic composite ply. Each component of ply stress is normalized with respect to its limiting strength. No relationship is assumed between normal and shear strengths. The directional interaction factor $K_{\ell 12\alpha\beta}$ defined by Eq. (2.8) reduces to unity for homogeneous isotropic materials. The MDE criterion has been demonstrated to be a good predictor of combined stress failure in composites. Details of the MDE criterion, as well as other options for the assessment of local failure in composites are given in reference [14].

The MDE failure criterion becomes active in the majority of cases during computational simulation of progressive damage. If the failure predicted by the MDE criterion is not accompanied by a specific failure mode given by Eqs. (2.1-2.6), then the type of failure is assessed by comparison of the magnitudes of the squared terms in equation (2.7). Depending on the dominant term in the MDE failure criterion, fiber failure or matrix failure is assigned. The generalized stress-strain relationships are revised locally according to the composite damage evaluated after each finite element analysis. The model is automatically updated with a new finite element mesh having reconstituted properties, and the structure is reanalyzed for further deformation and damage. If there is no damage after a load increment, the structure is considered to be in equilibrium and an additional load increment is applied leading to possible damage growth, accumulation, or propagation. Simulation is continued until global fracture, when the specimen is broken into two pieces.

Chapter 3

Structural Behavior of Composites with Progressive Fracture

Structural characteristics such as natural frequencies and buckling loads with corresponding mode shapes are investigated during progressive fracture of multi-layer angleplied polymer matrix composites. Variations in structural characteristics as a function of the previously endured loading are studied. Results indicate that overall structural properties are mostly preserved through a significant proportion of the applied loading to the ultimate fracture load. For the cases studied, changes in structural behavior begin to occur after seventy percent of the ultimate fracture load has been applied. However, the individual nature of structural change is rather varied depending upon the laminate configuration, fiber orientation, and the boundary conditions.

The overall dynamic behavior and stability of partially damaged composite structures is of interest from two perspectives. (1) The need to predict whether a structure or component will remain safe and perform the required function when local damage and/or fracture occur at various locations and (2) the use of dynamic test response measurements with a structural identification procedure to assess the total damage sustained because of previous loading or environmental effects. The free vibration response of damaged angleplied fiber composites has been studied in the past both experimentally and by computational simulation [1], [2]. Whereas these past studies of structural response for damaged composites have shown remarkable agreement between experimental and computational predictions, proper assembly of the computational model for the simulation of load induced damage has required considerable judgement and intuition. In a parallel course of investigation, a computational and experimental program was launched at NASA-Lewis to study the progressive fracture of fiber composite laminates with regard to their performance in aerospace propulsion structures [3], [4]. The computational procedure to simulate progressive fracture has resulted in the computer code CODSTRAN (COmposite Durability STructural ANalyzer). CODSTRAN has been validated by an experimental program for fiber composites subjected to progressive fracture under axial loading. This chapter unifies the computational tools that have been developed at NASA-Lewis for the prediction of progressive damage and fracture

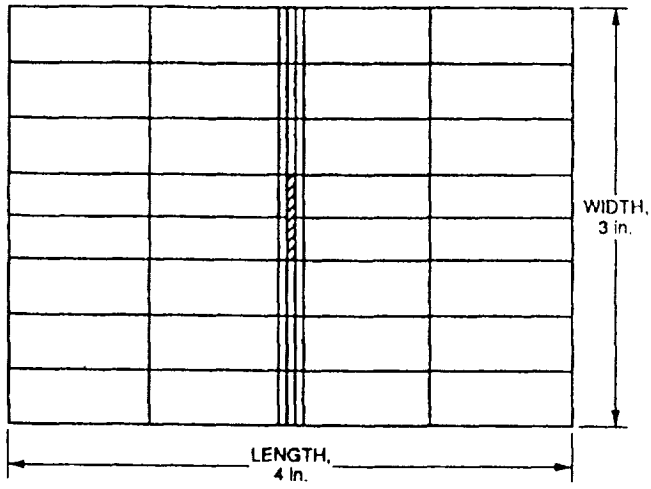

Figure 3.1: Composite plate finite element model with central notch

with efforts in the prediction of overall response of damaged composite structures. In the present approach, the computational finite element model for the damaged structure is constructed by the computer program as a byproduct of the analysis of progressive damage and fracture. Thus, a single computational investigation is able to predict progressive fracture and the resulting variation in structural properties of angleplied composites. The combined numerical procedure is amenable to development as a non-destructive evaluation method for the structural integrity of multi-ply composites.

An intermediate stiffness T-300/Epoxy composite structure is selected for initial investigations. A simple planar computational model with a small rectangular central notch is used as shown in Figure 3.1. The symmetric laminate for the present study has fiber orientations of $[\pm 15]_s$, with zero degrees corresponding to the axial loading direction. A rectangular plate of L=4 inches in length, w=3 inches in width, and t=0.13 inch in thickness is considered. Support conditions are (1) Simply supported on the 3 inch edges but free on the longer edges along the axial direction; and (2) Simply supported on all four edges. In each case the plate is analyzed under a gradually applied uniform axial tensile loading. Progressive damage and fracture are monitored as the applied loading is increased. As the composite structure deteriorates under loading, its overall response properties such as natural frequencies and buckling loads with the associated mode shapes are expected to degrade as well. The buckling load is a uniformly distributed compressive load applied at the ends of the plate in the axial direction. Figure 3.2 shows, for support condition (1), the decline in the first three natural frequencies and in the fundamental buckling load as a function of the load endured by the plate. On the ordinate, in Figure 3.2, F_i/F_{io} denotes the ith natural frequency, normalized with respect to its undamaged value. Similarly, B_i/B_{io} denotes the

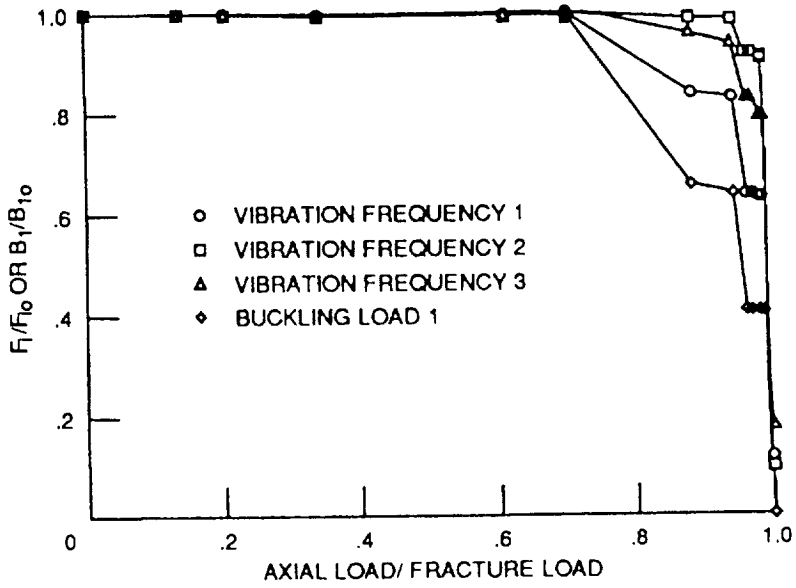

Figure 3.2: Structural degradation for composite plate; support condition 1

normalized value of the first buckling load. It is noted that there is no perceivable degradation in the plotted structural properties for up to about 70 percent of the ultimate fracture loading. This is consistent with the absence of any internal damage in the composite plate up to the same load level. After damage, both the natural frequency and the buckling load are reduced significantly, as seen in Figure 3.2. Free vibration and buckling eigenvector mode shapes are similarly affected because of damage and fracture. Figures 3.3(a,b,c,d) show the mode shape fringes for the first three free vibration modes and the first buckling mode before loading. Figures 3.4(a,b,c,d) and 3.5(a,b,c,d) show the same mode shapes for 94 percent and 97 percent of the ultimate fracture load, respectively. As expected, there are some changes in the overall structural behavior after the application of such high levels of loading. Nevertheless, the structure still behaves as a continuous unit in spite of a significant amount of internal damage and fracture. It may be noted that free vibration and buckling mode shapes are not completely symmetrical even though the composite laminate fiber orientations are symmetrical. The lack of complete symmetry in the mode shapes is because even though the fiber orientations are symmetrical with regard to axial loading, the orientation of the outer fiber layers have a much greater influence on the flexural properties of the laminate.

Figure 3.6 shows the degradation of buckling load and natural frequencies for the same plate, but now simply supported on all four edges (support condition 2). The normalized plots for overall mechanical properties depicted in Figure 3.6 are similar to those corresponding to support condition (1), depicted in Figure 3.2. One significant difference is that the buckling load increases above the original undamaged value just before ultimate failure. This effect is caused by the fragmentation of the plate structural behavior under the combined influences of the buckling load and the boundary conditions. Because of local degradation a partial

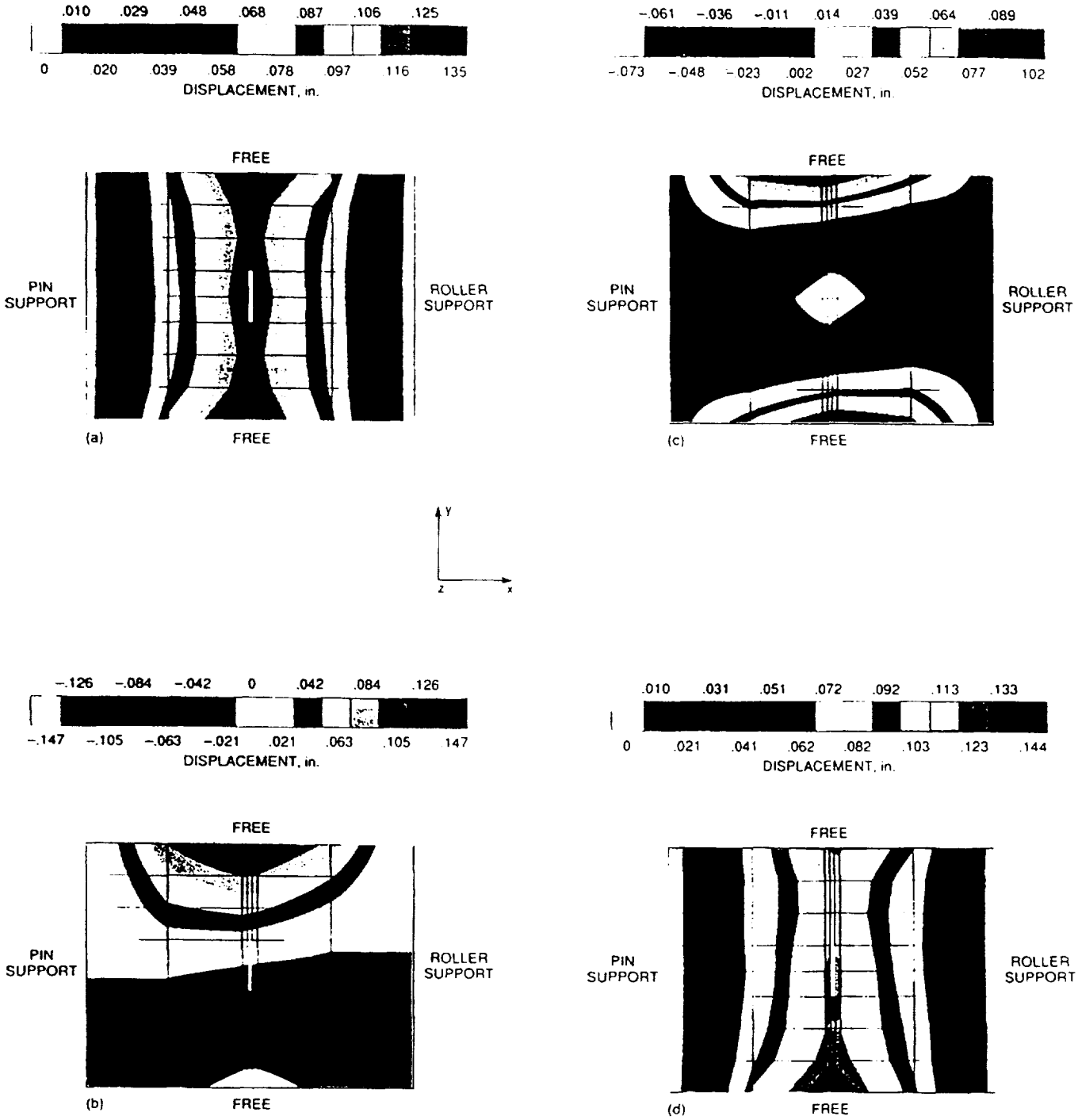

(a) Vibration mode 1. (c) Vibration mode 3.
(b) Vibration mode 2. (d) Buckling mode 1.

Figure 3.3: Mode shape fringes before loading. Fracture load, 5889 lb; support condition 1

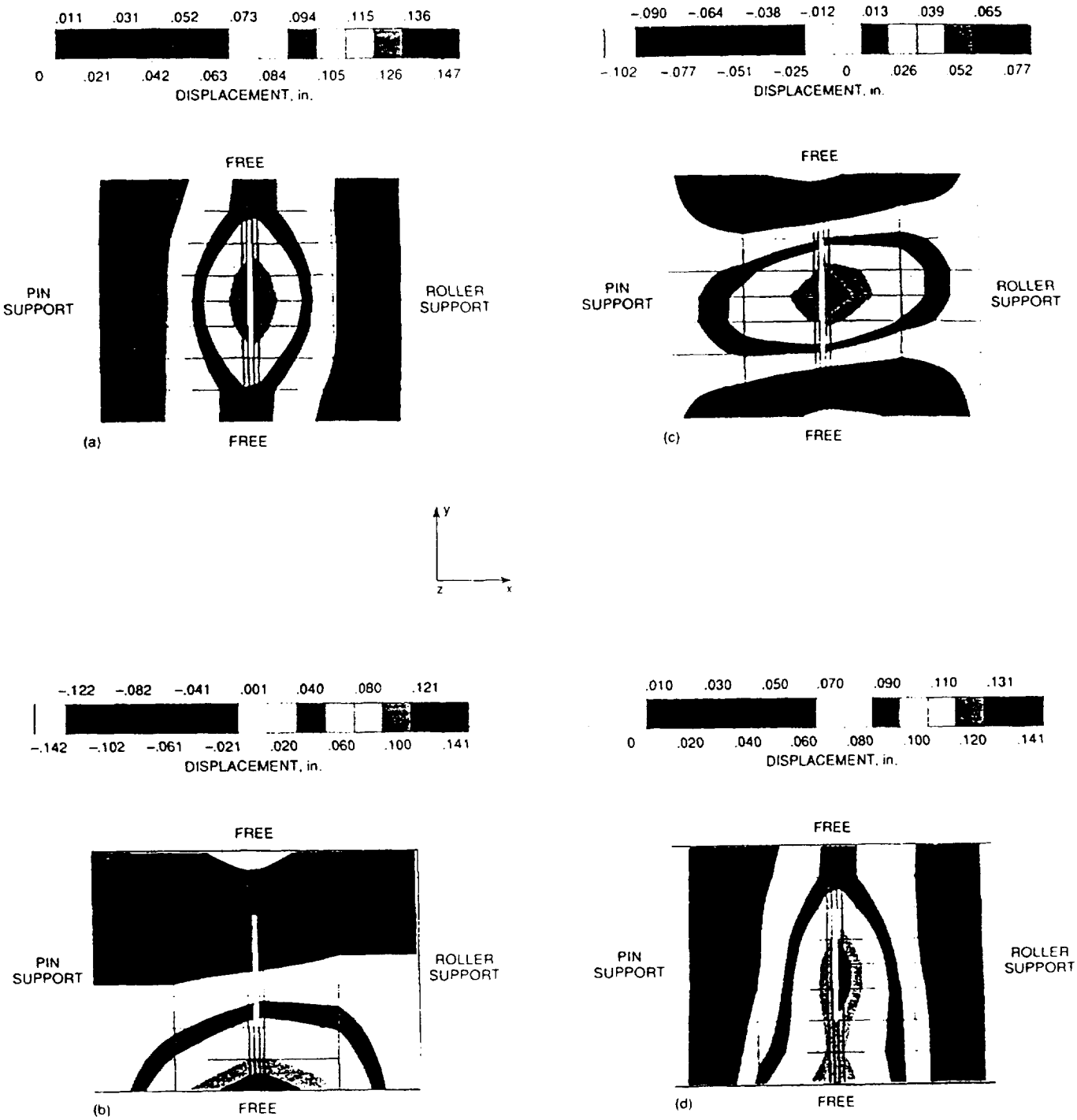

(a) Vibration mode 1.
(b) Vibration mode 2.
(c) Vibration mode 3.
(d) Buckling mode 1.

Figure 3.4: Mode shape fringes after 94 percent loading. Fracture load, 5889 lb; support condition 1

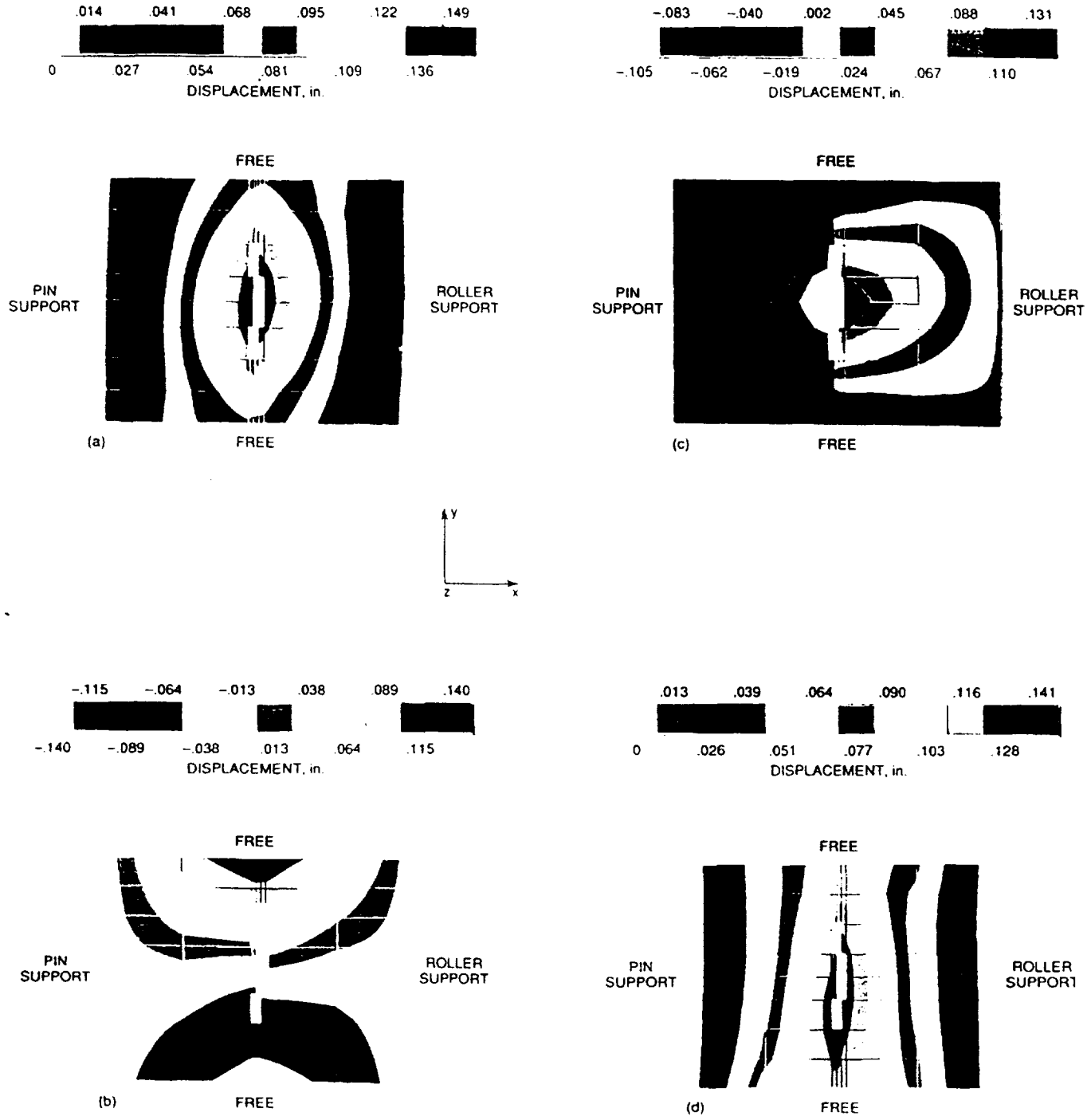

(a) Vibration mode 1. (c) Vibration mode 3.
(b) Vibration mode 2. (d) Buckling mode 1.

Figure 3.5: Mode shape fringes after 97 percent loading. Fracture load, 5889 lb; support condition 1

flexural hinge forms at the center of the plate along the existing notch, effectively separating the plate into two halves from an elastic stability viewpoint. When the two halves of the plate behave independently, the buckling load is increased. Also, after a certain amount of loading, the second and the third vibration frequencies switch their mode shapes. These effects are to be examined further in later paragraphs with the help of the corresponding mode shape fringes.

Figures 3.7(a,b,c,d) show the mode shapes for the first three free vibration modes and the first buckling mode before loading. Because of the additional restraints at the boundaries for support condition 2, the mode shapes are more significantly affected by the boundary conditions. For that reason, the first vibration mode, Figure 3.7a, and the fundamental buckling mode, Figure 3.7d, are virtually identical, indicating that in this case boundary conditions, rather than external effects, have the controlling influence on structural behavior. It is also noteworthy that the second and the third vibration mode shapes are now more obviously affected by composite laminate fiber orientations that make the plate significantly more stiff in the axial direction. As a result, the vibration mode producing a transverse full wave, mode 2, is lower in frequency than the vibration mode producing a longitudinal full wave, mode 3, in spite of the transverse central notch in the plate. The mode 3 natural frequency is almost double of the mode 2 frequency.

Figures 3.8(a,b,c,d) show the same mode shapes for support condition 2, for 91 percent of the ultimate fracture load. At 91 percent of loading the central notch has been extended in the transverse direction by failure of the elements adjacent to the notch. There is some decoupling of the two sides of the plate separated by the notch as indicated by the reduction of modal symmetry across the center of the plate. This reduction in symmetry may be observed in vibration modes 1 and 3 and the buckling mode. The overall mode shape configurations for the second and third free vibration frequencies remain as they were prior to loading. There is some reduction in all three natural frequencies and the buckling load. However, because of the extension of the central notch, the third natural frequency is reduced more significantly as compared to that of mode 2, with the vibration frequency of mode 3 now only 18 percent higher than the vibration frequency of mode 2.

Figures 3.9(a,b,c,d) show the mode shapes for support condition 2, for 94 percent of the ultimate fracture load. At this loading stage additional elements on either side of the central notch as well as the nodes at both ends of the notch have failed. As a result, the natural frequency corresponding to the vibration mode with the longitudinal full wave has been reduced below that of the mode with the transverse full wave. In other words, the second and third vibration modes have switched the order of their natural frequencies. Nevertheless, the structure still appears to behave as a continuous unit in spite of a significant amount of internal damage and fracture.

The buckling mode, as depicted in Figure 3.9d, shows significant decoupling of the two sides of the plate separated by the central notch. Because of boundary restraints, the result of structural decoupling is the reduction in the effective buckling length and a resulting significant increase in the fundamental buckling load at this advanced stage of local damage.

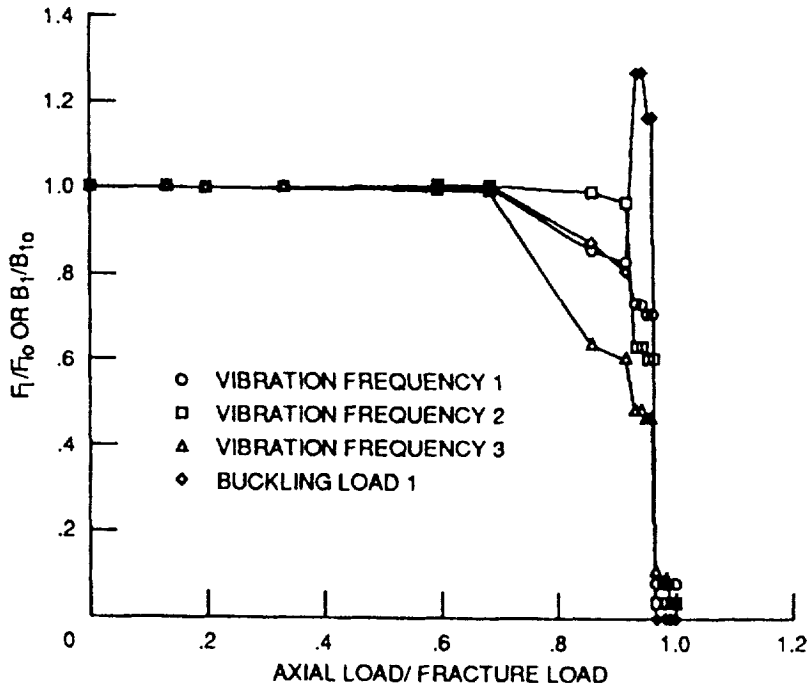

Figure 3.6: Structural degradation for short plate; support condition 2

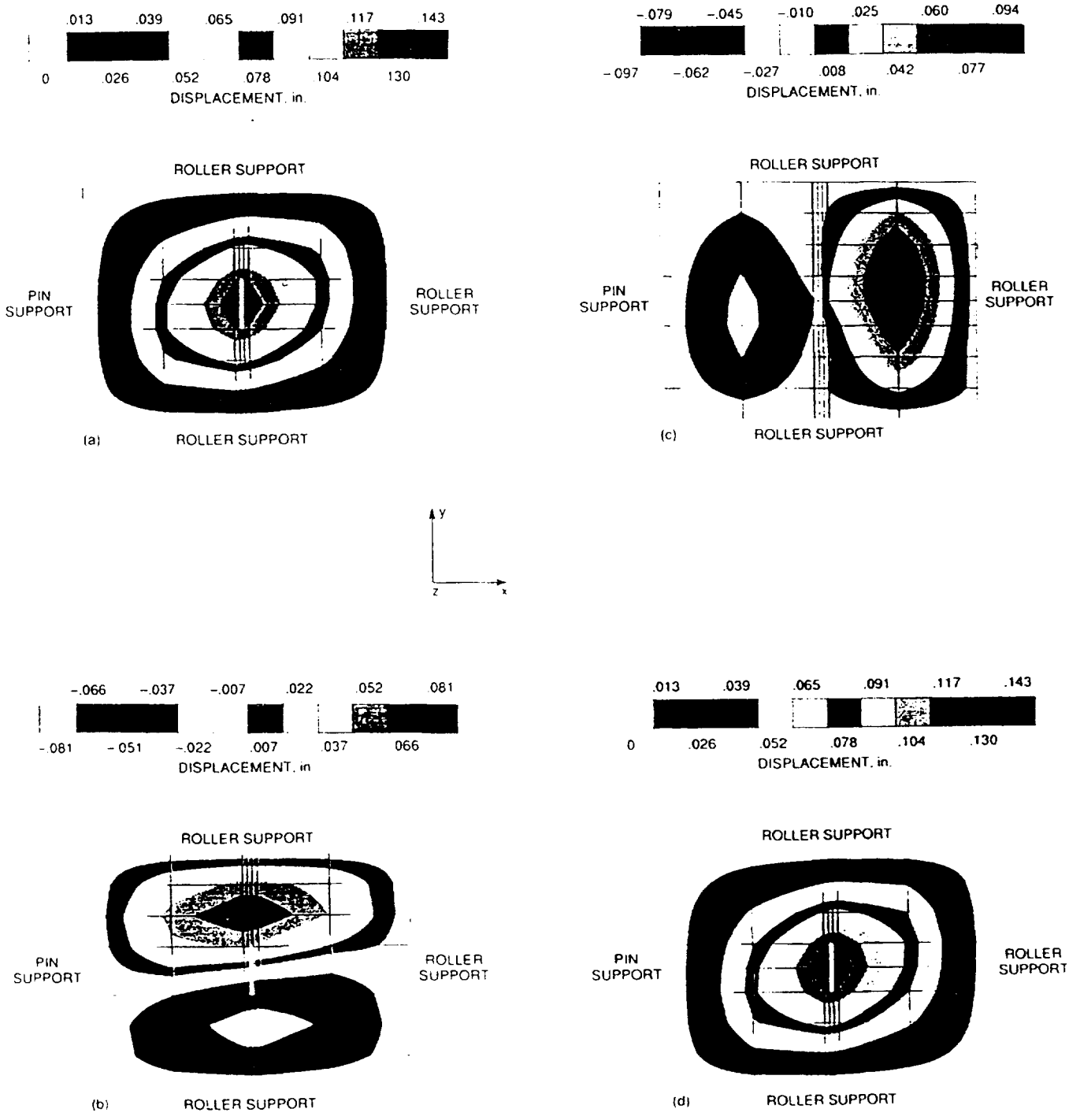

(a) Vibration mode 1. (c) Vibration mode 3.
(b) Vibration mode 2. (d) Buckling mode 1.

Figure 3.7: Mode shape fringes before loading. Fracture load, 6082 lb; support condition 2

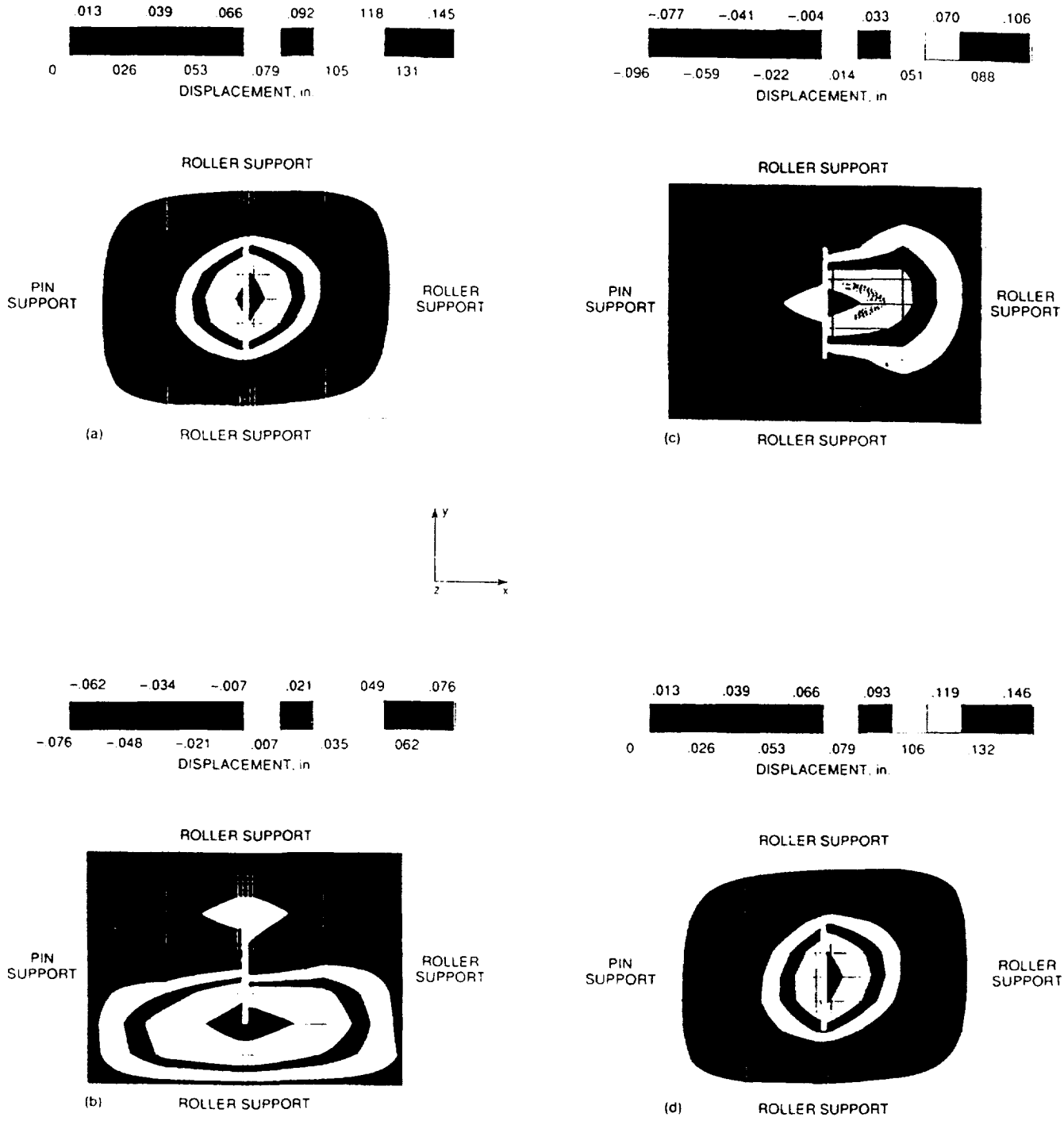

(a) Vibration mode 1. (c) Vibration mode 3.
(b) Vibration mode 2. (d) Buckling mode 1.

Figure 3.8: Mode shape fringes after 91 percent loading. Fracture load, 6082 lb; support condition 2

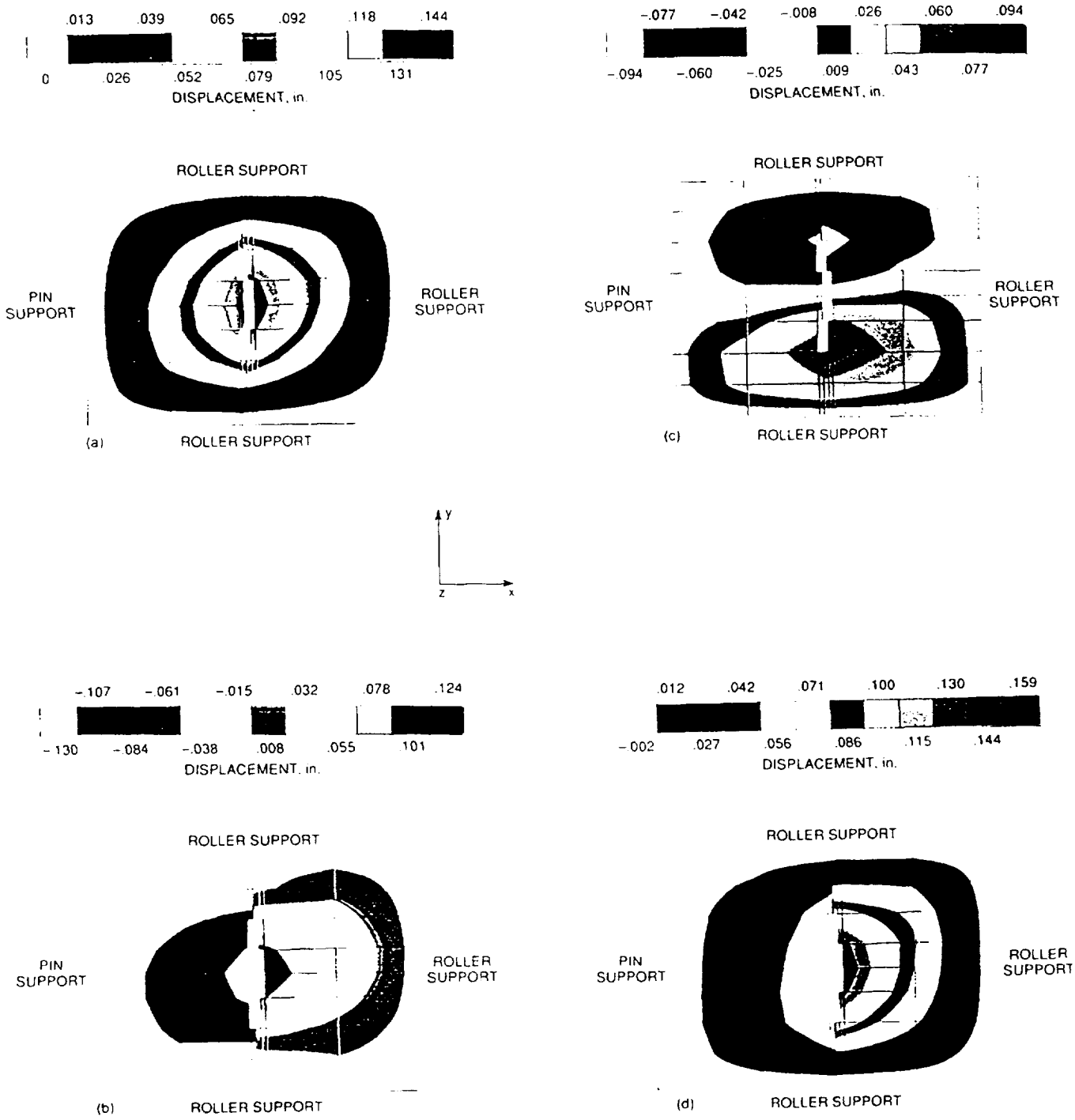

(a) Vibration mode 1. (c) Vibration mode 3.
(b) Vibration mode 2. (d) Buckling mode 1.

Figure 3.9: Mode shape fringes after 94 percent loading. Fracture load, 6082 lb; support condition 2

At very high levels of loading structural damage becomes pervasive at all parts of the plate which ceases to behave as a continuous structure. Figs. 3.10a and 3.10b show, respectively, the shapes of the third vibration mode and the buckling mode after 98 percent of the ultimate fracture load has been applied. The first two vibration modes are not shown as they are trivial cases with zero eigenvalue involving only disjoint elements similar to the buckling mode. The third vibration mode, shown in Figure 3.10a, involves only a small portion of the plate that appears to have been spared complete degradation due to its remoteness from applied loading and the stress relief provided by the existing central notch. Figure 3.10b indicates that at this highly damaged stage the first buckling mode computed by the analysis module, no longer represents a structural response characteristic. This buckling mode has no significance other than to indicate that the structure has completely lost its integrity.

To investigate the effects of dimensional changes on structural degradation, computational investigations with both support conditions are repeated with a longer plate. The length of the composite plate is increased from 4 to 6 inches while keeping all other properties the same. The finite element model for this longer geometry is shown in Figure 3.11. The number of finite elements have been increased to keep the element sizes similar to that of the shorter model. Normalized degradation curves for support condition (1) are plotted in Figure 3.12. The degradation curves depicted in Figure 3.12 show characteristics similar to Figure 3.2 which was for the shorter model with the same boundary conditions and identical composite laminate configuration. As it was for the shorter plate, there is no structural degradation up to the application of approximately 70 percent of the ultimate fracture load. After the initiation of structural damage, the general character of the degradation curves are similar, however, there are some differences because of the change in geometry. The second and third natural frequencies degrade identically in this case and the buckling instability is reached before complete structural fracture. The early instability may be expected from a longer specimen. However, to explain the identical degradation of the second and third natural frequencies will require an examination of the corresponding mode shapes.

Figures 3.13(a,b,c,d) show the mode shapes for the first three free vibration modes and the first buckling mode before loading under support condition (1). It may be noted that the second and third vibration modes both have their controlling wavelengths approximately in the transverse direction of the plate, in fact, vibratory wave direction at the center of the plate appears to be perpendicular to the orientation of the outer layer fibers for these two modes. The second and the third vibration modes degrade identically due to the fact that both are influenced only by the transverse properties of the plate at the early stages of damage. On the other hand, the first vibration mode and the fundamental buckling mode are influenced more by the longitudinal properties and the overall geometry of the model.

Figures 3.14(a,b,c,d) show the same mode shapes at 91 percent of the ultimate fracture load. At 91 percent of loading the central notch has been extended in the transverse direction by failure of the elements adjacent to the notch, similar to the case of the shorter model. Also similar to the shorter model under the same boundary conditions, there does not appear to be any significant change in the mode shapes at this stage of loading.

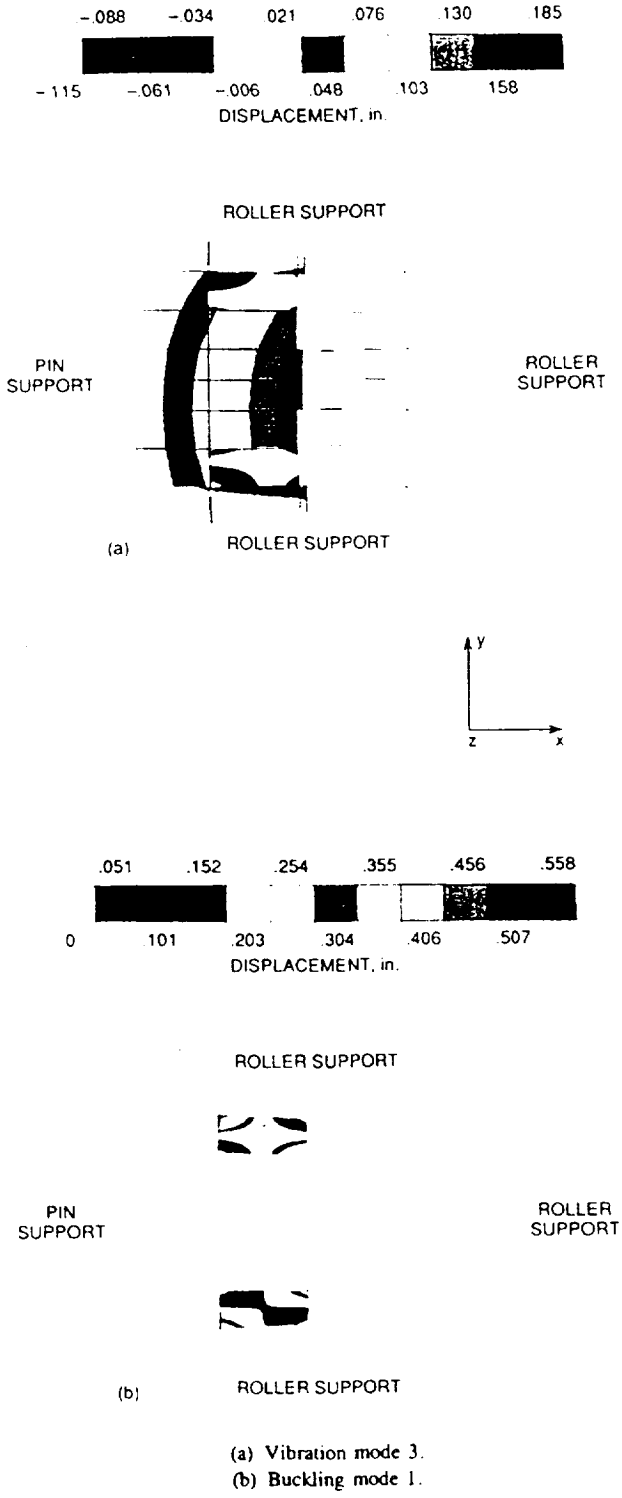

(a) Vibration mode 3.
(b) Buckling mode 1.

Figure 3.10: Mode shape fringes after 98 percent loading. Fracture load, 6082 lb; support condition 2

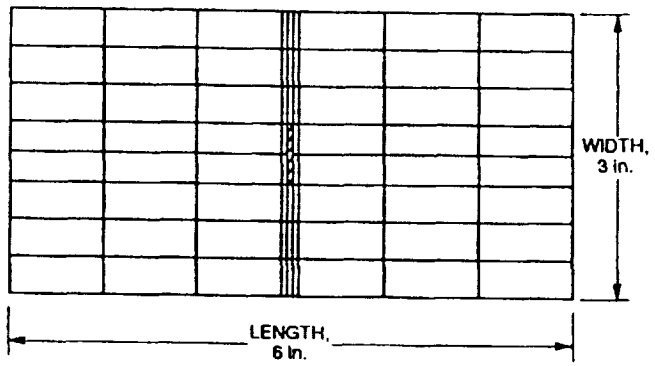

Figure 3.11: Long plate finite element model with central notch

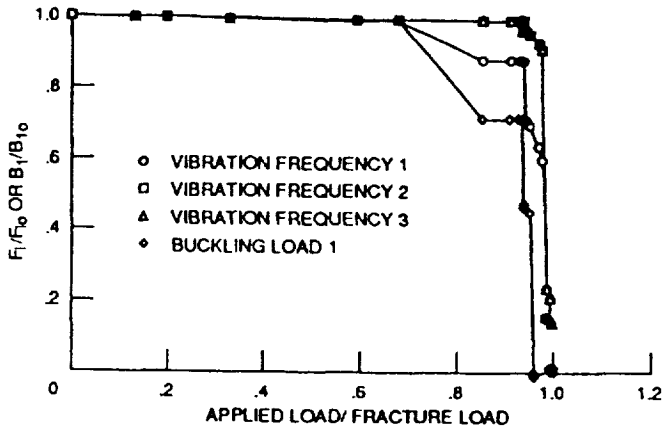

Figure 3.12: Structural degradation for long plate; support condition 1

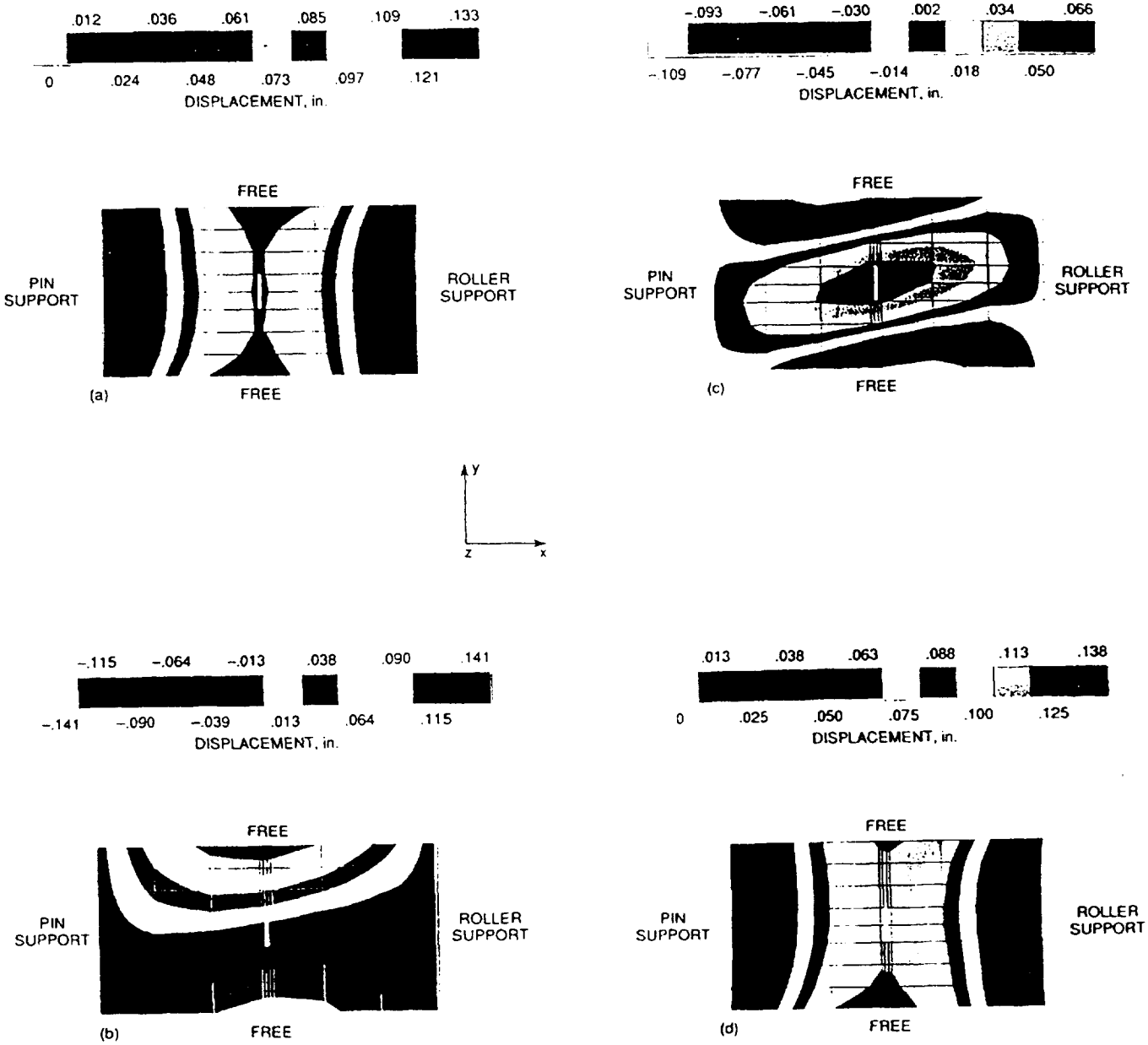

(a) Vibration mode 1. (c) Vibration mode 3.
(b) Vibration mode 2. (d) Buckling mode 1.

Figure 3.13: Mode shape fringes before loading. Fracture load, 6086 lb; support condition 1

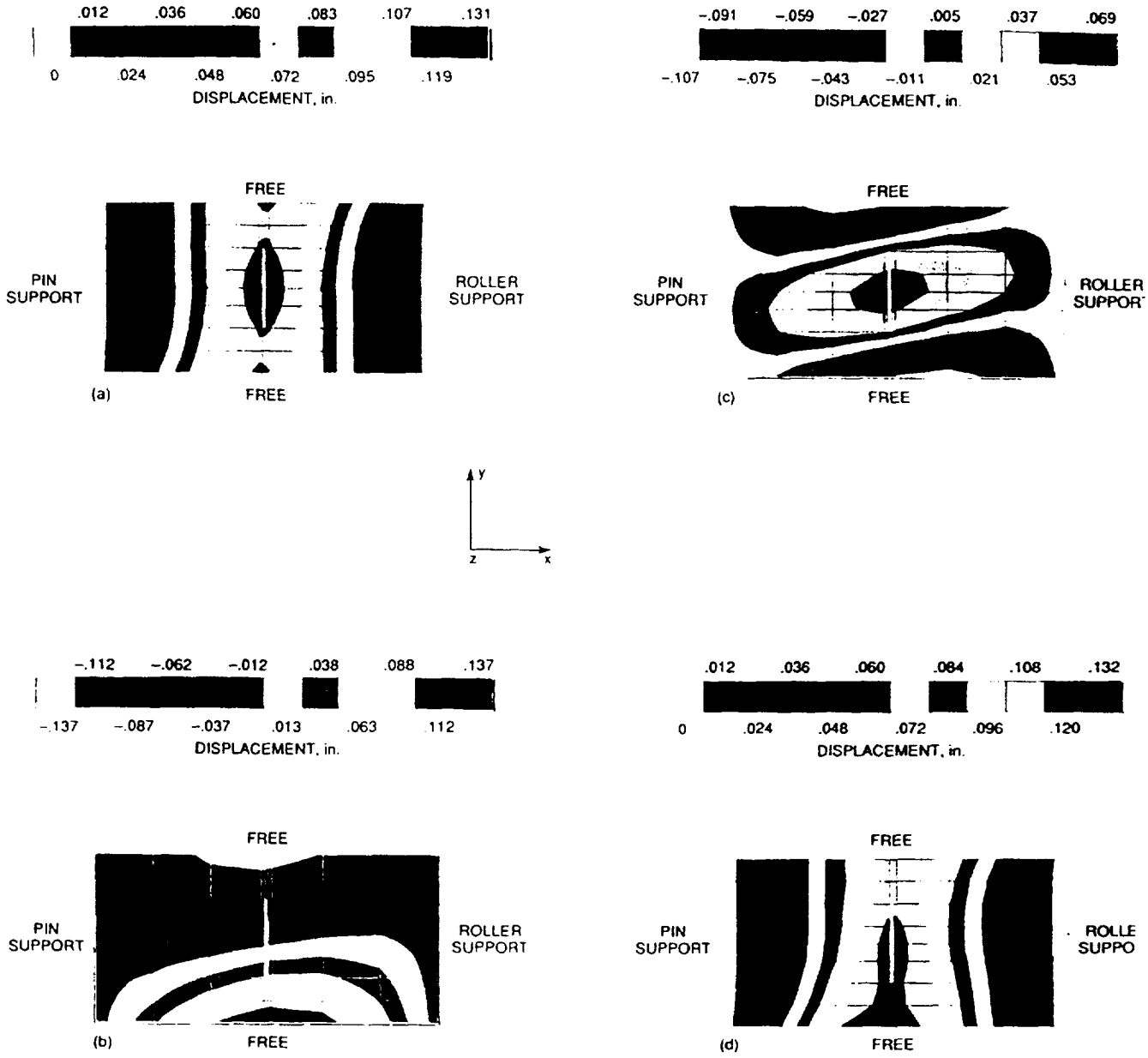

(a) Vibration mode 1. (c) Vibration mode 3.
(b) Vibration mode 2. (d) Buckling mode 1.

Figure 3.14: Mode shape fringes after 91 percent loading. Fracture load, 6086 lb; support condition 1

Figures 3.15(a,b,c,d) show the mode shapes after 95 percent of the ultimate fracture load is applied. There is additional damage and failure at the central notch of the model. The second vibration mode switches to a transverse wave pattern because of the weakening of the center of the plate and increased structural decoupling of the two sides separated by the central notch. The other three mode shapes that are depicted do not appear to be significantly affected from the weakness of the center. However, any additional loading causes rapid structural deterioration and disintegration of the plate model.

Figure 3.16 shows the normalized degradation curves for the buckling load and natural frequencies for the same 3 in. by 6 in. plate, but now simply supported on all four edges (support condition 2). As in the previously studied cases with the same material, structural degradation begins after 70 percent of the ultimate fracture load is applied. However, once degradation is initiated there are some differences of behavior compared to the other cases. The buckling load increases early with structural damage because of the higher tendency of the two halves of the plate to behave independently. The order of vibratory mode frequencies are changed as it was in the shorter model under support condition (2).

To look into the effects of relative stiffnesses of fiber and matrix in the composite structure, an S-glass/HMHS (S-glass fibers with a high modulus, high strength matrix) laminate with a more congruent modular ratio is analyzed using the 3 in. x 6 in. computational model under support condition (1). Degradation curves for investigated structural properties are shown in Figure 3.17. The results are in general similar to those of the T300/Epoxy composite except that in the S-glas/HMHS composite, structural damage is more uniformly distributed exhibiting a more nonlinear behavior with smoother degradation curves; also, higher frequency modes are more severely affected near the ultimate load for the S-Glass/HMHS composite.

According to computational predictions and general observations of depicted structural response characteristics, overall mechanical properties of the plate structure are most strongly influenced by composite fiber orientations and boundary conditions. Dimensional variations play a less important role, yet, there are perceivable changes in modal behavior when dimensional changes are accompanied with overconstrained boundary conditions. For example, changing the plate length from 4 to 6 inches under support condition (2) has a more significant influence on modal behavior as compared to the effect of the same dimensional change under support condition (1).

The variation in the detailed composite behavior in the limited examples examined in this chapter indicate that general conclusions regarding the behavior of damaged composites remain elusive and that there is no simple generalization or rule relating the degraded structural characteristics of damaged angleplied composite structures to the actual amount of damage present in the composite material. Accordingly, the necessity of reliable computational composite mechanics to predict the significant structural behavior patterns for each type, laminate, fiber orientations, geometry, boundary conditions, and loading of a composite structure is reacknowledged.

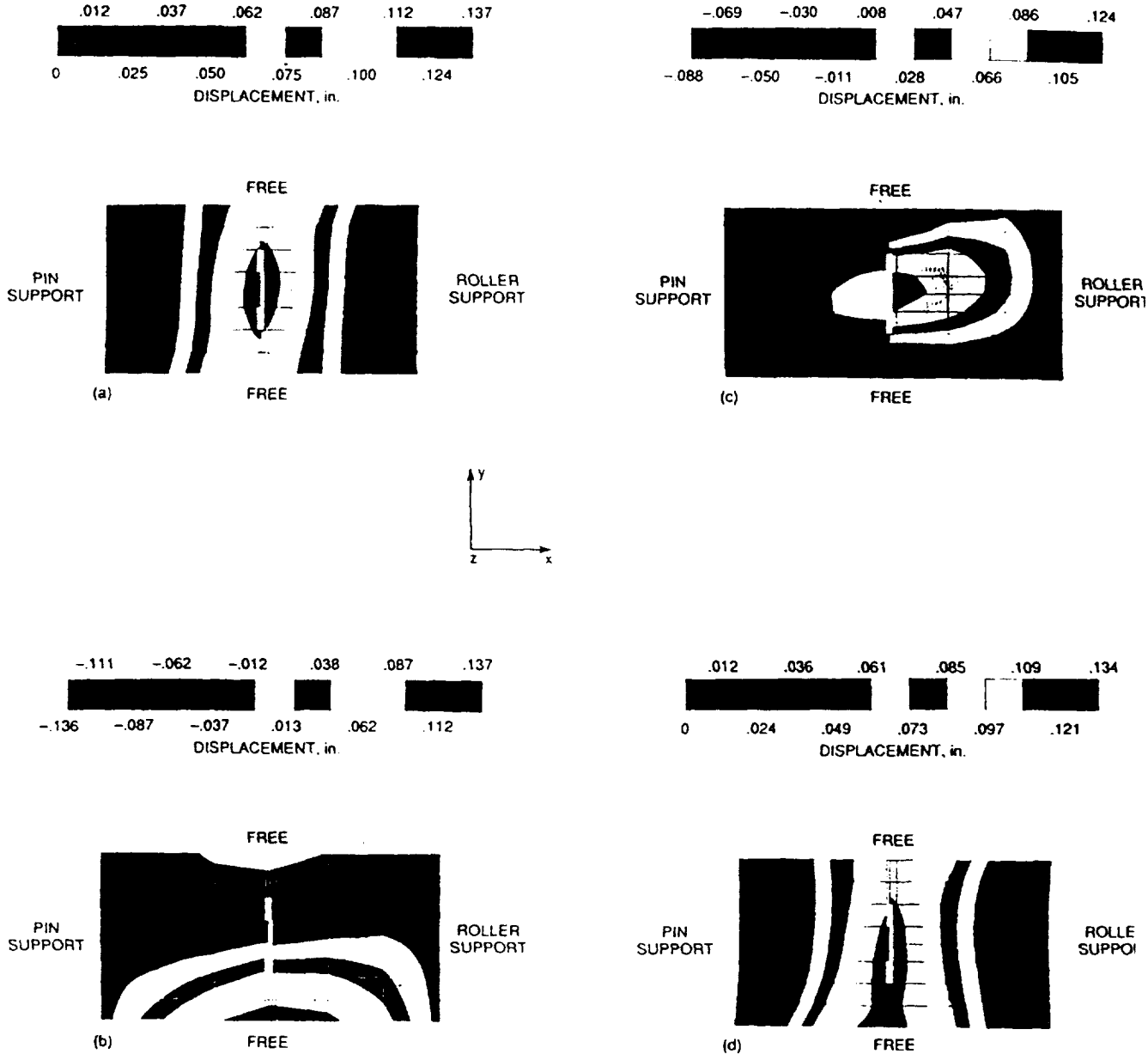

(a) Vibration mode 1. (c) Vibration mode 3.
(b) Vibration mode 2. (d) Buckling mode 1.

Figure 3.15: Mode shape fringes after 95 percent loading. Fracture load, 6086 lb; support condition 1

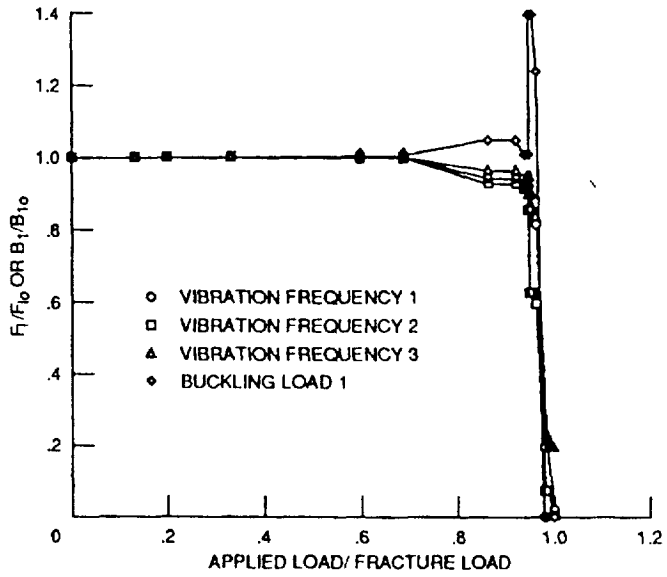

Figure 3.16: Structural degradation for long plate; support condition 2

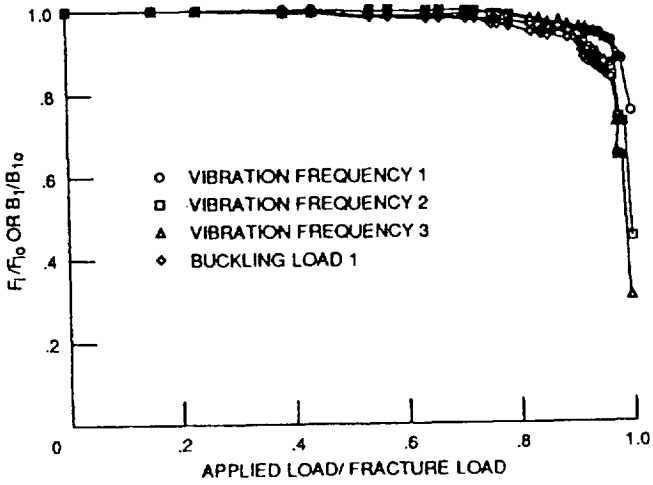

Figure 3.17: Structural degradation for S-glass/HMHS plate; support condition 1

Chapter 4

Progression of Damage and Fracture in Composites under Dynamic Loading

An angle-plied composite plate structure under normal impact loading is used as an example to demonstrate the dynamic simulation method. An intermediate stiffness T-300/Epoxy (Thornel-300 graphite fibers in an epoxy matrix) composite structure is selected for analysis of dynamic response under impulsive loading. A composite square plate (3 inch x 3 inch), supported along its four edges is loaded by a concentrated normal dynamic load at the center as shown in Figure 4.1. Large deformations are included in the computational simulation. The finite element model consists of sixty-four plate elements as shown in Figure 4.2. The finite element model is chosen to be somewhat coarse to enable a reasonable computer turnaround time for this demonstration example. The laminate configuration is [+45/-45/-45/+45]s, with a total composite plate thickness of 0.02 inch. All edges have been restrained against displacement in the normal z direction in all cases. Within this constraint, two types of support conditions are considered. In the first type, support nodes are allowed to move in the x-y plane (the plane of the undeformed composite plate). In the second type support, boundary nodes are restrained against displacement in all directions. The first and second types of support conditions will be referenced to as released and restrained supports, respectively.

The concentrated transient load is assumed to increase linearly with time, as shown in Figure 4.3, until global fracture of the composite plate structure. Three loading rates are considered. These loading rates are 0.1, 2.0, and 3.5 lbs/microsecond. Figure 4.4 shows the dynamic load-deflection histories at these three rates for the first type (released) boundary support condition. The displacements are very small for the first load increment because of the large inertial load imparted when the structure is initially set in motion. Also, the higher the loading rate, the smaller the displacement because of the higher inertial force. After the first load increment, there is a dramatic increase in displacement, especially for the 0.1 lbs/microsecond loading rate. In this case, the time is sufficiently long for the entire plate

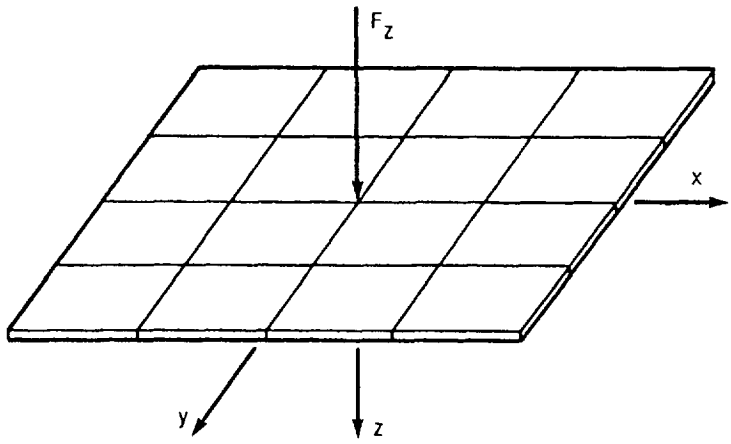

Figure 4.1: Rectangular plate model with normal load

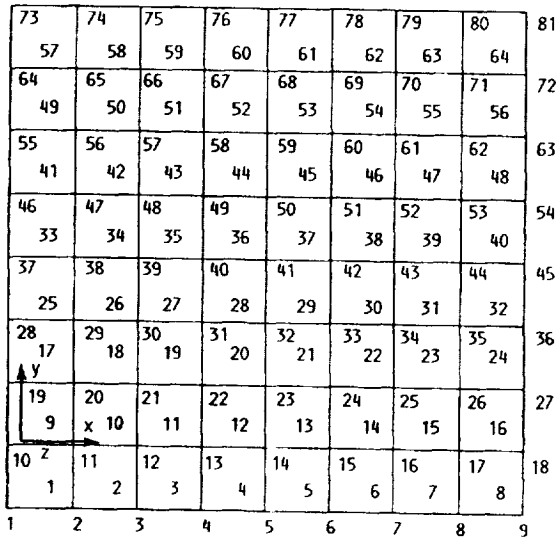

Figure 4.2: Finite element model

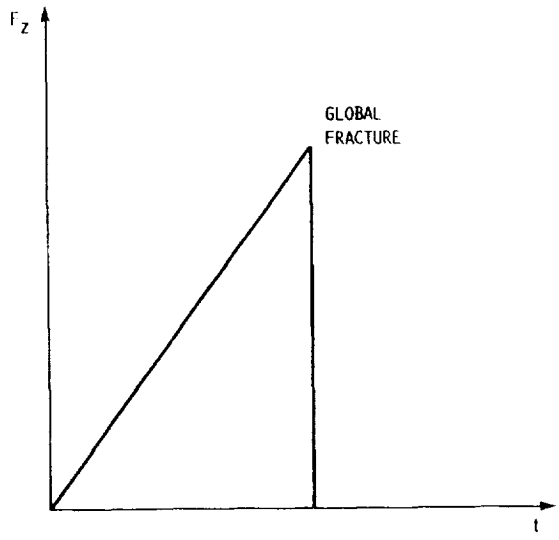

Figure 4.3: Variation of applied loading with time

to be set in motion. After a center deflection of approximately 0.3 inch, membrane forces become significant and the incremental deflections are reduced. The corresponding load is 60 lbs. This loading level also causes an initial local damage in the composite laminate (ply 1 - the first ply on the tension side of the plate). The failure mode is ply transverse tensile stress.

Figure 4.5 shows the contours of ply 1 transverse stresses that cause the damage. Figure 4.6 shows the much lower intensities of the same stresses after CODSTRAN accounts for the damage, redefines the material properties, and reaches a dynamic equilibrium with the redefined properties. It may be noted that Figure 4.6 indicates the transverse ply stress to be zero at the damaged center node. Figure 4.7 shows the deformed finite element mesh with displacement contours immediately after initial damage. A discontinuity in curvature at the failed center node may be observed. The remaining deformed structure continues to carry additional load, sustaining approximately constant incremental displacements with each load increment. Other plies participate in the laminate damage growth at approximately 240 lbs loading. The maximum deflection at the center node under 240 lbs loading is 0.7 inch. The entire structure participates in the dynamic response similar to a static loading. The deformed finite element mesh with displacement contours corresponding to 240 lbs loading at 0.1 lbs/microsecond is shown in Figure 4.8.

For the 2.0 lbs/microsecond loading case, damage is initiated by the same transverse stress limit criterion in the tension plies. However, initial damage occurs at a higher dynamic load of 75 lbs. The center node displacement corresponding to the 75 lbs damage initiation load is approximately 0.07 inch, as it may be observed from Figure 4.4. For the 3.5 lbs/microsecond

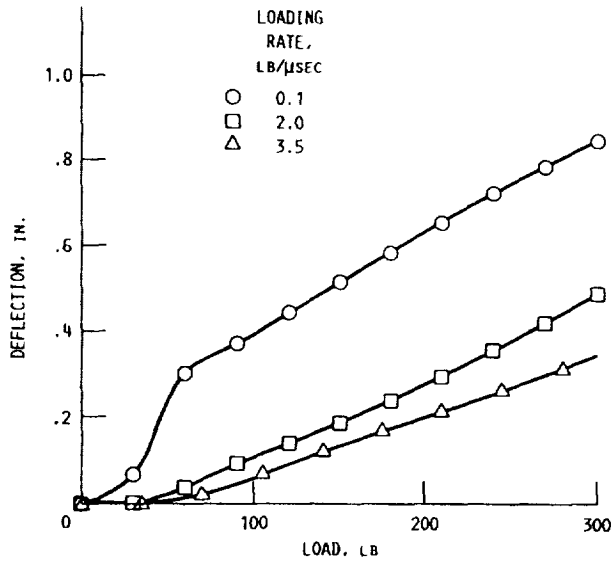

Figure 4.4: Load-deflection relationships for released supports

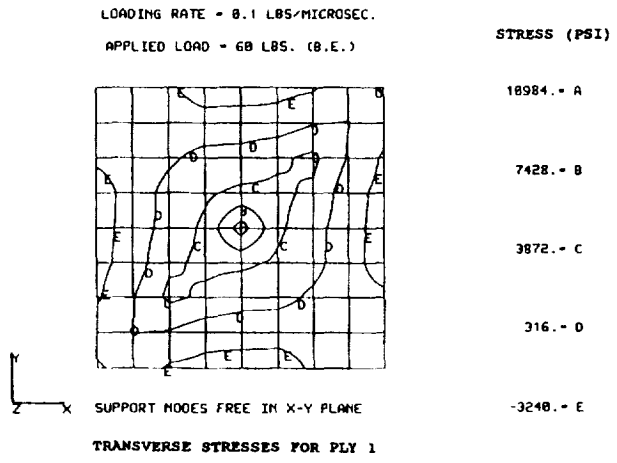

Figure 4.5: Stress contours at initial damage

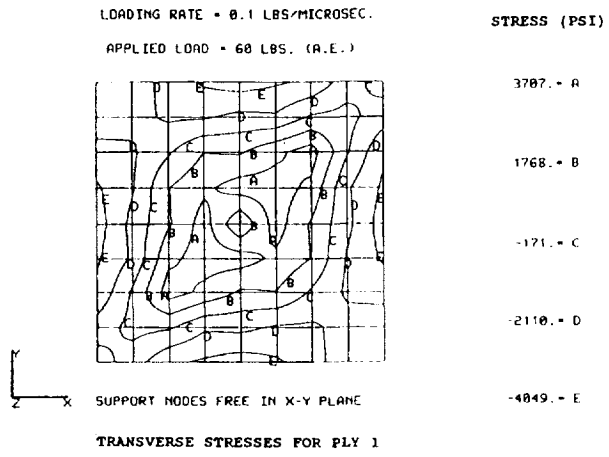

Figure 4.6: Stress contours at dynamic equilibrium after initial damage

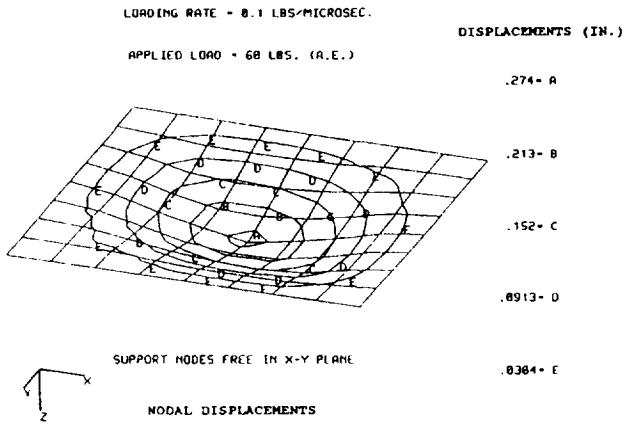

Figure 4.7: Deformed plate after initial damage

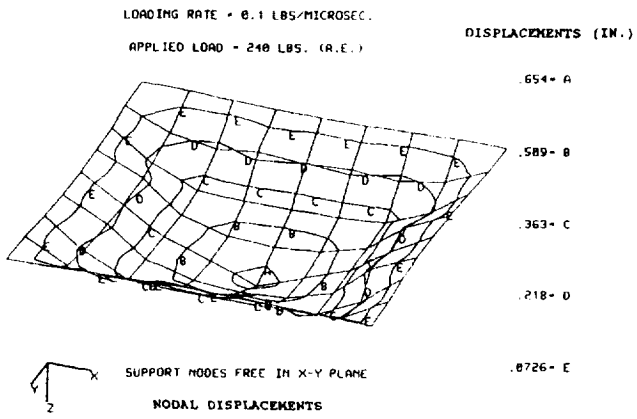

Figure 4.8: Deformed plate after damage growth

loading rate initial damage occurs at a load of 105 lbs. The maximum deflection corresponding to 105 lbs for this case is also approximately 0.07 inch. The 2.0 lbs/microsecond and 3.5 lbs/microsecond loading rates both cause the same type of response that is characterized by significant local deformations that do not engage the entire plate.

Figure 4.9 shows the deformed finite element mesh and the displacement contours corresponding to the initial damage load of 105 lbs applied at the rate of 3.5 lbs/microsecond. The initial damage mode is the transverse stress limit as in the slower loading cases. However, in this case three plies are failed simultaneously. Figures 4.10 and 4.11 show the ply 1 transverse stresses, before and after dynamic equilibrium, respectively, at the time of initial damage. Further loading after initial damage does not significantly change the displacement pattern. However, the local deformations under the load are further increased and longitudinal stress failure occurs in ply 1 at 122.5 lbs. The ply 1 longitudinal (fiber direction) stresses are shown in Figures 4.12 and 4.13, before and after dynamic equilibrium is reached by CODSTRAN. In Figure 4.12, ply 1 longitudinal stresses at the center node are seen to reach their limit. In Figure 4.13 ply 1 has failed under the load and the corresponding longitudinal ply stress at the center of the plate is zero. The corresponding finite element mesh and displacement contours are shown in Figure 4.14. It is noteworthy that ply failures that are usually initiated by the tensile stress limits, also activate the modified distortion energy failure criterion simultaneously.

Next, the same loading at the same rates is applied to the composite plate with the second type support where all boundary nodes are restrained from translation in all directions. Figure 4.15 shows the load-deflection relations for the three loading rates applied to the

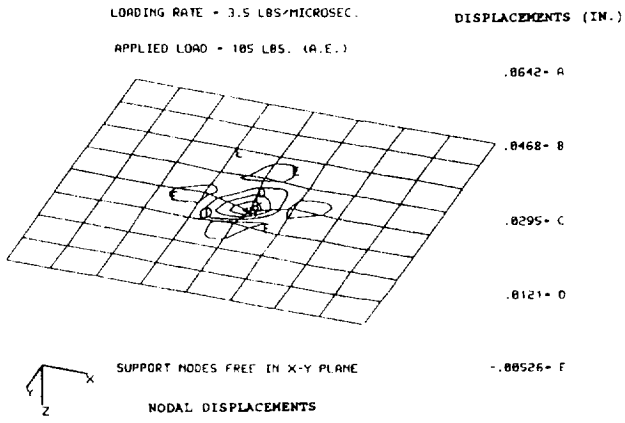

Figure 4.9: Deformed plate after initial damage

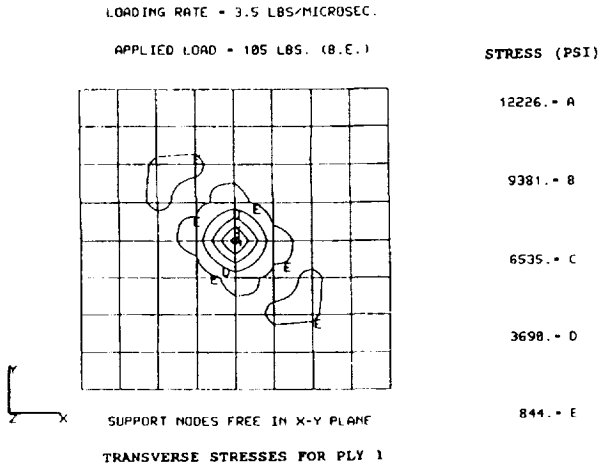

Figure 4.10: Transverse stresses at initial damage

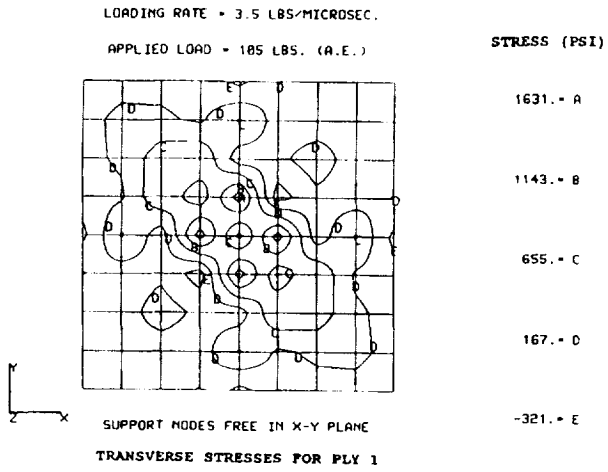

Figure 4.11: Transverse stresses at dynamic equilibrium after initial damage

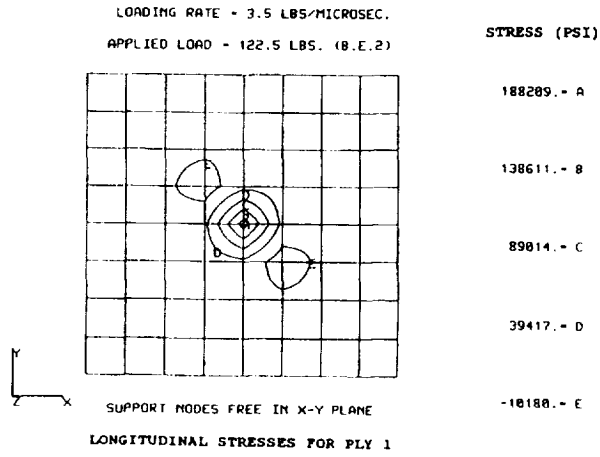

Figure 4.12: Longitudinal stresses at damage growth

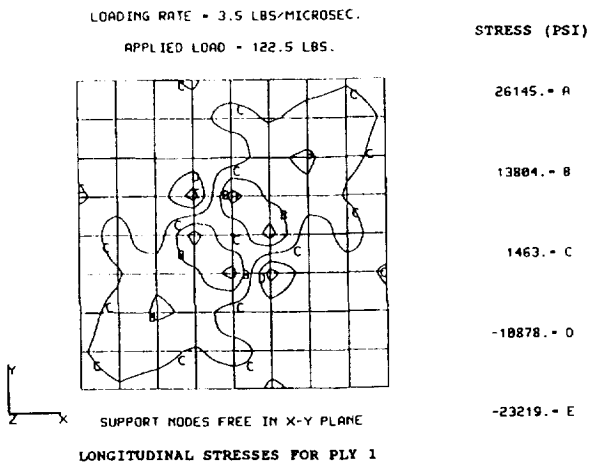

Figure 4.13: Longitudinal stresses at dynamic equilibrium after damage growth

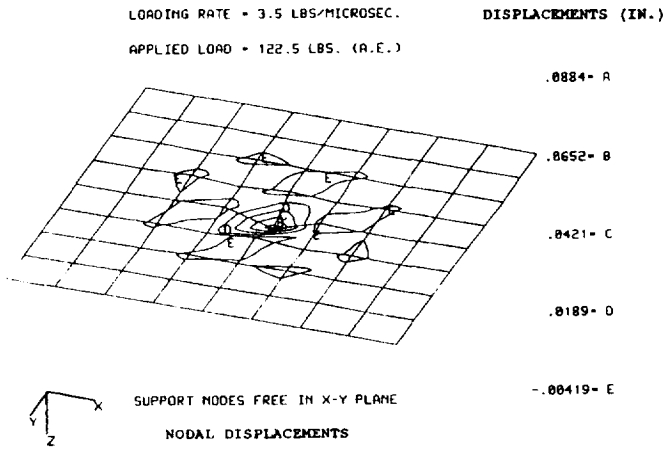

Figure 4.14: Deformed plate after damage growth

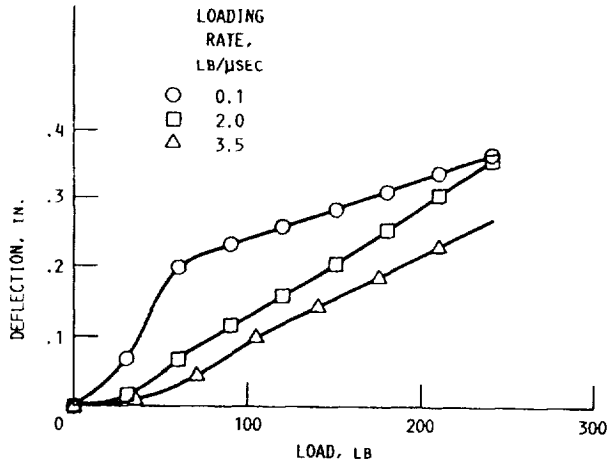

Figure 4.15: Load-displacement relationships for restrained supports

plate with the restrained supports. For the 0.1 lbs/microsecond loading rate, membrane action becomes immediately important as the entire plate is involved in the response as soon as the load is applied. The restrained boundaries do not allow the majority of the plate to participate in transverse motion. Inertial forces are negligible because the load is applied slowly. A minimum deformation is necessary before dynamic equilibrium can be reached by CODSTRAN. CODSTRAN analysis shows a 0.07 inch center deflection at the start of loading, under negligible load. During the next load increment, damage is initiated at the center node in ply 1 by reaching the stress limit in the transverse tensile stress. The 30 lbs load that initiates damage is half what was required to initiate damage under the released type support condition. This is to be expected because under restrained boundary conditions local deformations are greater under the load even though the central deflection of the plate is less. Figure 4.16 shows the transverse stresses that cause damage at the center node in ply 1. Figure 4.17 shows the same stresses at much reduced levels immediately after damage when dynamic equilibrium is reached with the new structural properties that take the damage into account. Figure 4.17 indicates zero transverse stress in ply 1 at the center node where the damage occurred. Figure 4.18 shows the deformed finite element model with values of the displacements after the initial damage. Damage growth continues gradually as the transverse stress limits are exceeded in the other plies. Ply 2 fails at 180 lbs, ply 3 fails at 210 lbs, and ply 4 fails at 240 lbs. All ply failures at this stage are in the transverse directions. Figure 4.19 shows the deformed plate with displacement contours after all plies are damaged in their transverse directions.

The restrained boundary conditions affect the structural response at higher loading rates as well. With the restrained supports, initial damage occurs at lower magnitudes of the applied

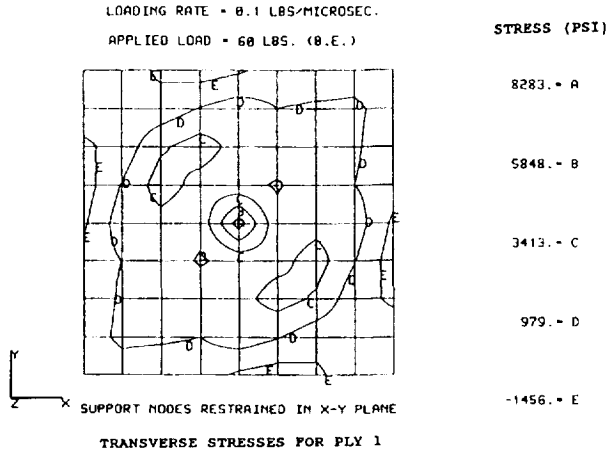

Figure 4.16: Transverse stresses at initial damage

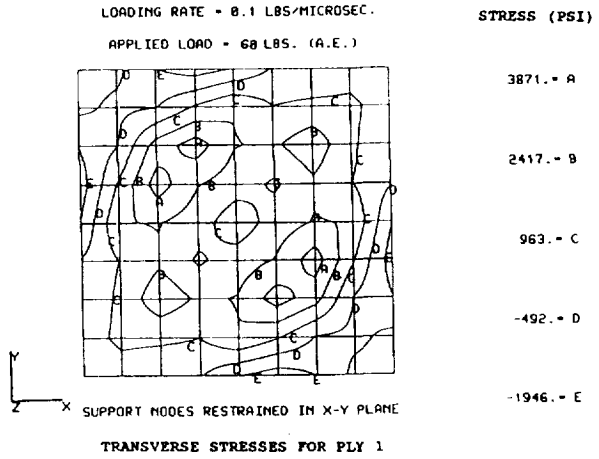

Figure 4.17: Transverse stresses at dynamic equilibrium after initial damage

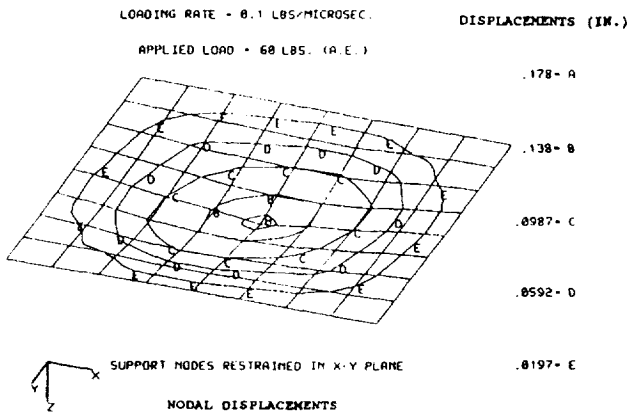

Figure 4.18: Deformed plate after initial damage

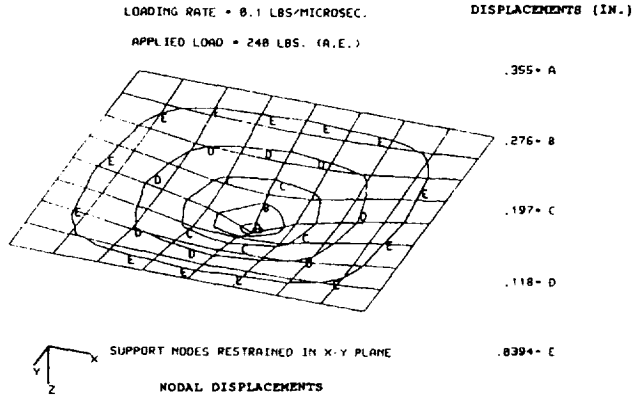

Figure 4.19: Deformed plate after damage growth

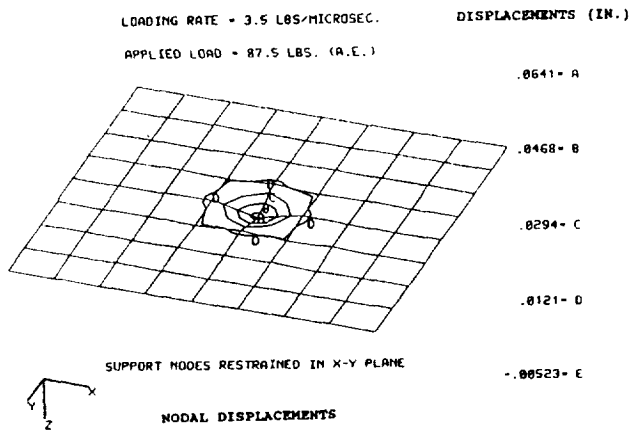

Figure 4.20: Deformed plate after initial damage

load since stresses are built up more quickly. However, the qualitative effect of the loading rate is similar in that the higher the rate of loading, the larger is the applied load to initiate damage.

Figure 4.20 shows the deformed finite element model immediately after the initiation of damage, under 87.5 lbs at 3.5 lbs/microsecond. Figure 4.20 is comparable to Figure 4.9 which shows the deformed structure at the time of initial damage by the same load under the released support conditions. Failure modes are also comparable as the first, second, and third plies fail simultaneously in their transverse directions. However, there are some differences. First, the initiation of damage under the restrained boundary conditions starts at a lower load intesity. Second, the damage region is more widespread under the restrained boundaries. Figure 4.21 shows the transverse stress contours in ply 1 immediately before equilibrium iteration by CODSTRAN at the time of damage initiation. Approximately one third of the entire plate is participating in damage. Whereas in the case of the released supports, for which initial failure stresses are depicted in Figure 4.10, initial damage was limited to the center node. For the restrained support condition, Figure 4.22 shows much lower transverse stresses in ply 1 after CODSTRAN has progressed fracture until the structure reaches dynamic equilibrium.

Additional loading after initial damage causes the fourth ply to fail in the transverse direction and the first ply to fail in the longitudinal direction at 105 lbs.

Table 4.1 summarizes the initial damage and damage growth modes for all six loading cases considered.

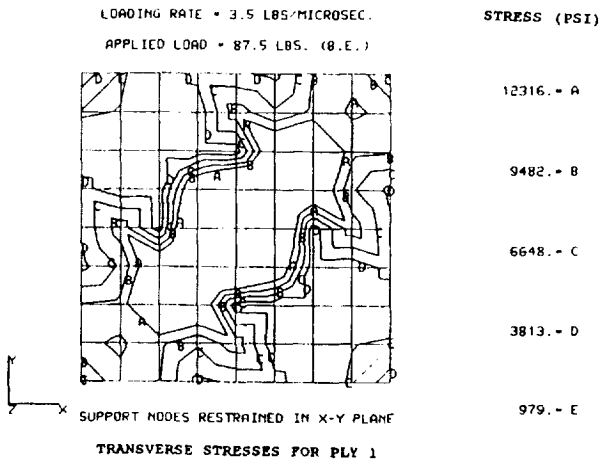

Figure 4.21: Transverse stresses at initial damage

Table 4.1: Summary of failure modes for presented results

Support boundary condition	Released			Restrained		
Loading rate, lb/μsec	0.1	2.0	3.5	0.1	2.0	3.5
Load at initial damage, lb	60	75	105	60	60	87.5
Initial damage modes	σ_{22}^T, ply 1 MDE, ply 1	σ_{22}^T, plies 1,2	σ_{22}^T, plies 1,2,3 MDE, plies 1,2	σ_{22}^T, ply 1	σ_{22}^T, plies 1,2 MDE, ply 1	σ_{22}^T, plies 1,2,3
Load at damage growth, lb	240	90	122.5	180	75	105
Damage growth modes	σ_{22}^T, plies 2,3 RR, ply 2	σ_{22}^T, ply 3	σ_{22}^T, ply 4 σ_{11}^T ply 1	σ_{22}^T, ply 2	σ_{22}^T, ply 3	σ_{22}^T, ply 4 σ_{11}^T, ply 1

Notation: σ_{22}^T - Tensile failure at transverse stress limit for ply.
σ_{11}^T - Tensile failure atlongitudinal stress limit for ply.
MDE - Failure according to modified distortion energy criterion.
RR - Failure according to relative rotation limit.

4.1 Summary

An example structure is used to demonstrate the simulation of composite behavior under different loading rates, with two different boundary support conditions. At a relatively slow loading rate the dynamic response behavior is similar to that of a static loading; as the failure mode under slow dynamic loading has all characteristics of the failure that would also occur under a statically applied loading. This static failure mode is characterized by large deflections involving most of the structure. When the loading rate is sufficiently high, inertial forces become significant and the failure mode changes to a dynamic failure mode. In the dynamic failure mode inertial forces are significant, structural deflections are small, and large deformations are localized to the impact zone. At high loading rates, overall structural deformations at the time of damage initiation do not appear to be affected by the support conditions at the boundaries. However, stresses and damage propagation are influenced significantly by the boundary conditions. If the supports are restrained, damaged zones are much more widespread. On the other hand if supports are not restrained damage zones are localized to a small region under the applied load.

Chapter 5

Composite Structures Global Fracture Toughness via Computational Simulation

A quantitative evaluation of the global fracture toughness of composites is shown as a tool for monitoring the fracture stability of composites under sustained loading. Changes in overall structural properties such as natural frequencies and the fundamental buckling load are also computed with increasing load-induced damage. Structural degradation, delamination, fracture, and damage propagation are included in the simulation. An angle-plied composite plate structure subjected to in-plane tensile loading is used as an example to demonstrate some of the features of the computational method.

In the present chapter, CODSTRAN has been augmented to compute a quantitative measure of the total global structural damage including individual ply damage and also through the thickness fracture of the laminate. The quantity of internal damage generated due to laminate ply damage at a node is computed as the tributary area of that node multiplied by the number of plies that sustain incremental damage at the node. The tributary area of a node is defined as the area enclosed by joining together the half-way points to all nodes that are adjacent to the damaged node. For example, let us consider a segment of a composite plate structure that is discretized by rectangular plate elements as shown in Figure 5.1a. The central node A is considered to sustain ply damage. The nodes B, C, D, E, F, G, H, and I are adjacent to node A. The tributary area of node A is outlined by the dashed line. For this example, the tributary area of node A is equal to the area of one of the adjacent finite elements.

In the case of through-the-thickness fracture of a node, the quantity of incremental damage at that node is taken as the number of plies multiplied by the area of the fracture zone which is the area of the polygon obtained by connecting the adjacent unfractured nodes that were directly connected to the fractured node by interelement boundaries. Referring to the example geometry depicted in Figure 5.1b; the center node A is considered to have

a through-the-thickness fracture, and the adjacent nodes are assumed not fractured. Only the nodes B, D, F, and H are connected to node A by the interelement boundaries AB, AD, AF, and AH. Accordingly, the perimeter of the fracture zone is outlined by the dashed line as shown in Figure 5.1b. For this example, the fracture zone is equal to twice the area of one of the adjacent finite elements. The definition of the fracture zone is consistent with the numerical implementation of fracture progression computation in CODSTRAN. In simulating progressive fracture, CODSTRAN deletes a fractured node and creates new separate nodes at the same location for the finite elements that previously had connectivity to the fractured node.

Total structural damage is defined as the sum of incremental contributions due to ply damage and nodal fracture. The measure of global fracture toughness is defined as a "Strain Energy Release Rate" (SERR) that is equal to the amount of energy expanded for the creation of unit damage in the structure. The magnitude of SERR varies during progressive degradation of the composite structure under loading, reflecting the changes in the fracture toughness of the laminate. Computation of SERR during progressive fracture is needed to evaluate the composite fracture toughness and the degree of imminence of failure. The concepts of composite fracture toughness and SERR have been previously used as indicators of composite structural degradation rate and stability during fracture [10], [11], [12]. In these past studies fracture toughness at an existing individual end notch or at a specific interface in the composite structure has been considered with a more traditional definition of SERR as the amount of energy expanded per unit area of crack surface created. However, the need for a more global definition of the fracture toughness of a composite structure has lead to the current global definition of SERR. CODSTRAN has the capability of predicting the locations of crack and delamination initiation as well as fracture progression and coalescence. The systematic computation of the total SERR and the corresponding quantity of damage and fracture provide valuable information for the prediction of durability of a composite structure under a given load. The emphasis of the current chapter is to implement and demonstrate a capability to compute SERR to provide a measure of global fracture toughness, considering all modes of damage and fracture during progressive degradation of composites.

SERR is computed as the ratio of incremental work expanded by the applied forces for the creation of structural damage, to the corresponding incremental damage and fracture that is generated. The traverse of a local minimum value by SERR during the progression of fracture typically precedes a very high rate of damage propagation and generally predicts the imminence of total failure. The cumulative total of the generated internal damage serves also as an index of structural degradation. The relationship between internal damage and structural properties such as natural frequencies and vibration mode shapes is useful for the in-service evaluation of the safety and reliability of composites.

For the purpose of this study an intermediate stiffness T-300/Epoxy (Thornel-300 graphite fibers in an epoxy matrix) composite structure is selected as a demonstration example. A rectangular composite plate with a small rectangular central notch is used for the computational model as shown in Figure 5.2. The finite element model consists of seventy rectangular

elements as shown in Figure 5.2. The discretization is deliberately chosen to be somewhat coarse to ensure a reasonable computer time for this demonstration example. The plate is subjected to an in-plane tensile loading in the longitudinal direction. The laminate configuration is +15/-15/-15/+15 degrees, with zero degrees corresponding to the direction of the applied loading. The progression of damage and fracture is studied for a composite plate that is 152.4 mm (6 in.) in length, 76.2 mm (3 in.) in width and 3.3 mm (0.13 in.) in thickness, with a 15.875 mm (0.625 in.) central notch as shown in Figure 5.2. The plate is laterally supported along the ends where the longitudinal tensile loading is applied but it is left free along the sides of its longer edges. This composite plate model is analyzed under a gradually applied uniform tensile load. Progressive damage and fracture are simulated as the applied loading is increased. The overall internal damage is computed, as outlined in the previous section, as a measure of composite structural degradation. Figure 5.3 shows the simulated relationship between the applied loading and the resulting total damage in the composite plate. The specific locations of damage and fracture for similar notched composite laminates under tension are shown elsewhere [4] and will not be presented here. The predicted ultimate failure load for this structure is 27.1 KN (6,086 lbs). Figure 5.3 indicates that most of the damage is created at load intensities that are near the ultimate failure load of the plate. The data points used to construct the figure are the points of equilibrium reached in the CODSTRAN incremental loading analysis procedure. Figure 5.4 shows SERR as a function of the damage created. At the stage of damage initiation there is a rather high rate of energy release that dissipates a significant portion of the strain energy stored in the composite structure before the onset of initial damage. After the first burst of energy release, SERR drops down to a much lower level, indicating the significant reduction in fracture stability of the damaged composite under the applied loading.

The non-destructive evaluation (NDE) of damage in composites is often based upon the measurement of changes in the overall structural properties such as natural frequencies, vibration modes, buckling loads, and buckling modes. Changes in the first three natural frequencies and the first buckling load are computed for this example. The buckling load is taken as a uniformly distributed compressive load applied in the reverse sense of the tensile loading.

Figures 5.5, 5.6, 5.7, and 5.8 show the degradation of the first three natural frequencies and the first buckling load as a function of the applied loading endured by the plate. These figures are consistent with Figure 5.3 in indicating that the composite structure remains undamaged until the applied loading approaches the ultimate failure load. Details of the changes in the modes of vibration and buckling for this composite plate model are shown in the previous chapter. The first vibration mode and the first buckling mode are both longitudinal modes. On the other hand, the waveforms for the second and the third vibration modes are formed in the transverse direction of the plate. As a result, the first vibration frequency and the first buckling load show much better sensitivity to structural deterioration that occurs in the transverse direction of the plate. The locations of structural damage and damage propagation are dictated by the existing central notch and the laminate ply fiber orientations.

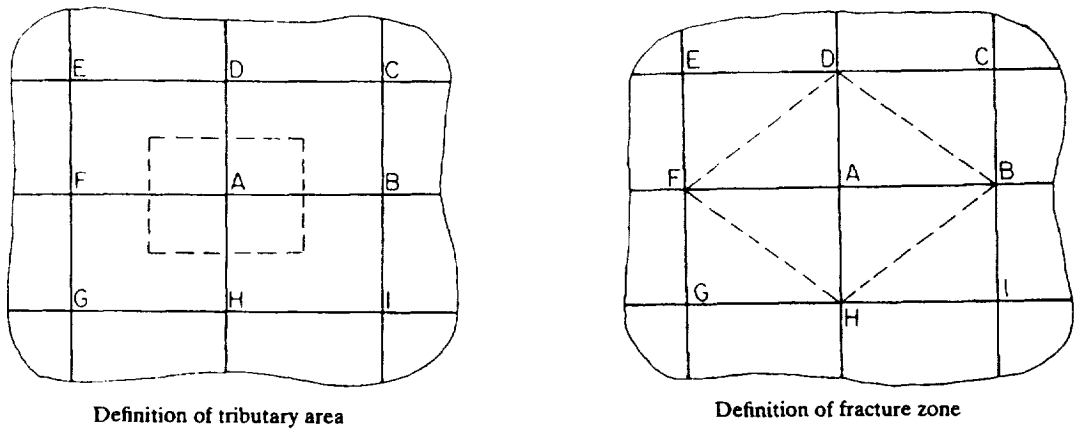

Figure 5.1: Definitions of Tributary Area and Fracture Zone of a Node

The direct relationships between the externally measurable structural properties and the load-induced internal damage are given in Figures 5.9, 5.10, 11, and 12. These last four figures indicate the sensitivities of the natural frequencies and the buckling load to progressive damage and fracture computed under the applied loading. The capability of CODSTRAN to quantify the load-induced damage in the composite structure and to relate this damage to the changes in the measurable structural properties is a key feature of the augmented code. Combining this feature with the evaluation of SERR during fracture, CODSTRAN is able to predict the quantity of internal damage as well as the fracture stability of the damaged composite laminate.

In summary, an example composite structure was used to demonstrate the simulation of composite behavior under in-plane tensile loading. With the presented simulation, a computational capability has been implemented in CODSTRAN to quantify the internal damage and SERR. The previously available capabilities of the code to simulate the behavior of composites under any loading, geometry, material combinations, fiber orientations, tailoring, and boundary conditions were maintained. The computation of the amount of the internal damage and SERR allow for a more complete evaluation of structural degradation, damage propagation, and fracture stability. CODSTRAN is also capable of computing the relationships between composite degradation, and changes in the structural properties such as natural frequencies, vibration mode shapes, and buckling loads during progressive fracture. CODSTRAN predicts the global fracture toughness of the composite structure at all stages of load induced structural degradation as the complete history of damage and fracture is simulated.

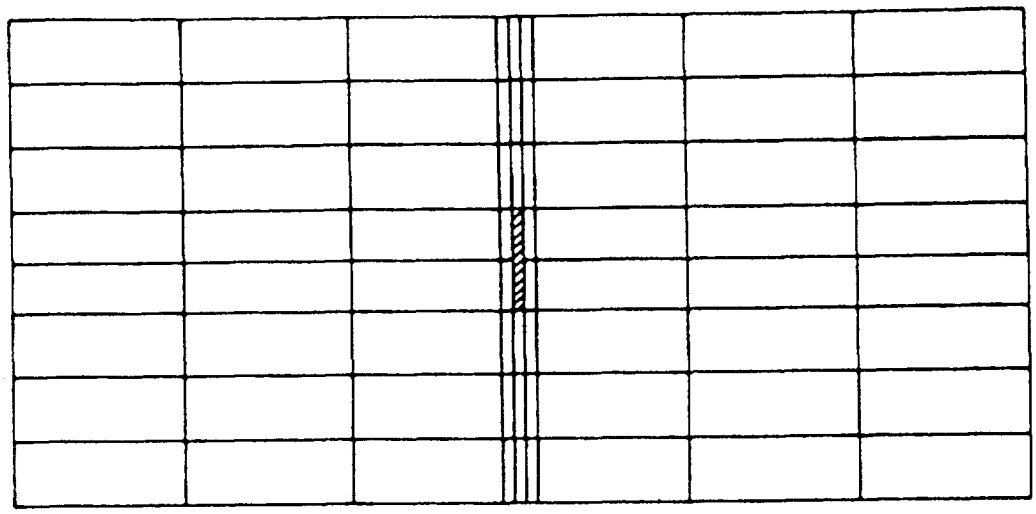

Figure 5.2: Finite Element Model

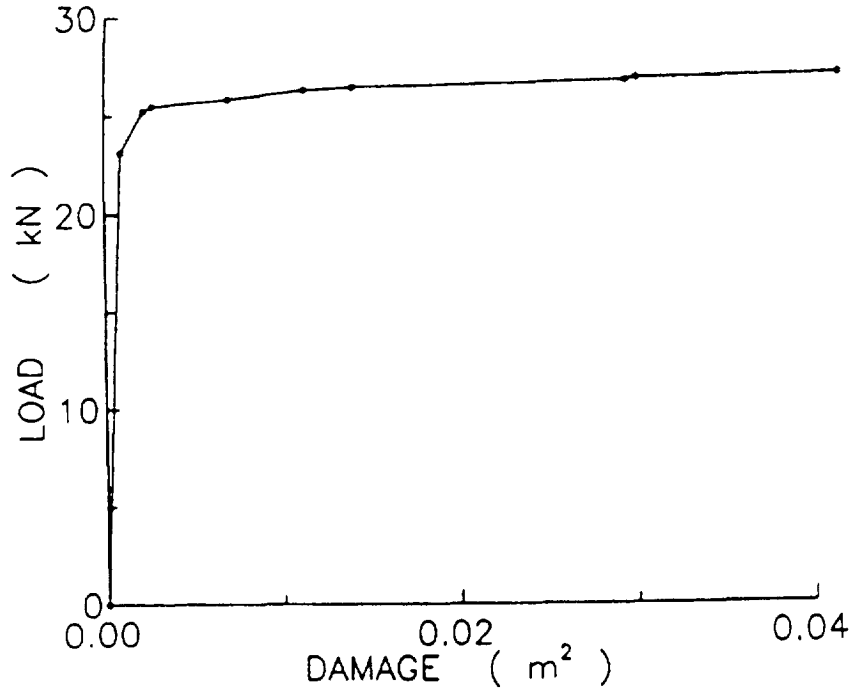

Figure 5.3: Created Damage with Applied Load

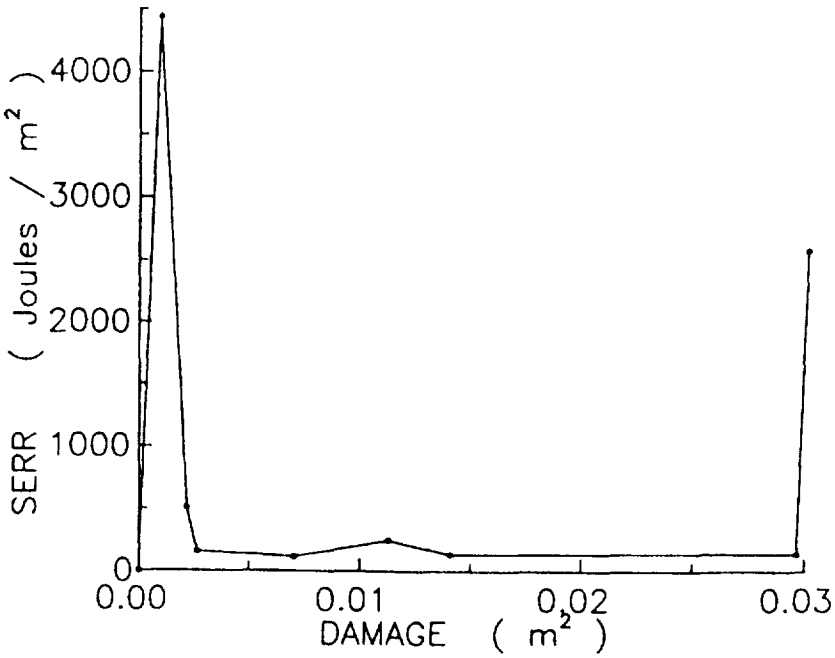

Figure 5.4: Variation of SERR with Damage

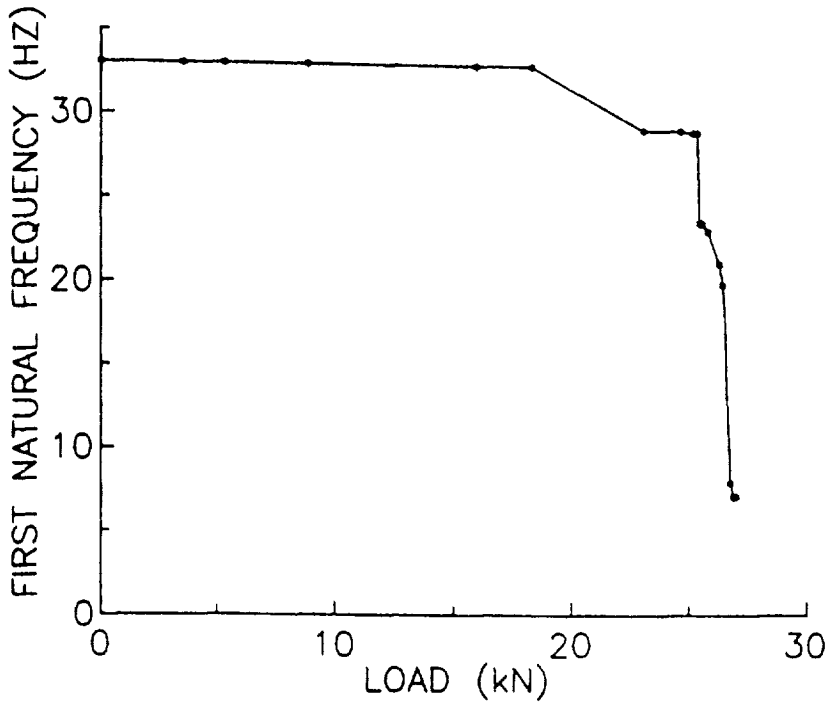

Figure 5.5: Degradation of the First Natural Frequency with Loading

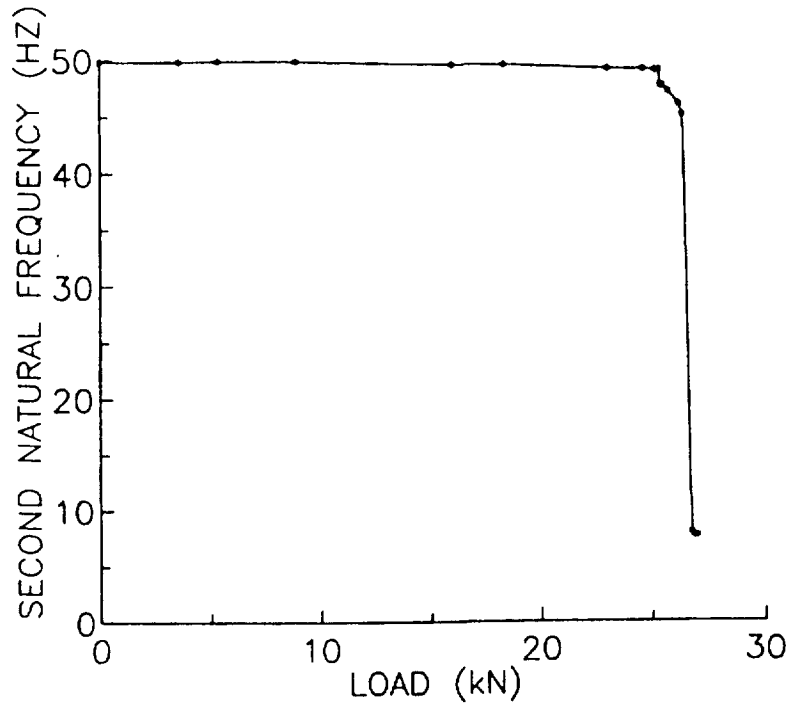

Figure 5.6: Degradation of the Second Natural Frequency with Loading

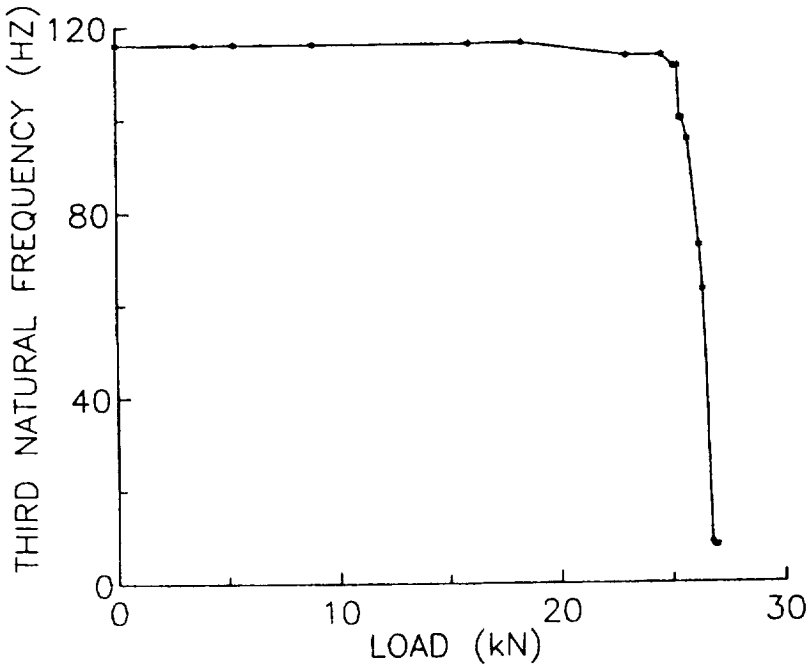

Figure 5.7: Degradation of the Third Natural Frequency with Loading

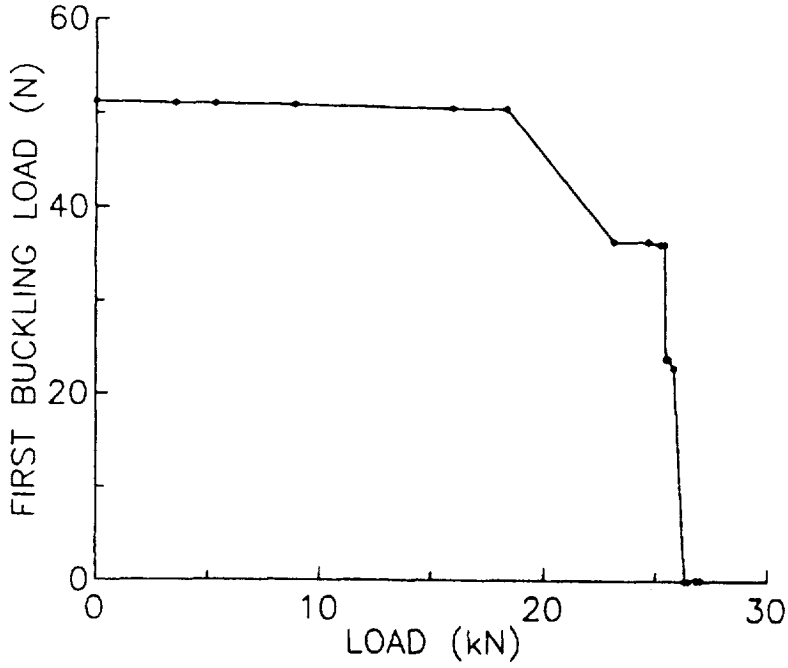

Figure 5.8: Degradation of the First Buckling Load with Loading

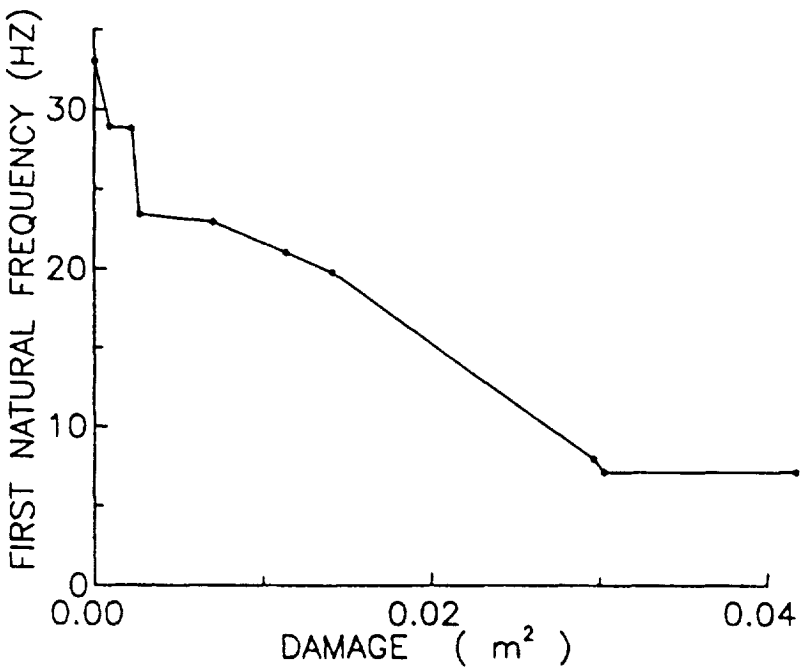

Figure 5.9: Changes in the First Natural Frequency due to Damage

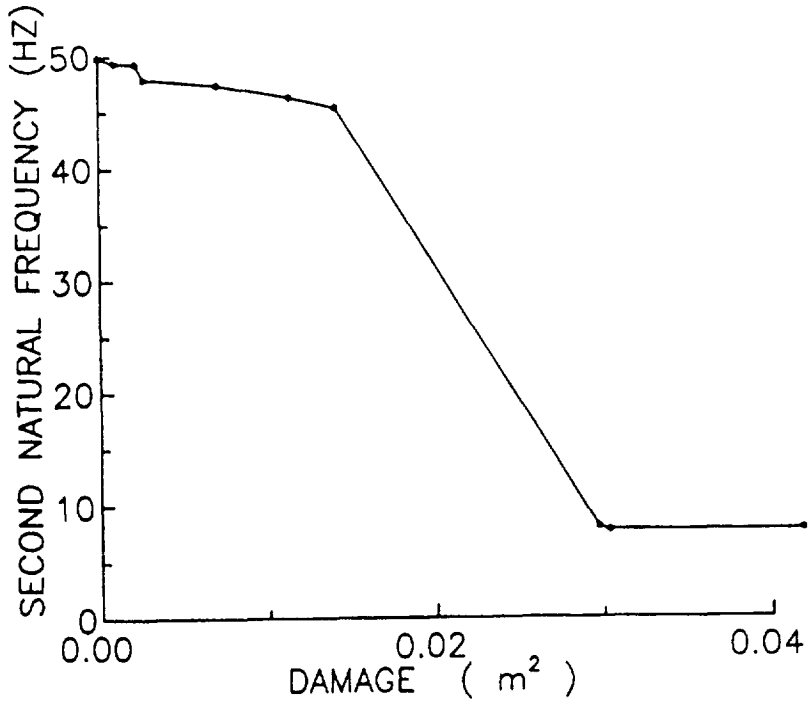

Figure 5.10: Changes in the Second Natural Frequency due to Damage

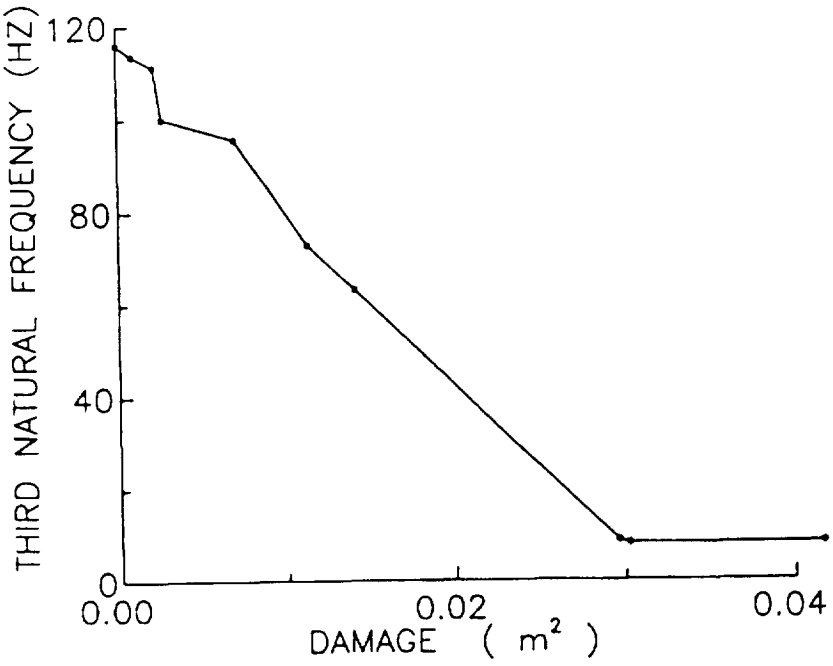

Figure 5.11: Changes in the Third Natural Frequency due to Damage

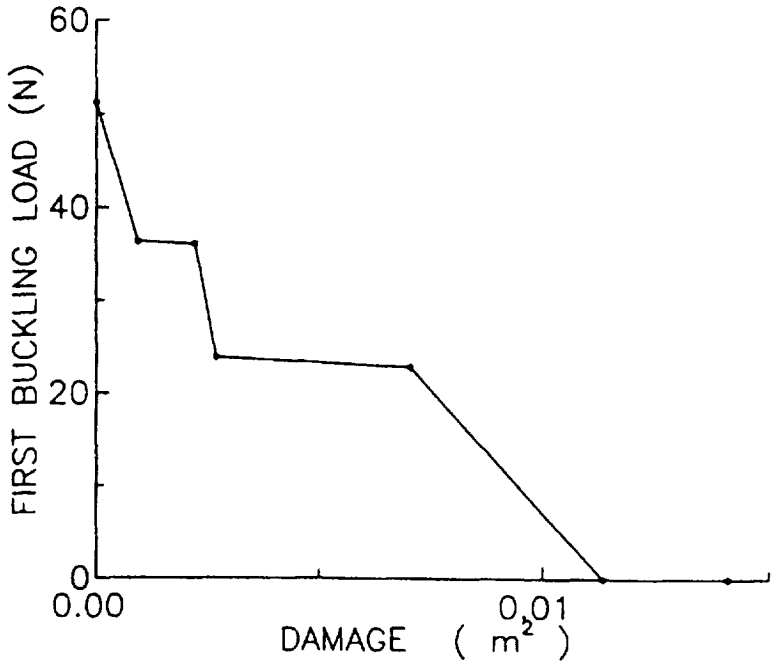

Figure 5.12: Changes in the First Buckling Load due to Damage

Chapter 6

Structural Durability of a Composite Pressure Vessel

Due to their high strength and stiffness, light weight laminated composite shells are used in many aerospace applications such as advanced aircraft fuselage and rocket motor cases. In these applications composite shells are required to withstand significant internal pressures. Any inadvertent ply damage such as transverse cracks and fiber fractures could weaken the overall structural strength and durability. It is neither practical nor feasible to design a composite shell to resist inadvertent damage at all times. A more practical approach is to allow for the existence of local defects due to accidental damage or fabrication error. It is therefore useful to quantify the reduction in the overall strength and durability of a composite structure due to preexisting defects.

The effect of local ply fiber fracture on the load carrying capability and structural behavior of a composite cylindrical shell under internal pressure is investigated. A composite system made of Thornel-300 graphite fibers in an epoxy matrix (T300/Epoxy) is used to illustrate a typical CODSTRAN durability analysis. The laminate consists of fourteen 0.127 mm (0.005 in.) plies resulting in a composite shell thickness of 1.778 mm (0.07 in.). The laminate configuration is $[90_2/\pm 15/90_2/\pm 15/90_2/\mp 15/90_2]$. The 90^o plies are in the hoop direction and the $\pm 15^o$ plies are oriented with respect to the axial direction (the global y coordinate in Figure 6.1a) of the shell. The cylindrical shell has a diameter of 1.016 m (40 in.) and a length of 2.032 m (80 in.). The finite element model contains 612 nodes and 576 elements as shown in Figure 6.1a. At one point along the circumference, at half-length of the cylinder, initial fiber fractures in two hoop plies are prescribed. The composite shell is subjected to an internal pressure that is gradually increased until the shell is fractured. To simulate the stresses in a closed-end cylindrical pressure vessel, a uniformly distributed axial tension is applied to the cylinder such that axial stresses in the shell wall are half those developed in the hoop direction. To impose the axial loading, one of the end sections is restrained against axial translation and axial tension is applied uniformly at the opposite end of the shell. The ratio of axial load to internal pressure is kept constant at all load increments.

For a structure without defects the ICAN [6] module using linear elastic laminate theory predicts that outer hoop fibers will fracture at 3.09 MPa (448 psi) internal pressure. Linear elastic laminate theory also predicts that, before hoop ply fracture, angle plies will experience matrix cracking at an internal pressure of 2.77 MPa (401 psi). The analysis presented in this chapter shows the reduction in the ultimate internal pressure because of local defects in selected plies of the composite shell structure.

Case I: Durability analysis of defect-free pressure vessel – Without imposing any initial defect, an internal pressure of 1.38 MPa (200 psi) is applied as the first load increment. Under this loading ply 1 (outermost ply) longitudinal stress is 647 MPa (93.8 ksi) and ply 14 (innermost ply) longitudinal stress is 640 MPa (92.8 ksi). Ply transverse stresses in the angle plies (± 15 degrees) vary between 44.8 MPa (6.50 ksi) in ply 3 to 43.6 MPa (6.32 ksi) in ply 12. After the first load increment the internal pressure is gradually increased. CODSTRAN simulation gives a first damage initiation pressure of 2.59 MPa (376 psi). Initial damage is in the form of matrix cracking in the outer angle plies. As the pressure is further increased, matrix cracking due to excessive transverse ply stresses prevails in all angle plies of all nodes. Ply fiber fractures occur at 3.07 MPa (445 psi), resulting in structural fracture.

Case II: Cylinder with initial fiber defect in the outer surface plies – Initial defect is prescribed in the form of fractured fibers in plies 1 and 2 (the two outermost hoop plies). Figure 6.2 shows a schematic of the laminate structure with ply numbers and locations of initial defects considered. Defect extends 127 mm (5.0 in.) along the axial direction of the shell at one node (node 307; Figure 6.1b). Table 1 shows the resulting damage progression through the thickness of the composite as well as damage growth to adjacent nodes.

Figure 6.3 depicts ply 1 longitudinal (hoop) stress ($\sigma_{\ell 11}$) contours showing the effect of fiber fracture in plies 1 and 2 at the defective node. Ply 1 longitudinal stresses are reduced to zero at that node. Ply 2 longitudinal stresses similarly diminish to zero at the same node. A significant effect of fractured fibers in plies 1 and 2 is that the shell hoop generalized membrane stresses induce local bending at the damaged node. Figure 6.4 shows the shell displacement contours with the influence of prescribed initial defects in plies 1 and 2. Radial displacements at the node with prescribed defects show a significant deviation from axial symmetry. Local displacements at the defective node are reduced significantly due to large displacements incited by the eccentricity of the hoop membrane stress resultant from the shell midsurface toward the interior of the shell. At the same time, the longitudinal stresses in plies 13 and 14 are, respectively, raised to 1.56 GPa (227 ksi) and 1.68 GPa (244 ksi), that are well above the 1.45 GPa (210 ksi) failure limit for this stress. Accordingly, CODSTRAN predicts that plies 13 and 14 experience fiber fractures subsequent to the prescribed defect in plies 1 and 2. Stresses in the remaining 10 plies remain within safe levels under the 1.38 MPa (200 psi) internal pressure. Figure 6.5 shows the displacements at equilibrium after plies 13 and 14 are also damaged. The deformed shape now has an outward bulge at the damaged node because of the weakening of the node after the four hoop plies develop fiber fractures. Excessive deformations at the two ends of the shell, depicted in Figures 6.4 and 5, are due to transition from the fixed boundary nodes to the displacements of the free interior

nodes. In this study, composite structural damage is not taken into account for the two axisymmetric rows of nodes at the two ends of the shell.

To investigate further structural degradation mechanisms, the internal pressure is gradually increased. There is no further degradation of the composite structure under as high as a 2.07 MPa (300 psi) internal pressure. The next load level to cause additional damage corresponds to an internal pressure of 2.30 MPa (333 psi). On the first iteration at 2.30 MPa internal pressure, transverse ply stresses in plies 3, 4, 7, 8, and 11 are raised, respectively, to the levels of 94.5, 91.7, 91.2, 90.8, and 90.6 MPa (13.7, 13.3, 13.2, 13.2, and 13.1 ksi), all exceeding the 89.9 MPa (13.0 ksi) strength limit for $\sigma_{\ell 22T}$ computed by the ICAN module, causing transverse tensile failures in these plies, as indicated in Table 1. On the second iteration under the same loading, the hoop plies 6, 9, and 10 fail in ply longitudinal tension (hoop tension). Simultaneously, the remaining angle ply (ply 12) fails in transverse tension. On the third iteration, the last remaining hoop ply (ply 5) fails in tension in both longitudinal and transverse directions. In addition, plies 13 and 14 sustain additional damage accumulation according to the Modified Distortion Energy (MDE) failure criterion. On the fourth iteration the angle plies (3, 4, 7, 8, 11, and 12) sustain additional damage due to high levels of $\sigma_{\ell 12}$ (in-plane shear) stresses. On the fifth iteration equilibrium is reached under the 2.30 MPa (333 psi) internal pressure.

When the pressure is further increased to 2.53 MPa (367 psi), nodes 306 and 308 that are adjacent to node 307 in the hoop direction (Figure 6.1b) sustain damage. On the first iteration, at 2.53 MPa internal pressure, all six angle plies at node 306 and the angle plies 3, 4, 7, 8, and 11 at node 308 fail in transverse tension. On the second iteration, all hoop plies at node 306, and the hoop plies 9, 10, 13, and 14 at node 308 fail in longitudinal tension. Also, the remaining angle ply (ply 12) at node 308 fails in transverse tension. On the third iteration, all angle plies at node 306 sustain additional damage accumulation due to high levels of in-plane shear stresses. At node 308, the hoop plies 1, 2, 5, and 6 fail in both longitudinal and transverse tension. On the fourth iteration all angle plies at node 308 sustain additional damage due to high in-plane shear stresses. On the fifth iteration equilibrium is reached under the 2.53 MPa (367 psi) internal pressure as there is no additional damage.

The next level of pressure to cause additional damage is at 2.61 MPa (379 psi) that causes ply 3 to fail in transverse tension at nodes 239 and 303. Although the composite structure is able to reach equilibrium at this load, the internal pressure cannot be increased significantly above this level without causing extensive damage in the composite shell. The displacement contours at this load level are shown in Figure 6.6. A significant portion of the shell is involved in the deformation pattern of the damaged region. It will be shown that this pressure level corresponds to impending structural fracture due to damage propagation.

Case III: Initial fiber defect in the inner surface plies – The opposite two hoop plies adjacent to the interior surface of the shell (plies 13 and 14) are prescribed to be defective. The overall results are very similar to Case II. Immediately after plies 13 and 14 are assigned the prescribed fiber defect, plies 1 and 2 fail in longitudinal tension and ply 3 fails in transverse tension. The subsequent damage progression follows the pattern of Case II.

Case IV: Initial fiber defect in the interior hoop plies near mid-thickness of shell – A significantly different degradation behavior is observed if the hoop plies near the mid-surface of the shell are the defective ones. Table 2 shows the damage progression due to initial fiber defects in plies 9 and 10. In this case, the prescribed defect does not cause the shell membrane stress resultant to develop a significant eccentricity, allowing the node with initial damage to resist damage progression up to an internal pressure of 2.38 MPa (344 psi). Figure 6.7 shows ply 1 longitudinal stresses at an internal pressure of 2.38 MPa that causes damage initiation by fiber fracturing in ply 1. Ply 1 $\sigma_{\ell 11}$ stresses at node 307 exceed the limiting value of 1.45 GPa (210 ksi) for the ply longitudinal stress. Because of ply damage under these stresses, CODSTRAN degrades the composite structural properties and reanalizes under the same loading. Figure 6.8 shows ply 1 $\sigma_{\ell 11}$ stresses after the second iteration at the same loading. Ply 1 longitudinal stresses are diminished to zero at the damaged node because of ply fiber fracture. Figure 6.8 also indicates the stress concentration patterns along the generator of the cylindrical shell and around the hoop, emanating from the defective node. If the 2.38 MPa internal pressure is exceeded, the damage progression mode changes to rapid propagation, involving multiple through-the-thickness laminate fractures resulting in the structural fracture of the shell.

Figure 6.9 shows the relationship between structural damage and the applied internal pressure for Cases II and IV. In Case IV, corresponding to initial defect in plies 9 and 10, there is insignificant damage growth from 1.38 MPa (200 psi) to 2.30 MPa (333 psi) internal pressure. However, there is a rather significant amount of damage from 2.30 MPa (333 psi) to 2.38 MPa (344 psi) internal pressure. Above the 2.38 MPa internal pressure, the damage progression rate becomes even greater, as the ultimate fracture load is reached. On the other hand, in Case II, corresponding to initial defect in plies 1 and 2, local damage growth at the defective node is significant below the 2.30 MPa (333 psi) internal pressure. Yet, above the 2.30 MPa pressure, Case II shows considerably greater resistance to damage propagation as compared to Case IV. The ultimate pressure for Case II is 2.61 MPa (379 psi). The ultimate pressure for Case III is the same as in Case II.

Figure 6.10 shows the strain energy release rate (SERR) as a function of the internal pressure for Cases II and IV. SERR is defined as the work done during structural degradation per unit volume of the damaged composite structure. SERR may be used as a measure of global fracture toughness for the assessment of damage tolerance of a composite structure [13]. SERR is computed at structural degradation levels beginning with through-the-thickness damage growth and progressing to structural fracture. In Case II, the SERR remains sufficiently high up to an internal pressure of 2.61 MPa (379 psi), indicating substantial resistance to global fracture up to this load level. However, immediately after the 2.61 MPa pressure level is exceeded, SERR drops to a very low level, indicating negligible resistance to global fracture after this stage. In Case IV, SERR drops to a low level immediately after the prescribed damage has progressed through the thickness of the shell at 2.38 MPa (344 psi).

The distinction between the fracture modes of Cases II and IV is shown in Figure 6.11 by plotting the SERR as a function of the induced damage. In Case II damage progression is

gradual with stable damage growth and accumulation that develops over many load increments. On the other hand Case IV indicates sudden/catastrophic fracture by rapid damage propagation during the two load increments immediately following damage initiation. The significantly higher damage level for Case IV at the time of structural fracture indicates that in Case IV, structural damage and fracture involve a substantial portion of the composite structure rather suddenly at the onset of structural fracture.

Table 3 shows the internal pressures corresponding to damage initiation and also corresponding to ultimate structural fracture. For the shell without initial defect both linear elastic laminate theory and CODSTRAN analysis (Case I) results are given. CODSTRAN results are given also for the shell with outer or inner surface fiber defect (Case II or III) and for the shell with mid-thickness fiber defect (Case IV). The ultimate structural fracture pressure of 3.07 MPa predicted by CODSTRAN for a composite shell without defect (Case I) is used as a reference. CODSTRAN predicts that initial damage will commence at 2.59 MPa or 84 percent of ultimate fracture loading for a defect-free shell. In case of prescribed fiber defect at surface hoop plies, first damage initiation starts at a pressure of 1.38 MPa (200 psi) or at 45 percent of the reference ultimate pressure, followed by structural fracture at 2.61 MPa (379 psi) or 85 percent of the reference loading. If initial fiber defect is in the hoop plies near the midsurface, first damage initiation is at an internal pressure of 2.30 MPa (333 psi) or 75 percent of the reference load, followed quickly by structural fracture at 2.38 MPa (344 psi) or 77 percent of the reference load.

The significant results from this investigation in which CODSTRAN (COmposite Durability STRuctural ANalysis) is used to evaluate damage growth and propagation to fracture of a thin composite shell subjected to internal pressure are as follows:

1. CODSTRAN adequately tracks the damage growth and subsequent propagation to fracture for initial defects located at the outer part, inner part, or in the mid-thickness of the shell.

2. Initial defect located in the outer part (outer surface defect) begins to grow at a lower pressure but exhibits localized gradual damage growth prior to structural fracture.

3. Initial defect located in the inner part (inner surface defect) shows an overall damage progression and fracture behavior closely similar to that of the outer surface defect.

4. Initial defect located near the mid-thickness of the shell (mid-thickness defect) requires a higher pressure to cause damage initiation. However, once the damage initiation pressure is reached, a sudden structural fracture stage is entered by rapid damage propagation at a slightly higher pressure. This structural fracture pressure is lower than that corresponding to a surface defect.

5. Inner or outer surface fiber defect reduces the ultimate internal pressure to 85 percent of the fracture pressure of a defect-free shell. Mid-thickness fiber defect reduces the ultimate pressure to 77 percent of the defect-free shell fracture pressure. With reference to the same defect-free fracture pressure, initial damage occurs at 45 percent pressure

for surface hoop ply initial defect and at 75 percent pressure for mid-thickness hoop ply initial defect.

Table 6.1: Damage Progression Due to Initial Defect in Plies 1 and 2 Composite Shell T300/Epoxy[$90_2/\pm 15/90_2/\pm 15/90_2/\mp 15/90_2$]

Pressure (MPa)	Iteration No.	Node with Damage	Plies with New Damage	New Damage Due to
1.379	1	307	1, 2	$\sigma_{\ell 11T}$, $\sigma_{\ell 13}$
	2	307	13, 14	$\sigma_{\ell 11T}$
2.298	1	307	3,4,7,8,11	$\sigma_{\ell 22T}$, RR
	2	307	6, 9, 10	$\sigma_{\ell 11T}$
		307	12	$\sigma_{\ell 22T}$, RR
	3	307	5	$\sigma_{\ell 11T}$, $\sigma_{\ell 22T}$, MDE, RR
		307	13, 14	$\sigma_{\ell 11C}$, MDE
	4	307	3,4,7,8,11,12	$\sigma_{\ell 12}$
2.528	1	306	3,4,7,8,11,12	$\sigma_{\ell 22T}$, RR
		308	3,4,7,8,11	$\sigma_{\ell 22T}$, RR
	2	306	1,2,5,6,9,10,13,14	$\sigma_{\ell 11T}$
		308	9,10,13,14	$\sigma_{\ell 11T}$
		308	12	$\sigma_{\ell 22T}$, RR
	3	306	3,4,7,8,11,12	$\sigma_{\ell 12}$
		308	1,2,5,6	$\sigma_{\ell 11T}$, $\sigma_{\ell 22T}$, MDE
	4	308	3,4,7,8,11,12	$\sigma_{\ell 12}$
2.613	1	239	3	$\sigma_{\ell 22T}$, RR
		303	3	$\sigma_{\ell 22T}$, RR
2.625	1	239	8	$\sigma_{\ell 22T}$, RR
	2	239	12	$\sigma_{\ell 22T}$, RR
2.628	1	303	8	$\sigma_{\ell 22T}$, RR
		311	11	$\sigma_{\ell 22T}$, RR
	2	303	12	$\sigma_{\ell 22T}$, RR
		311	4, 7	$\sigma_{\ell 22T}$ (Ply 4 also RR)
	3	311	3	$\sigma_{\ell 22T}$, RR

Conversion Factor: 1 MPa = 145.04 psi

Notation: $\sigma_{\ell 11T}$ - ply longitudinal tensile stress
$\sigma_{\ell 22T}$ - ply transverse tensile stress
$\sigma_{\ell 12}$ - ply in-plane shear stress
$\sigma_{\ell 13}$ - ply longitudinal shear stress
MDE - modified distortion energy failure criterion
RR - delamination due to relative rotation

Table 6.2: Damage Progression Due to Initial Defect in Plies 9 and 10 Composite Shell T300/Epoxy[$90_2/\pm 15/90_2/\pm 15/90_2/\mp 15/90_2$]

Pressure (MPa)	Iteration No.	Node with Damage	Plies with New Damage	New Damage Due to
1.379	1	307	9, 10	$\sigma_{\ell 11T}$, $\sigma_{\ell 13}$
2.298	1	307	3	$\sigma_{\ell 22T}$, RR
2.375	1	274	1	$\sigma_{\ell 22T}$
		304	14	$\sigma_{\ell 22T}$
		307	1, 2	$\sigma_{\ell 11T}$
			4	$\sigma_{\ell 22T}$, RR
		310	1	$\sigma_{\ell 22T}$
	2	307	6, 13, 14	$\sigma_{\ell 11T}, MDE$
			13, 14	MDE (ply 13 also RR)
			7,8,11,12	$\sigma_{\ell 22T}$, MDE, RR
	3	307	5	$\sigma_{\ell 11T}$, $\sigma_{\ell 22T}$, MDE, RR
	4	307	3,4,7,8,11,12	$\sigma_{\ell 12}$
2.400	1	307	3,4,7,8,11,12	$\sigma_{\ell 11C}$

Conversion Factor: 1 MPa = 145.04 psi

Notation: $\sigma_{\ell 11T}$ - ply longitudinal tensile stress
$\sigma_{\ell 11T}$ - ply longitudinal tensile stress
$\sigma_{\ell 22T}$ - ply transverse tensile stress
$\sigma_{\ell 12}$ - ply in-plane shear stress
$\sigma_{\ell 13}$ - ply longitudinal shear stress
MDE - modified distortion energy failure criterion
RR - delamination due to relative rotation

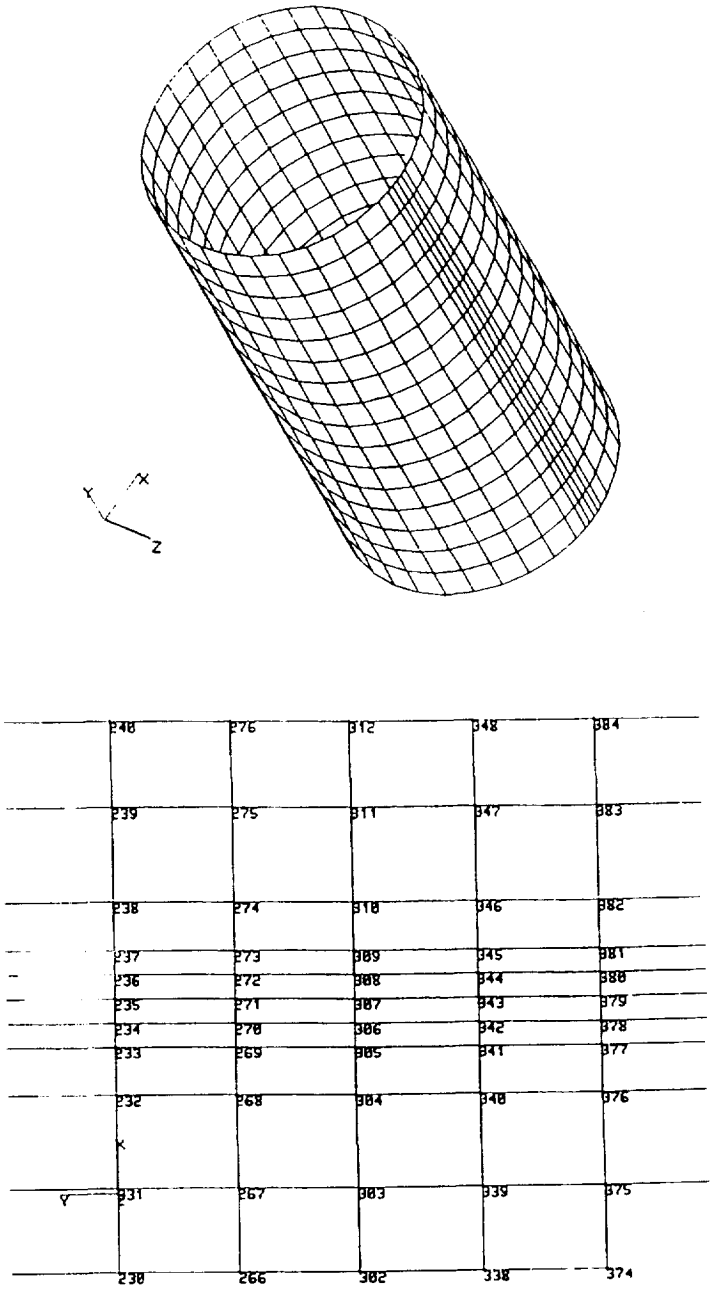

Figure 6.1: Finite Element Model and Nodes in the Damaged Region; Composite Shell T300/Epoxy$[90_2/\pm 15/90_2/\pm 15/90_2/\mp 15/90_2]$

Table 6.3: Internal Pressures at First Damage Growth and Structural Fracture Composite Shell T300/Epoxy[$90_2/\pm15/90_2/\pm15/90_2/\mp15/90_2$]

	Internal Pressure (MPa)			
	Linear Elastic Laminate Theory	CODSTRAN		
		Without Initial Damage	Initial Damage in Surface Ply Fibers	Initial Damage in Mid-thickness Ply Fibers
First Damage Growth	2.765	2.590	1.379	2.298
Ultimate Structural Fracture	3.086	3.068	2.613	2.375

Conversion Factor: 1 MPa = 145.04 psi

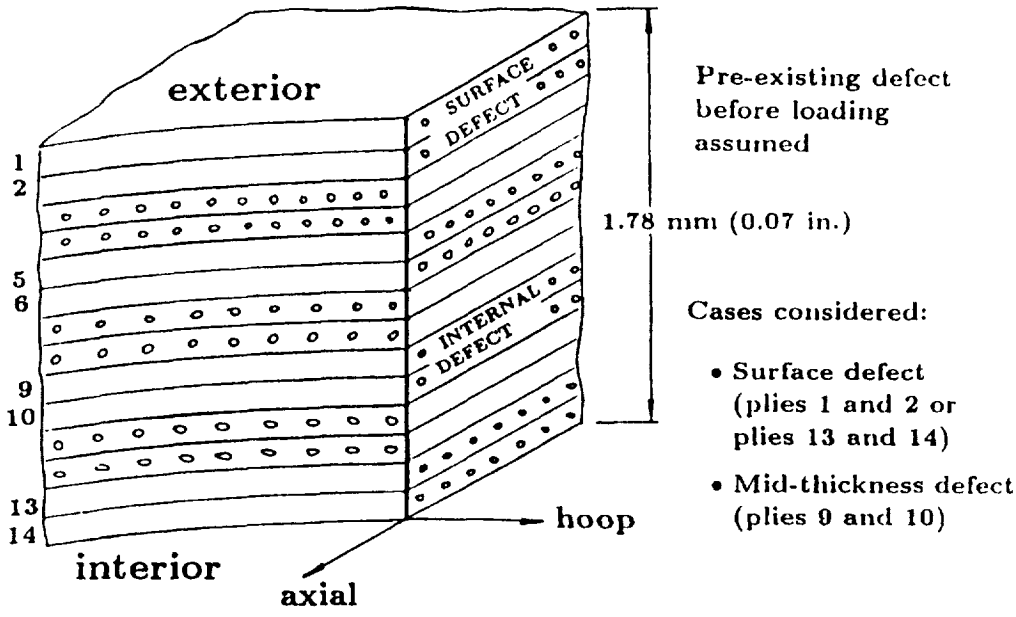

Figure 6.2: Laminate Structure Schematic; Composite Shell T300/Epoxy[$90_2/\pm15/90_2/\pm15/90_2/\mp15/90_2$]

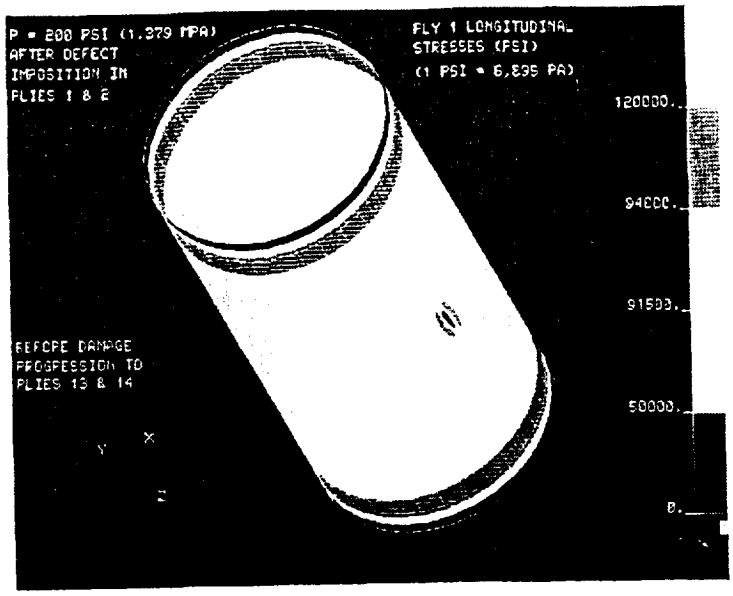

Figure 6.3: Ply 1 Longitudinal Stresses after Initial Fracture of Plies 1 and 2; Composite Shell T300/Epoxy$[90_2/\pm 15/90_2/\pm 15/90_2/\mp 15/90_2]$

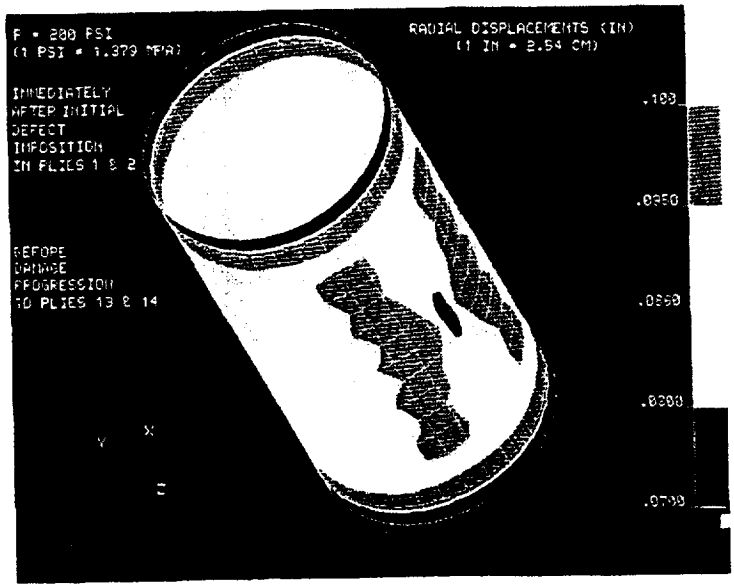

Figure 6.4: Radial Displacements after Initial Fracture of Plies 1 and 2; Composite Shell T300/Epoxy$[90_2/\pm 15/90_2/\pm 15/90_2/\mp 15/90_2]$

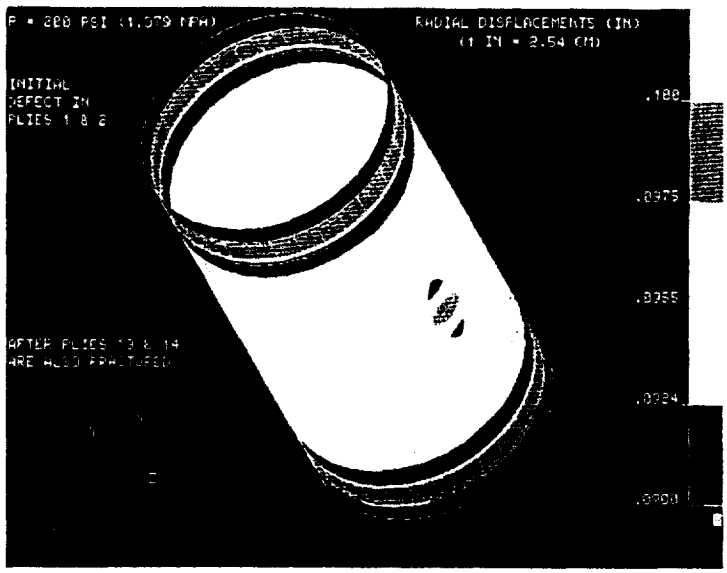

Figure 6.5: Radial Displacements after Damage Progression to Plies 13 and 14; Composite Shell T300/Epoxy[$90_2/\pm 15/90_2/\pm 15/90_2/\mp 15/90_2$]

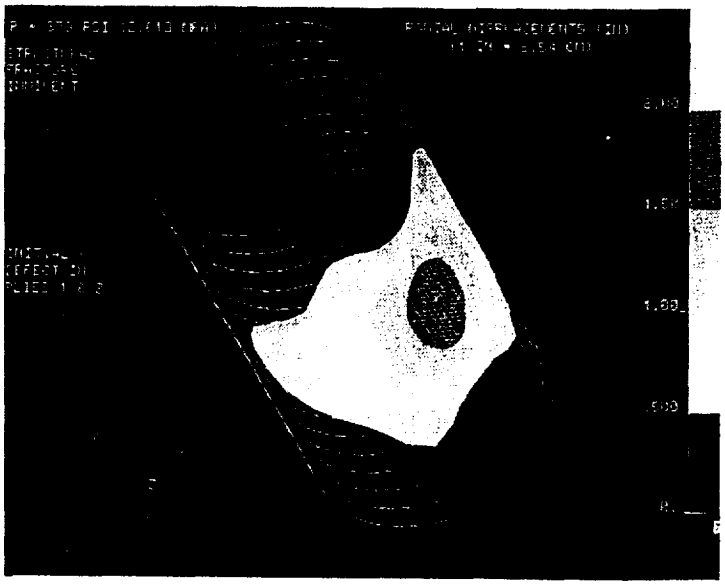

Figure 6.6: Radial Displacements at 2.613 MPa (379 psi) Internal Presssure; Composite Shell T300/Epoxy[$90_2/\pm 15/90_2/\pm 15/90_2/\mp 15/90_2$]

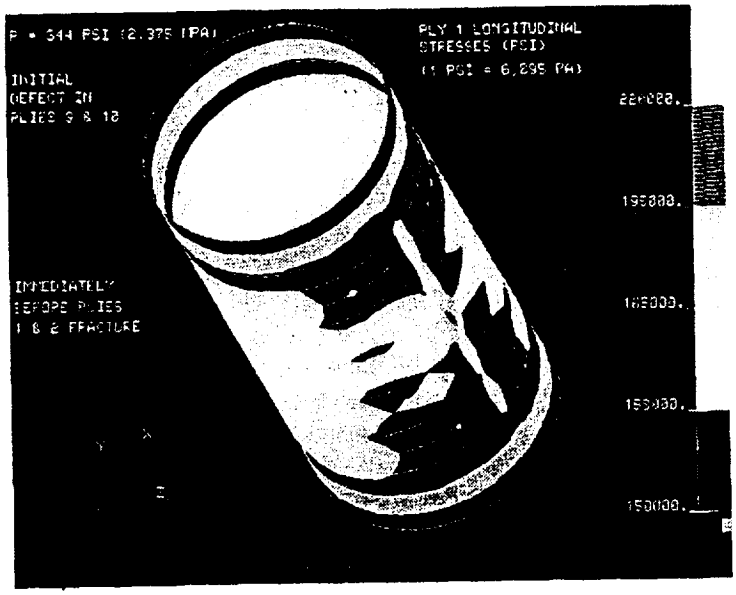

Figure 6.7: Ply 1 Longitudinal Stresses at 2.375 MPa; before Ply 1 Fractures; Composite Shell T300/Epoxy$[90_2/\pm 15/90_2/\pm 15/90_2/\mp 15/90_2]$

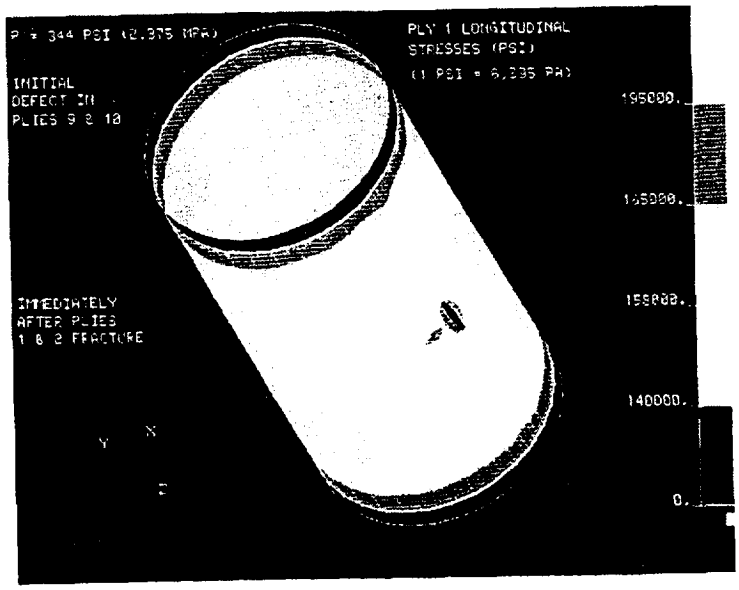

Figure 6.8: Ply 1 Longitudinal Stresses at 2.375 MPa; after Ply 1 Fractures; Composite Shell T300/Epoxy$[90_2/\pm 15/90_2/\pm 15/90_2/\mp 15/90_2]$

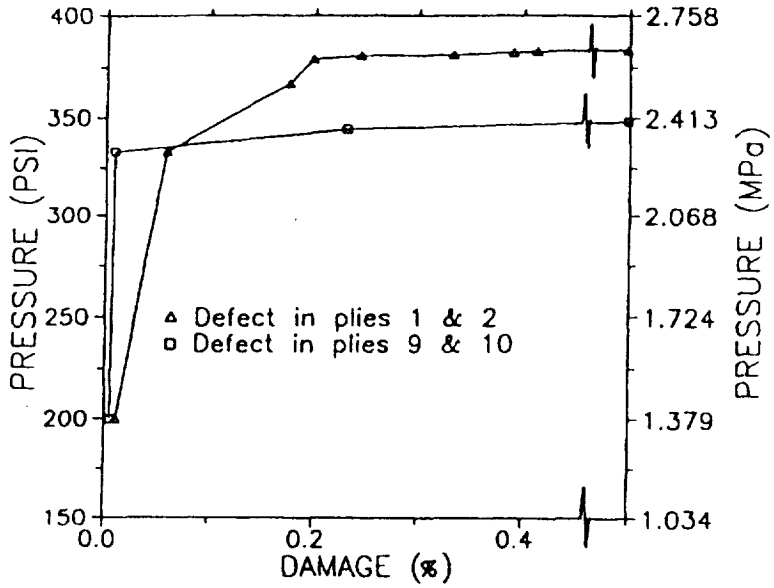

Figure 6.9: Damage Propagation with Pressure; Composite Shell T300/Epoxy[$90_2/\pm15/90_2/\pm15/90_2/\mp15/90_2$]

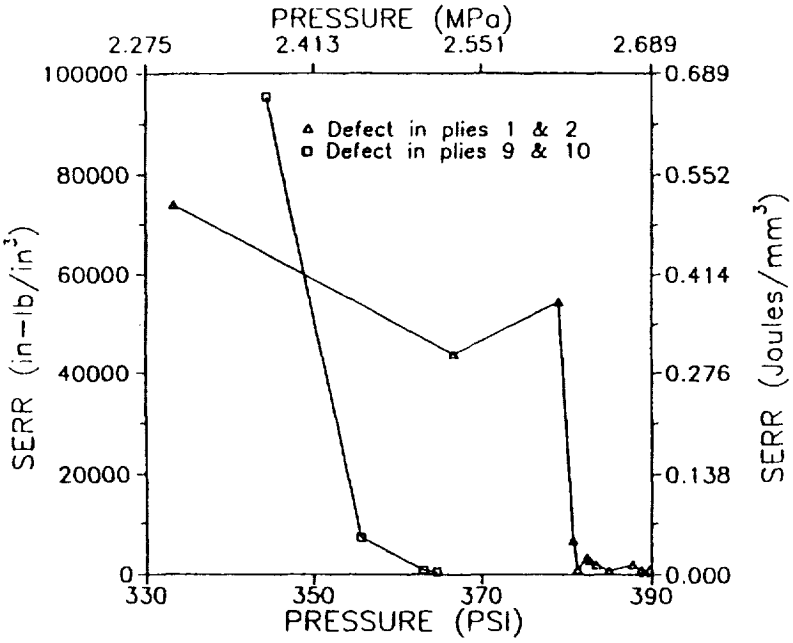

Figure 6.10: Strain Energy Release Rate with Pressure; Composite Shell T300/Epoxy[$90_2/\pm15/90_2/\pm15/90_2/\mp15/90_2$]

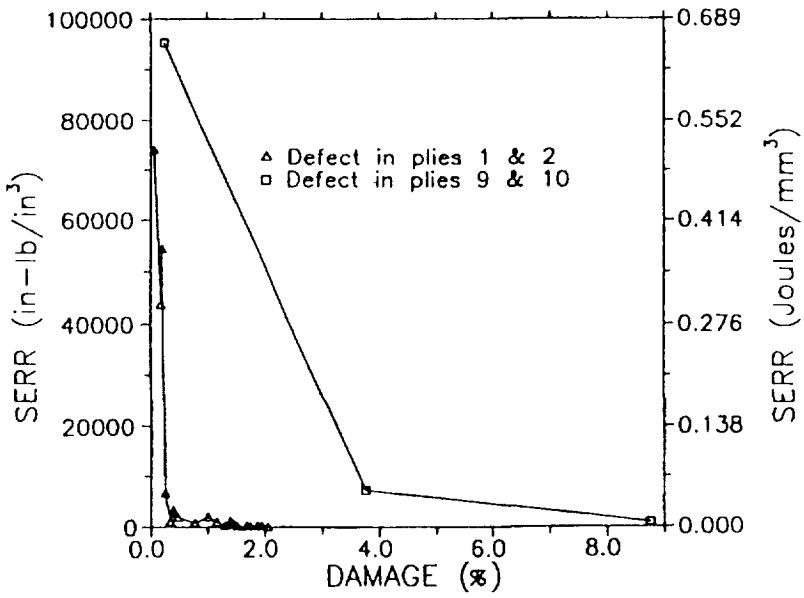

Figure 6.11: Strain Energy Release Rate with Damage; Composite Shell T300/Epoxy[$90_2/\pm 15/90_2/\pm 15/90_2/\mp 15/90_2$]

Chapter 7

Progressive Fracture in Composites Subjected to Hygrothermal Environment

The influence of hygrothermal environmental conditions on the load carrying ability and response of composite structures are investigated via computational simulation. The COD-STRAN code is utilized for the simulation of composite structural degradation under loading. Damage initiation, damage growth, fracture progression, and global structural fracture are included in the simulation. Results demonstrate the significance of hygro-thermal effects on composite structural response, toughness, and durability.

7.1 Introduction

Composite structures lend themselves to tailoring to achieve desirable characteristics such as a high strength to weight ratio and dimensional stability under extreme thermal and hygral fluctuations. Applications of composites in airframes, engine structures, space structures, marine and surface transportation structures, and high precision machinery require near flawless structural performance even when exposed to adverse loading and environmental effects during service.

Design specifications require accurate prediction of composite properties under the expected range of environmental conditions. Structural response characteristics and durability of composites depend upon their exposure to various hygro-thermal conditions as well as mechanical loading. Accordingly, a helpful tool for the design of composite structures is the simulation of the response of a structure possessing arbitrary material properties, under any loading or environmental effects. The design of laminated composite structures requires the prediction of overall structural properties, damage resistance, fracture toughness, and durability, given the constituent thermo-mechanical properties and fiber orientations. The effects of static, dynamic, point impact, shock pressure, cyclic fatigue, and thermal loading, as well as that

of the hygro-thermal environment are often important design concerns.

In polymer-matrix composites, effects of the hygro-thermal environment are primarily observed in the matrix properties. Composite strength is closely related to the strength and orientations of the fibers. Nevertheless, matrix properties have a fundamental effect on damage resistance and structural durability. Matrix properties are a deciding factor with respect to the location and nature of damage initiation, damage growth, and subsequent damage progression. For most composite structures, initial damage occurs in the matrix material as transverse tensile failure or shear failure depending on geometry and loading.

7.2 Background and Objective

The effect of the hygro-thermal environment on the performance of composites has been the subject of numerous investigations. Simplified procedures for incorporating hygro-thermal effects into composite behavior have been given [14]. Experimental and numerical results relating the hygro-thermal effects on flexural and interlaminar strength and defect growth in composites have been reported [15]. The influence of hygro-thermal effects on the free-edge delamination in composites has been investigated [16]. Hygro-thermal effects have been included in an optimal design procedure for composite turbine blades [17]. Effects of the hygro-thermal environment on damping properties of composites have been investigated [18]. Hygro-thermal effects have been included in the formulation of design procedures for fiber composite structural components and joints [19]. The Integrated Composite ANalyzer (ICAN) code has incorporated hygro-thermal effects in the prediction of through-the-thickness stress-strain relationships and strength of laminated composites [6]. The fatigue of fiber composite structures under hygrothermomechanical cyclic loading has also been investigated [20].

Previous investigations of hygro-thermal effects on composites have concentrated on the effects of temperature and moisture on composite structural properties and damage initiation propensity. The objective of the current chapter is to extend the investigation of hygro-thermal effects with regard to structural durability and with regard to the changes in structural properties as composite degradation occurs. Existing validated computational infrastructures are used to simulate the changes in structural durability, and degradation behavior of overall composite structural properties under loading, in relation to the hygro-thermal conditions. The effects of moisture and temperature on mechanical properties of composite constituents are taken into account in the composite mechanics module (ICAN) [6].

In this chapter, the step size criterion is set so that no more than four nodes may be damaged in any iteration cycle during the application of a load increment.

7.3 Example Composite Structures and Analysis

Three composite systems are studied. An intermediate stiffness, T-300/Epoxy composite laminate is selected as a first example. A rectangular composite plate that is 152.4 mm (6 in.) long, 76.2 mm (3 in.) wide and 0.51 mm (0.02 in.) thick, with a 15.88 mm (0.625 in.) central notch is used (Figure 7.1a). The finite element model consists of seventy rectangular four-node isoparametric shell elements [7] as shown in Figure 7.1b. The plate is subjected to a uniaxial in-plane tensile loading. The laminate configuration is $+15/-15/-15/+15$ degrees, with zero degrees corresponding to the direction of the applied loading. The plate is clamped at one end, laterally supported along the opposite end where the tensile loading is applied, and unsupported along the remaining two sides. Progressive damage and fracture evolve as the applied loading is increased. Changes in the first three natural frequencies and the first buckling load are computed. The buckling load is taken as a uniformly distributed compressive load applied in the reverse sense of the tensile loading. The overall internal damage is computed as a measure of composite structural degradation. Six cases of temperature and moisture combinations are considered. Service temperatures of 21.11, 93.33, and 148.89°C (70, 200, and 300°F) are considered with moisture contents of either 0 or 1 percent. The progression of damage and fracture is evaluated for each case.

Table 7.1 shows the total tensile load carried by the composite at four different stages of loading under varied hygro-thermal conditions. Of the given four loading stages, the initial fracture load is defined as the load to initiate a through-the-thickness laceration of the composite at one node. There may be degradation due to ply damage prior to the through-the-thickness fracture of the laminate. The secondary fracture load is the load that causes either propagation of the initial fracture or initiation of fracture at another location. The critical load is the load corresponding to the minimum value of the strain energy release rate (SERR) during fracture progression. As defined in reference Chapter 4, the minimum value of the SERR represents a critical stage of loading that signals the approach of global fracture. CODSTRAN analysis indicates that composite structures may show some additional resistance to increased loading after the critical load. However, in an actual loading condition, damage propagation induces load fluctuations and the structure is not likely to survive beyond the critical load. This is due to the low level of SERR at this stage, indicating that the structure is showing little resistance against fracture propagation. The global fracture load is the final load at which CODSTRAN predicts the laminate is broken apart into two pieces under static loading.

Figure 7.2 shows the relationship between the applied loading and the resulting internal damage in the composite for the temperature and moisture combinations considered. The individual load-damage curves terminate when the composite plate is broken into two pieces. The applied loading is the total in-plane tensile load in the longitudinal direction of the plate. Figure 7.2 indicates that the overall strength of the composite structure is reduced with increasing temperature. In general, it is observed that increasing moisture also reduces the structural strength. However, the effect of moisture on strength becomes more important at higher temperatures. For temperatures of 21.11 or 93.33°C (70 or 200°F) at either zero

or one percent moisture content, initial damage happens at the same load level. However, damage growth and fracture progression vary considerably. When the service temperature is 148.89°C (300°F), initial damage starts under a lower loading.

The overall quantity of damage includes individual ply damage as well as through-the-thickness fracture of the composite laminate. The details of damage computation are given in Chapter 4. The definition of damage is such that the composite structure would be considered 100 percent damaged if all plies of all nodes were to develop some damage. In general, global fracture or structural fracture will occur before the 100 percent damage level is reached. Computed results up to impending global fracture of the composite structure are presented as described below.

Figures 7.3, 7.4, 7.5, and 7.6 show the changes in the first three natural frequencies and the first buckling load, respectively, as functions of the applied load and also as functions of the load-induced damage for the six hygro-thermal conditions considered. An interesting observation from these figures is that the case corresponding to the most severe hygrothermal environment considered (148.89°C temperature and one percent moisture) shows the least sensitivity of its structural properties to damage. The reason for this is that the reduction of matrix moduli due to moisture and temperature makes part of the composite structure more compliant without showing excessive changes in the global structural response. However, the adverse hygro-thermal conditions also degrade the strength of the overall structure; resulting in the separation of the composite into two pieces under a lower loading, as seen from Table 7.1. For the case of one percent moisture, at the 148.89°C temperature, the apparent structural response properties remain considerably high even when the composite is being torn into two pieces. This phenomenon is because the restrained half of the composite laminate has absorbed most of the damage and fracture due to overconstrained boundary conditions, and the computed vibration frequencies represent merely the other half of the structure that has been spared degradation.

A second example uses the same T-300/Epoxy composite as in the first example. However, the ply fiber orientations are changed to 0/90/90/0 degrees with respect to the loading direction. The combinations of loading and environmental conditions are the same as in the first case. Figure 7.7 shows the relationships between the applied load and the produced damage for this composite. Table 7.2 shows the four loading stages corresponding to initial and secondary fracture, critical stage, and global fracture, under the six hygro-thermal conditions considered. Strength of the composite structure is considerably lower compared to the first example because half of the plies have their fibers orthogonal to the direction of loading in this case. Also, the difference between the damage initiation load and the global fracture load is less than the first example because of fiber orientation. Higher temperature and moisture levels significantly reduce the strength of the composite as usual. Figures 7.8 through 7.11 show changes in the first three natural frequencies and the first buckling load in relation to the applied load and also in relation to the load-induced damage.

For a third example, a composite structure with the same geometry and fiber orientations as in the first case but made of a different composite system is considered. The composite

system for the third example is S-Glass/high modulus, high strength epoxy matrix system (S-Glass/HMHS). Figure 7.12 shows the relationships between loading and damage for the six hygrothermal conditions on the S-Glass/HMHS composite. This composite shows a more nonlinear behavior with a more uniform distribution of structural damage. Because of the lower fiber strength, initial damage starts at a lower load compared to the T-300/Epoxy composite with the same $(\pm 15)_s$ fiber orientations. Table 7.3 shows the four load levels for the six hygro-thermal conditions on the S-Glass/HMHS composite. The effects of increasing temperature and moisture are to lower the overall structural strength as in the previous cases. However, the degradation process is more complex. Figures 7.13 through 7.16 depict the changes in the first three natural frequencies and in the first buckling load, respectively, as functions of the applied load and also as functions of the induced damage. At a service temperature of 148.89°C, the fundamental vibration frequency and the first buckling load are temporarily increased after damage. The fluctuations in the natural frequencies and the fundamental buckling load are because of changes in the composite structure from its original plane geometry due to load-induced damage and distortions. Changing the geometric shape of the composite structure causes significant changes in the fundamental vibration and buckling modes that reverberate to the changes in the corresponding natural frequencies and the buckling load. For this particular example, the first vibration mode and the first buckling mode both have their maximum amplitudes at the geometric center of the plate where the initial notch is located [22]. However, when the geometry is significantly distorted, mode shapes change such that the maximum amplitudes split and move to the sides of the plate away from the notch, increasing the first natural frequency and the first buckling load significantly. If the applied loading is further increased, damage propagation in the distorted regions cause a relief from some of the distortion and cause the maximum modal amplitudes to shift back to the center notch location; thus, the affected natural frequencies and the first buckling mode are reduced back to lower levels. The process continues in cycles as out of plane distortions are formed and relieved repeatedly between the notch and the edge of the plate due to gradually increased loading.

Load induced geometric distortions are significant only at the highest temperature considered. At increased temperatures the polymer-matrix becomes less brittle and redistributes stress more effectively. This thermal softening effect is more pronounced in the S-Glass/HMHS composite because the composite behavior is more strongly influenced by the matrix properties. These results are not surprising since hygro-thermal loading is assumed to influence only the matrix properties.

7.4 Conclusions

Computational simulation shows that the strength of a composite structure is in general decreased with increasing temperature and moisture. Also, in general, ductility is increased and stiffness is decreased with increasing temperature. On the other hand, increasing the moisture content does not improve ductility because moisture does not have as much of a

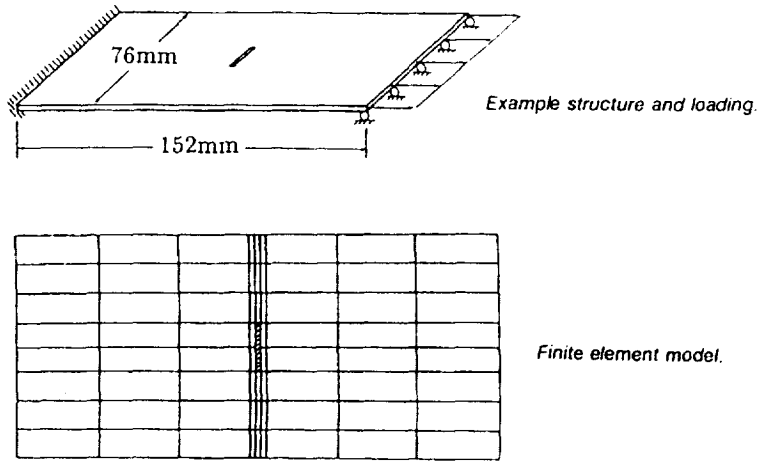

Figure 7.1: Example Structure with Loading and Finite Element Model

softening effect as temperature in the constitutive relationships. Lower temperatures make the composite structure more brittle and facilitate local fracture. As it is observed from the present results, there are exceptions to all of these generalizations.

It would have been difficult to quantify the overall effects of hygro-thermal conditions on structural behavior, damage initiation, and fracture propagation for the specific cases, without the computational simulation capability. The CODSTRAN computer code, using verified micromechanics definitions of material laws, takes into account the effects of temperature and moisture in the prediction of structural behavior and structural durability of composites.

The evaluation of damage in composites is often based upon the measurement of changes in the overall structural properties such as natural frequencies, vibration modes, buckling loads, and buckling modes. Hygro-thermal conditions affect the structural response. For reliable interpretation of NDE measurements under varied environmental conditions it is requisite to evaluate the effects of temperature and moisture on structural behavior. The present computational simulation method illustrates the computation of changes in overall composite properties and durability due to variations in temperature and moisture.

This paper demonstrates that computational simulation, with the use of established composite mechanics and finite element methods, can be used to predict the effects of temperature and moisture, as well as loading, on structural properties and durability of composites.

Table 7.1: T300/Epoxy (±15)s Hygrothermal Environment and Loads.

Temperature (^oC)	Moisture (%)	Initial Fracture Load (kN)	Secondary Fracture Load (kN)	Critical Load (kN)	Global Fracture Load (kN)
21.11	0	23.13	26.29	27.58	27.58
21.11	1	23.13	26.29	27.58	27.97
93.33	0	23.13	25.42	26.94	27.10
93.33	1	23.13	24.71	26.20	26.42
148.89	0	19.18	22.34	24.31	24.83
148.89	1	18.38	19.44	22.69	22.69

Table 7.2: T300/Epoxy (0,90)s Hygrothermal Environment and Loads.

Temperature (^oC)	Moisture (%)	Initial Fracture Load (kN)	Secondary Fracture Load (kN)	Critical Load (kN)	Global Fracture Load (kN)
21.11	0	16.01	18.38	18.38	18.38
21.11	1	16.01	17.20	18.64	18.67
93.33	0	17.20	18.31	18.94	18.94
93.33	1	12.46	15.88	16.00	17.52
148.89	0	12.46	13.51	13.51	14.87
148.89	1	10.08	11.27	12.24	13.29

Table 7.3: S-Glass/HMHS (±15)s Hygrothermal Environment and Loads.

Temperature (^oC)	Moisture (%)	Initial Fracture Load (kN)	Secondary Fracture Load (kN)	Critical Load (kN)	Global Fracture Load (kN)
21.11	0	19.18	20.76	25.20	26.85
21.11	1	20.76	24.00	24.72	27.10
93.33	0	21.16	21.86	23.87	26.37
93.33	1	21.16	24.65	23.93	28.47
148.89	0	19.04	19.39	20.61	22.17
148.89	1	15.88	16.58	21.86	21.92

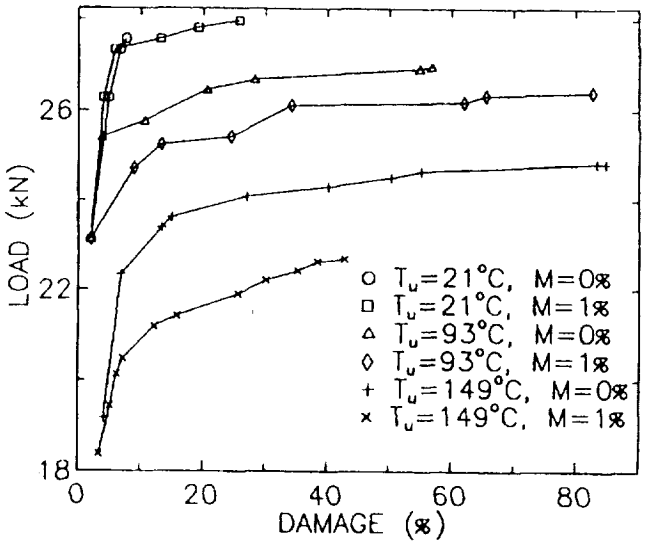

Figure 7.2: T-300/Epoxy $(\pm 15)_s$ Created Damage with Loading

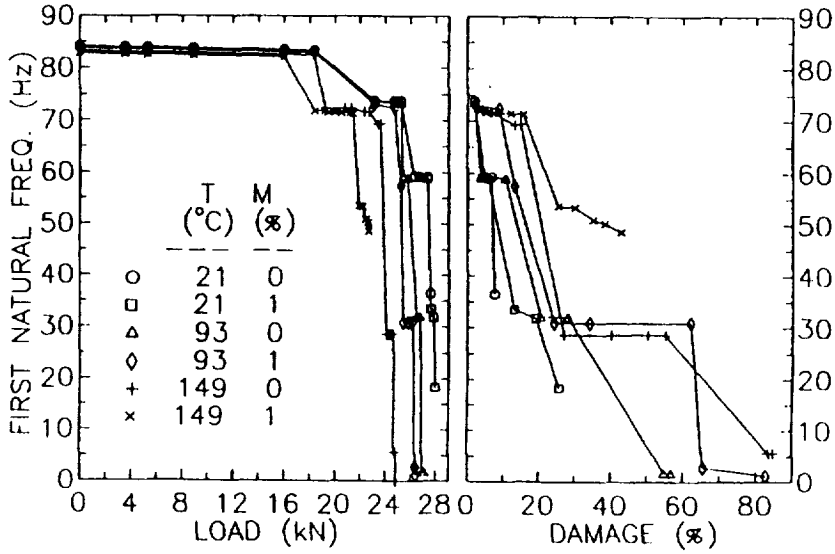

Figure 7.3: T-300/Epoxy $(\pm 15)_s$ Degradation of the First Natural Frequency

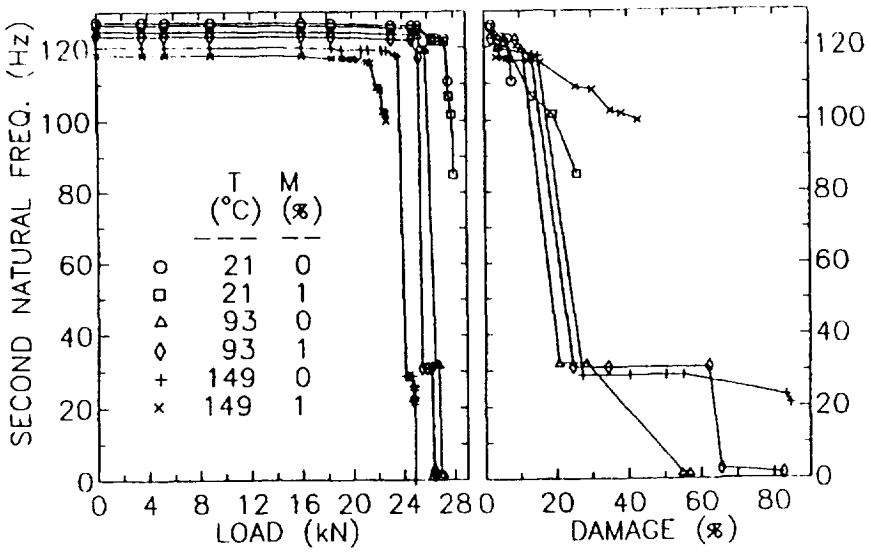

Figure 7.4: T-300/Epoxy $(\pm 15)_s$ Degradation of the Second Natural Frequency

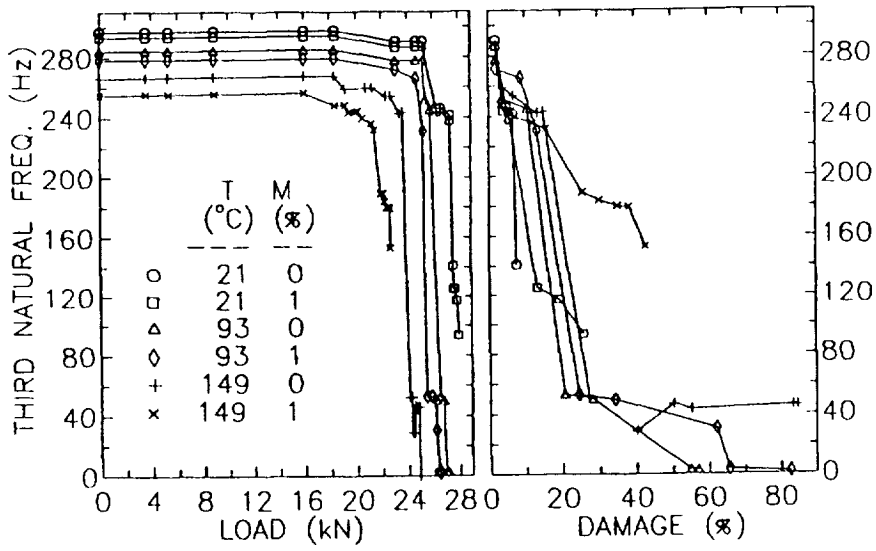

Figure 7.5: T-300/Epoxy $(\pm 15)_s$ Degradation of the Third Natural Frequency

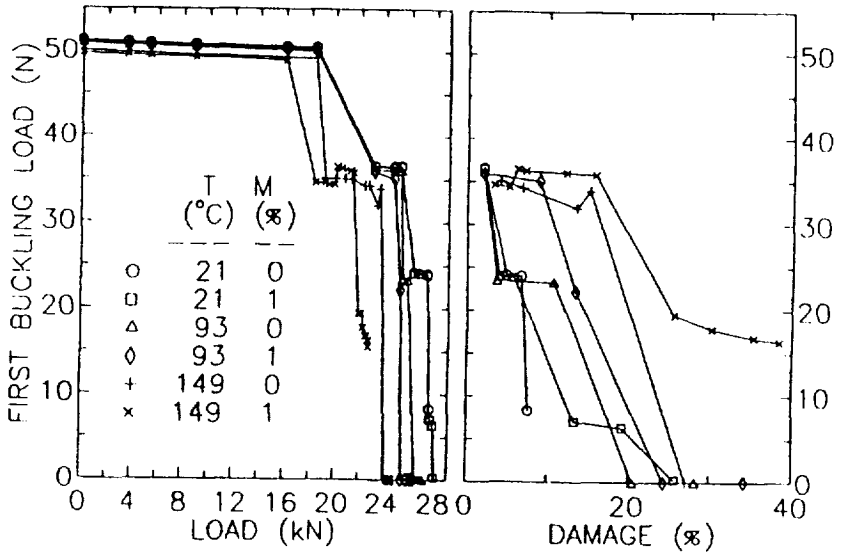

Figure 7.6: T-300/Epoxy $(\pm 15)_s$ Degradation of the First Buckling Load

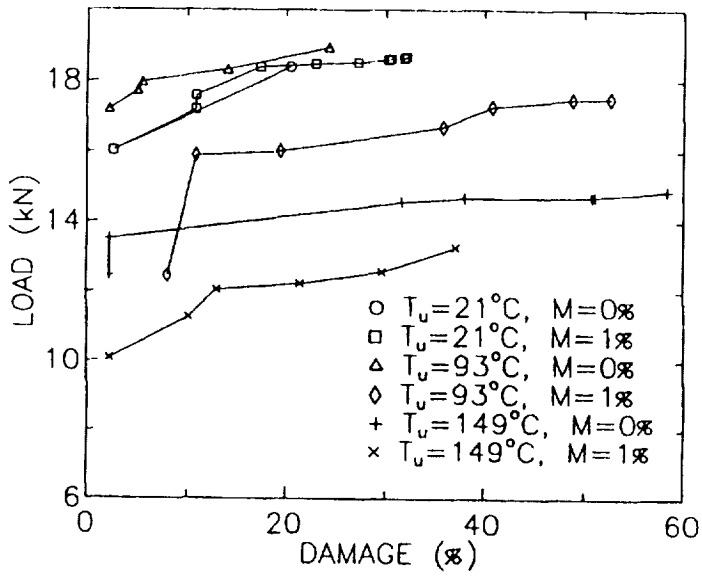

Figure 7.7: T-300/Epoxy $(0,90)_s$ Created Damage with Loading

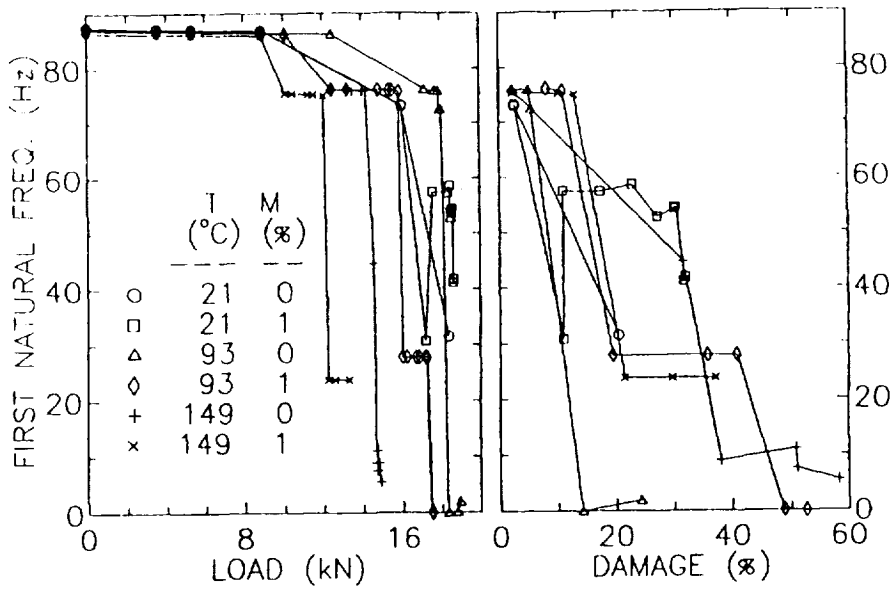

Figure 7.8: T-300/Epoxy $(0,90)_s$ Degradation of the First Natural Frequency

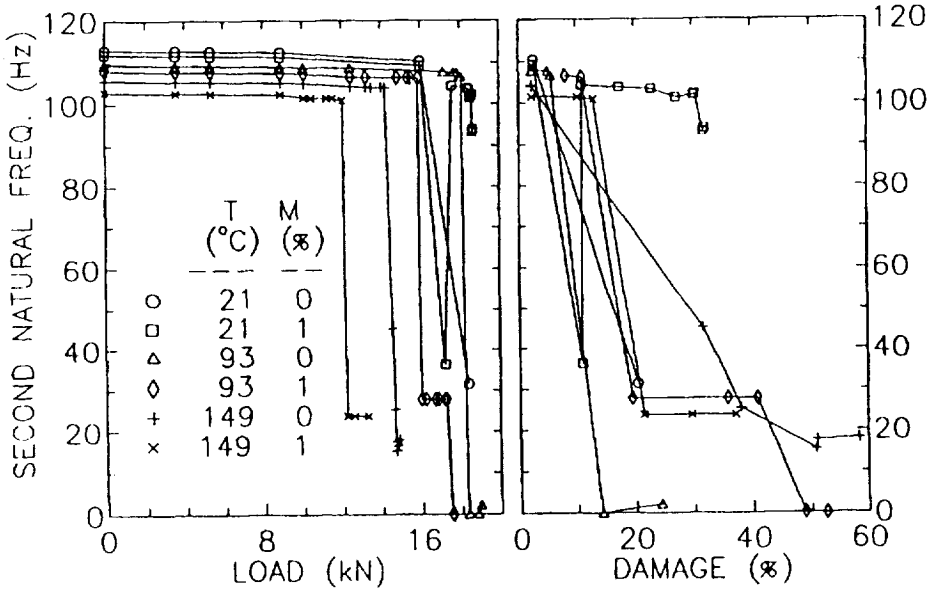

Figure 7.9: T-300/Epoxy $(0,90)_s$ Degradation of the Second Natural Frequency

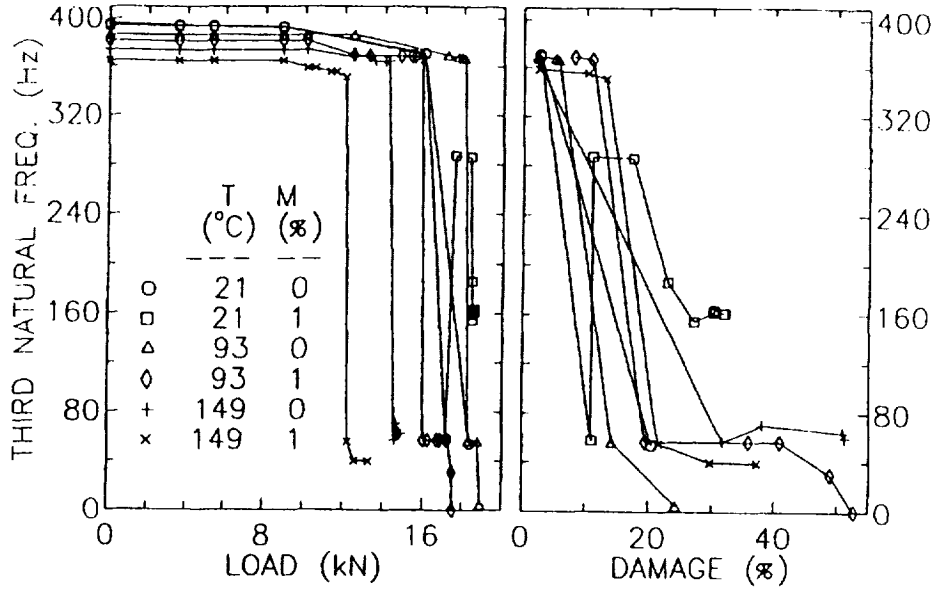

Figure 7.10: T-300/Epoxy $(0,90)_s$ Degradation of the Third Natural Frequency

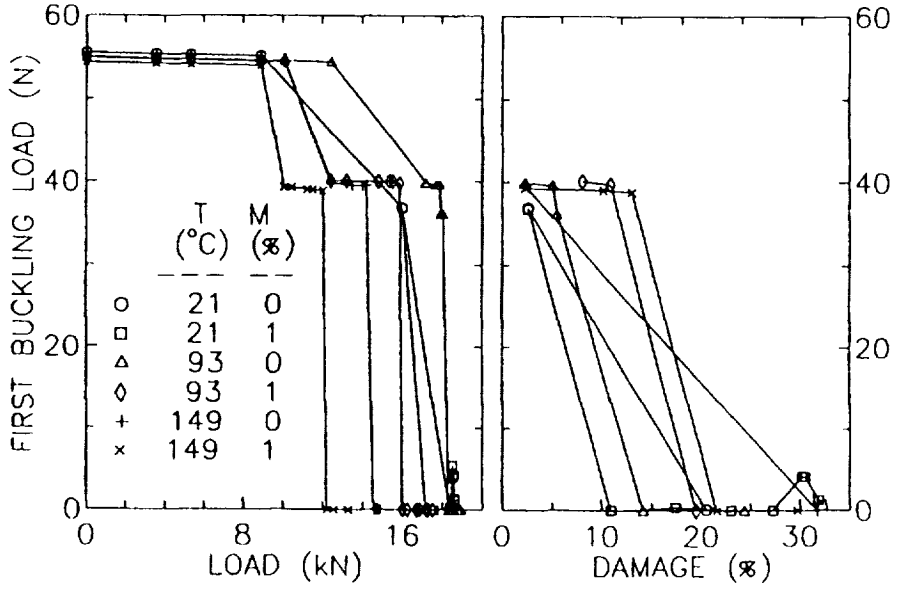

Figure 7.11: T-300/Epoxy $(0,90)_s$ Degradation of the First Buckling Load

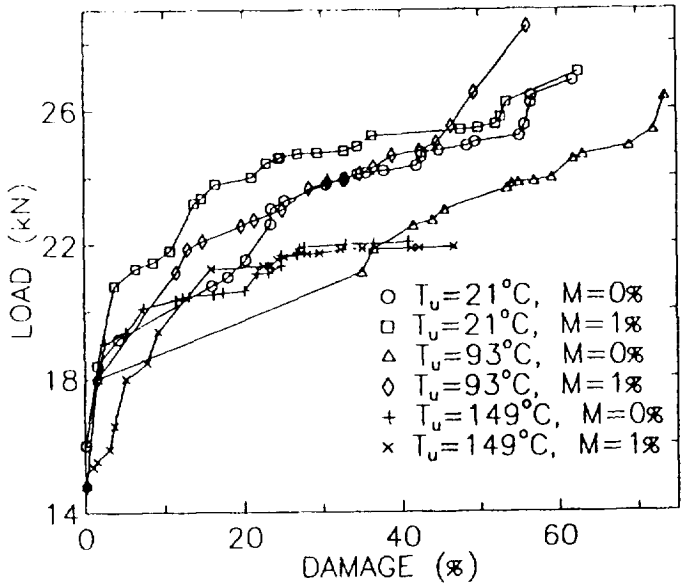

Figure 7.12: S-Glass/HMHS $(\pm 15)_s$ Created Damage with Loading

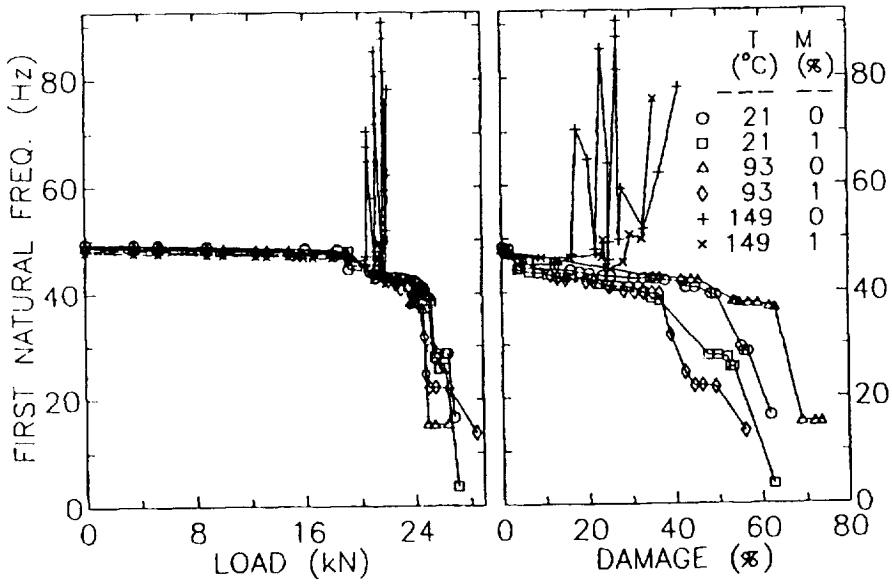

Figure 7.13: S-Glass/HMHS $(\pm 15)_s$ Degradation of the First Natural Frequency

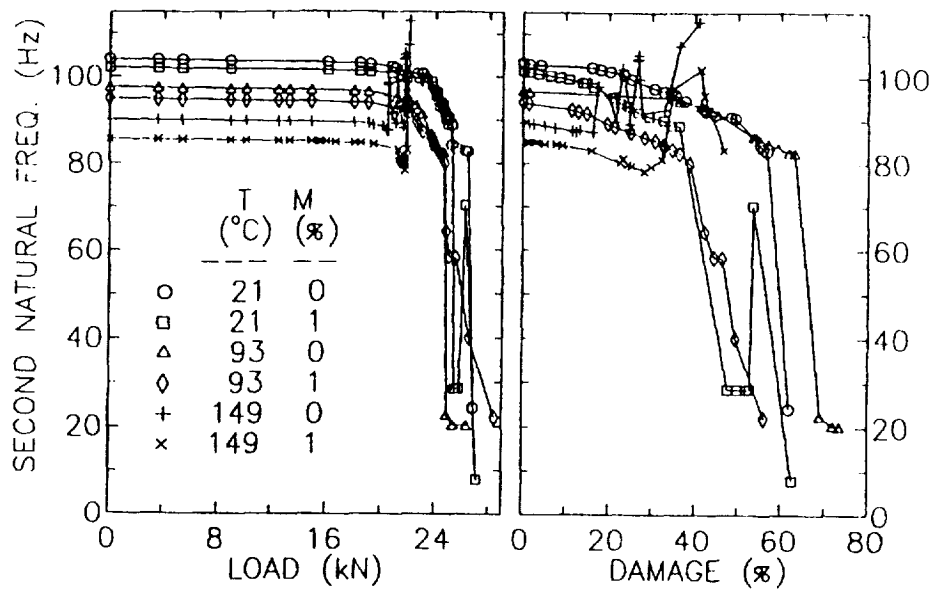

Figure 7.14: S-Glass/HMHS $(\pm 15)_s$ Degradation of the Second Natural Frequency

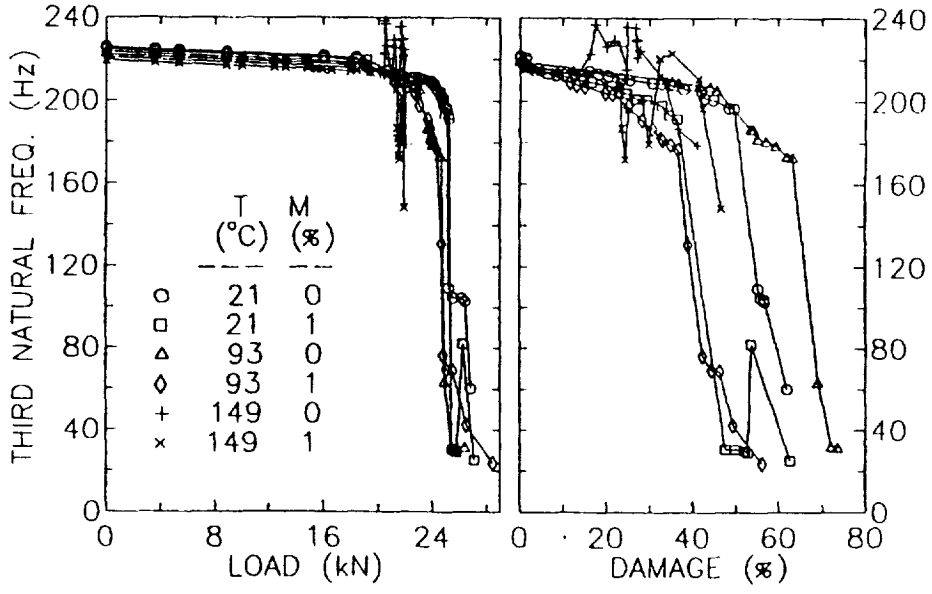

Figure 7.15: S-Glass/HMHS $(\pm 15)_s$ Degradation of the Third Natural Frequency

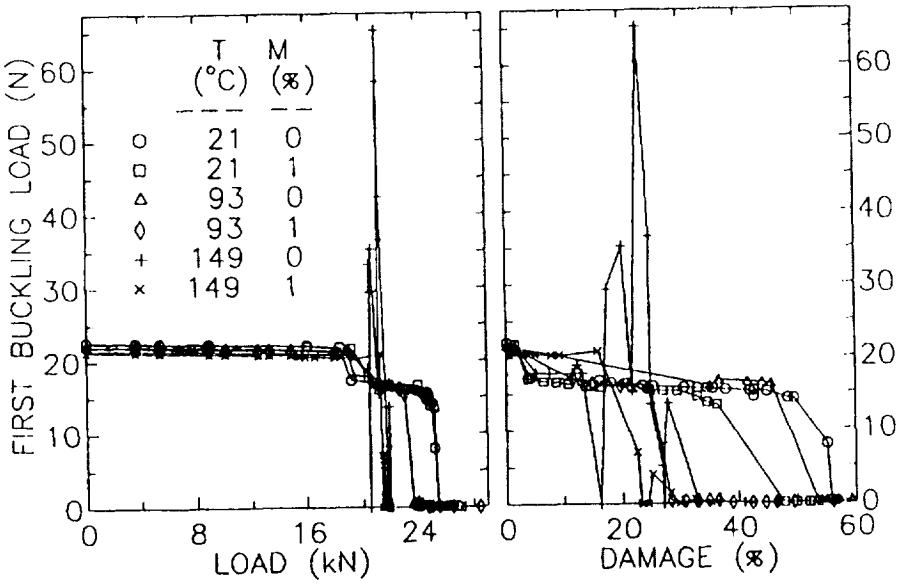

Figure 7.16: S-Glass/HMHS $(\pm 15)_s$ Degradation of the First Buckling Load

Chapter 8

Structural Durability of Stiffened Composite Curved Panels

The durability of a stiffened composite cylindrical shell panel is investigated under several loading conditions. Damage initiation, growth, and accumulation up to the stage of propagation to fracture are included in the computational simulation. Results indicate significant differences in the degradation paths for different loading cases. Effects of combined loading on structural durability and ultimate structural strength of a stiffened shell are assessed.

For aeronautical applications the standard design configuration to service the required loads with sufficient structural strength and stability is a composite shell structure that is stiffened by an integral structural framework. Along the axial direction of a cylindrical shell, composite stringers are used to provide additional strength and stiffness under axial tension, compression, and bending. Stringer stiffeners also contribute to the shear strength of the stiffened shell by providing stability to the composite outer shell which resists the shear loading. However, the degradation of stringer webs under shear loading due to damage initiation by shear distortion of the stiffened shell is a fundamental design consideration. The objective of this chapter is to examine the durability of stiffened composite shells via the simulation of damage growth, progression, and evaluation of structural fracture resistance under loading.

8.1 Stiffened Shell Panel

The demonstration example for this section consists of a stiffened composite cylindrical shell panel with imposed boundary conditions to represent the behavior of a segment of the entire cylindrical shell, as depicted in Figure 8.1, subjected to 1) axial tension, 2) axial compression, 3) shear, 4) internal pressure (with the associated axial and hoop generalized stresses), and combinations of these four fundamental loads. The composite system is made of Thornel-300 graphite fibers in an epoxy matrix (T300/Epoxy). The outer shell laminate consists of fifty 0.127 mm. (0.005 in.) plies resulting in a composite shell thickness of 6.35 mm. (0.25 in.).

The laminate configuration for the outer shell is $[90/([90/\pm 15/90]_s)_3]_s$. The 90° plies are in the hoop direction and the ±15° plies are oriented with respect to the axial direction of the shell. The cylindrical shell panel has a constant radius of curvature of R=2.286 m. (90 in.). The subtended angle of the shell panel arc is θ=30° or $\pi/6$, resulting in an arc length of s=Rθ=1.197 m. (47.12 in.). The length of the stiffened panel along the shell axis is 1.219 m. (48 in.).

The stiffener elements are made from the same T300/Epoxy composite as the outer shell. The stiffeners are glued to the outer shell at all surfaces of contact. The adhesive properties between the outer shell and the stiffeners are the same as those of the Epoxy matrix. In general, the stiffener laminate configuration consists of 20 plies of $([\pm 45]s)_5$ composite structure for the webs and for the continuous toe elements that attach to the outer shell. Stiffener flanges or caps have an additional 30 plies of 0° (axial) fibers. Figure 8.2 indicates laminate configurations in the structural elements of the stiffened shell.

The finite element model contains 168 quadrilateral thick shell elements, of which 96 are utilized to represent the outer shell, as indicated by the grid lines shown in Figure 8.1. The remaining 72 elements are used to represent the stiffener webs and flanges.

Because the finite element properties and resulting generalized stresses are specified at each node, duplicate nodes are needed where there are discontinuities in the finite element properties. Duplicate nodes have the same degree of freedom coordinates but allow the definition of different structural properties. Figure 8.3 shows typical duplicate nodes along a representative hoop segment of the shell panel. At points where duplicate nodal definitions are required, the node with the smallest number is designated as the master node and the other nodes are designated as the slave nodes that are assigned exactly the same degree of freedom coordinates as the master node. In Figure 8.3 the subscript m after a node number indicates a master node and the subscript s indicates a slave node. In Figure 8.3 separate points are noted to distinguish the master and slave nodes that are assigned the same degree-of-freedom coordinates. In the actual finite element model, however, corresponding master and slave nodes coincide at a point. The finite element model for the investigated stiffened shell panel requires 333 nodes of which 171 are master nodes and the remaining 162 are slave nodes.

Loading on the stiffened shell panel that is of interest for design purposes may include one or more of the following components: 1) Axial Tension or 2) Axial Compression, 3) Shear, and 4) Internal Pressure. Composite structural durability is first investigated under each one of these four loading cases. The four fundamental loading cases are illustrated in Figure 8.4. In addition, four combined loading cases are also investigated as follows: 5) Axial Tension and Shear, 6) Axial Compression and Shear, 7) Axial Tension and Shear under Internal Pressure, and 8) Axial Compression and Shear under Internal Pressure. Boundary conditions, as shown in Figure 8.1, are the same for all eight loading cases. In each case, computational simulation of structural durability under loading is carried out through the stages of damage initiation, damage growth, and damage accumulation, up to the stage of damage propagation.

1) Axial Tension– Axial loading is applied along the positive y axis on one face of the stiffened

shell panel. The share of axial loading on the stiffeners is proportional to the relative axial stiffness of the stiffener elements as compared to the outer shell. Table 8.1 summarizes damage progression highlights for this case. The axial load is given per unit length of the circumferential arc segment of the stiffened shell panel.

2) Axial Compression– Axial compression loading is applied using the same loading configuration as in axial tension, but the loads are applied in the opposite sense. Table 8.2 summarizes damage progression for the axial compression case.

3) Shear– Table 8.3 summarizes damage progression for the shear loading case. Shear loading is the most critical with regard to damage initiation in the stiffener webs by in-plane shear failures. For the examined composite structure and geometry, the damage initiation load is under one tenth of the nodal fracture node. These results indicate that structural durability performance under shear loading is an important design consideration and that shear loading effects need be carefully considered in the design of stiffened composite shells. Stiffener web thickness and laminate structure as well as the stiffener profile/geometry are important design parameters.

4) Internal Pressure– A gradually increasing pressure is applied to the outer shell from its interior or concave side of the panel. Uniformly distributed hoop and axial tensions are also applied to the cylindrical panel, to simulate loads on a closed-end cylindrical pressure vessel. Accordingly, axial tension in the shell wall is half that developed in the hoop direction. Table 8.4 summarizes three significant damage stages during pressurization. Durability analysis indicates that pressurization alone is not a critical design load for this composite structure since the damage initiation pressure of 1.68 MPa (259 psi) is approximately twenty times the static pressurization service load for typical aircraft structures.

5) Axial Tension and Shear– The first load increment consists of 17.5 KN/m (100 lbs/in.) shear and 473 KN/m (2,700 lbs/in.) tension. The relative magnitude of the shear component of loading is selected according to the expected service loading combinations indicated in the design of the stiffened shell example. The ratio of shear to axial tension loading is kept constant at 1/27 as the loading is increased. Table 8.5 summarizes the damage initiation, progression, and nodal fracture stages under this loading. The damage initiation load and the fracture load are reduced due to combined loading. The overall degradation pattern is similar to that of shear loading examined in Case 3 above.

6) Axial Compression and Shear– This is similar to case 5, except that the axial loading component is compressive rather than tensile. As it was in case 5, the effect of combined loading is to reduce the ultimate structural durability of the stiffened composite panel. Results under axial compression plus shear loading are summarized in Table 8.6 in terms of the axial compression component of the load. The ratio of shear loading per unit length of boundary, to axial compressive loading per unit length of the hoop side of the panel is 1/27 for all load levels. The axial compression and shear components of loading are as shown in Figure 8.4. In relation to axial compression loading described in case 2, the nodal fracture load is reduced by 24 percent. The damage initiation load is not significantly affected.

However, the initial damage mode now includes in-plane shear failures in the stringer webs. As loading is increased, damage accumulation in stringer webs results in nodal fractures in the web elements.

7) Axial Tension and Shear with Pressurization- The first load increment consists of 17.5 KN/m (100 lbs/in.) shear and 473 KN/m (2,700 lbs/in.) tension, and also 100 KPa (1.4 psi) internal pressure with the associated hoop and axial tensions also added. The load ratios are kept constant as the loading is increased. Results are described in Table 8.7. Degradation patterns are similar to those of case 5. The effect of pressurization is to increase the loading level corresponding to nodal fracture.

8) Axial Compression and Shear with Pressurization- Results are summarized in Table 8.8. Loading is similar to case 7 except that axial loading is compressive rather than tensile. Degradation is similar to case 6. The nodal fracture load is increased with pressure as in case 7.

Figure 8.5 shows the load versus damage curves for axial tension only, axial tension with shear, and axial tension with shear under pressurization (cases 1, 5, and 7, respectively). The scalar damage variable, shown on the abscissa, is derived from the total volume of the composite material affected by the various damage mechanisms. Computation of the shown scalar damage variable has no interactive feedback on the detailed simulation of composite degradation. The curves end when nodal fracture is predicted. When shear is added to axial tension, damage initiation and progression to fracture occur under a lower load. The amount of damage at the time of fracture is less than that corresponding to axial tension only. At the initial stages of structural degradation, pressurization does not affect damage progression. However, nodal fracture requires a considerably higher load compared to the tension plus shear case.

Figure 8.6 shows the structural response degradation with endured tensile loading. Structural response properties are represented by the first natural frequency of the stiffened shell panel and the fundamental buckling load under external pressure. On the ordinate, F/F_0 represents the ratio of damaged natural frequency to undamaged natural frequency. Similarly, B/B_0 represents the ratio of damaged buckling load to undamaged buckling load. At the time of local fracture, Figure 8.6 indicates that the fundamental buckling load is reduced by 12 percent and the first natural frequency is reduced by 8 percent as compared to those of an undamaged stiffened shell panel.

Figure 8.7 shows the load to damage relationships for axial compressive load, axial compression with shear, and axial compression with shear under pressurization (cases 2, 6, and 8, respectively). Compressive load levels for damage initiation and progression are lower compared to the tensile load cases due to material properties as well as structural effects. Effect of the shear loading component is to reduce the load levels that cause damage initiation and progression. Pressurization does not play an important role at the start of damage. However, the nodal fracture load is raised considerably due to the stabilizing effect of internal pressure.

oo

Table 1: Axial Tension Loading Damage Progression Summary

Load (MN/m)	Description of Damage
1.75	Damage initiation by tensile and combined stress failures (σ_{f1T}, MDE) at the 0° (axial) surface plies in the flanges of the stiffeners.
1.78	Damage growth into the webs of stiffeners due to in-plane shear, combined stress, and relative rotation (σ_{f12S}, MDE, RR) failures in the stringer web plies.
1.92	Ply damage growth through the web thickness. Tensile failures in nearby flanges progress through five plies.
2.62	Damage Progression to the outer hoop plies of the main shell because of transverse tensile and combined stress (σ_{f12T}, MDE) failures. At this stage much of the stringer webs have failed in shear through all their plies. Stringer flanges show tensile failures in up to 13 axial plies.
4.03	A stringer flange node fractures. Outer shell has up to 12 damaged plies, all outer shell damage is in the 0° hoop plies due to transverse tension, and combined stress (σ_{f12T}, MDE) failures. Simulation is stopped.

Table 2: Axial Compression Loading Damage Progression Summary

Load (MN/m)	Description of Damage
1.12	Damage initiation by compressive and combined stress failures (σ_{f1C}, MDE) at the 0° (axial) surface plies in the flanges of the stiffeners.
1.60	Damage growth into the webs of stringers due to in-plane shear, combined stress, and relative rotation (σ_{f12S}, MDE, RR) failures in the web plies. Compressive damage in stiffener flanges grows to 10 plies.
1.70	Ply damage growth through the web thickness.
2.16	Stringer webs fail in shear (σ_{f12S}, MDE, RR) in all plies. Stringer flanges show compressive failures in all 50 plies. Simulation is stopped as the imminence of structural collapse is indicated by the compressive failure of a flange node.

Table 3: Shear Loading Damage Progression Summary

Load (kN/m)	Description of Damage
64.7	Damage initiation by in-plane shear, combined stress, and excess relative rotation failures (σ_{f12S}, MDE, RR) in the ±45° plies of the stiffeners. In-plane shear damage grows through the thickness of the webs without significant structural resistance.
424	Damage progression to the outer shell elements (σ_{f12S}, MDE, RR) the same in-plane shear, combined stress, and relative rotation (σ_{f12S}, MDE, RR) failures in the stringer web plies.
429	Ply damage grows through the web thickness. Tensile failures in nearby flanges progress through five plies.
482	Damage Progression to the outer hoop plies of the main shell because of in-plane shear and combined stress (σ_{f12S}, MDE) failures. At this stage all of the stringer webs have failed in shear through all their plies. Stringer flanges do not show any failure.
696	Outer shell node fractures at a stringer web connection point. Simulation is stopped.

Table 4: Internal Pressure Loading Damage Progression Summary

Pressure (MPa)	Description of Damage
1.68	Damage initiation by ply longitudinal tension and combined stress failures (σ_{f1T}, MDE) in the 0° plies in the flanges of the stringers.
1.78	Damage progression to the outer shell plies. Transverse tension, combined stress, and relative rotation failures (σ_{f12T}, MDE, RR) in ±15° angle plies; longitudinal tension and combined stress failures (σ_{f1T}, MDE) in the 90° hoop plies.
1.93	Ply damage growth through the outer shell thickness. Tensile failures in nearby stringer flanges progress through eight plies. Simulation is stopped.

Table 5: Axial Tension and Shear Loading Damage Progression Summary

Tension (MN/m)	Description of Damage
1.18	Damage initiation by in-plane shear, combined stress, and excess relative rotation failures (σ_{n12S}, MDE, RR)in the ±45° plies of the stiffeners. In-plane shear damage grows through the thickness of the webs with negligible structural resistance.
1.97	Damage grows into the flanges of stiffeners due to longitudinal tension and combined stress (σ_{n1T}, MDE) failures in the 0° axial plies. As many as 6 axial plies are damaged.
3.03	Damage progression to the outer shell elements due to transverse tension and combined stress (σ_{n2T}, MDE) failures in the outermost 6 hoop plies. Damage accumulation under the same loading results in the fracturing of stiffener flange nodes due to the failure of all 50 plies under longitudinal tension. Simulation is stopped.

Table 6: Axial Compression and Shear Loading Damage Progression Summary

Compression (MN/m)	Description of Damage
1.18	Damage initiation by in-plane shear, combined stress, and excess relative rotation failures (σ_{n12S}, MDE, RR) in the ±45° plies of the stiffeners. Also, by longitudinal compression and combined stress (σ_{n1C}, MDE) failures in some of the 0° axial plies in the flanges. In-plane shear damage grows through the thickness of the webs with negligible structural resistance.
1.34	Damage accumulation in the webs and flanges of stringers.
1.65	Nodal fracture in web due to longitudinal compression (σ_{n1C}) failures in all plies. Simulation is stopped.

Table 7: Axial Tension and Shear Loading with Pressurization Damage Progression Summary

Tension (MN/m)	Description of Damage
1.19	Damage initiation by in-plane shear, combined stress, and excess relative rotation failures (σ_{n12S}, MDE, RR) in the ±45° plies of the stiffeners. In-plane shear damage grows through the thickness of the webs with negligible structural resistance.
1.76	Damage growth into the flanges of stiffeners due to longitudinal tension and combined stress (σ_{n1T}, MDE) failures in the 0° axial plies. As many as 4 axial plies damaged.
2.97	Damage progression to the outer shell elements due to transverse tension and combined stress (σ_{n2T}, MDE) failures in the outermost 4 hoop plies. Damage accumulation under the same loading results in the fracturing of stiffener flange nodes due to the failure of all 50 plies under longitudinal tension. Simulation is stopped.

Table 8: Axial Compression and Shear Loading with Pressurization Damage Progression Summary

Compression (MN/m)	Description of Damage
1.00	Damage initiation by in-plane shear, combined stress, and excess relative rotation failures (σ_{n12S}, MDE, RR) in the ±45° plies of the stiffeners. In-plane shear failures grow across the web thickness. Longitudinal compression and combined stress (σ_{n1C}, MDE) failures in some of the 0° axial plies in the flanges.
1.95	Nodal fracture in web due to longitudinal compression (σ_{n1C}) failures in all plies. Simulation is stopped.

Figure 8.8 shows contours for the z component of nodal displacements under 2.0 MN/m axial compressive load, immediately before fracture. The global z axis is in the outward normal direction of the shell at the center of the panel. Figure 8.8 indicates that the outer shell bulges out at the unstiffened regions under compression.

Figure 8.9 shows the load versus damage curves for shear only and the shear component of the combined loading cases. The overall damage progression curves under shear only and combined loading are quite different. However, it is significant that the initial stages of damage progression are similar, indicating the influence of the shear loading component in establishing the structural degradation characteristics under combined loading.

Figure 8.10 shows pressure and the pressure component of combined loading versus damage progression. Pressure does not play a major role in the damage progression under combined loading as the pressurization component is less than 10 percent of the damage initiation load under pressure only.

Table 8.9 summarizes the damage progression sequence for all eight loading cases, indicating the structural elements affected during the damage initiation, growth, progression, and fracture stages. It is important to note that for any structure the damage progression sequence depends on fiber orientations and laminate structure as well as loading. The computational capability demonstrated in this report is useful for answering design questions with regard to durability as well as stiffness and strength for alternative laminate configurations.

8.2 Summary and Conclusions

The present investigation was limited to a composite stiffened shell panel under static loading. The presented results were computed assuming that the composite structure is at room temperature and contains no moisture. The significant results derived from this investigation in which CODSTRAN was used to evaluate damage initiation, growth, and progression in a stiffened composite shell are as follows:

1. For stiffened shells, combined loading effects are significant in the overall structural durability behavior. Shear loading is the most significant with regard to the durability of stiffened composite shells. A relatively small shear component may affect and control the damage initiation and progression patterns under combined loading. At the presence of shear, damage initiation and progression is by in-plane shear failures in the webs of the stringers. The presence of shear reduces the structural durability of the example stiffened composite shell when combined with any other loading.

2. Pressurization plays a minor role in the structural durability at the initial stages of degradation under combined loading. The effects of pressurization are more pronounced at the advanced stages of structural degradation. If pressurization is added to axial and shear loads, nodal fracture is delayed for the investigated stiffened composite shell panel.

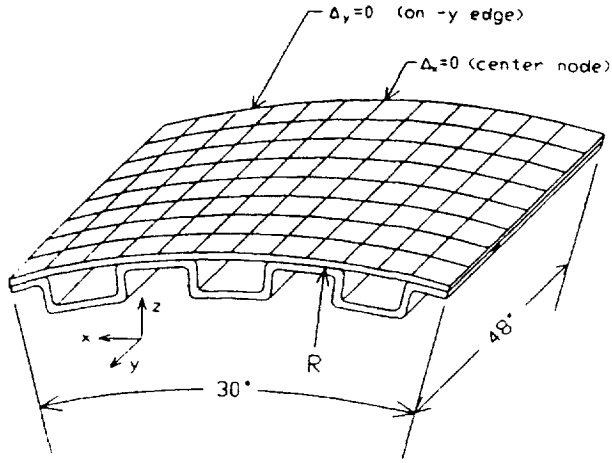

Figure 8.1: Stiffened Composite Cylindrical Shell Panel; T300/Epoxy Laminate: Skin$[90/([90/\pm 15/90]_s)_3]_s$; Web and toe$([\pm 45]s)_5$; Cap$[0_{30}/([\pm 45]s)_5]$

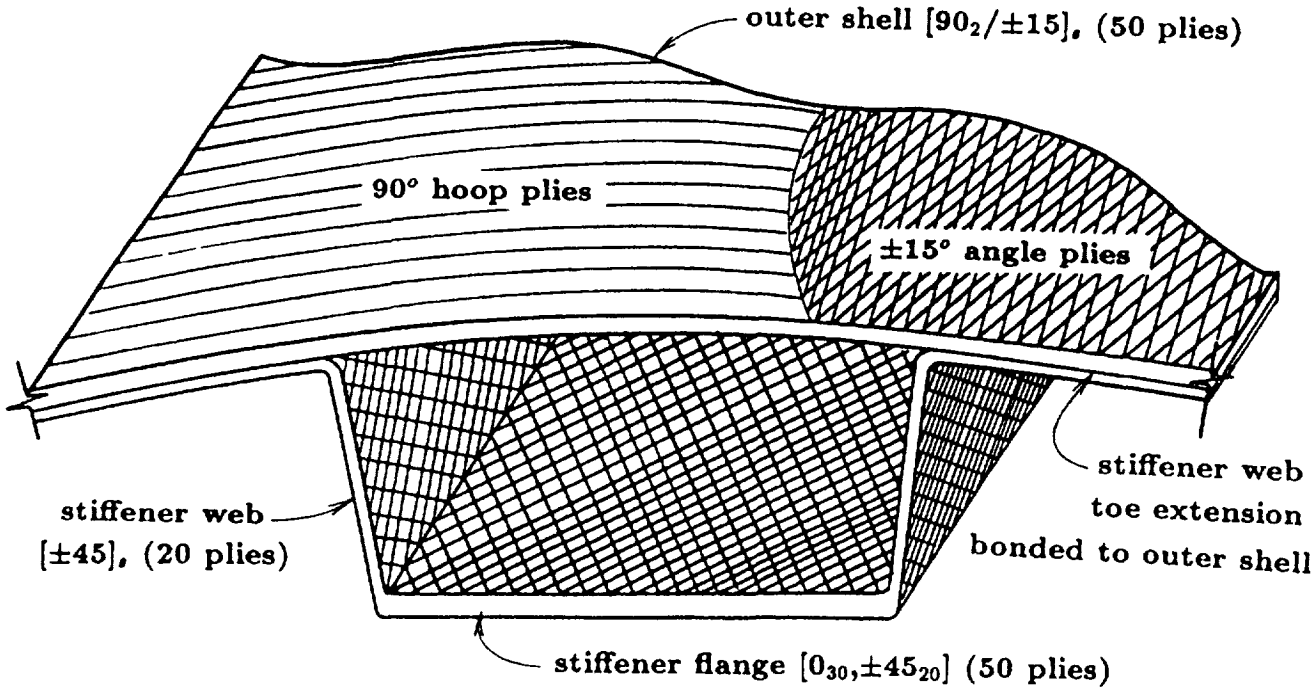

Figure 8.2: Schematic of Laminate Structure

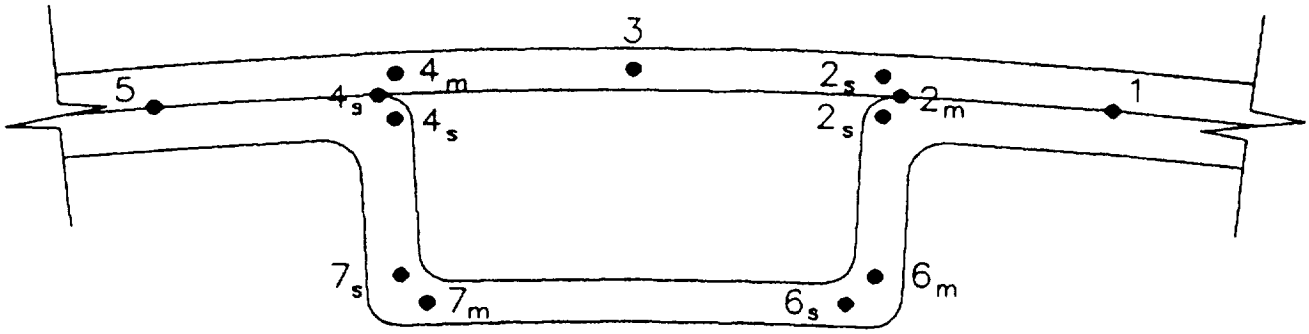

Figure 8.3: Typical Duplicate Node Assignments

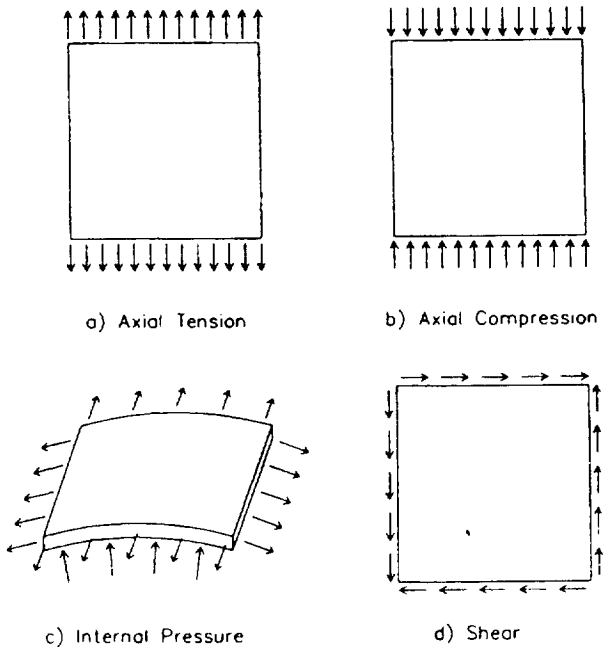

Figure 8.4: Fundamental Load Components

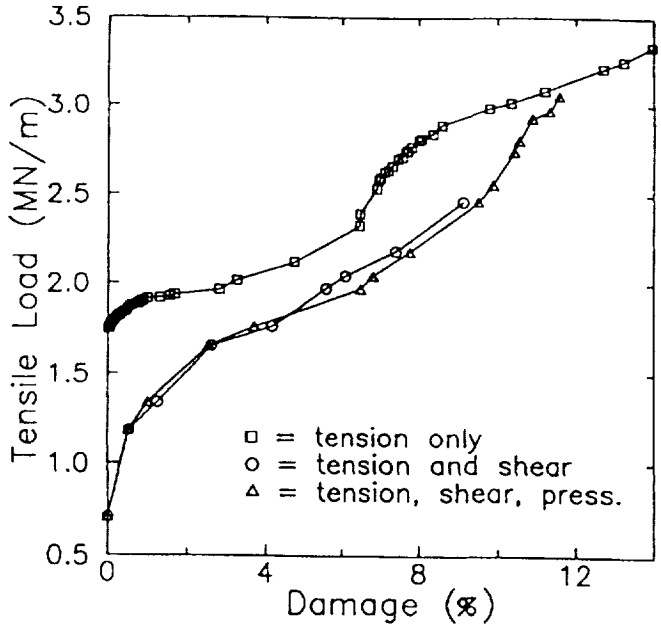

Figure 8.5: Axial Tension Load and Damage Progression; T300/Epoxy Laminate: Skin$[90/([90/\pm 15/90]_s)_3]_s$; Web and toe$([\pm 45]s)_5$; Cap$[0_{30}/([\pm 45]s)_5]$

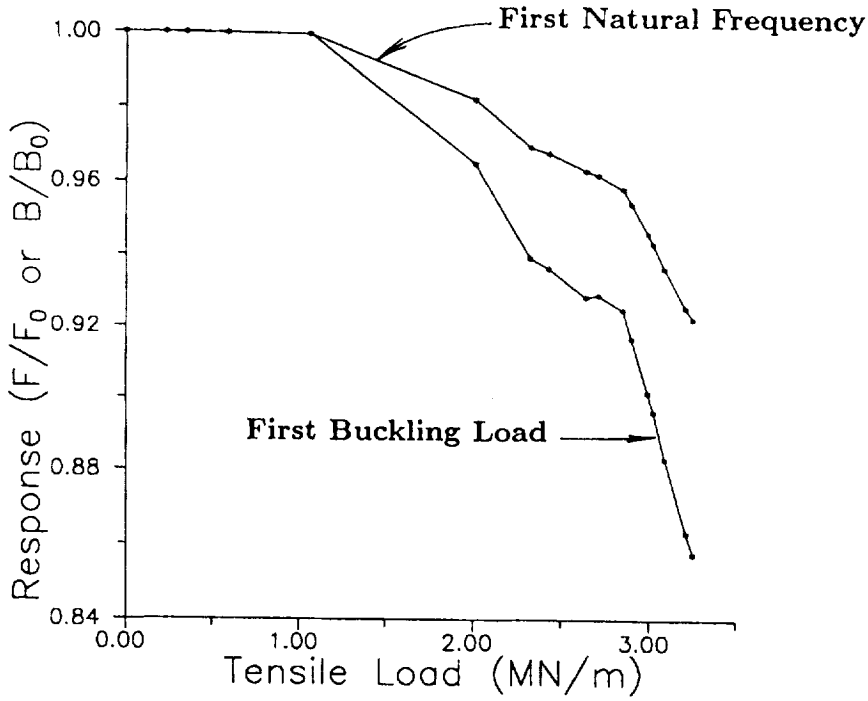

Figure 8.6: Response Degradation with Loading; T300/Epoxy Laminate: Skin$[90/([90/\pm 15/90]_s)_3]_s$; Web and toe$([\pm 45]s)_5$; Cap$[0_{30}/([\pm 45]s)_5]$

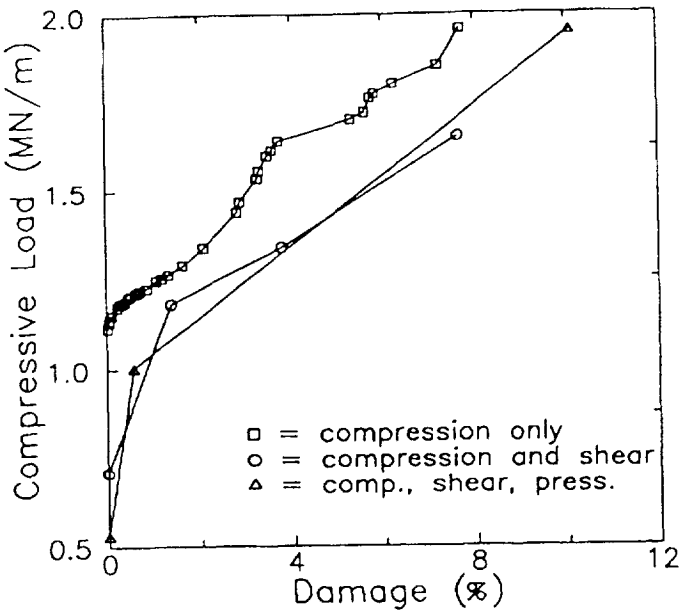

Figure 8.7: Axial Compression Load and Damage Progression; T300/Epoxy Laminate: Skin$[90/([90/\pm 15/90]_s)_3]_s$; Web and toe$([\pm 45]s)_5$; Cap$[0_{30}/([\pm 45]s)_5]$

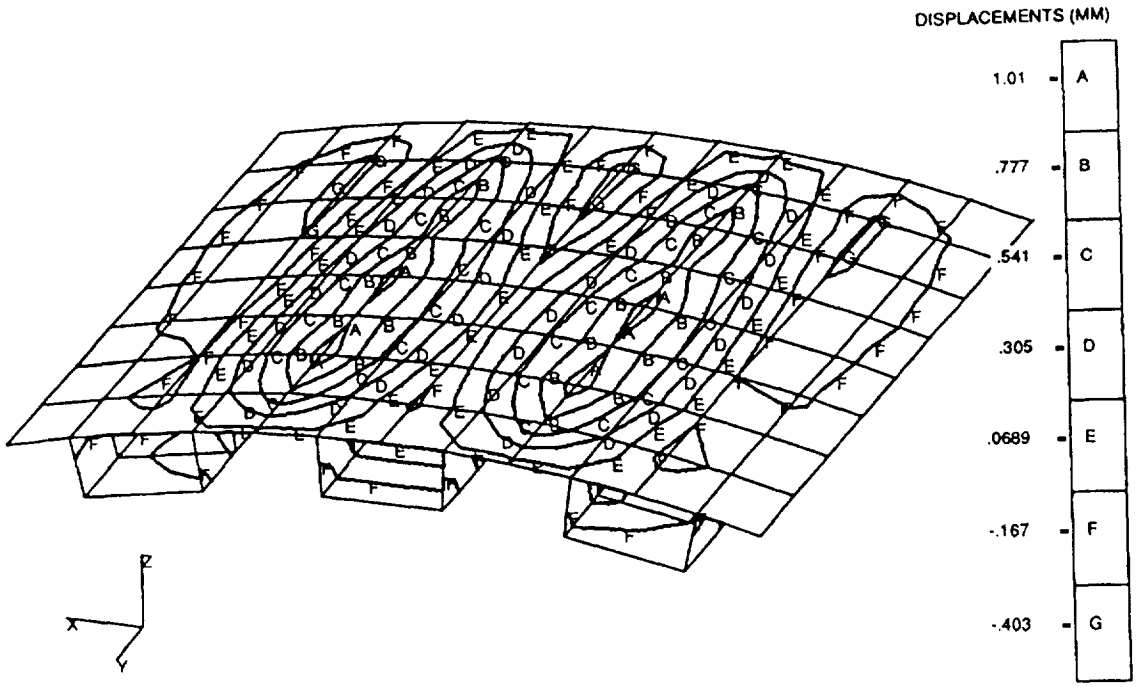

Figure 8.8: Displacement Contours under Axial Compression; T300/Epoxy Laminate: Skin$[90/([90/\pm 15/90]_s)_3]_s$; Web and toe$([\pm 45]s)_5$; Cap$[0_{30}/([\pm 45]s)_5]$

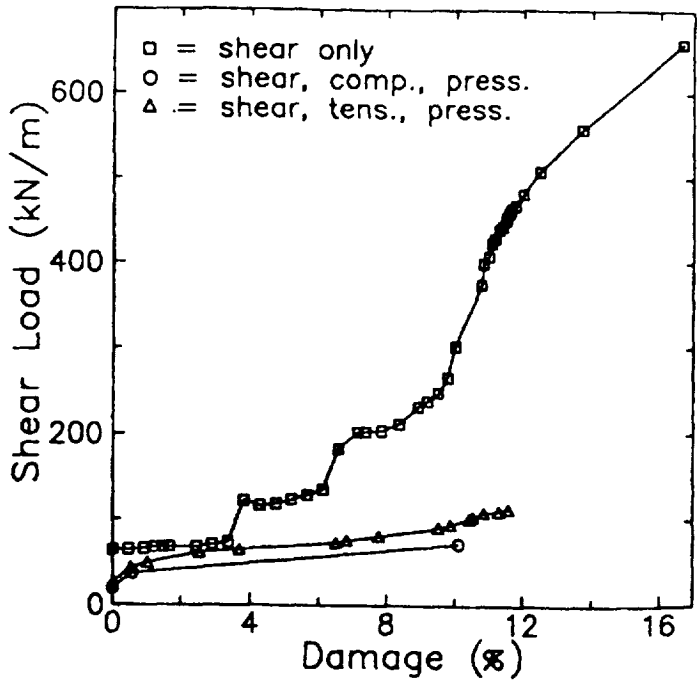

Figure 8.9: Damage Progression under Shear Loading for T300/Epoxy Laminate; Skin$[90/([90/\pm15/90]_s)_3]_s$; Web and toe$([\pm45]s)_5$; Cap$[0_{30}/([\pm45]s)_5]$

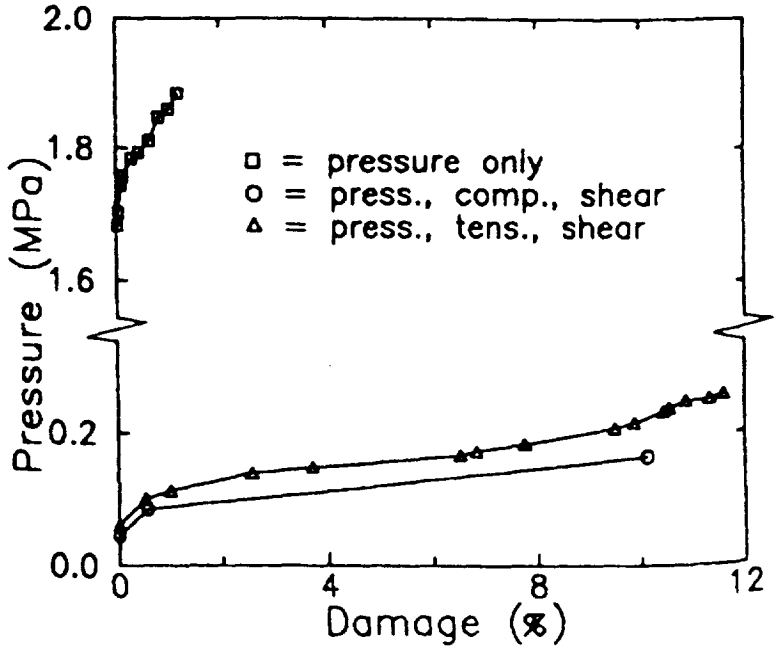

Figure 8.10: Internal Pressure and Damage Progression; T300/Epoxy Laminate: Skin$[90/([90/\pm15/90]_s)_3]_s$; Web and toe$([\pm45]s)_5$; Cap$[0_{30}/([\pm45]s)_5]$

Table 8.9: Damage Progression Sequence

LOADING COMPONENTS	DAMAGE INITIATION	DAMAGE GROWTH	DAMAGE PROGRESSION	FRACTURE IN
Tension(T)	CAP	WEB	SKIN	CAP
Compression(C)	CAP	WEB		CAP
Shear(S)	WEB	SKIN	CAP	SKIN
Pressure(P)	CAP	SKIN		CAP
S+T	WEB	CAP	SKIN	CAP
S+C	WEB	CAP		WEB
S+T+P	WEB	CAP	SKIN	CAP
S+C+P	WEB	CAP		WEB

Chapter 9

Effects of Progressive Fracture on the Buckling Resistance of Composite Structures

The effect of local and regional damage on the load carrying capability and structural behavior of a composite cylindrical shell under external pressure is investigated. Damage initiation, growth, accumulation, and propagation to structural fracture are included in the simulation. Results identify cases in which local damage has a significant effect on structural collapse under external pressure. Effect of the laminate structure on stability is investigated.

In some applications such as submerged vehicles and undersea shelters composite shells are required to withstand significant external pressure. In general, any accidental damage or fabrication defect is expected to weaken the overall structural strength, durability, and stability. Standard design practice accepts the possibility of local defects and requires structural safety under probable accidental damage. It is therefore useful to quantify the reduction in the overall strength, durability, and stability of a composite shell structure due to existing defects and accidental damage.

Under external pressure composite shells display two types of global failure mode: 1) elastic buckling and 2) stress fracture. Design cases involving low to moderate levels of external pressure are typically satisfied with a sufficiently large radius-to-thickness ratio such that buckling stability is the fundamental design constraint. On the other hand, when relatively high external pressures are to be serviced, the radius-to-thickness ratio becomes small and stress fracture becomes the primary design concern. The purpose of this section is to examine the evaluation of buckling stability and durability for a composite shell under external pressure. A full size cylindrical shell is considered under increasing levels of external pressure. Buckling stability is examined with regard to the design of the laminate structure to carry the external pressure. Damage propagation studies identify structural stabilization requirements to assure structural safety.

9.1 Stability under External Pressure

The buckling stability of a prototype cylindrical shell is considered. The composite system is made of Thornel-300 graphite fibers in an epoxy matrix (T300/Epoxy). The investigated cylindrical shell has a diameter of 4.572 m (15 ft.) and a length of 15.24 m (50 ft.). The finite element model contains 800 nodes and 768 equal size quadrilateral thick shell elements. The composite shell is subjected to an external pressure. To simulate the stresses in the walls of a closed-end cylindrical vessel, a uniformly distributed axial compression is applied to the cylinder such that axial compressive stresses in the shell wall are half those developed in the hoop direction. To impose the axial loading, one of the end sections is restrained against axial translation and axial compression is applied uniformly at the opposite end of the shell.

9.1.1 Effect of Shell Thickness and Composite Structure on Stability

: Using a basic composite layup of $[90_2/\pm 15/90_2/\mp 15/90]_s$ with 0.127 mm (0.005 in.) plies, three different thicknesses of the shell are investigated via CODSTRAN with respect to buckling stability. Table 9.1 summarizes the results of this investigation. Figure 9.1 shows the buckling pressure as a function of the number of plies comprising the shell structure. Figure 9.1 also shows the fundamental buckling mode of the closed end cylindrical shell having 576 plies with $[90_2/\pm 15/90_2/\mp 15/90]_{s6}$ composite structure. The corresponding external buckling pressure is 2,323 KPa (337 psi). The first free vibration frequency is 25.6 Hz. The fundamental vibration mode is similar to the first buckling mode except that the vibration mode has four full sinusoidal waves around the circumference of the shell whereas the buckling mode has six.

9.1.2 Effect of Laminate Structure on Stability:

Alternative composite structures are examined via CODSTRAN with regard to buckling stability as summarized in Table 9.2. Table 9.2 indicates the significance of composite layup with regard to buckling stability. Of the three cases investigated, the best layup with regard to buckling stability is $[90_2/\pm 15/90_2/\mp 15/90]_s$.

9.2 Damage Progression and Damage Tolerance

The T300/Epoxy composite system that was investigated with regard to buckling stability is retained to illustrate a typical CODSTRAN durability analysis. The laminate consists of five hundred and seventy-six 0.127 mm (0.005 in.) plies resulting in a composite shell thickness of 73.2 mm (2.88 in.). The laminate configuration is $[90_2/\pm 15/90_2/\mp 15/90]_{s6}$. The 90° plies are in the hoop direction and the ±15° plies are oriented with respect to the axial direction

Table 9.1: Effect of Shell Thickness on Stability

Number of Plies	Shell Thickness (mm)	Composite Structure (T300/Epoxy)	Buckling Pressure (KPa)
144	18.3	$[90_2/\pm 15/90_2/\mp 15/90]_{s4}$	73.8
288	36.6	$[90_2/\pm 15/90_2/\mp 15/90]_{s5}$	392
576	73.2	$[90_2/\pm 15/90_2/\mp 15/90]_{s6}$	2,323

Conversion Factor: 1 KPa = 0.14504 psi

of the shell. The cylindrical shell has a diameter of 4.572 m (15 ft.) and a length of 15.24 m (50 ft.) as it was for the stability investigation. At one point along the circumference, at half-length of the cylinder, initial damage in a number of plies is prescribed. External pressure is applied on the cylindrical vessel with closed ends. The pressure is gradually increased until the shell is fractured, or until the buckling pressure is reached.

For a structure without defects CODSTRAN predicts that outer hoop plies will fracture at 19.5 MPa (2.83 ksi) external pressure if buckling instability is prevented. The 19.5 MPa fracture pressure for a defect free shell is 8.4 times the elastic buckling pressure. Therefore, unless the shell is stiffened against buckling, the design will be controlled by stability considerations. Nevertheless, structural collapse by damage propagation need also be considered due to the possibility of accidental damage. Durability analysis quantifies the reduction in the ultimate external pressure because of accidental mutilation of the composite shell structure.

Figure 9.2 shows the length of accidental damage by crushing or scraping of the outer 3/4 of the shell thickness along the shell axis and the external pressure at which the damage remains stable. The damaged length shown on the horizontal axis in Figure 9.2 is normalized with respect to the total length of the cylindrical shell. Damage stability in the pressure range of 0.69 to 2.32 MPa (100 to 337 psi) is depicted; where the 2.32 MPa upper limit corresponds to the buckling pressure. Information presented in Figure 9.2 is useful for the design of required framework spacing to assure structural integrity in case of accidental damage.

These results indicate that for thick shells under external pressure the ultimate structural fracture pressure is not sensitive to the location and the existence of minor defects.

Table 9.2: Effect of Composite Structure on Stability

Number of Plies	Shell Thickness (mm)	Composite Structure (T300/Epoxy)	Buckling Pressure (KPa)
576	73.2	$[\pm 15/\mp 15/90/\pm 15/\mp 15]_{s6}$	1,087
576	73.2	$[\pm 45/\mp 45/90/\pm 45/\mp 45]_{s6}$	1,608
576	73.2	$[90_2/\pm 15/90_2/\mp 15/90]_{s6}$	2,323

Conversion Factor: 1 KPa = 0.14504 psi

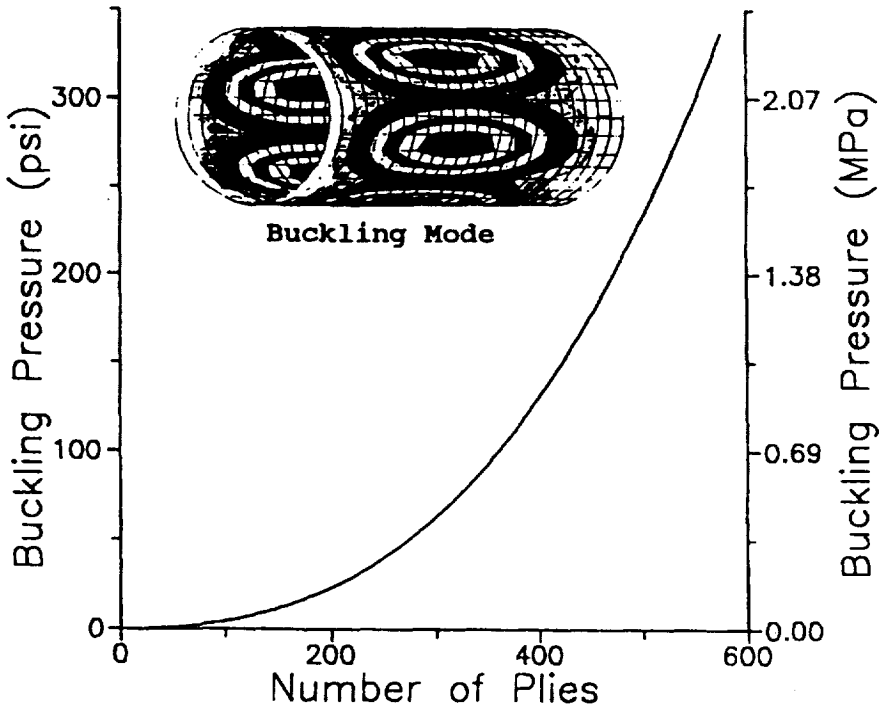

Figure 9.1: Buckling under External Pressure T300/Epoxy Composite Shell; 576 Plies: $[90_2/\pm 15/90_2/\mp 15/90]_{s6}$

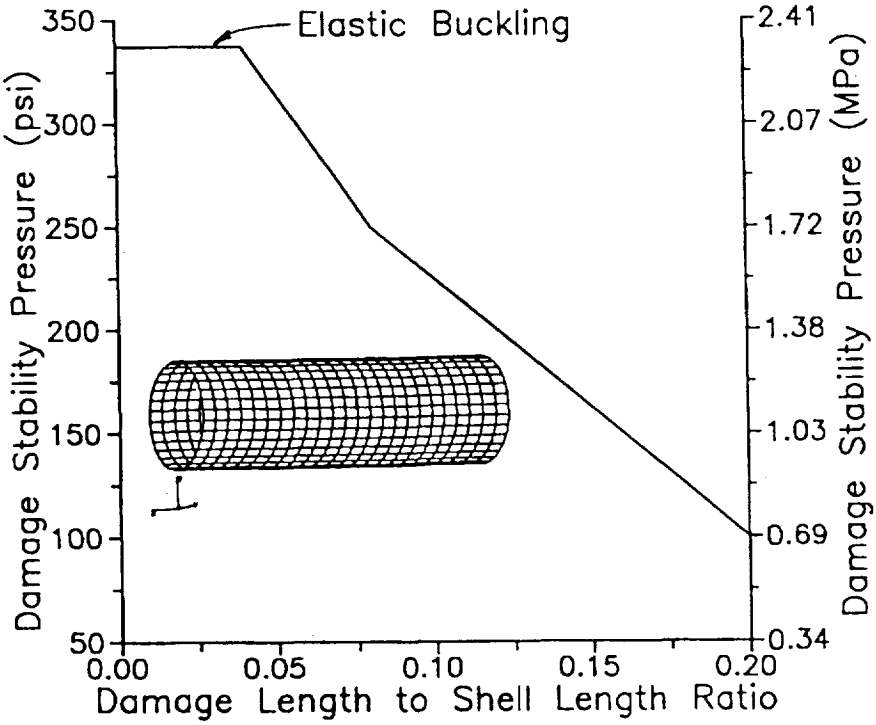

Figure 9.2: Damage Tolerance under Pressure T300/Epoxy Composite Shell; 576 Plies: $[90_2/\pm 15/90_2/\mp 15/90]_{s6}$

Chapter 10

Damage Tolerance of Thick Composite Shells under External Pressure

Progressive fracture of thick laminated graphite/epoxy composite cylindrical shells is investigated under external hydrostatic pressure. Results indicate that local defects do not have a significant effect on structural survivability under hydrostatic loading for thick composite shells. Influence of constituent material properties and the effects of residual stresses from the curing process on damage initiation and progression under external pressure is investigated.

10.1 Damage Progression in Subscale Composite Shell I

A subscale composite shell with 111.8 mm (4.405 in) internal diameter, 6.21 mm (0.2445 in) thickness, and 216 mm (8.5 in.) length is considered under hydrostatic pressure. The composite system is made of AS-4 graphite fibers in a high-strain ER-2258 epoxy matrix (AS-4/ER-2258). The fiber volume ratio is 0.60 and the void volume ratio is two percent. The laminate consists of forty eight 0.129 mm (0.0051 in.) plies. The laminate configuration is $[0/90_2]_{16}$. The 90° plies are in the hoop direction and the 0° plies are oriented in the axial direction of the shell. The finite element model contains 544 nodes and 512 elements. The composite shell is subjected to an external hydrostatic pressure that is gradually increased until the shell is fractured. To simulate the stresses in the walls of a closed-end cylindrical pressure vessel, a uniformly distributed axial compression is applied to the cylinder such that axial compressive stresses in the shell wall are half those developed in the hoop direction. To impose the axial loading, one of the end sections is restrained against axial translation and axial compression is applied uniformly at the opposite end of the shell. The geometry, laminate structure, and loading for this example correspond to those of an experimental investigation reported in [26].

Figure 10.1 shows the simulated damage progression with increasing hydrostatic pressure on the subscale composite cylinder I. There is a significant shift in the damage progression response when residual stresses due to curing at a temperature of 177°C (350°F) are taken into account. CODSTRAN simulation without taking into account residual fabrication stresses would indicate a structural fracture pressure of 43.73 MPa (6,342 psi). On the other hand, when the residual stresses are included in the simulation, the predicted fracture pressure is 40.01 MPa (5,803 psi). The average test pressure for the fracture of this specimen has been reported [26] as 39.76 MPa (5767 psi). Taking the residual stresses into account, CODSTRAN indicates damage initiation under 34.48 MPa (5,001 psi) by longitudinal compressive failure at the outermost axial ply near the end supports. Initial damage is negligibly small and very stable. Minor damage growth occurs in a second axial ply when the pressure is increased to approximately 37.6 MPa (5,453 psi). The damage growth stage is also very brief and very stable similar to the damage initiation stage. In contrast, the final structural fracture stage is very abrupt, without any additional damage progression after the damage growth stage. At the fracture pressure all 48 plies fail in compression at a node that has been slightly degraded during damage initiation. Structural fracture begins from one end of the cylindrical shell and propagates along an axial generator.

A structural stability analysis of the simply supported subscale cylindrical shell on the basis of elastic properties indicates a critical pressure of 59.0 MPa (8,550 psi). The ultimate fracture pressure of 40.0 MPa (5,800 psi) is considerably lower than the critical pressure for elastic instability. Therefore, interaction between the elastic buckling mode and stress induced fracture is neglected. Similarly, a computational simulation would indicate that the structural fracture of shells subject to external pressure is not sensitive to minor local defects. On the other hand, for the $[0/90_2]_{16}$ composite cylinder under the hydrostatic external pressure considered, structural durability is very sensitive to matrix shear strength. Figure 10.2 shows effect of varying the matrix shear strength on the damage initiation and ultimate fracture pressures.

The composite layup also influences the damage progression and fracture process. In particular a cross-ply $[0/90]_{24}$ laminate is more sensitive to the effects of residual stresses as compared to the $[0/90_2]_{16}$ laminate. Figure 10.3 shows the difference in fracture pressures of the two laminates. The damage initiation and growth modes are also different for these two laminates. Whereas the $[0/90_2]_{16}$ laminate begins its degradation in the axial plies, the $[0/90]_{24}$ laminate initiates damage in the hoop plies at the inner and outer surface of the laminate. Accordingly, the $[0/90]_{24}$ laminate is much more sensitive to residual stresses introduced in the hoop plies during the fabrication process.

10.2 Damage Progression in Subscale Composite Shell II

A second subscale composite shell with 203 mm (8 in) internal diameter, 16.8 mm (0.66 in) thickness, and 203 mm length is considered under external pressure. The composite system

is made of Thornel-300 graphite fibers in an epoxy matrix (T300/Epoxy). The laminate consists of one hundred and twenty 0.140 mm (0.0055 in.) plies resulting in a composite shell thickness of 16.8 mm (0.660 in.). The laminate configuration is $[[90_3/0]_{15}]_s$. The 90° plies are in the hoop direction and the 0° plies are oriented in the axial direction of the shell. The finite element model contains 288 nodes and 256 elements. At one point along the circumference, at half-length of the cylinder, initial fiber fractures in a number of plies are prescribed. The composite shell is subjected to an external pressure that is gradually increased until the shell is fractured. The example shell geometry, laminate structure, and loading correspond to those of an experimental investigation reported in Reference [28] where concern for the influence of fabrication defects on the ultimate strength was expressed.

CODSTRAN simulations were carried out for 1) a defect free laminate, 2) laminate with local surface defect 25 mm long in the axial direction at half-length of cylinder penetrating 8 plies, and 3) laminate with interior defect 25 mm long in the axial direction through 8 plies at the mid thickness of the shell wall. Results indicate that structural fracture occurs at 76.8 MPa (11.14 ksi) external pressure. The 76.8 MPa fracture load is well defined and is not sensitive to the presence of the considered minor defects. Damage initiation is typically by the activation of the combined stress failure criterion (MDE), dominated by $\sigma_{\ell 11}$ longitudinal compression and $\sigma_{\ell 12}$ in-plane shear stresses. CODSTRAN simulation indicates that when the critical pressure level is reached, damage initiation starts along a shell generator line containing any minor defect. Initial damage is not contiguous to the initial defect but begins at the quarter points on the axial generator on both sides of the defect. Damage initiation is at first in the inner and outer surface hoop plies. Within the same load increment damage progresses to include all plies through the thickness of the shell.

Figure 10.4 shows damage progression with external pressure for the three cases corresponding to 1) an initial defect at surface plies of shell, 2) an initial defect near mid-thickness of shell, and 3) defect free shell. Case (1) with initial defect at surface plies undergoes damage initiation at the lowest pressure which is at 99.73 percent of its fracture pressure. Case (1) results are not affected by the exact location of the defect. When the defect location is moved off center by L/8 there is no difference in damage progression. Also, the degradation mode is unaffected if initial defect is located at the inner surface of the shell instead of the outer surface. Case (2) with initial defect near the mid-thickness of the shell initiates damage at 99.97 percent of its fracture pressure. Case (3) without any initial defect enters the global fracture stage directly without any structural degradation. Structural fracture pressures for cases (1), (2), and (3) are computed by CODSTRAN as 76.8154, 76.8289, and 76.8311 MPa (11.1413, 11.1433, and 11.1436 ksi), respectively. There is no significant difference among these cases as there would be no difference in the three fracture pressures if results were presented to three significant digits.

A structural stability analysis without considering local failure of the small scale cylindrical shell indicates a critical elastic buckling pressure of 565 MPa (81.9 ksi) which is more than seven times the ultimate fracture pressure of 76.8 MPa (11.14 ksi). CODSTRAN simulation agrees well with experimental results [28] where an external pressure under 12 ksi was re-

ported to fracture similar test specimens. The properties of AS-4 graphite fiber and ER-2258 epoxy matrix are given in Appendix A.

10.3 Damage Tolerance of a Prototype Size Composite Shell

For prototype size composite shells with a relatively large radius-to-thickness ratio, elastic buckling is the salient design consideration under hydrostatic pressure. Nevertheless, in case of accidental damage, structural collapse may be precipitated by compressive/shear fracture propagation even when the overall design of the defect-free shell is governed by elastic stability. Computational simulation is able to predict the conditions under which compressive failure occurs. In the design process, CODSTRAN can be used for (1) quantifying the stress fracture loading, (2) evaluating the shell laminate structure with regard to buckling stability, and (3) evaluating the level of accidental damage a particular shell structure is able to tolerate. Progressive fracture and damage tolerance aspects are the focus of this paper.

A T300/Epoxy composite system is used to illustrate quantification of the damage tolerance of a prototype size structure. The laminate consists of five hundred and seventy-six 0.127 mm (0.005 in.) plies resulting in a composite shell thickness of 73.2 mm (2.88 in.). The laminate configuration is $[90_2/\pm 15/90_2/\mp 15/90]_{s6}$. The 90° plies are in the hoop direction and the $\pm 15°$ plies are oriented with respect to the axial direction. The cylindrical shell has a diameter of 4.572 m (15 ft.) and a length of 15.24 m (50 ft.). The finite element model contains 800 nodes and 768 elements. At one point along the circumference, at half-length of the cylinder, initial fiber fractures in a number of plies are prescribed. The external hydrostatic pressure is gradually increased until the shell fractures or until the elastic buckling pressure of 2,323 KPa (337 psi) is reached.

For a structure without defects CODSTRAN predicts that outer hoop plies will fracture at 19.5 MPa (2.83 ksi) external pressure if buckling instability can be prevented. The 19.5 MPa fracture pressure for a defect free shell is 8.4 times the buckling pressure. Therefore, unless the shell is stiffened against buckling, the design will be controlled by stability considerations. Nevertheless, structural collapse by damage propagation need also be considered if major accidental damage tolerance is a design criterion. Durability analysis presented in this section shows the reduction in the ultimate external pressure because of possible accidental mutilation of the composite shell structure.

An external pressure of 1.38 MPa (200 psi) which is 59 percent of the buckling pressure is considered as the service load level for this shell. With reference to this service loading, a number of different accidental damage levels are considered as follows:

1. Accidental damage causing failure of the 288 plies in the outer half of the shell thickness at one node at half-length of the cylinder. The damage has a tributary axial length of 610 mm (24 in) and a surface area of 0.285 m^2 (3.07 ft^2). CODSTRAN durability analysis indicates that this level of accidental damage does not progress any further

under the service pressure of 1.38 MPa. If the external pressure level is raised 25 percent above the service pressure to 1.72 MPa (250 psi), damage grows across the thickness of shell and then stabilizes. Through-the-thickness damage remains stable up to the buckling pressure of 2,323 KPa (337 psi).

2. Accidental damage by crushing of the 432 plies in the outer three-quarters of the shell thickness at one node. CODSTRAN indicates damage growth across the shell thickness at the service load of 1.38 MPa. However, damage stabilizes and does not propagate to adjoining regions of the shell under the service pressure. Damage remains stable up to the buckling pressure of 2.32 MPa (337 psi) as stress concentrations adjacent to the damage zone remain at relatively low levels compared to the compressive strength $\sigma_{\ell 11C}$ of the ply.

3. Accidental damage by crushing of the 432 outer plies at two adjacent nodes along the shell axis with a total tributary length of 1.219 m (4 ft). Damage immediately grows across the thickness of the shell then stabilizes. Damage remains stable up to an external pressure of 1.72 MPa (250 psi). Above 1.72 MPa damage becomes unstable and propagates to adjacent regions of the shell.

4. Accidental damage by crushing of the 432 outer plies at three adjacent nodes along the shell axis with a total tributary length of 1.829 m (6 ft). Damage immediately grows across the thickness of the shell then stabilizes. However, damage becomes unstable if the external pressure is increased above the 1.38 MPa service pressure.

5. Accidental damage by crushing of the 432 outer plies at five adjacent nodes along the shell axis with a total tributary length of 3.048 m (10 ft). Damage immediately grows across the thickness of the shell and is unstable at the service pressure of 1.38 MPa. The external pressure level corresponding to damage stability for this case is 0.69 MPa (100 psi).

Figure 10.5 shows the length of an accidental damage by crushing or scraping the outer 3/4 of the shell thickness along the shell axis and the external pressure at which the damage remains stable. Damage stability in the pressure range of 0.69 to 2.32 MPa (100 to 337 psi) is depicted. The 2.32 MPa upper limit on the pressure corresponds to the buckling load.

10.4 Summary of Results

The significant results from this investigation in which CODSTRAN (COmposite Durability STRuctural ANalysis) is used to evaluate damage growth and propagation to fracture of thick composite shells subjected to external pressure are as follows:

1. CODSTRAN adequately tracks the damage growth and subsequent propagation to fracture for composite shells subject to external pressure.

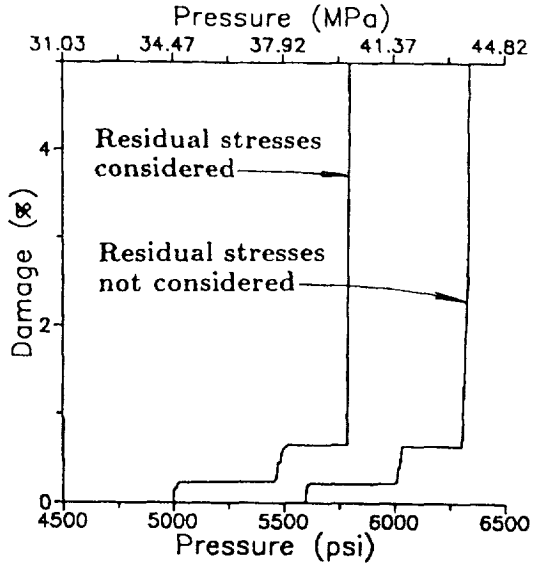

Figure 10.1: Damage Progression for Subscale Composite Shell I, AS-4/ER-2258 Composite System: 48 Plies $[0/90_2]_{16}$

2. The ultimate pressure to cause compressive fracture is sensitive to the matrix shear strength and to the residual stresses retained from the fabrication process.

3. For thick shells under external pressure the ultimate structural fracture pressure is not sensitive to the location and the existence of minor defects.

4. Damage stability after a major accident can be evaluated by CODSTRAN as an index of structural damage tolerance.

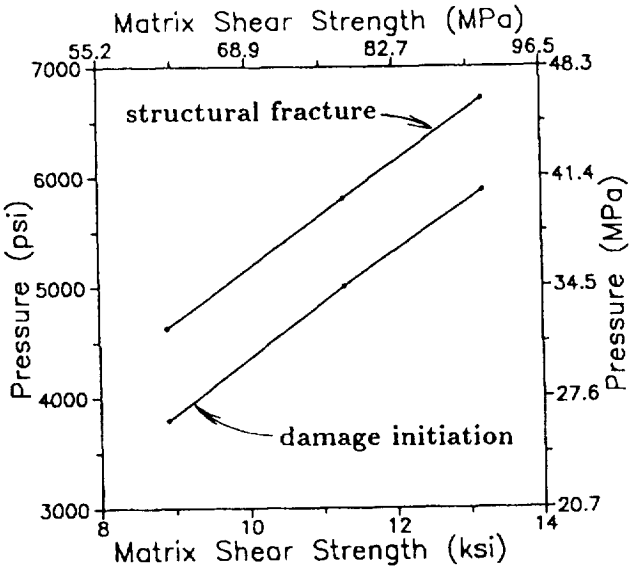

Figure 10.2: Effect of Matrix Shear Strength on Fracture Pressure, AS-4/ER-2258 Composite System: 48 Plies $[0/90_2]_{16}$

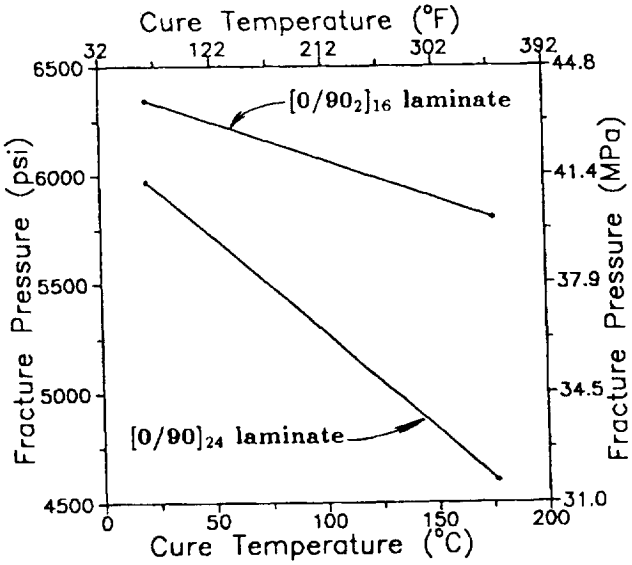

Figure 10.3: Effect of Cure Temperature on Fracture Pressure; AS-4/ER-2258 Composite System: 48 Plies $[0/90_2]_{16}$ and $[0/90]_{24}$

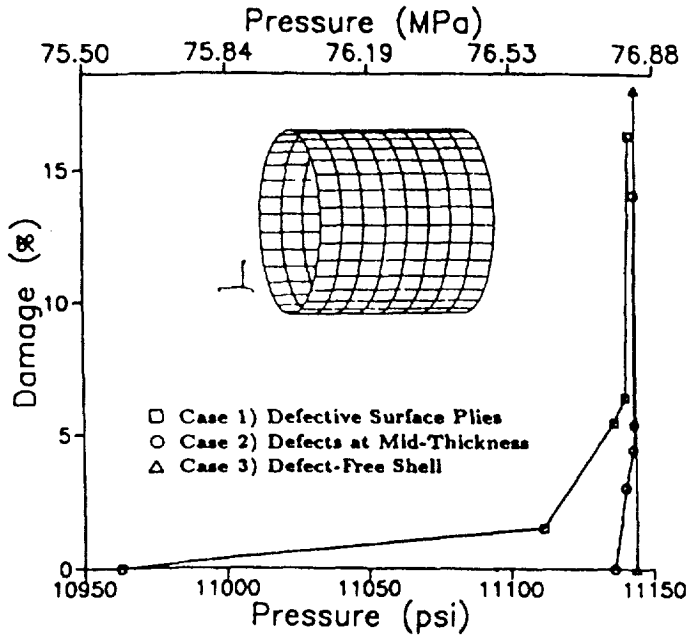

Figure 10.4: Damage Propagation for Subscale Composite Shell II; T300/Epoxy Composite System: 120 Plies $[90_3/0]_{15}$

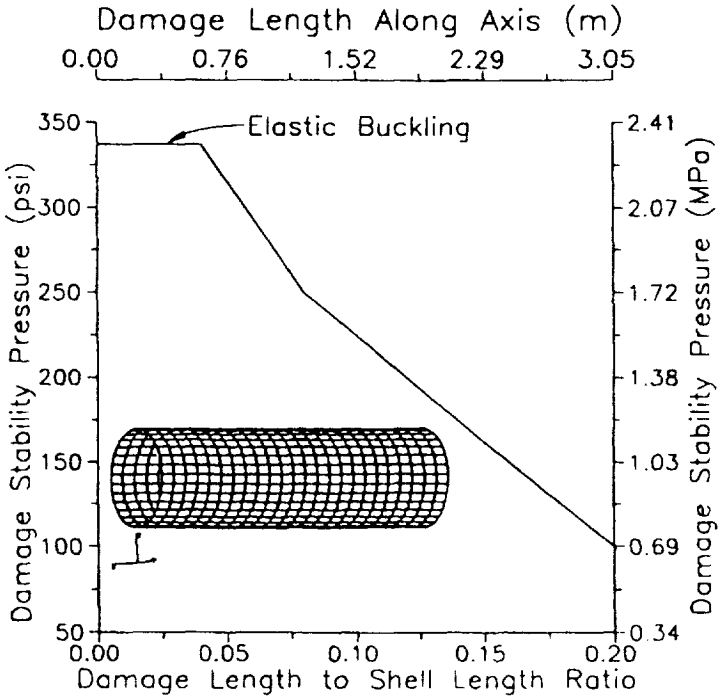

Figure 10.5: Damage Tolerance of Prototype Composite Shell; T300/Epoxy Composite System: 576 Plies $[90_2/\pm 15/90_2/\mp 15/90]_{s6}$

Chapter 11

Progressive Fracture of Adhesively Bonded Joints

Damage initiation and progressive fracture of adhesively bonded graphite/epoxy composites is investigated under tensile and compressive loading. Results indicate that adhesive properties have a significant effect on structural durability even when damage initiation/progression is not in the adhesive bond. Influence of the type of loading and the choice of adhesive on damage initiation and progression for adhesively bonded composites are investigated.

The purpose of this chapter is to examine damage progression in adhesively bonded composite joints. Due to the tendency of adhesively bonded structural elements to deform independently and to pull apart, adhesive joints present potential nucleation points for damage initiation and fracture. A double lap adhesive joint under tensile and compressive loading is examined.

Damage propagation studies are conducted to evaluate adhesively bonded joint performance. In general, the choice of adhesive properties for structural durability depends on the geometry, composite structure, and laminate configurations of the joined elements.

11.1 Stacked Laminate Modeling

In order to track the behavior of adhesive and structural elements independently, adhesive layers are represented separately from the composite structural elements. An adhesive layer is described typically as a single ply with zero fiber content; with matrix properties corresponding to those of the adhesive bond. To enable accurate representation of adhesively bonded joints, independent finite elements for laminates and adhesive layers are stacked in the appropriate order and tying equations are imposed to enforce the continuity of surface displacements between contacting layers. Figure 11.1 shows a schematic of two layers in contact with shell element nodes at he mid-thickness of each layer. In the local coordinate system, as shown in Figure 11.1, the nodal degree of freedom dependencies are expressed by the three tying equations for each pair of bonded nodes as follows:

$$D_1{}^{top} = D_1{}^{bottom} + 0.5(t^{bottom})D_5{}^{bottom} + 0.5(t^{top})D_5{}^{top} \tag{11.1}$$

$$D_2{}^{top} = D_2{}^{bottom} - 0.5(t^{bottom})D_4{}^{bottom} + 0.5(t^{top})D_4{}^{top} \tag{11.2}$$

$$D_3{}^{top} = D_3{}^{bottom} \tag{11.3}$$

Where D_i represents nodal displacement in the ith coordinate direction ($D_i = D_x, D_y, D_z, \theta_x, \theta_y, \theta_z$) and t represents layer thickness. Superscript *top* and *bottom* indicate the relative spatial location of the referenced layer. Tying equations are imposed between an adhesive layer and each structural element that is being joined by the adhesive layer. If the adhesive layer fails, the adhesive node is deleted and the corresponding tying equations are eliminated.

11.2 Damage Progression in a Double Lap Joint

A double lap joint of a graphite/epoxy laminate is considered as shown in Figure 11.2. The laminate consists of 48 plies that are configured as $[0/\pm 45/90]_{s6}$ with a total thickness 0f 0.25 in (6.35 mm). The 0° plies are oriented in the load direction and the 90° plies are oriented transverse to the load direction. The specimen has a width of 4.0 in (102 mm) and a length of 16.0 in (406 mm). The finite element model contains 260 nodes and 184 elements.

The composite system is made of AS-4 graphite fibers in a high-modulus, high strength (HMHS) epoxy matrix. The fiber volume ratio is 0.60 and the void volume ratio is 2 percent. The adhesively bonded double lap joint has been cured at a temperature of 350°F (177°C). The use temperature is 70°F (21°C). Two types of adhesives are considered. Type 1 adhesive has properties that are exactly the same as the HMHS matrix properties. Type 2 adhesive is a toughened epoxy resin adhesive (TERA) that is 42 percent stronger in tension compared to the HMHS adhesive but 43 percent weaker in compression and has an elastic modulus that is 44 percent lower than the elastic modulus of the HMHS adhesive.

The double lap joint is first subjected to a gradually increasing tensile load. The specimen is loaded by restraining one end and applying a uniformly distributed tensile load to the other end. Damage progression is computationally simulated as the loading is increased.

Figure 11.3 shows the simulated damage progression with increasing tensile loading on the double lap joint. The progressive damage response of the double lap joint is evaluated for both HMHS and TERA adhesives. Damage initiation for the HMHS adhesive bonded joint is at a 3.60 kip (16.0 KN) load by adhesive failure at the beginning of the lap joint near the left end support (Figure 11.2). In case of the TERA bonded joint, damage initiation is at 4.13 kips (18.4 KN) by simultaneous adhesive failure at the beginning of the lap joint and by matrix failures in two 90° plies closest to the adhesive bond near the center of the lap joint.

Although the TERA bonded joint performs better than the HMHS bonded joint during damage initiation, in the subsequent damage growth and progression stages the opposite case holds true. In Figure 11.3, load versus damage performance of the HMHS bonded joint, as plotted by the solid line, is considerably better than the performance of the TERA bonded joint shown by the dashed line. Figure 11.4 shows displacements versus loading for the HMHS and TERA bonded joints. Larger displacements are indicated for the TERA bonded joint as compared to the displacements of the HMHS bonded joint under the same loading.

Damage progression in the double lap joint is also evaluated under compressive loading. Figure 11.5 shows damage levels under compressive loading. The overall damage progression response under compressive loading is similar to that of tensile loading. Under both tensile and compressive loads the TERA bonded joint performs better at damage initiation; whereas the HMHS bonded joint performs better during damage growth and progression. The overall volume of damage under compressive loading is lower than that under tensile loading since compressive loading does not cause extensive matrix cracking in the 90° plies of the laminate as is the case under tensile loading.

Figure 11.6 shows displacements under compressive loading. It may be noted that the displacements of TERA bonded and HMHS bonded joints are the same prior to the damage initiation stage. However, after damage initiation, the TERA bonded joint behaves softer. Since the difference in displacements appears after damage initiation, it is a characteristic of the adhesive/laminate combined damage progression response rather than an effect of the more compliant elastic deformation of the TERA bond.

Figure 11.7 shows the DERR as a function of tensile and compressive loading for the HMHS bonded joint. The DERR for damage initiation is much higher under compressive loading, indicating greater resistance to damage initiation under compressive loading. However, after the damage initiation stage is completed DERR becomes much lower, indicating the lack of structural resistance to damage propagation. On the other hand, when the loading is tensile, as indicated by the solid line plot in Figure 11.7, the initial DERR level is relatively low and damage growth immediately after damage initiation does not encounter significant structural resistance. However, there is a secondary peak in DERR during damage progression. The initially low DERR level is because of matrix cracking in the 90° plies near the adhesive bond due to the relatively low tensile strength of the matrix. The secondary peak in SERR preceeds the involvement of the ±45° plies and fiber fractures in the damage propagation process.

Figure 11.8 shows the DERR levels for the TERA bonded joint. Similar to the HMHS bonded joint, initially the DERR level is higher under compressive loading. However, in the case of the TERA bonded joint, the secondary tensile DERR peak does not develop during damage progression. Also, comparing Figure 11.8 with Figure 11.7, it is seen that overall DERR levels are considerably lower for the TERA bonded joint as compared to the HMHS bonded joint. Computational simulation results collectively indicate that the HMHS bond performs better than the TERA bond with regard to damage tolerance of the graphite/epoxy

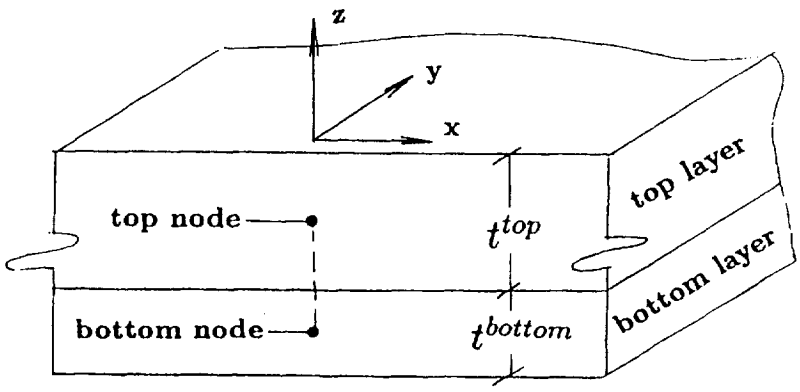

Figure 11.1: Consecutive Bonded Layers

double lap joint.

11.3 Conclusions

In the light of the durability investigation of the example composite double lap joint under uniaxial loading the following conclusions are drawn:

1. CODSTRAN adequately tracks damage initiation, growth, and subsequent propagation for adhesively bonded composite laminates subject to uniaxial loading.

2. Adhesive properties affect the damage progression response for bonded joints.

3. With regard to the structural durability of bonded graphite/ epoxy laminates, a high modulus adhesive bond is preferable to a toughened but lower modulus adhesive bond.

4. Computational simulation, with the use of established composite mechanics and finite element modules, can be used to predict the influence of adhesive characteristics as well as loading and composite constituent properties on the durability of adhesively bonded composite structures.

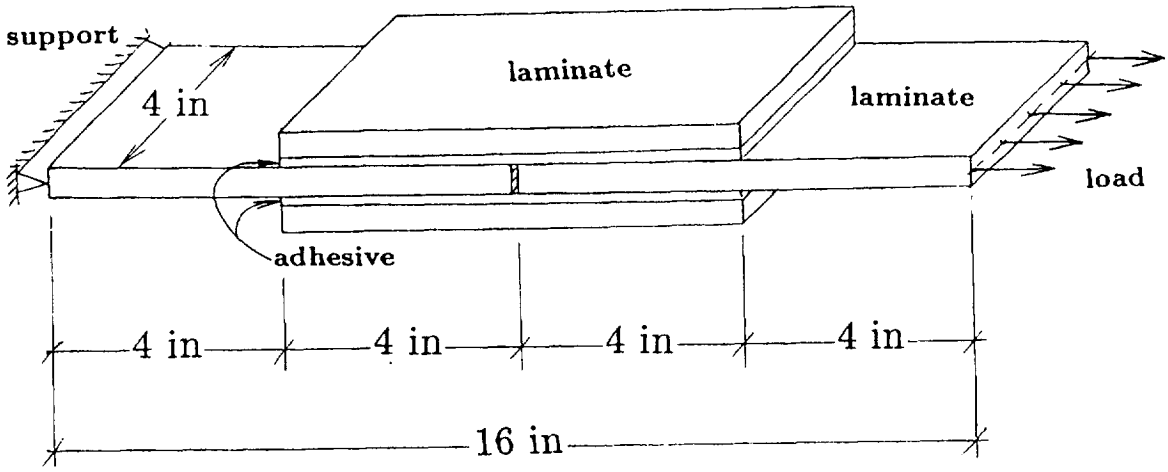

Figure 11.2: Double Lap Joint under Uniaxial Loading; Graphite/Epoxy: 48 Plies $[0/\pm 45/90]_{s6}$

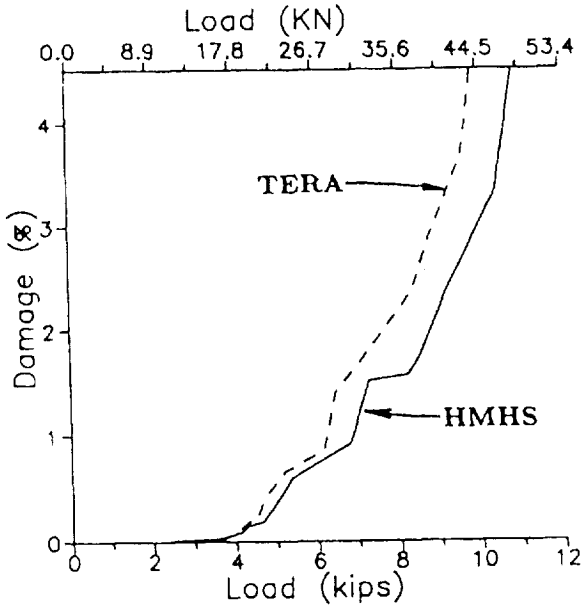

Figure 11.3: Damage Progression under Tension; Graphite/Epoxy: 48 Plies $[0/\pm 45/90]_{s6}$

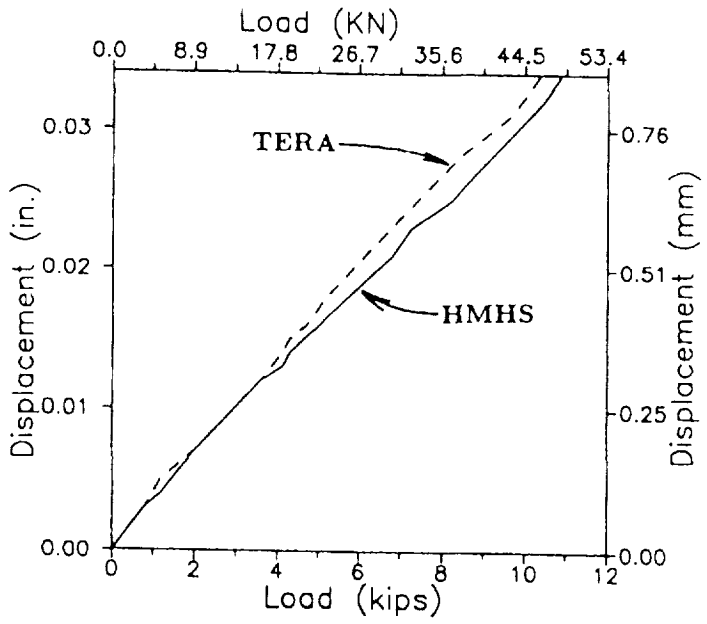

Figure 11.4: Displacements under Tension; Graphite/Epoxy: 48 Plies $[0/\pm 45/90]_{s6}$

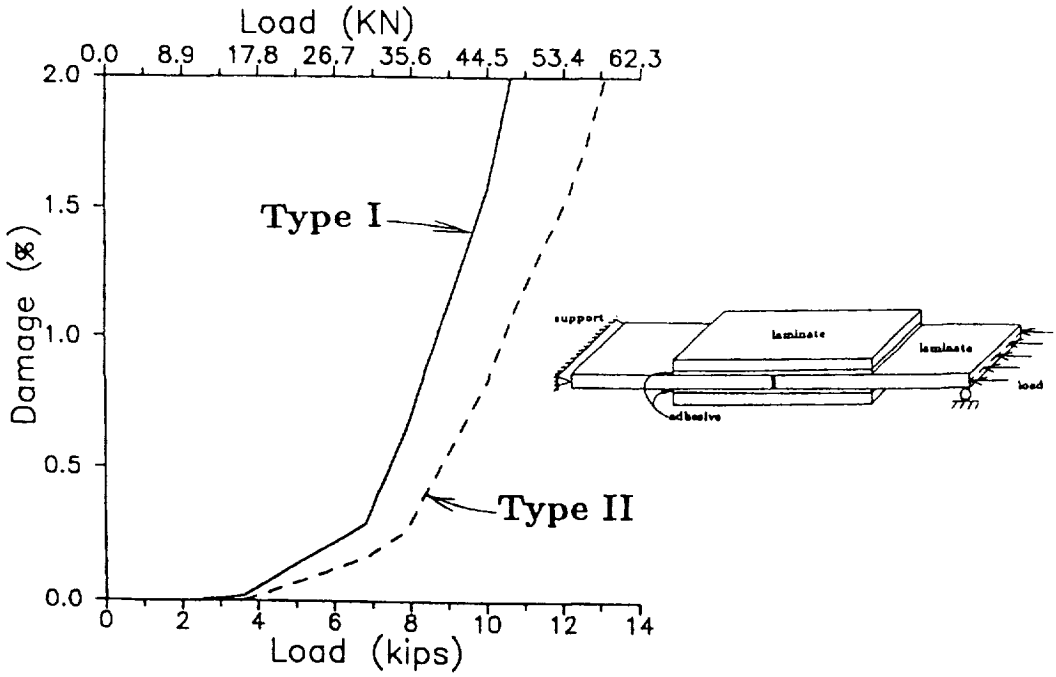

Figure 11.5: Damage Progression under Compression; Graphite/Epoxy: 48 Plies $[0/\pm 45/90]_{s6}$

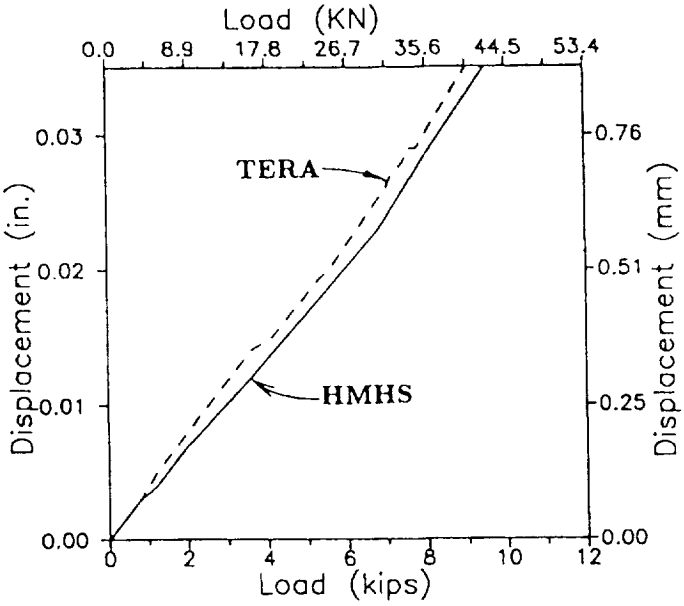

Figure 11.6: Displacements under Compression; Graphite/Epoxy: 48 Plies $[0/\pm 45/90]_{s6}$

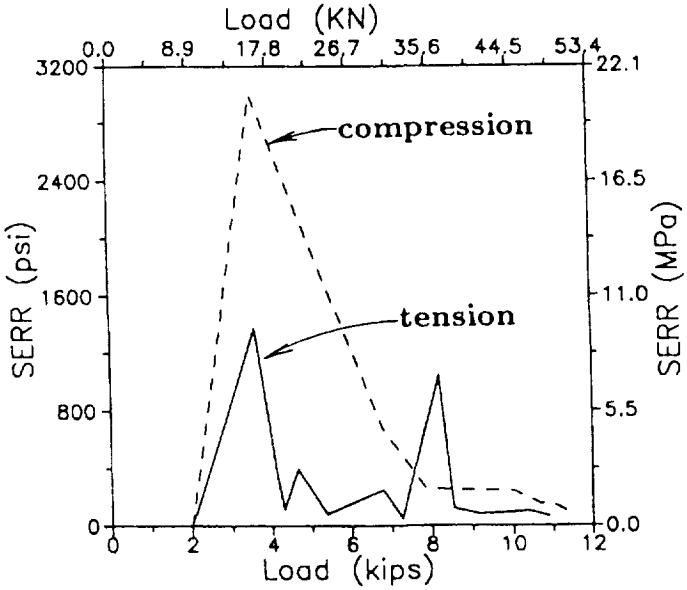

Figure 11.7: Strain Energy Release Rates; Graphite/Epoxy: 48 Plies $[0/\pm 45/90]_{s6}$; HMHS Bonded Adhesive Joint

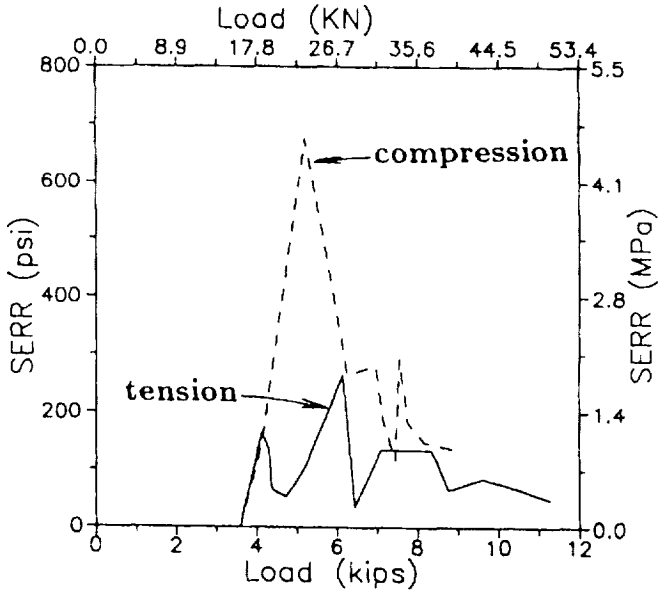

Figure 11.8: Strain Energy Release Rates; Graphite/Epoxy: 48 Plies $[0/\pm 45/90]_{s6}$; TERA Bonded Adhesive Joint

Chapter 12

Effect of Adhesive Thickness on the Durability of a Stiffened Composite Panel

Progressive damage and fracture of an adhesively bonded graphite/epoxy composite structure is evaluated. Load induced damage in both the adhesive bond and the adjoining laminate is considered. Damage initiation, growth, accumulation, and propagation to fracture are included in the simulation. Results show in detail the damage progression sequence and structural fracture resistance during different degradation stages. Influence of the type of loading as well as adhesive thickness on damage initiation and progression for an adhesively bonded composite structure is investigated.

Built-up graphite/epoxy composite structures have found extensive use in fulfilling many design requirements in aircraft structures, automotive vehicles, and marine applications. A cost effective method to fabricate composite structures is by adhesive bonding of structural elements. However, the durability and damage tolerance of adhesively bonded joints is difficult to evaluate due to the high level of interaction between the structural and adhesive response. The purpose of this chapter is to examine damage progression in adhesively bonded composite joints. Due to the tendency of adhesively bonded structural elements to deform independently and to pull apart, adhesive joints present potential nucleation points for damage initiation and fracture. Damage progression in a double lap adhesive joint as well as a stiffened composite panel is examined.

12.1 Stiffened Composite Panel

The investigated structure is a composite panel stiffened by a hat type stringer that is adhesively bonded to the skin. The finite element model, shown in Figure 12.1, uses stacked thick shell elements with tying equations between consecutive stacked layers. Figure 12.2 shows a cross section through the stiffened panel with physical dimensions. The composite system is

made of the same high strength AS-4 graphite fibers in a high-modulus, high-strength epoxy matrix (AS-4/HMHS) as in the double lap joint. The adhesive properties are the same as the HMHS epoxy matrix. The influence of adhesive thickness on the global damage progression is investigated. Durability of the stiffened panel with adhesive thicknesses of 0.1323, 0.2647, and 0.5293 mm (0.00521, 0.01042, and 0.02084 in) is evaluated under tensile, compressive, and lateral pressure loading. The three adhesive bond thicknesses are designated as Type I, Type II, and Type III joints, respectively, in the order of increasing adhesive thickness.

The skin laminate consists of forty-eight 0.132 mm. (0.00521 in.) plies resulting in a composite thickness of 6.35 mm. (0.25 in.). The fiber volume ratio is 0.60. The laminate configuration is $[[0/\pm 45/90]_s]_6$. The 0° plies are in the axial direction of the stiffener, along the x axis indicated in Figure 12.1. The width of the stiffened panel is 991 mm (39 in.) and it has a length of 559 mm (22 in.). Only half of the panel is represented in the computational model by defining a plane of structural symmetry at half length of the panel. The stiffener hat sections are made from the same AS-4/HMHS composite structure as the skin laminate. The stiffener is adhesively bonded to the skin at all surfaces of contact. Composite constituent level progressive damage simulation in the adhesive layer as well as in the joined elements is integrated into the structural analysis of the stiffened panel.

Axial tension or compression is applied by imposing a gradually increasing uniform axial loading at the clamped left edge of the panel. Damage initiation and progression are monitored as the panel is gradually loaded. Figure 12.3 shows the relationship between applied tensile loading and the produced damage during damage initiation and progression. Damage initiation is by ply failure in the top surface ply of the skin near the end of the stiffener. Figure 12.3 indicates that the stiffened panel experiences damage initiation sooner for a thicker adhesive bond. However, the effect of adhesive thickness on the damage initiation load is very small under tension. Figure 12.4 shows the SERR levels for the three adhesive thicknesses investigated. Figure 12.4 indicates that although a thicker adhesive bond has a lower damage initiation load, structural resistance to damage progression under tension is considerably higher for the thicker bond.

Figure 12.5 shows damage initiation and progression under compressive loading. Similar to tensile loading, a thicker adhesive bond experiences damage initiation sooner. Figure 12.6 shows the SERR levels under compression. Unlike tensile loading, SERR levels do not monotonically increase with adhesive thickness. Type II joint with an adhesive thickness of two plies has the best SERR performance. However, if the thickness is increased to Type III joint with an adhesive thickness of four plies, the SERR level is significantly degraded. Figure 12.6 indicates the existance of an optimal adhesive thickness under compressive loading.

The same stiffened panel is also investigated under lateral pressure applied to the skin. Figure 12.7 shows the damage progression under lateral pressure for Type I and Type II adhesive bonds with one and two ply adhesive thicknesses, respectively. The effect of adhesive thickness is not significant with regard to damage initiation and progression under normal pressure. Figure 12.8 shows the SERR levels under lateral pressure. The SERR levels for the thicker adhesive bond are higher, indicating better structural resistance against damage

propagation for the thicker adhesive. Figure 12.9 shows the maximum lateral deflection versus the applied pressure for the stiffened panel. The maximum lateral deflection is at the center of the plane of symmetry on the skin. Due to geometric effects the panel behaves stiffer with increasing pressure. There is no adhesive thickness effect on the deflection-pressure relationship.

12.2 Conclusions

In the light of the durability investigation of the example composite adhesively bonded stiffened panel the following conclusions are drawn:

1. CODSTRAN adequately tracks damage initiation, growth, and subsequent propagation to fracture for adhesively bonded stiffened composite structures.

2. Adhesive thickness may affect the damage progression response for adhesively bonded built-up composite structures.

3. Under tensile loading, a thicker adhesive bond improves the structural resistance to damage propagation even though the damage initiation load is lowered.

4. Under compressive loading, there is a critical thickness of the adhesive bond. If the adhesive bond is made thicker than the critical value, both the damage initiation load and the structural resistance to damage propagation are lowered.

5. Under lateral pressure loading, the difference in damage progression is not significant for adhesive thicknesses of one or two plies. The structural resistance to damage propagation is better for the stiffened panel with the Type II adhesive bond of two-ply thickness.

6. Computational simulation, with the use of established composite mechanics and finite element modules, can be used to predict the influence of adhesive thickness as well as loading and composite properties on the durability of adhesively bonded composite structures.

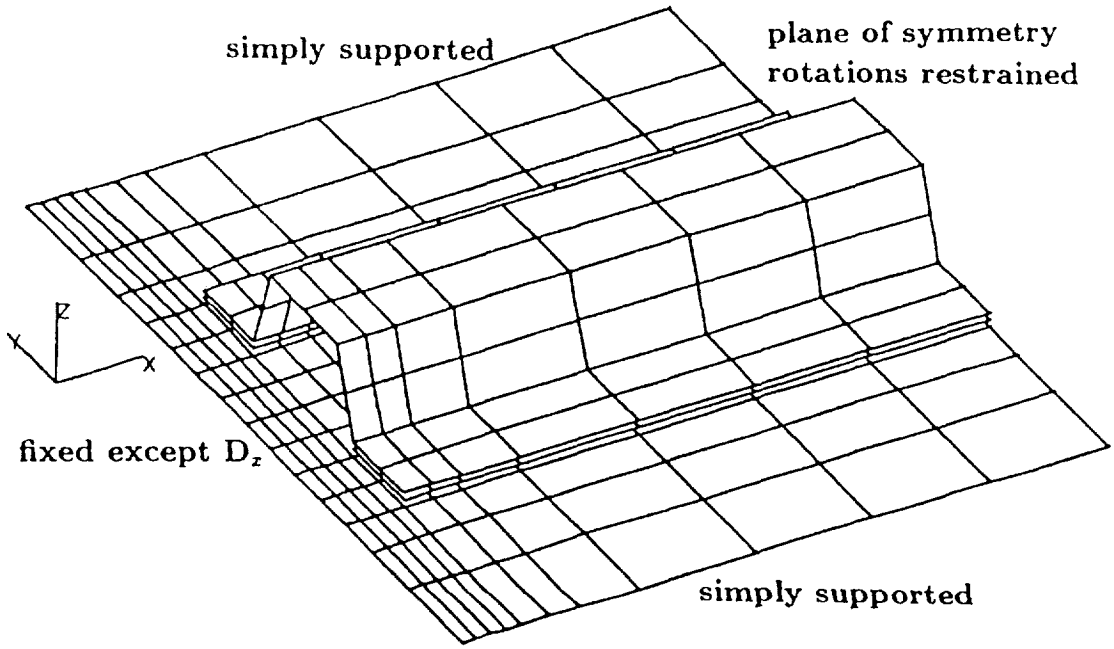

Figure 12.1: Stiffened Panel Finite Element Model; Graphite/Epoxy: 48 Plies $[0/\pm 45/90]_{s6}$

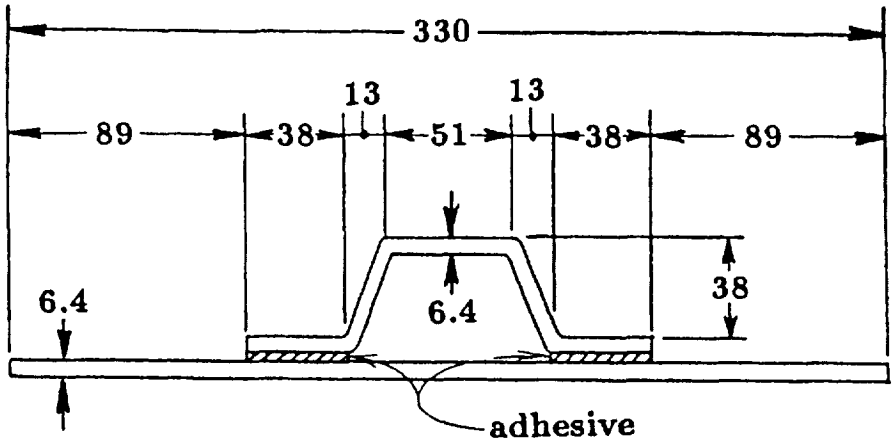

Figure 12.2: Cross Section through Stiffened Panel (All dimensions are in millimeters); Graphite/Epoxy: 48 Plies $[0/\pm 45/90]_{s6}$

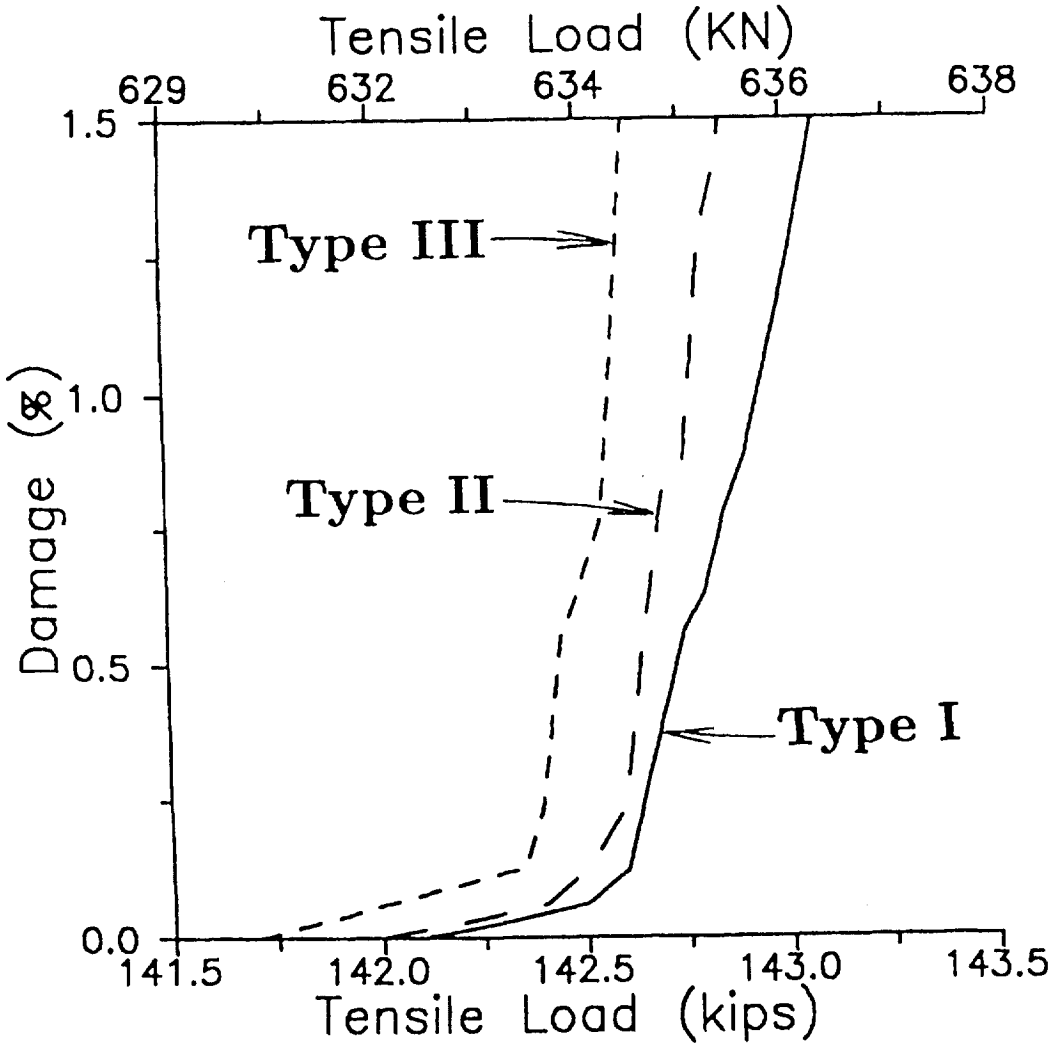

Figure 12.3: Damage Progression under Tension; Graphite/Epoxy:$[0/\pm 45/90]_{s6}$

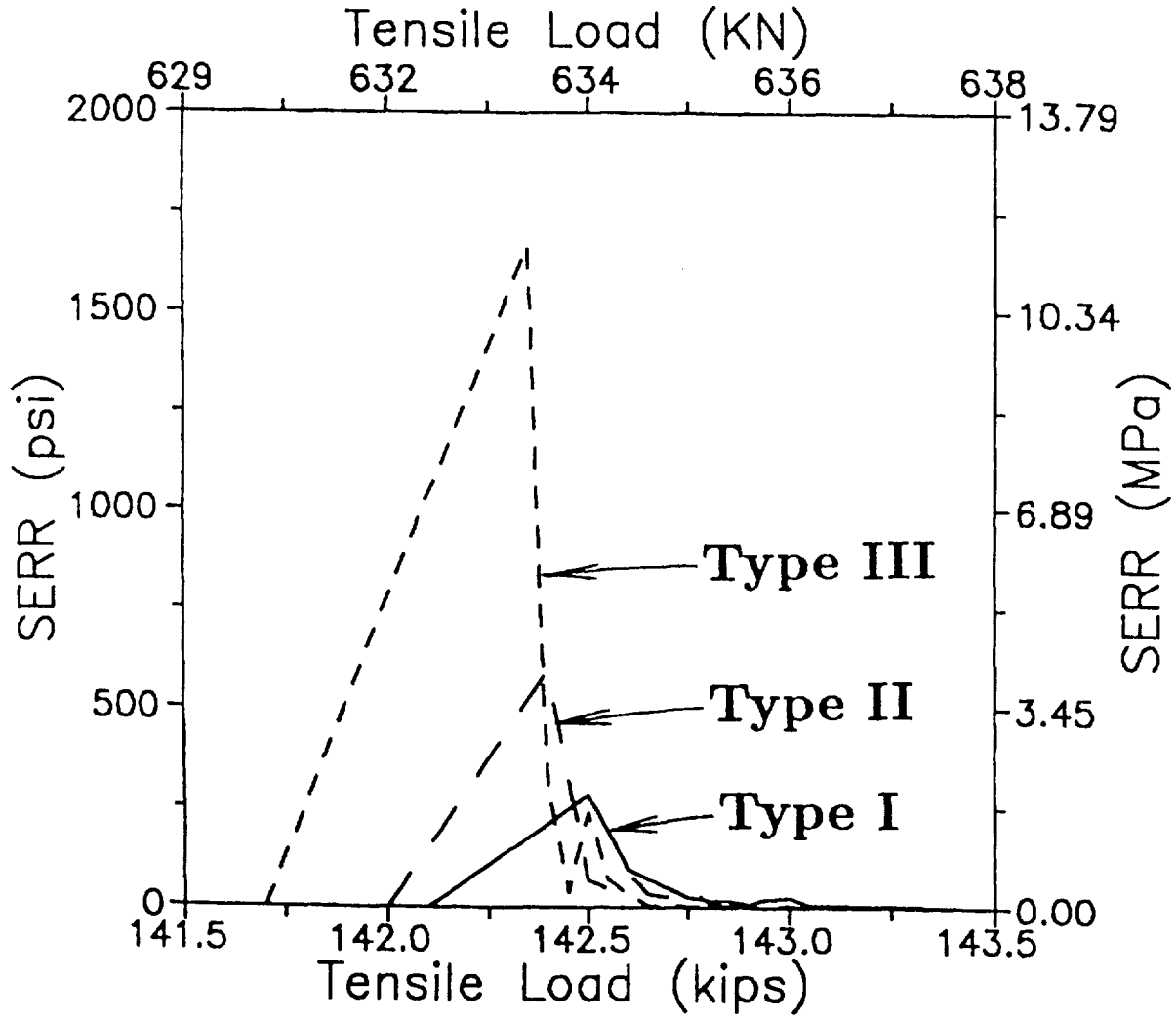

Figure 12.4: Strain Energy Release Rates under Tensile Loading; Graphite/Epoxy:$[0/\pm 45/90]_{s6}$

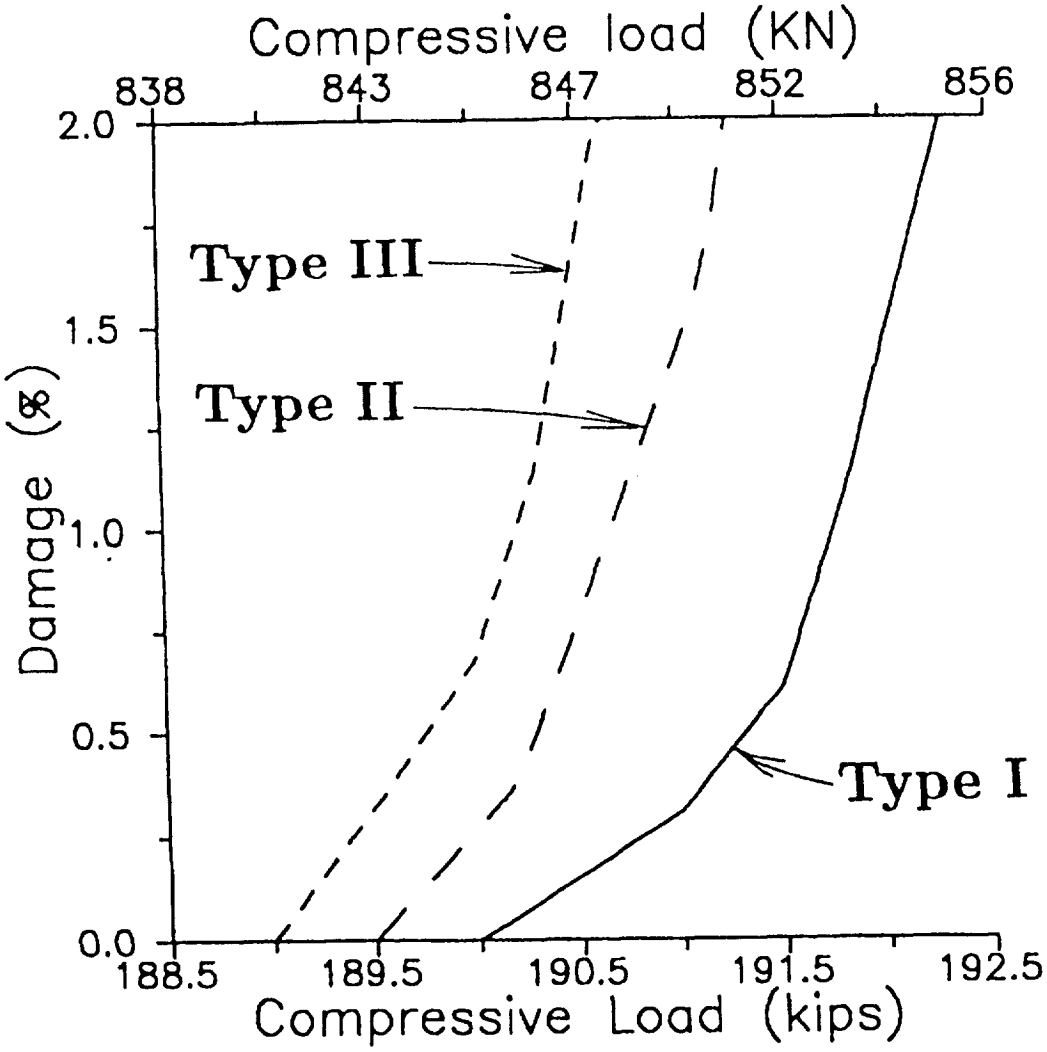

Figure 12.5: Damage Progression under Compressive Loading; Graphite/Epoxy:$[0/\pm 45/90]_{s6}$

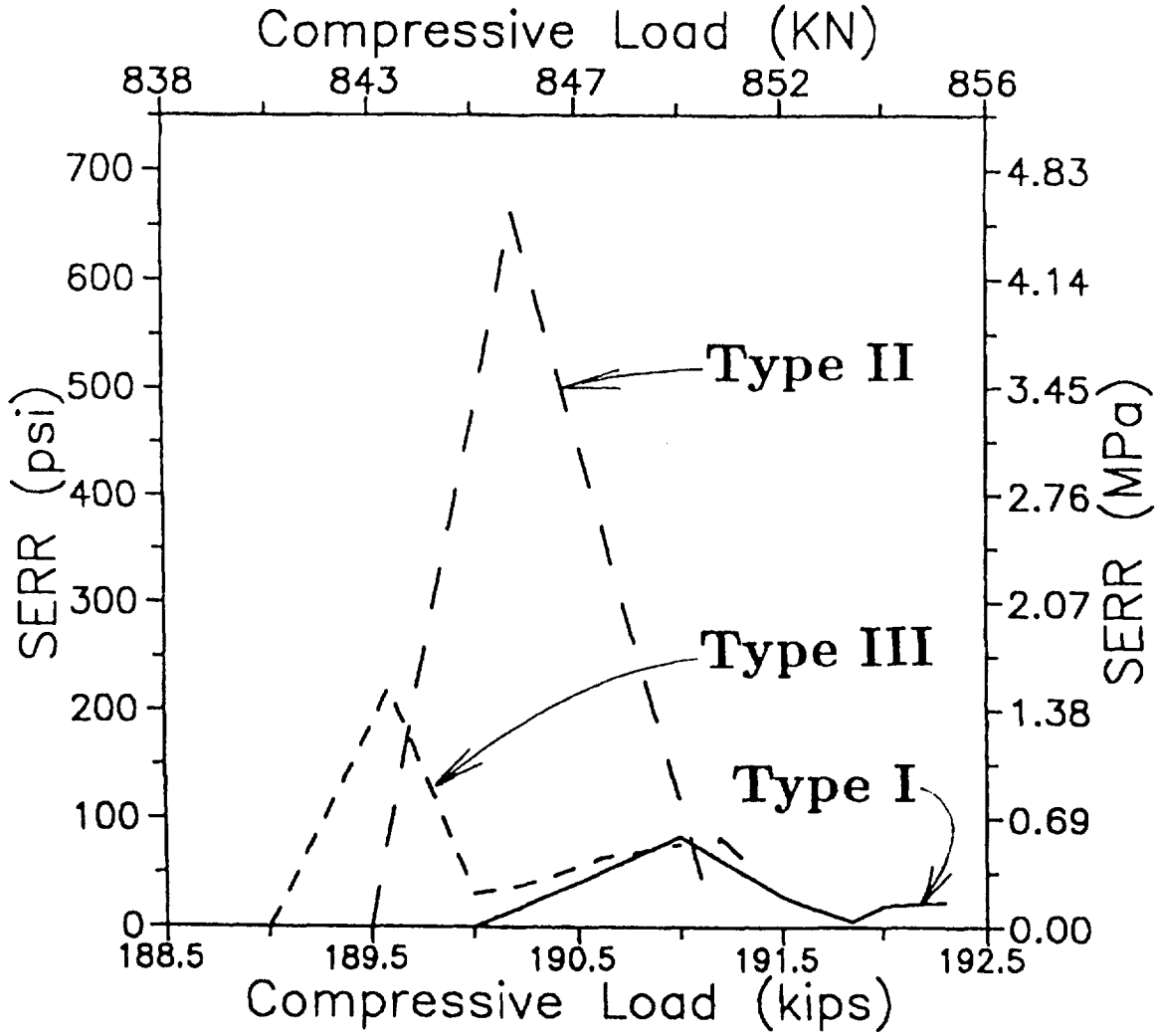

Figure 12.6: Strain Energy Release Rates under Compressive Loading; Graphite/Epoxy:$[0/\pm 45/90]_{s6}$

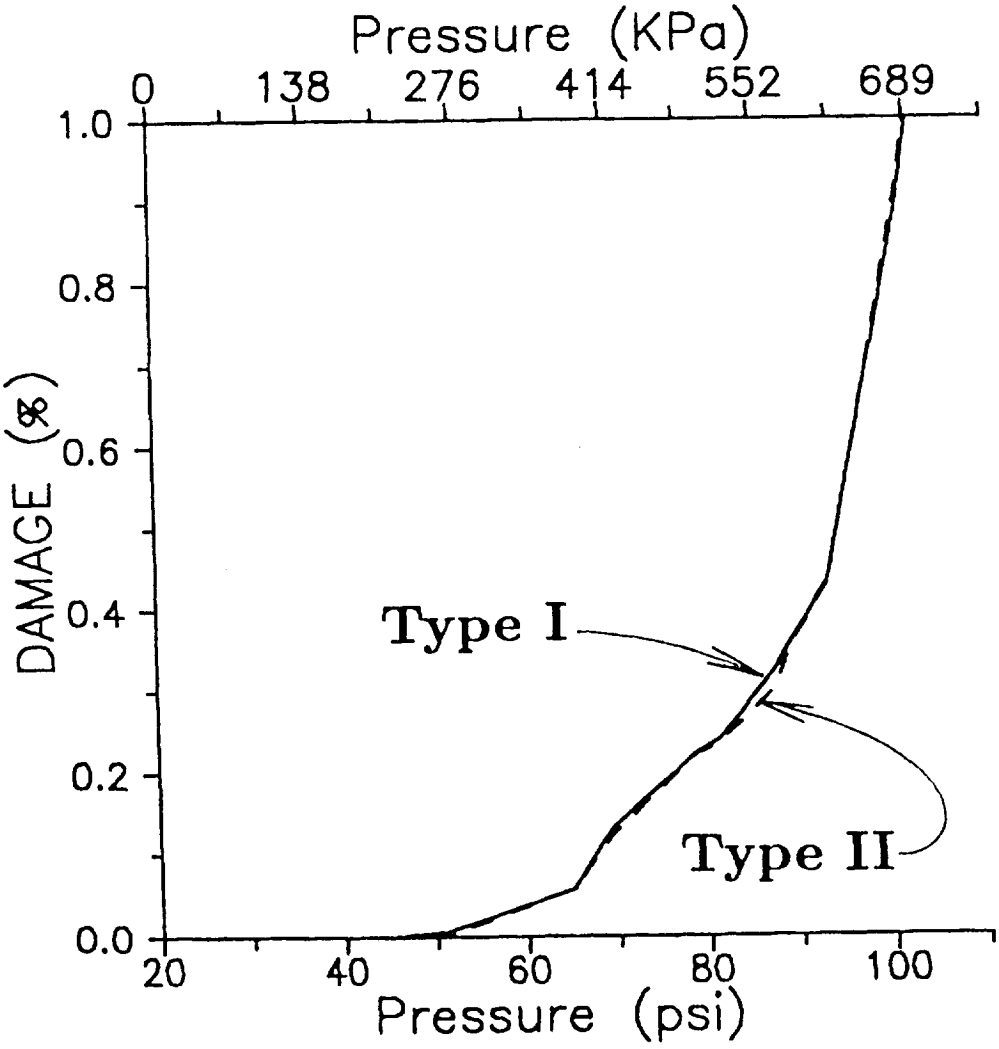

Figure 12.7: Damage Progression under Lateral Pressure; Graphite/Epoxy:$[0/\pm 45/90]_{s6}$

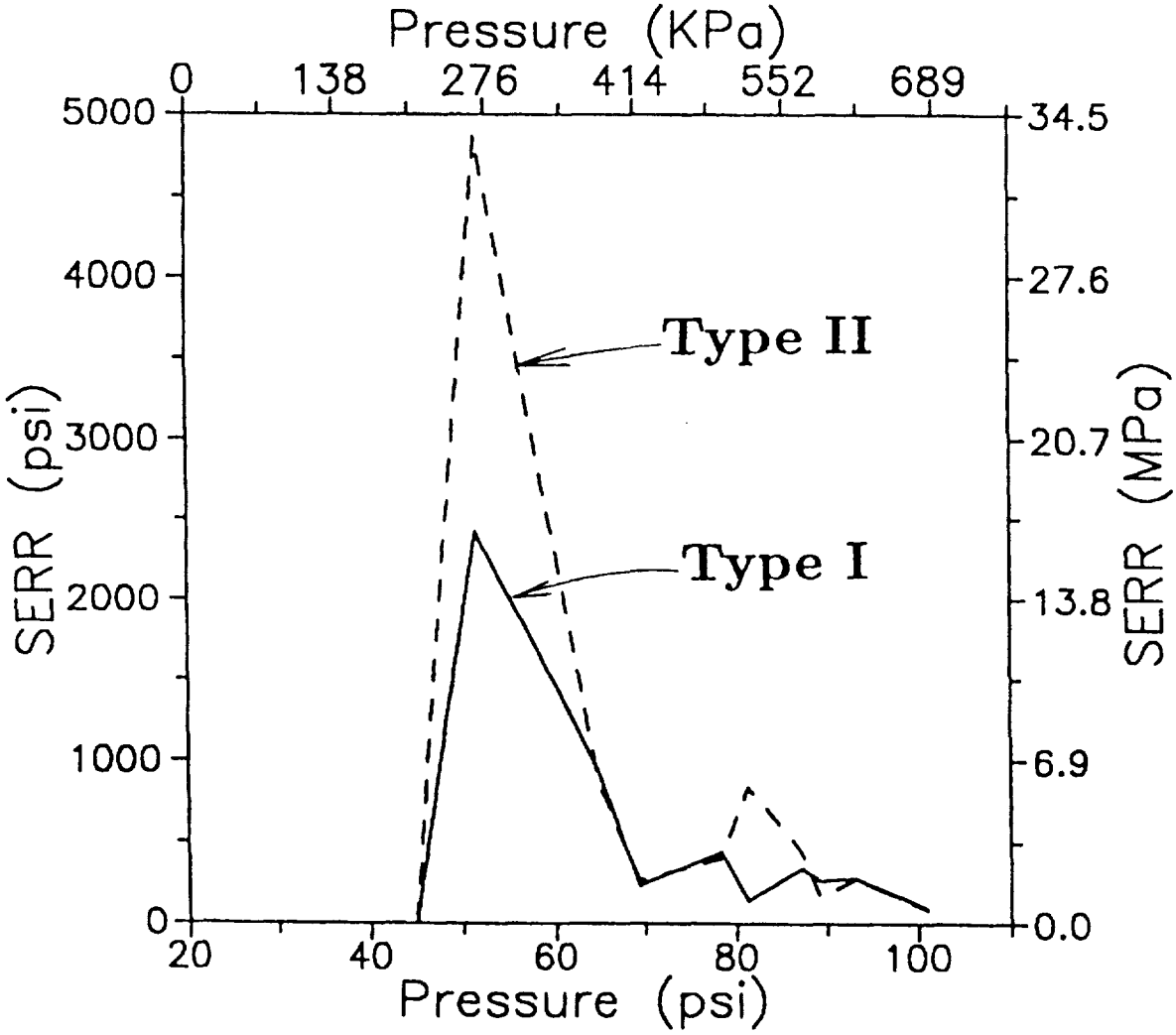

Figure 12.8: Strain Energy Release Rates under Lateral Pressure; Graphite/Epoxy:$[0/\pm 45/90]_{s6}$

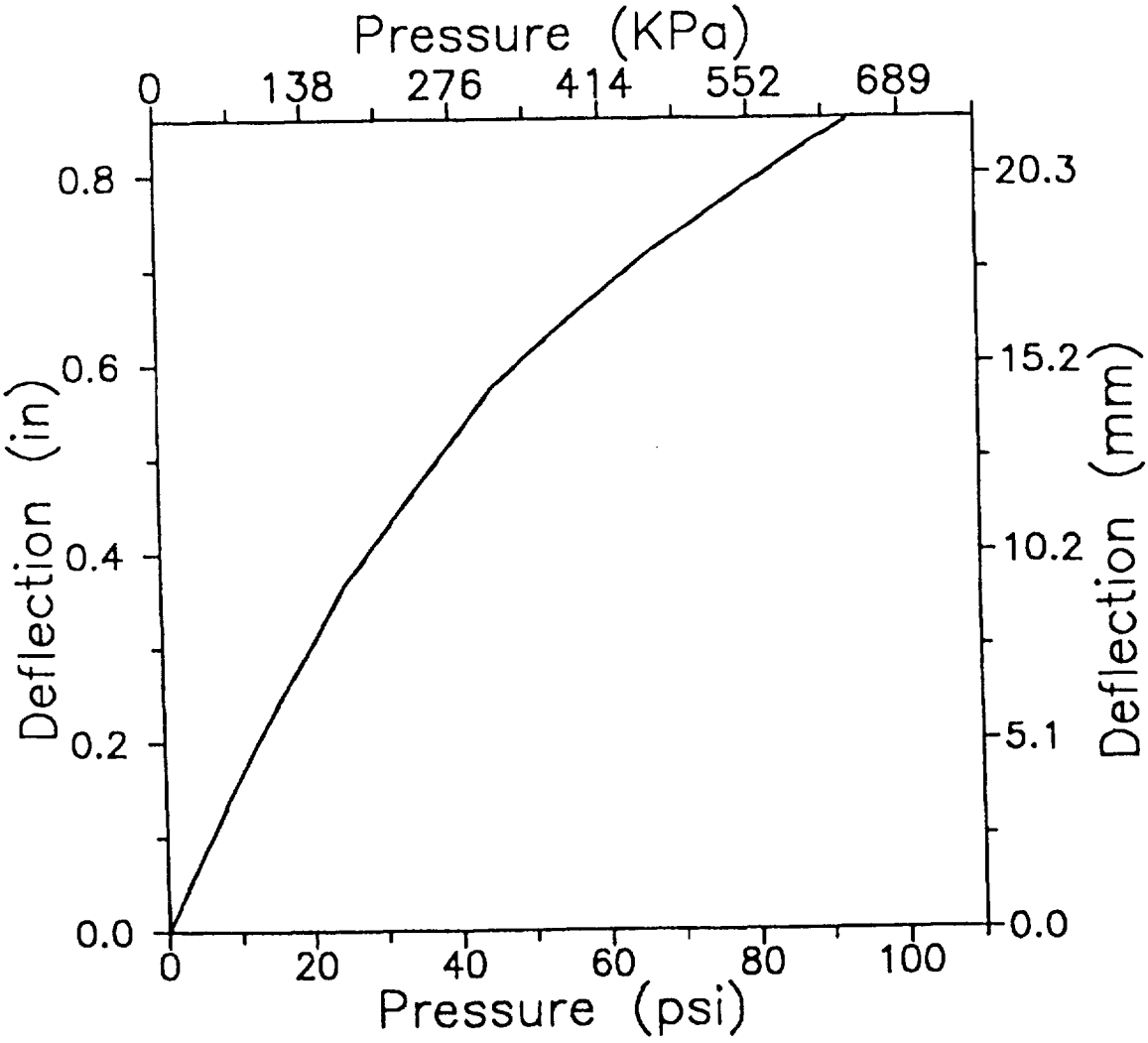

Figure 12. 9 : Deflection with Pressure; Graphite/Epoxy:$[0/\pm 45/90]_{s6}$

Chapter 13

Damage Tolerance of Thin Composite Reinforced Membrane Structures

Structural performance of fiber reinforced flexible composite membranes, designed as pressurized shelters for space exploration, is investigated via computational simulation. COD-STRAN is utilized for the simulation of damage initiation, growth, and propagation under pressure. Aramid fibers are considered in a rubbery polymer matrix for the composite system. Effects of fiber orientation and fabrication defect/accidental damage are investigated with regard to the safety and durability of the shelter. Results show the viability of fiber reinforced membranes as damage tolerant enclosures for space colonization.

13.1 Introduction

Future Lunar and planetary exploration and colonization attempts require the planning, design, and construction of shelters to accommodate expeditionary communities for extended periods of time. As a first priority, a Lunar shelter must provide a breathable atmosphere with sufficient interior pressure for pulmonary function. The most efficient shelter configuration will exploit the lunar surface to provide the foundation and structural support for a reinforced inflatable membrane that will also act as the roof of the shelter.

Candidate ply layups for the fiber composite inflatable membrane are investigated with regard to progressive damage and fracture of the shelter due to pressurization. The performance of aramid fibers in a rubbery polymer matrix is evaluated. For a standard thickness and geometry, membranes with different fiber orientations are investigated to examine the influence of ply fiber layup on the ultimate pressure and damage tolerance. Results indicate that structural fracture pressure is sensitive to ply fiber orientations.

In addition to defect-free membranes, the behavior of membranes with fabrication defects at the surface and at the mid thickness is examined. An additional case with local through-the-thickness damage is evaluated for damage tolerance.

Progressive fracture investigations providing design insight under lateral pressure are presented. Utilization of the CODSTRAN computer code for structural durability analysis is examined in the context of the structural design of a reinforced membrane inflatable roof. The type/extent of fabrication defect and accidental damage that results in an unstable damage propagation to structural fracture is quantified for the examined membranes. The internal pressure is gradually increased until the composite membrane bursts. Damage initiation, growth, accumulation, and propagation to structural fracture are included in the simulations.

13.2 Reinforced Membrane Structure

The design example consists of a composite membrane shelter subjected to internal pressure. Loading is applied by imposing a gradually increasing uniform lateral pressure from the underside of the membrane. Large displacements are taken into account before and during damage initiation and progression.

The pressurized membrane enclosure has a circular foundation of 20.32 m (66.67 ft) diameter. When inflated, the mid height is raised to 6.1 m (20 ft) relative to the edges. The inflated membrane is shaped as a spherical cap. A computational model of the shelter is prepared using 220 rectangular shell elements with 237 nodes, as shown in Figure 13.1. The quadrilateral finite element properties are based on the laminate structure at each node.

The composite system is made from Kevlar aramid fibers in a rubbery polymer matrix. The fiber volume ratio is 50 percent. The fiber and matrix properties are given in Appendix A.

The laminated membrane is manufactured from twelve 0.127 mm (0.005 in) plies, resulting in a total thickness of 1.524 mm (0.060 in).

13.3 Results

Three different ply layups are considered to investigate the influence of fiber orientation on load carrying capability and durability. The three layups are $[0/90]_6$, $[0/\pm45/90]_3$, and $[0/\pm60]_4$. Each layup is independently investigated due to gradual pressurization of the shelter. Results are summarized in Table 13.1. Also, the damage initiation and growth stages are depicted in Figure 13.2. The ordinate in Figure 13.2 shows the percent damage based on the volume of the membrane that is affected by the various damage mechanisms. The percent damage parameter is used as an overall indicator of damage progression. Computation of this overall damage parameter has no interactive feedback on the detailed evaluation and accounting of local ply damage modes.

Computational simulation shows the $[0/\pm60]_4$ layup to be the most effective for this flexible membrane shelter. Damage initiation and global fracture stages are consistently related for all three cases. Damage initiation is typically by local fiber failures near the apex of

the pressurized membrane. After damage initiation, damage usually grows through the membrane thickness before global fracture. Global fracture is initiated by tearing near a through-the-thickness damage with coalescence of damage zones.

After selecting the design layup as $[0/\pm 60]_4$, damage tolerance of the membrane is investigated by prescribing local defects near the apex of the shelter. Three cases are examined as follows: 1) Surface defect prescribed by cutting the first three surface plies of the membrane; 2) interior defect where three interior plies (plies 5-7) are cut; and 3) a through-the-thickness defect where all plies are cut. Ply cuts in all cases are 700 mm long and made perpendicular to the fiber directions. The defective membranes are simulated by subjecting them to gradually increasing pressure. A summary of the pressures for further damage growth from the existing defects is given in Table 13.2. A comparison of the initial damage growth stages for these cases is also shown graphically in Figure 13.3. Results indicate that the $[0/\pm 60]_4$ flexible membrane shelter has excellent damage tolerance. Even though the initial damage pressure is considerably lower for the defective membranes, the global fracture pressure is very close for the defect-free, the surface-defective, and the internally defective membranes. The worst case membrane considered with through-the-thickness damage has 18 percent lower ultimate pressure compared to the defect-free case.

13.4 Concluding Remarks

The significant results from this investigation in which CODSTRAN is used to evaluate damage growth and propagation to fracture of a pressurized composite membrane shelter are as follows:

1. Computational simulation, with the use of established composite mechanics and finite element modules, can be used to predict the influence of existing defects as well as loading, on the safety and durability of fiber composite membrane structures.

2. CODSTRAN adequately tracks the damage growth and subsequent propagation to fracture for initial defects located at the surface, or in the mid-thickness of composite membranes, as well as through-the-thickness defects.

3. Initially defective membranes begin damage growth at a lower pressure compared to a defect free membrane. However, the ultimate pressure is not significantly reduced for partial-thickness defects. For the membrane with a through-the-thickness defect the ultimate pressure is reduced by 18 percent.

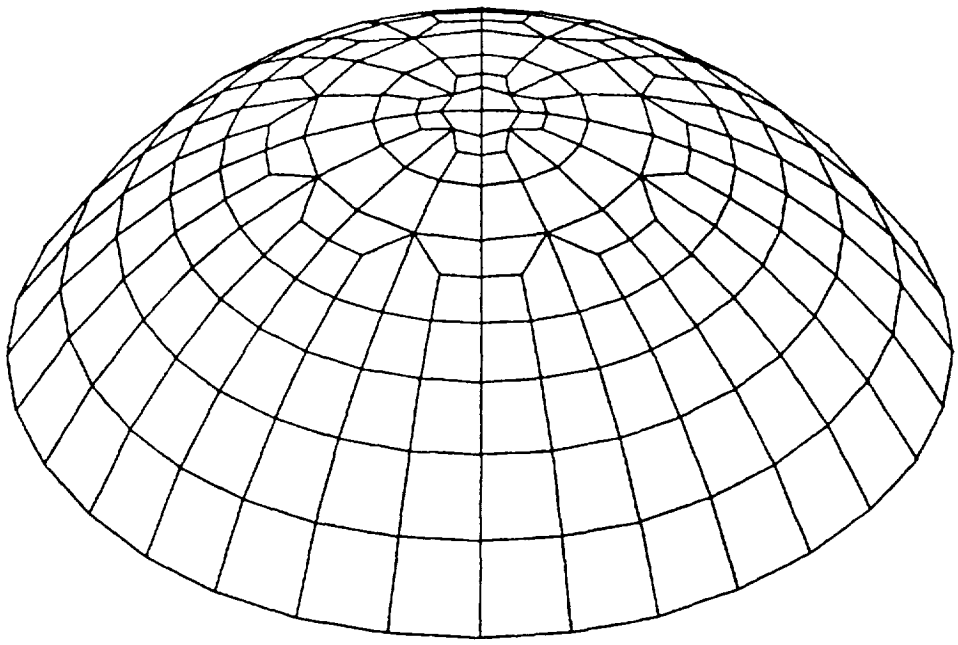

Figure 13.1: Finite Element Model

Table 13.1: Effect of Ply Layup on Durability

PLY LAYUP	PRESSURE (KPa) DAMAGE INITIATION	DAMAGE THROUGH THE THICKNESS	GLOBAL FRACTURE
$[0/90]_6$	95.95	99.22	115.42
$[0/\pm45/90]_3$	124.01	125.99	129.35
$[0/\pm60]_4$	132.72	134.36	140.65

Table 13.2: Effect of Initial Defect on Durability

INITIAL DEFECT	PRESSURE (KPa) DAMAGE INITIATION	DAMAGE THROUGH THE THICKNESS	GLOBAL FRACTURE
NONE	132.72	134.36	140.65
SURFACE	122.92	130.91	140.61
INTERIOR	122.92	129.46	131.45
THROUGH	95.95	99.22	115.38

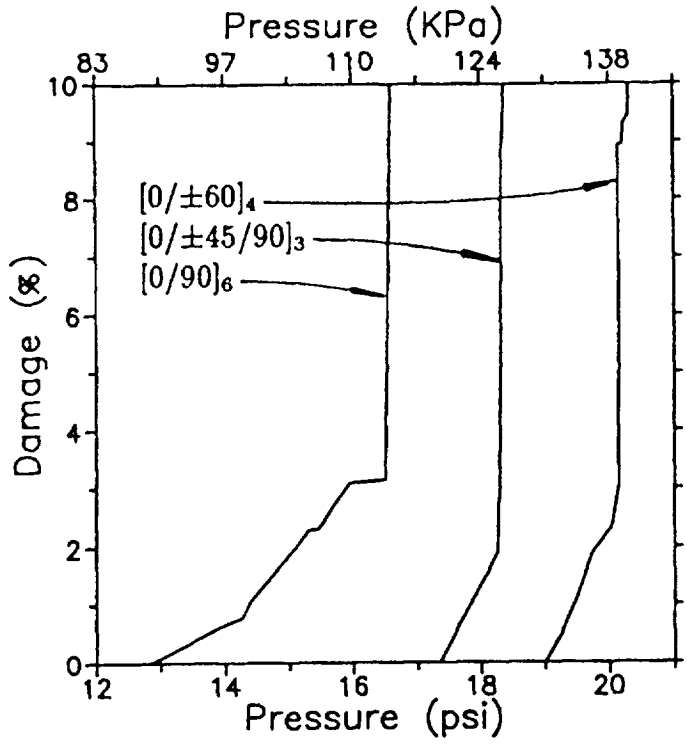

Figure 13.2: Ply Layup and Structural Durability

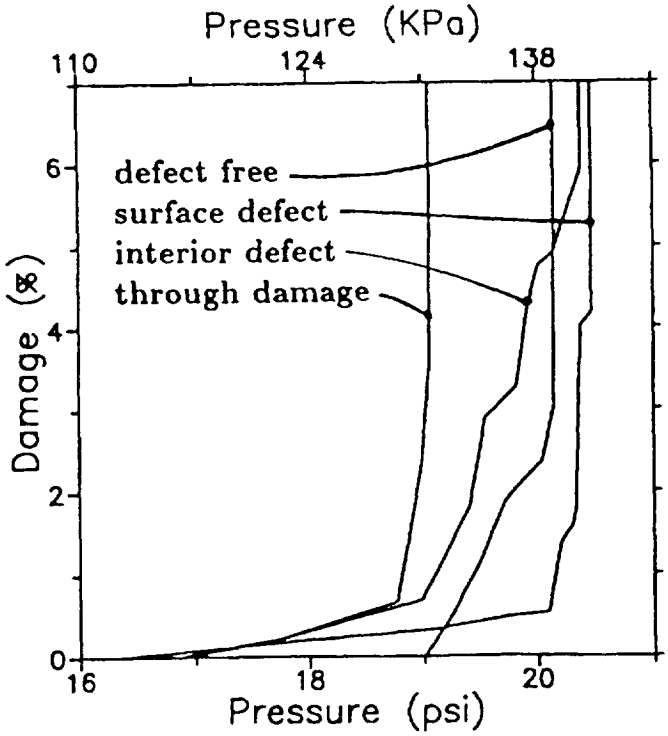

Figure 13.3: Defect and Damage Tolerance

Chapter 14

Damage Progression in Bent Composite Structural Members

Computational simulation of progressive damage and fracture in laminated composites is investigated for bent composite specimens under tension. A unidirectional graphite/epoxy composite is considered. For the simulated cases, damage initiation is by delamination due to interlaminar stretch tension at the point of maximum bending in the bent segment of the laminate. Effects of curvature, laminate thickness, and matrix tensile strength on damage initiation and progression are investigated. Comparison of differences in the damage progression mode with variation in laminate thickness indicate that thicker laminates tend to localize the damage growth to the region of sharp curvature. The damage initiation load is sensitive to matrix tensile strength. However, reasonable variations in matrix tensile strength do not change the damage initiation and progression characteristics. Results are consistent with experimental data from the literature.

14.1 Introduction

Built-up graphite/epoxy composite structures have found extensive use in fulfilling many design requirements in aircraft structures, automotive vehicles, sports equipment, and marine applications. A cost effective method to fabricate composite structures is by forming structural elements by tape layup on polished metallic forms. Often the shape of a composite laminate includes sharp curvatures that define structural form and function. However, the durability and damage tolerance of laminates with sharply curved parts is often a problem due to delamination initiated by interlaminar stretch tension generated by bending of a sharply curved part.

When the curvature is sharp, or the radius of curvature small, interlaminar stretch stress due to bending becomes the governing factor for damage initiation and delamination. Other factors such as thickness and constituent material properties are also important in affecting the damage progression. The objective of this chapter is to present an example evaluation

of the durability of composite structures with a sharp curvature. Damage progression in a family of sharply curved composite specimens is examined.

The structural durability of a bent composite specimen is investigated under an overall tensile loading that induces flexure, shear, interlaminar stretch, as well as tension in the member. Bent composite structural members are susceptible to delamination mainly due to the interlaminar tension stresses.

The CODSTRAN computational capability to simulate the initial damage caused by interlaminar tensile stresses and the subsequent damage progression in sharply curved composite structural members is demonstrated. Durability of a bent composite structural member is investigated by simulating its structural degradation under loading. The composite structure is made from unidirectional high-strength graphite fibers in a high-modulus high-strength epoxy matrix. Damage initiation, growth, accumulation, and propagation to structural fracture are included in the simulation. Computational results are compared with experimental data from the literature [31]. Results indicate that damage initiation and progression have significant effects on structural behavior under loading. Utilization of an CODSTRAN for the assessment of structural durability under a complex multiaxial stress state is demonstrated. The damage progression sequence and structural fracture resistance during different degradation stages are shown in detail.

14.2 Interlaminar Normal Stresses

The ICAN composite mechanics module is augmented by Lekhnitskii's solution for normal stresses in the thickness direction due to bending of a curved anisotropic plate [32]. These stresses are given as:

$$\sigma_r = -\frac{M}{b^2 g}\left[1 - \frac{1-c^{k+1}}{1-c^{2k}}\left(\frac{r}{b}\right)^{k-1} - \frac{1-c^{k-1}}{1-c^{2k}}c^{k+1}\left(\frac{b}{r}\right)^{k+1}\right] \tag{14.1}$$

where

$$g = \frac{1-c^2}{2} - \frac{k}{k+1}\frac{\left(1-c^{k+1}\right)^2}{1-c^{2k}} + \frac{kc^2}{k-1}\frac{\left(1-c^{k-1}\right)^2}{1-c^{2k}},$$

$k = \sqrt{E_{11}/E_{33}}$, M is the applied bending moment per unit width of the laminate, b is the outer radius of curvature, c is the ratio of inner to outer radii of curvature, and r is the distance from the center of curvature to where the stress is evaluated. The σ_r normal stresses due bending of the curved segment are added to normal stresses caused by applied pressures on the top and bottom surfaces of the laminate.

14.3 Bent Composite Specimen

Computational simulation of sharply curved composites is demonstrated on a bent composite

specimen of unidirectional graphite/epoxy laminate as shown in Figure 14.1. The specimen has a width of 25.4 mm (1.0 in). The finite element model contains 260 nodes and 184 thick shell elements. There are six equally spaced nodes in the width direction. The sharply curved segment is subdivided into eight elements along the quarter circular curve. The composite system is made of AS-4 graphite fibers in a high-modulus, high strength (HMHS) epoxy matrix. The fiber and matrix properties are obtained from a databank of composite constituent material properties resident in CODSTRAN [6]. The corresponding AS-4 fiber and HMHS matrix properties are given in Appendix A.

The HMHS matrix properties are representative of the 3501-6 resin. The fiber volume ratio is 0.60 and the void volume ratio is 2 percent. The sharply curved composite specimen has a forming or inner radius of curvature of 5.0 mm (0.2 in). The cure temperature is 177°C (350°F) and the use temperature is 21°C (70°F). Three different composite thicknesses are considered with 16, 24, and 48 plies. The corresponding specimen thicknesses are 1.96 mm, 3.35 mm, and 6.61 mm (0.0772 in, 0.132 in, and 0.260 in), respectively. Nominal ply thickness is 0.127 mm (0.005 in).

The simulated bent composite specimens are taken from an experimental investigation [31]. All specimens are subjected to unidirectional loading as shown in Figure 14.1. Each specimen is loaded by restraining translation of one of the load points and applying a tensile load to the other load point. Damage progression is computationally simulated as the loading is increased.

Figure 14.2 shows the damage progression with increasing loading on specimens with three different thicknesses. The progressive damage response of the bent composite is evaluated for 16 ply, 24 ply, and 48 ply unidirectional specimens. For all three specimens damage initiation is by interlaminar matrix failure under high tensile stresses in the thickness direction. Figure 14.2 shows that the damage progression mode is affected significantly with variation of composite thickness. The thinner 16 ply composite displays a linear increase in the damage volume after the damage initiation stage. On the other hand, the thicker 48 ply composite shows a nonlinear damage growth pattern due to the localization of damage near the point of damage initiation. For the 16 ply specimen the simulated fracture load of 1143 N (257 lbs) agrees well with the 1080 N (243 lbs) test [31] result. For the thicker specimens computational simulation results are not compared with test data because the experimental investigators [31] discount the test results on thicker specimens due to the discovery of significant defects in the sharply curved part during post-failure examinations. Nevertheless the scatter of test data for thicker specimens is predictable by quantifying the characteristics of structural resistance against damage propagation.

Figure 14.3 shows the DERR as a function of loading for all three specimen thicknesses. For each case, the first peak in DERR level corresponds to damage initiation by interlaminar stretch tension failure at the node with maximum bending moment and maximum curvature. The weakest DERR level for damage initiation is displayed by the thickest specimen, indicating the lack of a well defined structural resistance to damage initiation for the 48 ply specimen. The low DERR level at damage initiation renders the structure susceptible to spontaneous premature damage nucleation from local defects. Experimental observations

[31] agree with these computational simulation results.

Next, the effect of radius of curvature of the bent part is investigated. Figure 14.4 shows the damage progression for 24 ply thick composite for three different values of the inner radius of curvature; namely, 3.0 mm, 5.0 mm, and 8.5 mm. The damage initiation load is lower for the specimens with smaller radius of curvature. Also, damage growth is more nonlinear for sharply curved specimens due to the localization of damage at the bent corner. The SERR levels for specimens of the three different radii of curvature are shown in Figure 14.5. The SERR characteristics of the three specimens are similar at the damage initiation and growth stages. However, at the damage propagation stage, the specimen with the sharpest radius of curvature shows a distinctly higher slope due to damage localization.

The sensitivity of damage propagation to matrix tensile strength is also investigated. Figure 14.6 shows damage progression for the 24-ply composite with an inner radius of curvature of 5.0 mm. Both the standard HMHS matrix properties and a second matrix that has a fifty percent higher tensile strength of 128 MPa (18.5 ksi) are considered. The difference in damage initiation and growth loads indicate matrix tensile strength has a primary influence on the load levels that cause damage in sharply curved composite members. However, damage growth characteristics do not change with the change of matrix tensile strength. Figure 14.7 shows a comparison of the SERR levels for the two different matrix tensile strengths. The similar nature of the two SERR plots indicate that variation of matrix tensile strength does not change the characteristics of structural degradation stages.

14.4 Conclusions

The significant conclusions from this investigation in which CODSTRAN is used to evaluate structural damage initiation, progression, and ultimate fracture of a sharply curved composite specimen are as follows:

1. Computational simulation, with the use of established composite mechanics and finite element modules, can be used to predict the damage initiation and durability of composite structures, including those with sharply curved parts.

2. The availability of CODSTRAN facilitates composite structural design and certification by allowing the efficient and effective evaluation of design options and by providing comparisons of competing design concepts prior to prototype design and testing.

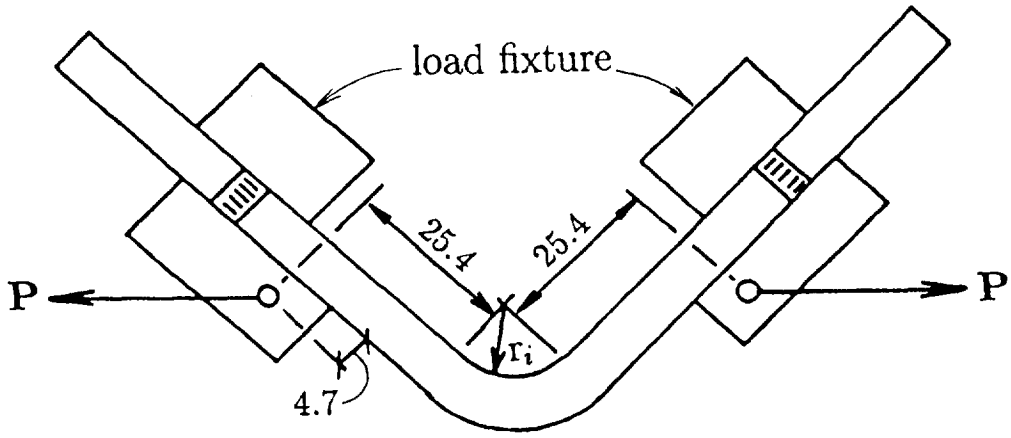

Figure 14.1: Bent Composite Specimen with Load Fixtures; AS-4/HMHS (all dimensions are in mm)

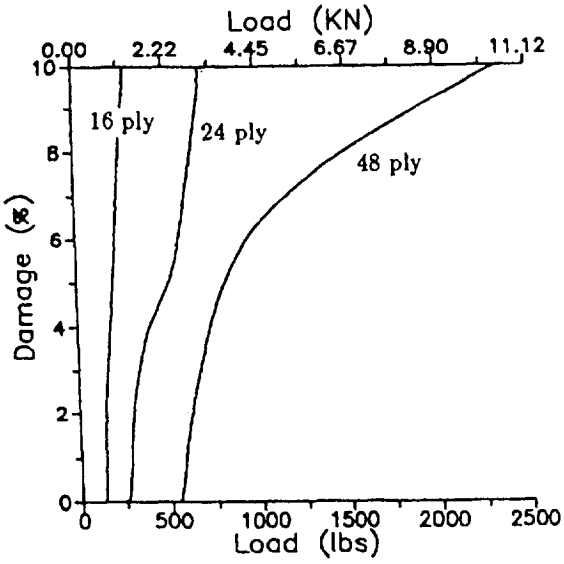

Figure 14.2: Effect of Thickness on Damage Propagation; AS-4/HMHS; r_i=5.0mm

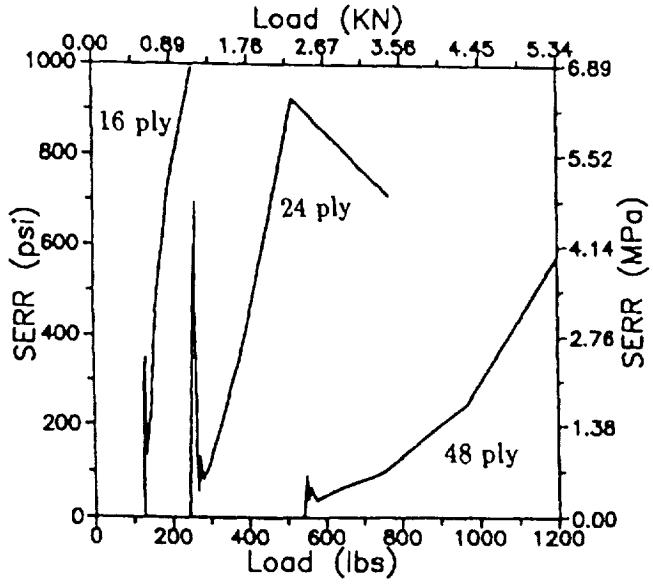

Figure 14.3: Effect of Thickness on Structural Fracture Resistance. AS-4/HMHS; r_i=5.0mm

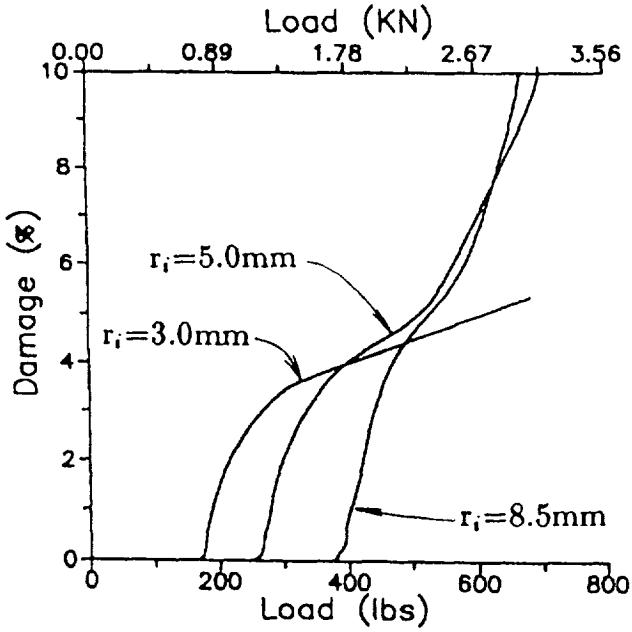

Figure 14.4: Effect of Curvature on Damage Propagation. AS-4/HMHS

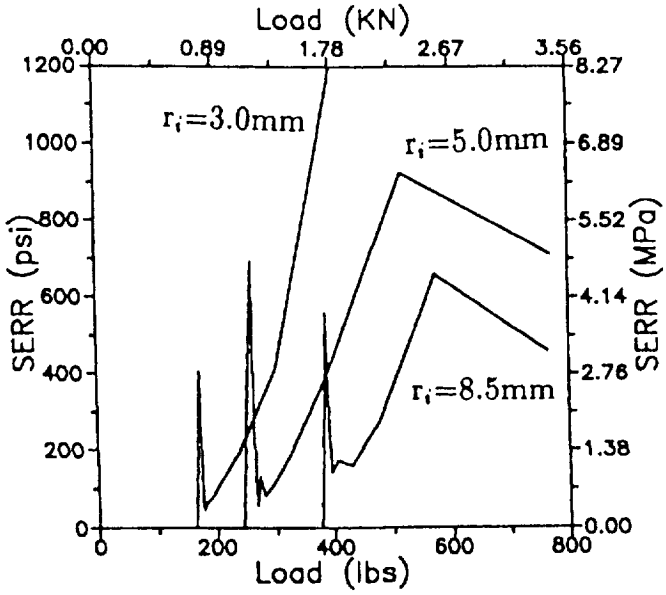

Figure 14.5: Effect of Curvature on Structural Fracture Resistance. AS-4/HMHS

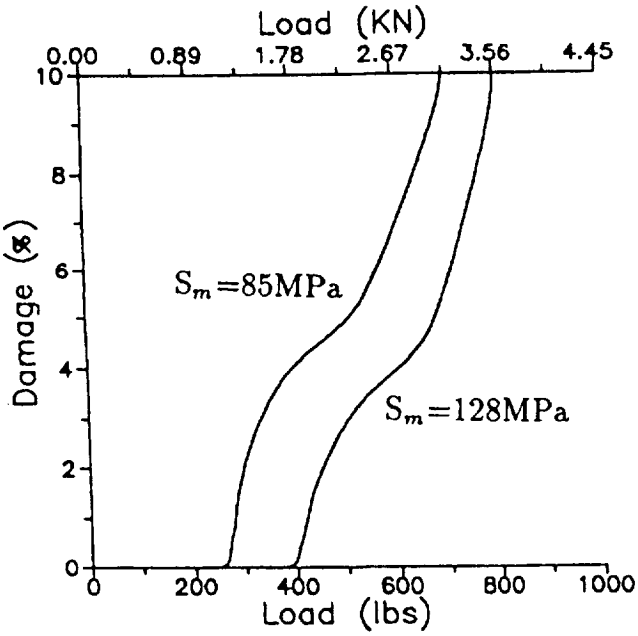

Figure 14.6: Effect of Matrix Tensile Strength on Damage Initiation and Progression. r_i=5.0mm

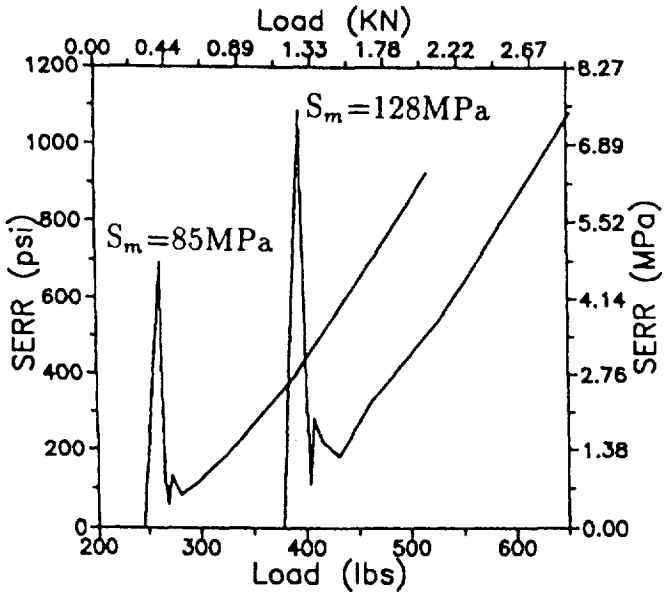

Figure 14.7: Effect of Matrix Tensile Strength on SERR; r_i=5.0mm

Chapter 15

Progressive Damage and Fracture of Stiffened Composite Pressure Vessels

Structural durability and damage tolerance characteristics of pressurized graphite/epoxy cylinders are investigated via computational simulation. Both unstiffened and hoop framework stiffened cylinders are considered. CODSTRAN is utilized for the simulation of composite structural degradation under loading. Damage initiation, growth, accumulation, and propagation to structural fracture are included in the simulation. Results demonstrate the significance of local defects on the structural durability of pressurized composite cylindrical shells.

15.1 Introduction

Laminated composite shell structures are used in many aerospace applications such as advanced aircraft fuselage, rocket motor cases, pressure vessels, containment structures, and other components with various shapes and sizes. In these applications composite shells are required to withstand significant internal pressures. Design considerations with regard to the durability of composite shell structures require an a priori evaluation of damage initiation and propagation mechanisms under expected service loading and hygrothermal environments. Concerns for safety and survivability of critical components require a quantification of the composite structural fracture resistance under loading.

Composite shells may be classified into a number of categories depending on their geometry and functional characteristics. Discussion in the current chapter is focussed on thin shells subject to internal pressure. Damage initiation, growth, accumulation, and propagation to fracture is simulated for a specific case. The influence of existing defects due to fabrication errors or inadvertent damage is examined with regard to the damage progression and structural durability assessment under applied loading. Changes in the damage initiation load and the structural fracture load are quantified due to the presence of a partial thickness defect and a through the thickness notch in composite shells.

Stiffened composite shells are used to achieve light weight as well as high strength and

stiffness. For certain designs structural interaction between skin and stiffener may adversely affect durability, especially in the presence of defects. The computational simulation method is well suited to investigate and identify the effects of structural interactions on damage and fracture propagation under design loads and overloads.

15.2 Thin Composite Shell

A composite system made of AS-4 graphite fibers in a high modulus high strength epoxy matrix (AS-4/HMHS) is used to illustrate CODSTRAN durability analysis of a representative shell structure. In the case of thin composite shells, structural flexibility plays an important role influencing the damage progression mechanisms. The thin shell laminate structure considered consists of eight 0.136 mm (0.00535 in.) plies resulting in a composite shell thickness of 1.088 mm (0.0428 in.). The laminate configuration is $[90/0/\pm 45]_s$. The 90° plies are in the hoop/circumferential direction of the shell. The cylindrical shell has a diameter of 305 mm (12.0 in.) and a length of 760 mm (29.9 in.). The finite element model contains 544 nodes and 512 elements as shown in Figure 15.1. The closed-end cylindrical pressure vessel is simulated by applying a uniformly distributed axial tension such that the generalized axial stresses in the shell wall are half those developed in the hoop direction. The composite shell is subjected to an internal pressure that is gradually increased until the shell is fractured.

CODSTRAN simulation takes into account the nonlinearities due to material and structural effects and shows the reduction in the ultimate internal pressure because of local defects in selected plies of the composite shell structure. Computed results are presented up to global fracture for defect-free shell, with partial-thickness defects, and through-the-thickness defects.

Unstiffened, defect-free shell.– CODSTRAN simulation gives a damage initiation pressure of 1.05 MPa (152 psi). Initial damage is in the form of matrix cracking in the zero degree axial plies. When the pressure is increased to 1.31 MPa (190 psi), matrix cracking spreads to the ±45 plies. At 2.03 MPa (295 psi) matrix cracking involves all plies. After the completion of the matrix failure phase, the pressure may be increased up to 3.00 MPa (436 psi) without any additional damage. Ultimate structural fracture occurs at 3.03 MPa (440 psi) due to fiber fractures at half length of the cylindrical shell, suddenly precipitating a structural fracture.

Unstiffened shell with through the thickness slit.– A composite shell with the same geometry as the defect-free specimen is modeled to have an existing 12.7 mm (0.5 in) long thin axial slit at mid-length of the shell. Damage initiation starts at 1.03 MPa (150 psi), which is slightly lower than the pressure to cause damage initiation in the defect-free shell. The damage growth mode is significantly different from that of the defect free shell due to localization of damage propagation at the slit. At 1.05 MPa (153 psi) the seven outer plies fail at the tip of the slit. However, through-the-thickness extension of the slit does not occur. Instead, damage near the slit becomes stable and damage progression continues by matrix cracking of all axial plies at remote locations. The damage stabilization phenomenon for

thin cylindrical shells subjected to internal pressure had been shown previously in Chapter 6.

Matrix cracking in the axial plies due to hoop tension is completed at 1.10 MPa (159 psi), similar to the defect-free shell. Further damage growth is concentrated near the slit. At 1.24 MPa (180 psi), the first seven plies surrounding the slit fail. However, damage growth encounters well defined stages of structural resistance. Through-the-thickness structural fracture occurs at 2.01 MPa (292 psi). The computed fracture load of 2.01 MPa is 17 percent lower than an experimental measurement of the bursting pressure for a similar shell [25]. It may be noted that the difference of computational simulation results from test data is within the variability limits of fiber tensile strength.

Figure 15.2 shows a comparison of the overall damage progression histories for the defect free shell and the shell with a slit. Initial damage pressure is the same. However the shell with a slit experiences more irregular damage growth stages as cycles of damage propagation and damage stabilization are repeated.

Figure 15.4 shows the SERR levels for the specimen with a slit. The fluctuation of the SERR level during damage propagation indicates that damage progression for the shell with the slit includes consecutive relatively quick damage expansion and damage stabilization stages.

Stiffened, defect-free shell.– Two hoop reinforcement bands are used to stiffen the shell in the radial direction. The reinforcements consist of 47.5 mm (1.87 in) wide unidirectional AS-4/HMHS composite that is wrapped 6 plies thick. The hoop reinforcements are placed symmetrically with respect to the centerline of the shell. The center to center space between hoop reinforcements is 380 mm (15.0 in) as shown in Figure 15.5.

Damage initiation pressure for the reinforced shell is 0.996 MPa (144 psi) which is slightly lower than the pressure to initiate damage in the unreinforced shell. However, immediately after damage initiation, damage progression pressure levels for the reinforced shell are considerably higher.

Figure 15.6 shows a comparison of damage progression for reinforced and unreinforced shells. In particular, hoop reinforcements significantly enhance the ultimate structural fracture performance.

Defective stiffened shell.– The shell with hoop reinforcements is considered to have a defect at midspan. The defect consists of prescribed damage in the form of fiber and matrix failures in the first seven plies of the laminate. The defect has a length of 12.7 mm (0.5 in) along the shell axis. Figure 15.7 shows a comparison of the performances of defective and defect-free stiffened shells. Damage initiation and progression stages involving matrix cracking are virtually identical. However, the defective stiffened shell has a considerably lower structural fracture pressure due to defect-induced localization of structural fracture propagation.

15.3 Concluding Remarks

The significant results from this investigation in which CODSTRAN (COmposite Durability STRuctural ANalysis) is used to evaluate damage growth and propagation to fracture of unstiffened and stiffened composite shells are as follows:

1. Computational simulation, with the use of established composite mechanics and finite element modules, can be used to predict the influence of existing defects as well as loading, on the safety and durability of composite shell structures.

2. CODSTRAN adequately tracks the damage growth and subsequent propagation to fracture for defect-free, partial-thickness defective, as well as through-the-thickness defective shells.

3. Hoop reinforcements improve the damage progression characteristics and structural fracture pressure for pressurized cylindrical shells.

4. Minor defects have a significant effect on the structural fracture pressure for the specimens considered. Damage initiation is not significantly affected.

5. The demonstrated procedure is flexible and applicable to all types of constituent materials, structural geometry, and loading. Homogeneous materials as well as composites can be simulated.

6. Fracture toughness parameters such as the structural fracture pressure and damage progression characteristics are identifiable for any structure with any defect by the demonstrated method.

7. Computational simulation by CODSTRAN represents a new global approach to progressive damage and fracture assessment for any structure.

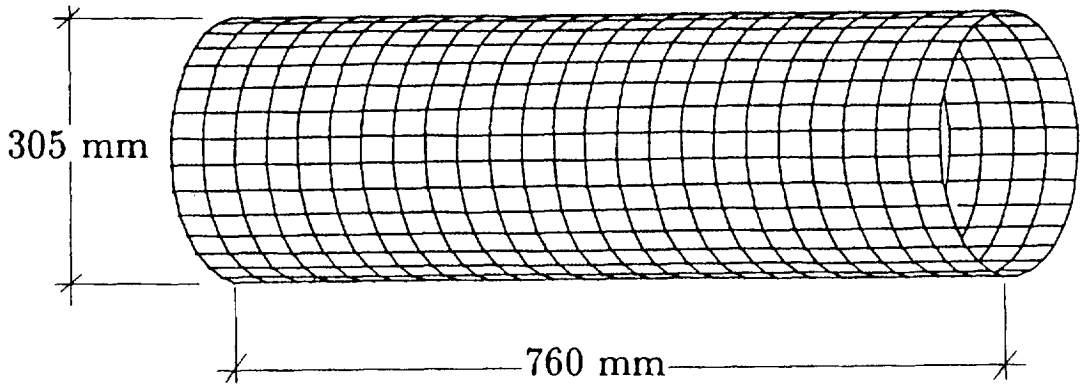

Figure 15.1: Cylindrical Shell Finite Element Model; Diameter = 305 mm, Length = 760 mm

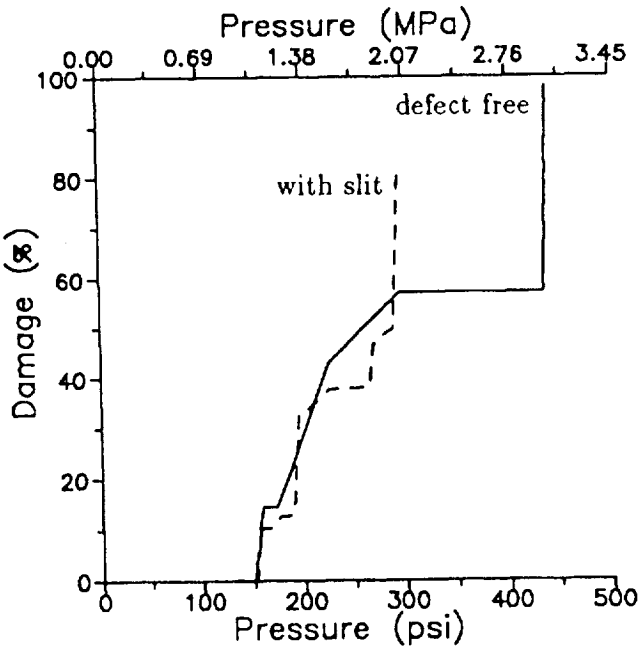

Figure 15.2: Damage Progression in Defective and Defect-free Shells; AS-4/HMHS$[90/0/\pm 45]_s$; Diameter = 305 mm, Length = 760 mm; Initial defect extends 12.7 mm.

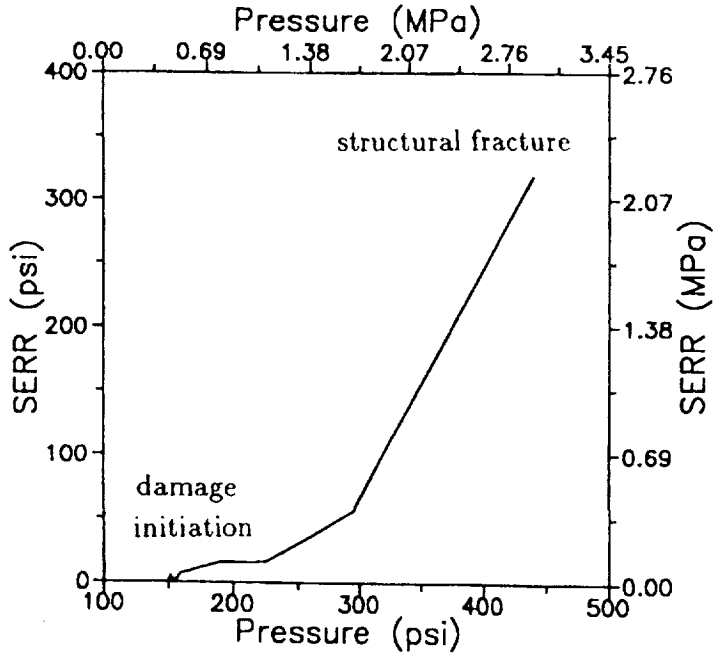

Figure 15.3: SERR Levels for Defect-free Shell; AS-4/HMHS$[90/0/\pm 45]_s$; Diameter = 305 mm, Length = 760 mm

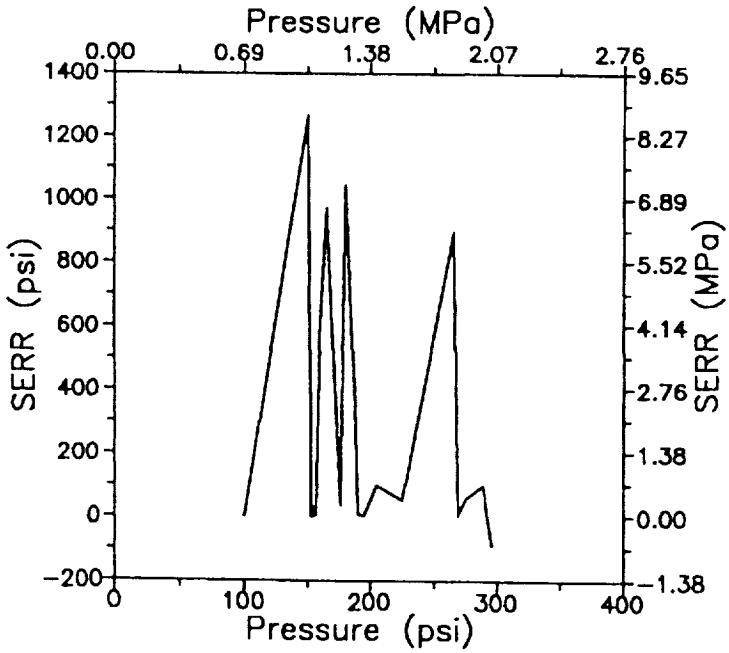

Figure 15.4: SERR Fluctuation in Defective Shell; AS-4/HMHS$[90/0/\pm 45]_s$; Diameter = 305 mm, Length = 760 mm; Initial defect extends 12.7 mm.

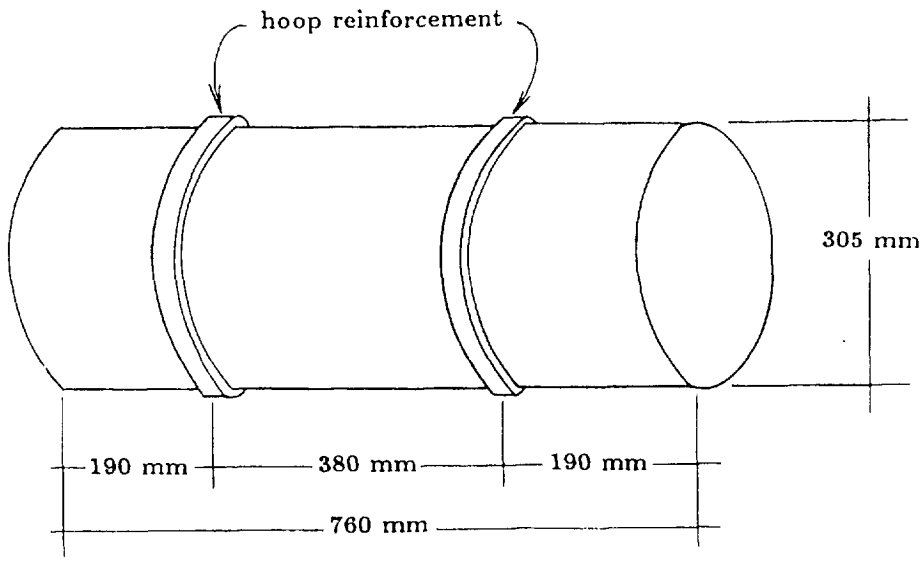

Figure 15.5: Hoop Reinforced Shell; AS-4/HMHS$[90/0/\pm 45]_s$; Diameter = 305 mm, Length = 760 mm; Initial defect extends 12.7 mm.

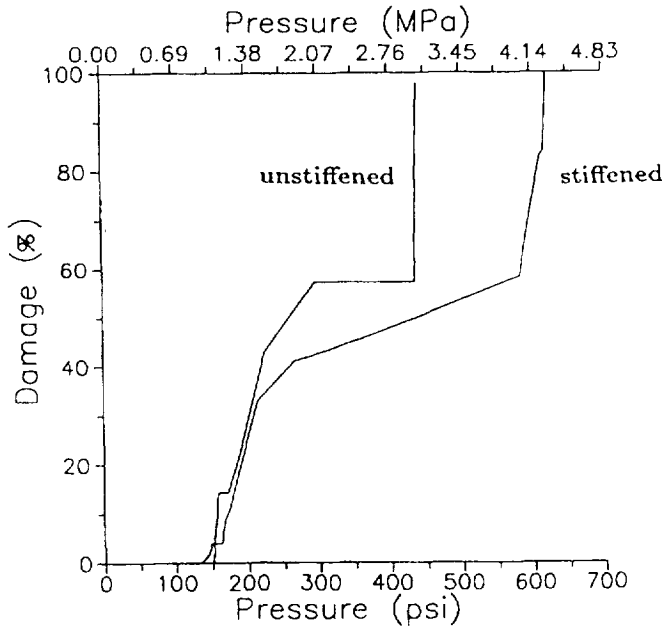

Figure 15.6: Effect of Hoop Reinforcement on Damage Progression; AS-4/HMHS$[90/0/\pm 45]_s$; Diameter = 305 mm, Length = 760 mm; Initial defect extends 12.7 mm.

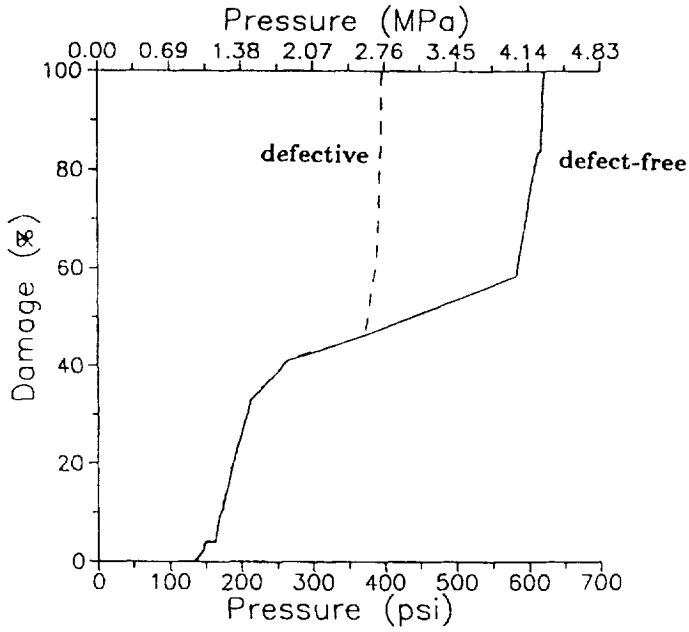

Figure 15.7: Effect of Initial Defect on Damage Progression in Hoop Reinforced Shell; AS-4/HMHS$[90/0/\pm 45]_s$; Diameter = 305 mm, Length = 760 mm, Initial defect extends 12.7 mm.

Chapter 16

Damage Progression in Mechanically Fastened Composite Structural Joints

Progressive damage and fracture of a bolted graphite/epoxy composite laminate is evaluated via computational simulation. The objective of this chapter is to demonstrate evaluation of the overall damage and fracture propagation for mechanically fastened composite structures. Results show the damage progression sequence and structural fracture resistance of a bolted composite during different degradation stages. The effect of fastener spacing is investigated with regard to the structural durability of a bolted joint.

16.1 Introduction

Modern applications of fiber composite structures require highly reliable structural joints that must remain safe under high tensile, compressive, shear, bending, and fatigue loads such as in aircraft wing and tail assemblies. In many cases critical composite structural components are assembled by mechanical fasteners such as bolts and rivets. The durability of a bolted graphite/epoxy laminated composite is evaluated via computational simulation. Damage and fracture propagation are considered due to tensile loading. An integrated computer code is used for the simulation of structural degradation. Damage initiation, growth, accumulation, and propagation to structural fracture are included in the simulation. The present approach by-passes traditional fracture mechanics to provide an alternative evaluation method, conveying to the design engineer a detailed description of damage initiation, accumulation, and propagation that would take place in the process of ultimate fracture of a mechanically fastened joint. Results show the damage progression sequence and structural fracture resistance during different degradation stages. This chapter demonstrates that computational simulation, with the use of established material modeling and finite element modules, adequately tracks the damage growth and subsequent propagation to fracture for mechanically fastened fiber composite structures.

16.2 Bolted Composite Joint

A graphite/epoxy laminate fastened by a single bolt as shown in Figure 16.1 is considered first. The laminate consists of 48 plies that are configured as $[0/\pm 45/90]_{s6}$ with a total thickness of 6.35 mm (0.25 in). The 0° plies are oriented in the load direction and the 90° plies are oriented transverse to the load direction. The specimen has a width of 102 mm (4.0 in) and a length of 204 mm (8.0 in).

In order to track the interactive behavior of the bolt and the composite structure, the bolt is represented separately from the laminated composite structure. The bolt has a diameter of 25.4 mm (1.0 in) and is made of high-strength steel. Independent finite elements for laminate and fastener with master/slave duplicate nodes at the bolt/laminate boundary are used to enforce the continuity of displacements between contacting elements. When generalized in-plane stresses become tensile at a boundary node of the bolt, the duplicate node relationship is terminated to allow the separation of the laminate from the fastener. Elastic deformations of the fastener are considered in the computational model. However, failure criteria are not imposed on the fastener elements.

The composite system is made of AS-4 graphite fibers in a high-modulus, high strength (HMHS) epoxy matrix. The fiber and matrix properties are obtained from a databank of composite constituent material properties resident in CODSTRAN. The fiber and matrix properties corresponding to this case are given in Appendix A.

The HMHS matrix properties are representative of the 3501-6 resin. The fiber volume ratio is 0.60 and the void volume ratio is 2 percent. The laminate cure temperature is 177°C (350°F) and the use temperature is 21°C (70°F).

The bolted laminate is investigated under uniaxial tensile loading. The specimen is loaded by restraining the center node of the bolt and imposing a uniformly distributed tensile load at the far end of the laminate. Damage progression is computationally simulated as the loading is increased.

Figure 16.2 shows the damage progression with increasing tensile loading on the bolted joint as the progressive damage response of the laminate is evaluated. During the first load increment of 3559 N (800 lbs), finite element connectivities between the bolt and the composite are released where generalized membrane stresses N_x and N_y are both tensile. Under a 30.25 KN (6.8 kip) loading damage is initiated adjacent to the bolt by matrix cracking in the 90° plies. After damage initiation by $\sigma_{\ell 22T}$ transverse tensile failures, the damaged plies also undergo $\sigma_{\ell 11C}$ longitudinal compressive failures during the next iteration. Subsequently, damage grows to the -45° and +45° plies under the same load. When the load in increased to 44.48 KN (10 kips) damage grows to adjacent nodes. Gradual damage accumulation in selective plies continues until a 145.9 KN (32.8 kip) load is reached when fracture begins at the same nodes where damage initiation had occurred. Fracture is rapidly propagated to cause the ultimate break of the connection due to the fracture line that started from the side of the bolt transverse to the loading direction. Figure 16.3 shows the primary, secondary, and ultimate fracture lines, as well as remote damage locations. Figure 16.4 shows the global SERR that is minimum under a 56.94 KN (12.8 kip) loading but recovers

to higher levels as damage progression continues. Figure 16.5 shows the end displacement with applied loading, indicating that initial damage stages will not be apparent from the observation of a test.

The second investigated structure is a composite panel fastened by two bolts. The composite system is made of the same high strength AS-4 graphite fibers in a high-modulus, high-strength epoxy matrix (AS-4/HMHS) as in the single bolt joint. The finite element model, shown in Figure 16.6, uses 72 thick shell elements with 99 nodes to represent the laminate and the two bolts. Figure 16.7 shows computational simulation results of the overall damage progression for laminate widths of w=76.2, 101.6, and 203.2 mm (3.0, 4.0, and 8.0 in) as functions of the applied load per unit width of the laminate. In all three cases the laminate is fastened by two 25.4 mm (1.0 in) diameter bolts and the center to center bolt spacing is equal to the half width of the laminate. In all three cases damage initiation occurs under a tensile line load of 289 KN/m (1650 lbs/in). Results indicate that damage progression characteristics are not sensitive to the laminate width or to the bolt spacing in the investigated range. Therefore, a bolted joint using the subject laminate configuration may be designed on the basis of bolt strength limits under tensile loading.

16.3 Conclusions

In the light of the durability investigation of the example bolted composite, and from the general perspective of the available CODSTRAN (COmposite Durability STRuctural ANalysis) computer code, the following conclusions are drawn:

1. CODSTRAN adequately tracks damage initiation, growth, and subsequent propagation to fracture for bolted composite structures.

2. For the examples considered, damage progression characteristics are not sensitive to bolt spacing under tensile loading.

3. Computational simulation, with the use of established composite mechanics and finite element modules, can be used to predict the influence of a bolted joint as well as loading and composite properties on the durability of mechanically fastened composite structures.

4. The demonstrated procedure is flexible and applicable to all types of constituent materials, structural geometry, and loading. Hybrid composites and homogeneous materials, as well as binary composites can be simulated.

5. CODSTRAN provides a new general methodology to investigate damage propagation, and progressive fracture for any structure.

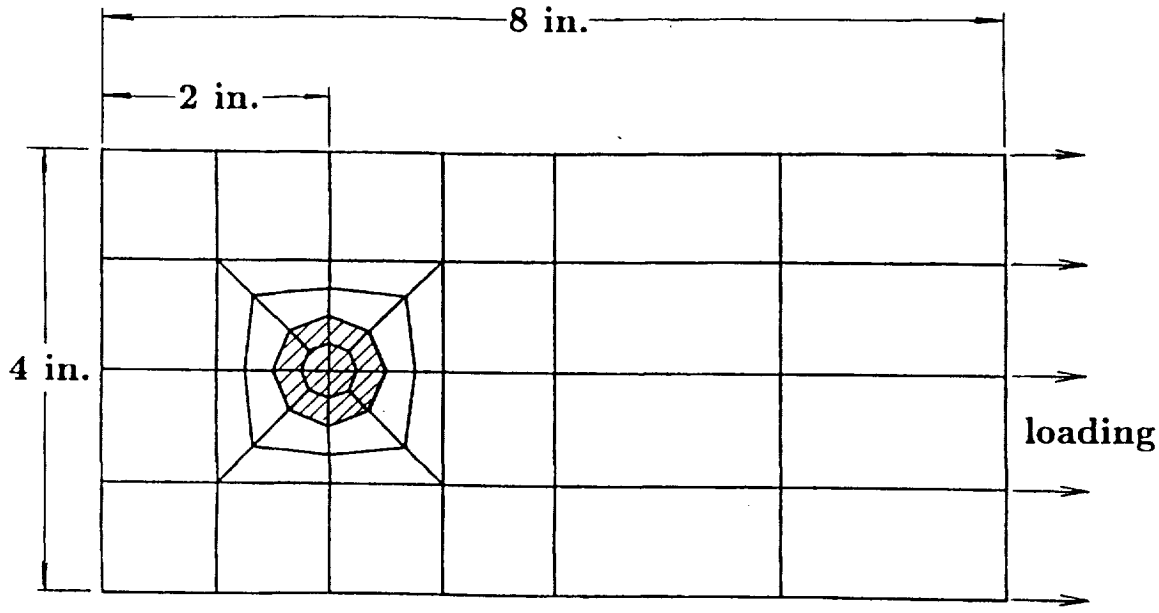

Figure 16.1: Bolted Laminate Finite Element Model

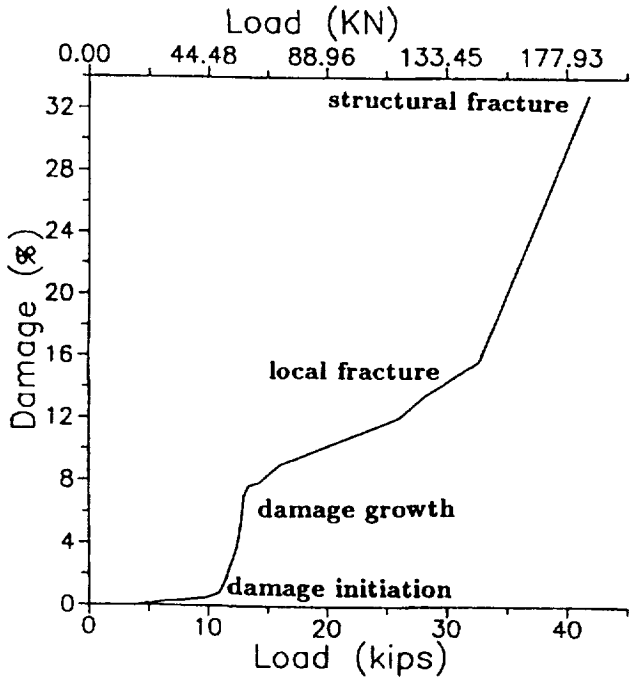

Figure 16.2: Damage Progression for Bolted Laminate; AS-4/HMHS: 48 Plies $[0/90/\pm 45]_{12}$

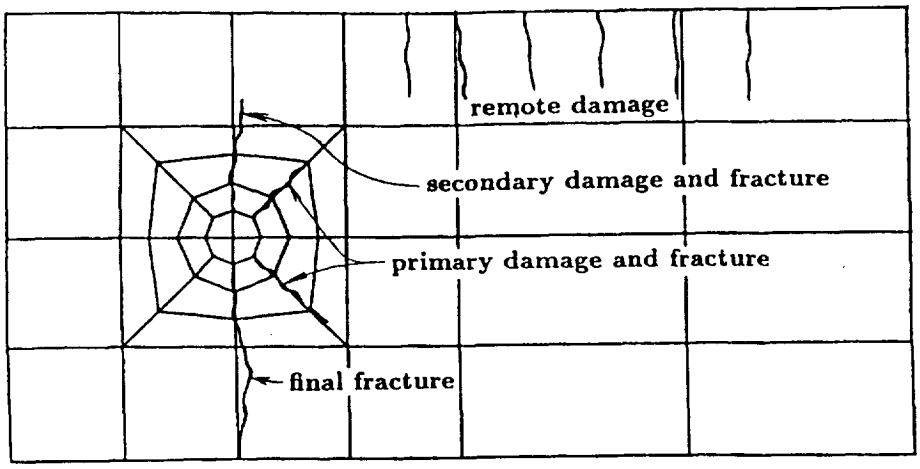

Figure 16.3: Laminate Damage and Fracture Lines; AS-4/HMHS: 48 Plies $[0/90/\pm45]_{12}$

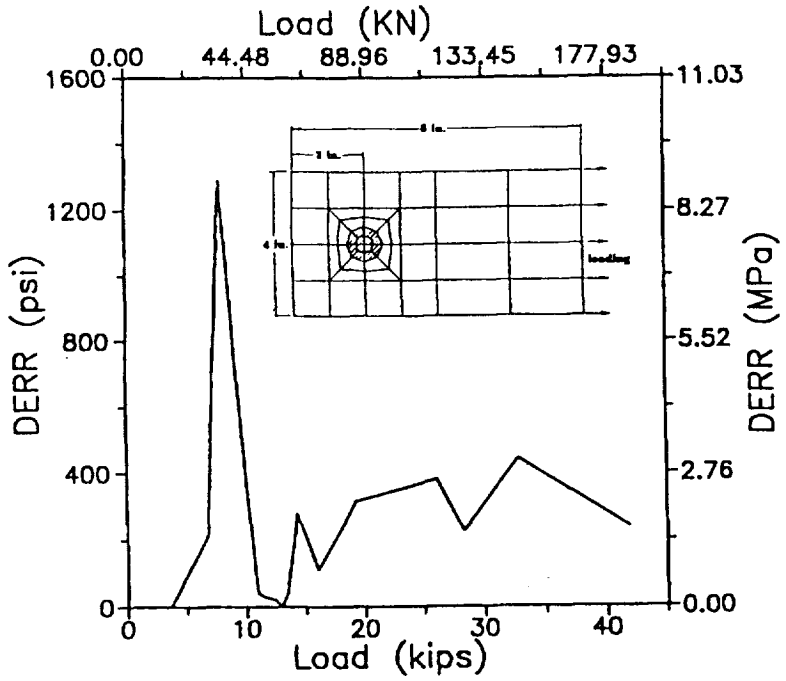

Figure 16.4: Energy Release Rates for Bolted Laminate; AS-4/HMHS: 48 Plies $[0/90/\pm45]_{12}$

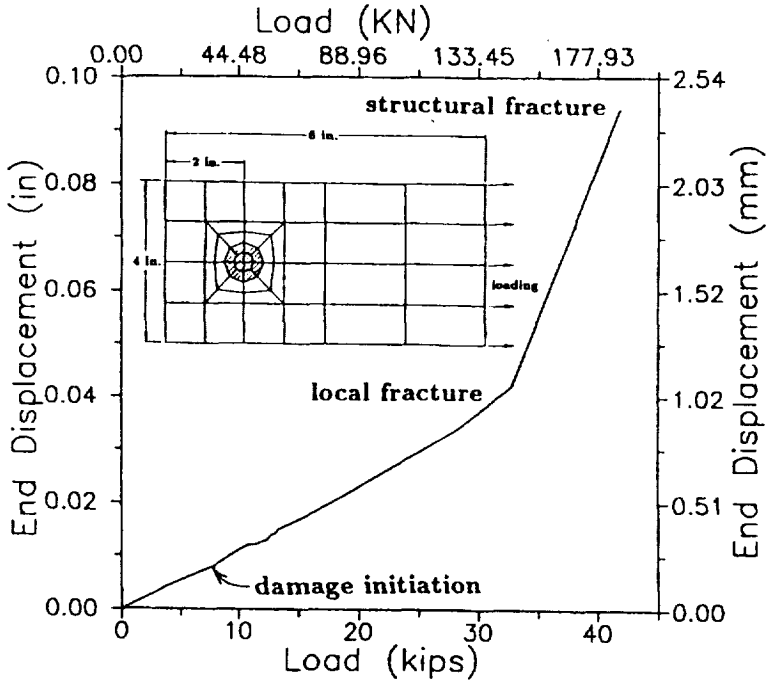

Figure 16.5: End Displacement for Bolted Laminate; AS-4/HMHS: 48 Plies $[0/90/\pm 45]_{12}$

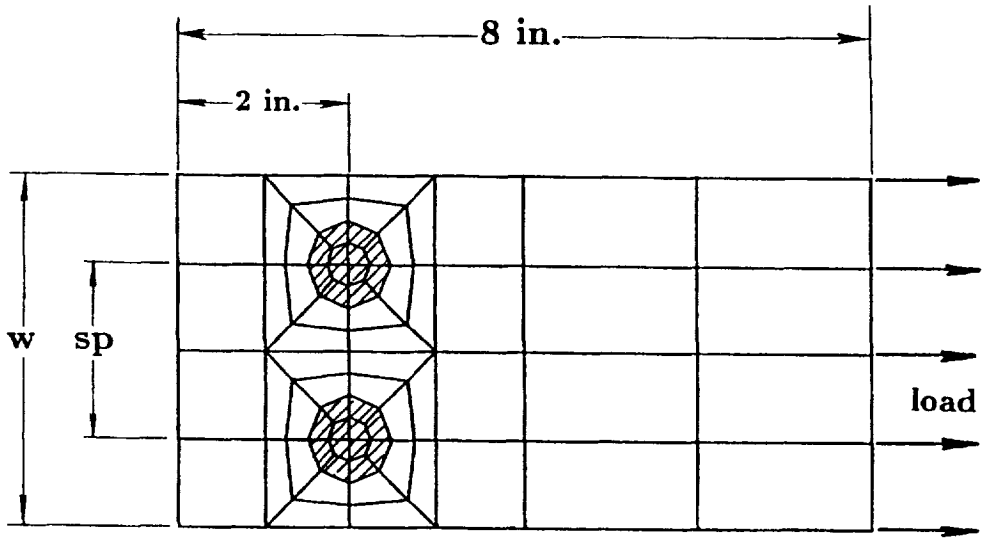

Figure 16.6: Double Bolted Laminate Model

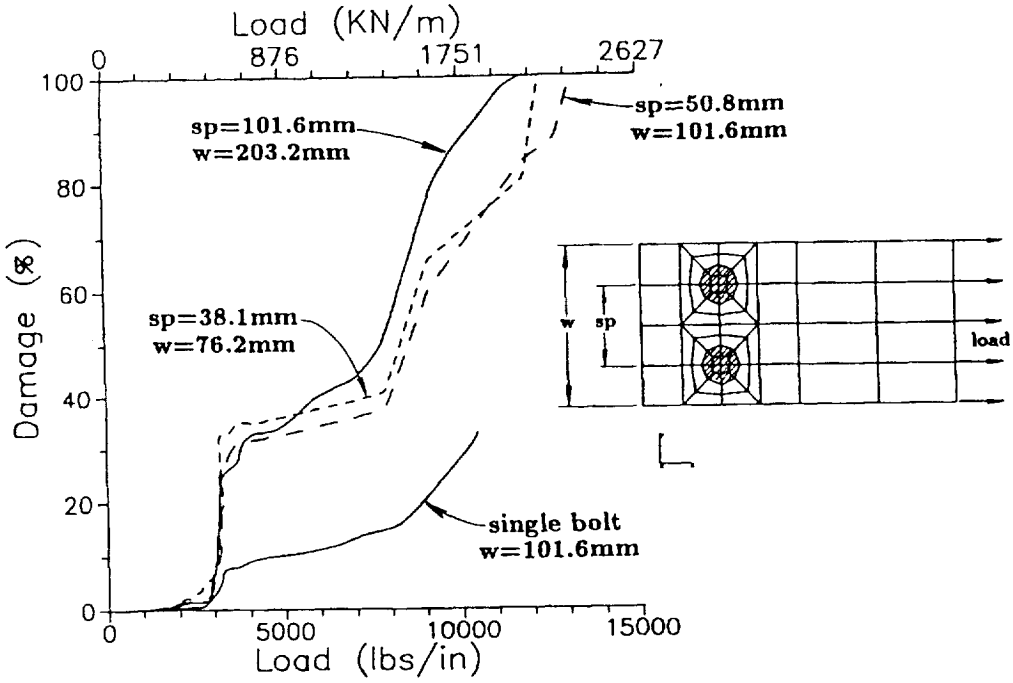

Figure 16.7: Damage Progression for Double Bolted Laminate; AS-4/HMHS$[0/90/\pm45]_{12}$

Chapter 17

Probabilistic Simulation of Failure in Bolted Joint Composite Laminates

Computational methods are described to probabilistically simulate fracture in bolted composite structures. The effect on structure damage of design variable uncertainties is quantified. The Fast Probability Integrator is used to assess the scatter in the composite structure response before and after damage. Sensitivity of the response to design variables is computed. Methods are general-purpose in nature and are applicable to bolted joints in all types of structures and fracture processes starting from damage initiation to unstable propagation and to global structure collapse. The methods are demonstrated for bolted joint polymer matrix composite panels under edge loads. The effects of fabrication process are included in the simulation of damage in the bolted panel. The results show that the most effective way to reduce the end displacement at fracture is to control the load and ply thickness. The cumulative probability for longitudinal stress is most sensitive to the load. Ply thickness contributes significantly to the cumulative probability for the ply longitudinal stresses in all plies. The cumulative probability for transverse stress is most sensitive to the thermal expansion coefficient of the matrix. Fiber volume ratio and fiber transverse modulus both contribute significantly to the cumulative probability for the transverse stresses in all the plies .

17.1 Introduction

Flawed structures, metallic or composites, fail when flaws grow or coalesce to a critical dimension such that (1) the structure cannot safely perform as designed and qualif fed or (2) catastrophic global fracture is imminent. However, fibrous composites exhibit multiple fracture modes that initiate local flaws compared to only a few for traditional materials. Hence, simulation of structural fracture in fibrous composites must include: (1) all possible fracture modes, (2) the types of flaws they initiate, and (3) the coalescing and propagation of these f laws to critical dimensions for imminent structural fracture.

The phenomena of fracture in composite structures is further compounded due to inherent

uncertainties in the multitude of material properties, structure geometry, loading, and service environments. The effect of all types of uncertainties must be designed-in for satisfactory, reliable, and affordable structures. The various uncertainties are traditionally accounted for via knockdown (safety) factors with generally unknown reliability. An alternate approach to quantify those uncertainties on structural fracture is to use probabilistic methods as described herein.

The objective of the present chapter is to present methods/codes for probabilistically assessing the effect of design variable uncertainties on the structural fracture. The methods and corresponding computer codes are demonstrated for the uncertainty in the damage load in bolted joint of polymer matrix composite panels.

17.2 Probabilistic Assessment of Structural Fracture

The effects on the fracture of the structure of uncertainties in all the relevant design variables are quantified. The composite mechanics, finite element structural simulation, and Fast Probability Integrator (FPI) have been integrated into IPACS (Integrated Probabilistic Assessment of Composite Structures' - [?]. A schematic of IPACS is shown in Figure 17.1 . FPI, contrary to the traditional Monte Carlo Simulation, makes it possible to achieve orders-of-magnitude computational efficiencies which are acceptable for practical applications. Therefore, a probabilistic composite assessment becomes feasible which can not be done traditionally, especially for composite materials/structures which have a large number of uncertain variables.

IPACS starts with defining uncertainties in material properties at the most fundamental composite scale, i. e., fiber/matrix constituents. The uncertainties are progressively propagated to those at higher composite scales subply, ply, laminate, structural, as shown in Figure 17.1. The uncertainties in fabrication variables are carried through the same hierarchy . The damaged/ fractured structure and ranges of uncertainties in design variables such as material behavior, structure geometry, supports, and loading are input to IPACS . Consequently, probability density functions (PDF) and cumulative distribution functions (CDF) can be obtained at the various composite scales for the structure response. Sensitivity of various design variables to structure response is also obtained .

17.3 Demonstration Case

The methods and computer codes discussed above are demonstrated for (1) simulating the fracture in a bolted joint of a composite panel and (2) evaluating the probability of the damage initiation load of the panel. A polymer matrix composite (8.0 x 4.0 x 0.25 inch) panel is fastened by a 1.0 inch diameter bolt at 2 inches from one of its ends and is subjected to a uniformly distributed load at the other end (Figure 17.2). The composite system is made of AS-4 graphite fibers in a high-modulus high-strength epoxy matrix (AS- 4/HMHS). The

fiber volume ratio is 0.60 and the void volume ratio is two percent. The laminate consists of forty eight 0.00521 inch plies. The laminate configuration is $[90/\pm45/0]_s$. The 90 plies are in the y direction and the 0 plies are in the x direction. The effect of fabrication-induced residual stresses is simulated via a cure temperature of 350 F. The bolt is modeled using high strength steel properties. The finite element model of the bolt jointed panel is also shown in Figure 17.2. The bolt is fixed with respect to all displacement and rotational degrees of freedom at its center. The composite system is subjected to gradually increasing load until it is fractured and broken into two pieces.

Figure 17.3 shows the simulated damage progression with increasing load on the panel. During the first load increment of 800 lbs (= 0.8 kips), finite element connectivities between the bolt and the composite are released where generalized membrane stress N_x and N_y are both tensile. Under a 6.8 kip loading, damage is initiated around the right half circumference of the panel at the bolted joint by matrix cracking in the 90 plies. When the load is increased, damage grows outward of the bolted joint. Gradual damage accumulation in selective plies continues until a 32.8 kip load is reached when fracture begins around the right half circumference of the panel at the bolted joint. Fracture is rapidly propagated to cause the ultimate break of the joint due to the fracture line that started from the bottom connection point.

The deterministically simulated panel fracture provides no information on its respective reliability. The probabilistic end displacement (a global indicator of structural integrity) is probabilistically assessed. The end displacement depends on uncertainties in relevant panel geometry and material properties of the panel and bolt, bolt hole geometry and the load.

The cumulative distribution function of the panel end displacement before damage initiation is shown in Figure 17.4. The probability that the panel end displacement before damage initiation will be less than 0.002 inch is about 0.01 and the probability of it being greater than 0.0065 inch is about 0.001. There is about 50

The sensitivity of the 0.001 and 0.999 cumulative probability for the panel end displacement to uncertainties in design variables is shown in Figure 17.5. The load is the most significant design variable which affects the end displacement before damage initiation. The effect of uncertainties in ply thickness on end displacement in also substantial. The effect of uncertainties in composite material properties on end displacement is minor. These effects are the same on both probability levels. These results indicate that: (1) the damage initiation is strongly dependent on uncertainties in the load and (2) the panel end displacement damage initiation can be most effectively reduced by controlling the ply thickness.

Cumulative distribution functions of longitudinal stress in various plies (at point A - Figure 17.2) before and after damage are shown in Figure 17.6. The damage is initiated at 90 ply. Therefore the 90 ply will not carry any load after damage initiation. The stresses were redistributed to the remaining plies (±45 and 90) as shown in Figure 17.7. Also shown in this figure is that the load carried by the 90 ply before damage initiation is now carried mostly by ±45 plies. The sensitivity of 0.001 probability for the ply longitudinal stress to uncertainties in design variables is shown in Figure 17.7. For 90 ply, it is most sensitive to load followed by thermal expansion coefficient of the matrix, fiber volume ratio and ply thickness. For 0

ply, it is most sensitive to the load followed by fiber volume ratio and ply thickness. For ± 45 plies, the probability of their respective longitudinal stresses is most sensitive to the random load followed by ply thickness. The remaining random variables have little contribution to the cumulative probability.

Cumulative distribution functions of transverse stress in various plies (at point A - Figure 17.2) before and after damage are shown in Figure 17.8. Again, the 90 ply will not carry any load after damage initiation. The unbalance in load due to damage initiation is redistributed to remaining plies. The sensitivity of 0.001 probability for the ply transverse stress to uncertainties in design variables is shown in Figure 17.9. For all plies, their respective probability is most sensitive to the thermal expansion coefficient of the matrix followed by fiber modulus in the transverse direction. The fiber volume ratio and matrix modulus contribute similarly to the probability for each transverse ply stress.

Cumulative distribution functions of in-plane shear stress before and after damage are shown in Figure 17.10. The stress and its scatter for each ply is insignificant. The 0.001 probability for ply shear stress in the respective ply is most sensitive to the load followed by longitudinal fiber modulus, fiber volume ratio and ply thickness.

17.4 Conclusions

Methods and corresponding computer codes were discussed for probabilistically assessing composite structure fracture. The approach described herein is inclusive in that it integrates composite mechanics (for composite behavior) with finite element analysis (for global structural response) and incorporates probability algorithms to perform a probabilistic assessment of composite structural fracture. The effect on the composite structure fracture of all the design variable uncertainties was accounted for at all composite scales. Probabilistic scatter range and sensitivity factors are key results obtained from the probabilistic assessment of fractured structures. The sensitivity factors provide quantifiable information on the relative sensitivity of structural design variables on the respective structure response/fracture.

The methods/codes were demonstrated by application to a bolt jointed composite panel. The scatter in the panel end displacement (a global indicator of structural integrity) was probabilistically quantified based on uncertainties in the associated design variables. The results obtained indicated that: (1) the scatter range of the end displacement is about 0.005 inch; (2) the end displacement at fracture is most sensitive to the load followed by the ply thickness; (3) the most effective way to reduce the end displacement at fracture is to control the load and ply thickness; (4) after the damage initiated in the 90 ply, unbalanced stresses are redistributed to the remaining plies; (5) the cumulative probability for longitudinal stress is most sensitive to the load and the ply thickness has important contribution to the cumulative probability for the stress in all plies; (6) the cumulative probability for transverse stress is most sensitive to the thermal expansion coefficient of the matrix. Fiber volume ratio and fiber transverse modulus both contribute significantly to the cumulative probability for stress in all plies.

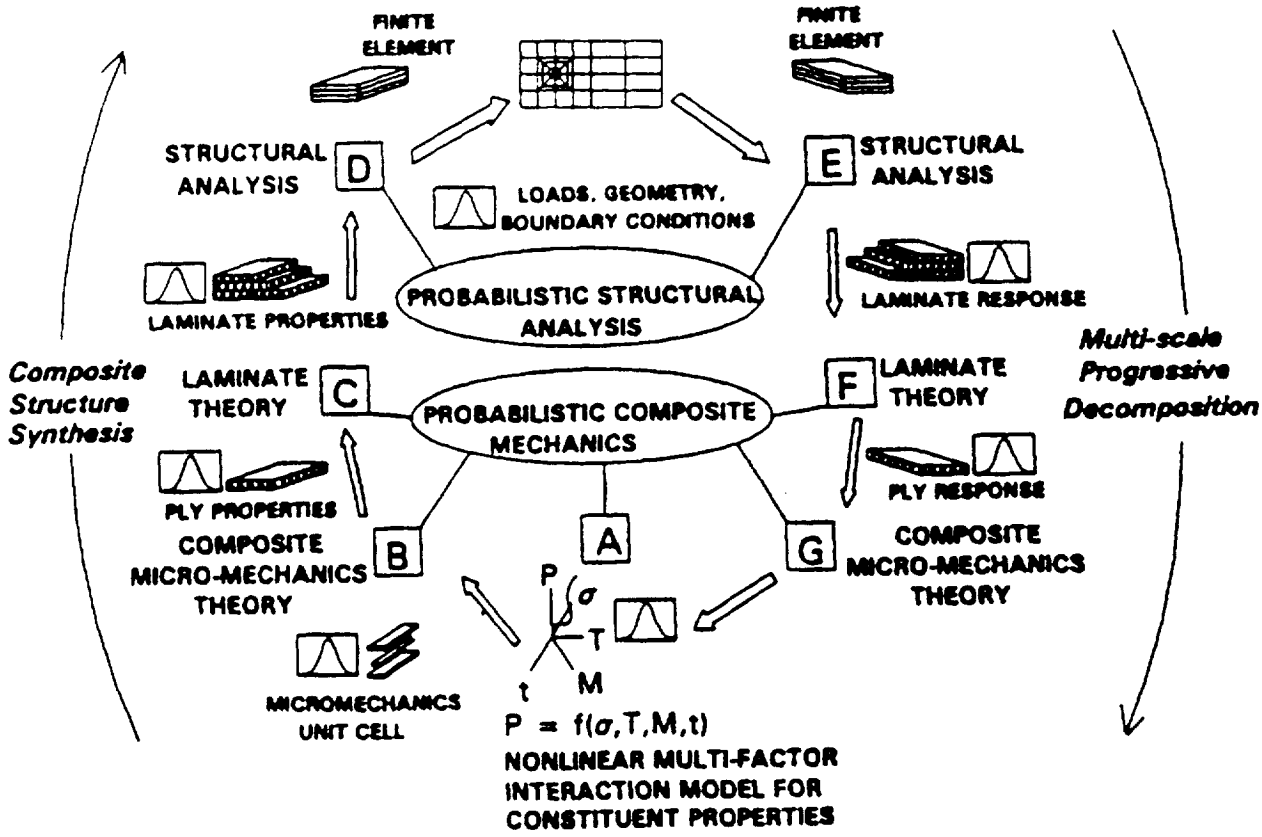

Figure 17.1: Integrated Probabilistic Assessment of Composite Structures

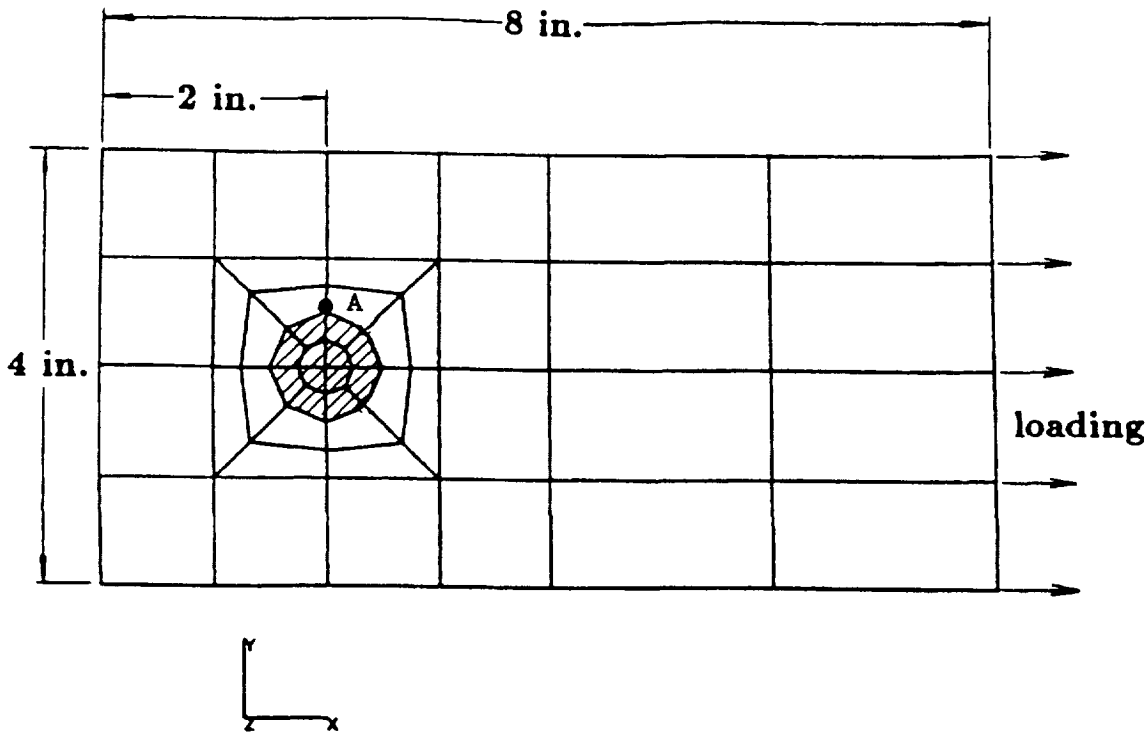

Figure 17.2: Bolted Joint Composite Panel and Finite Element Model

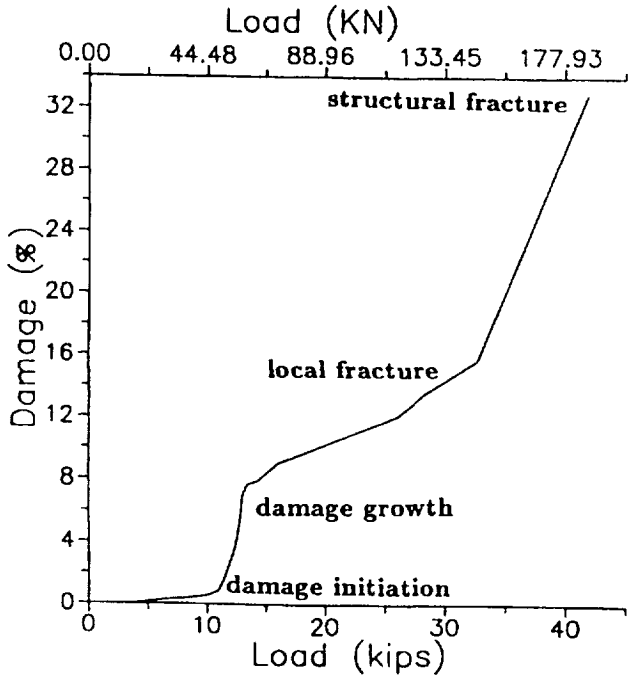

Figure 17.3: Damage Progression for Bolted Laminate

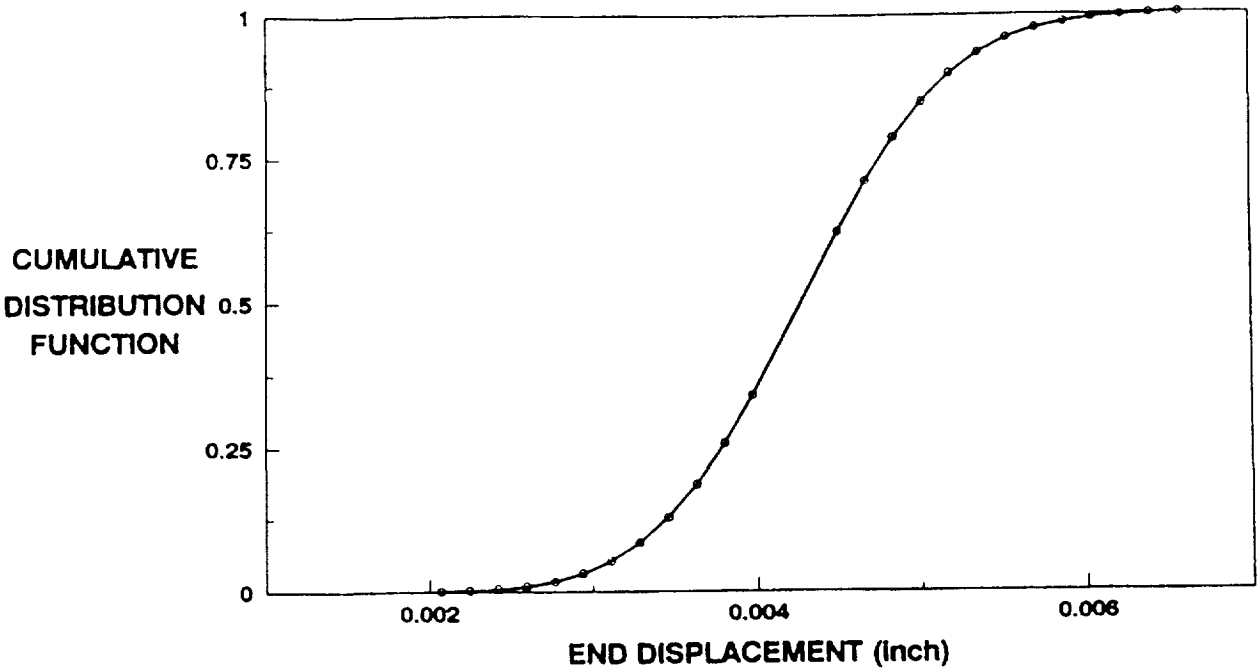

Figure 17.4: CDF of Bolted Laminate End Displacement Before Damage Initiation

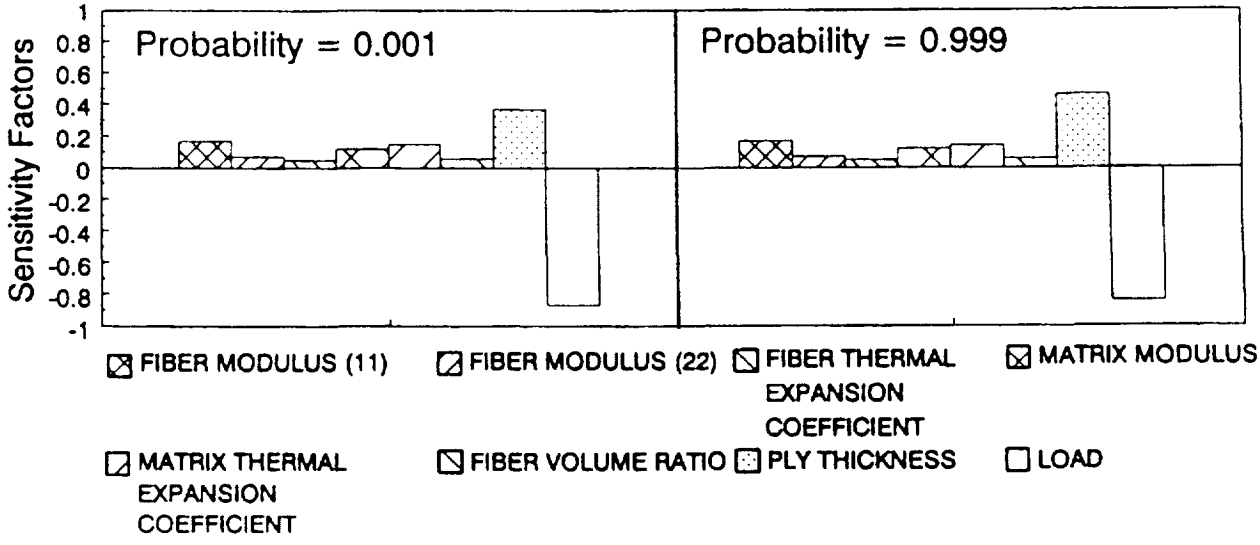

Figure 17.5: Sensitivites of Uncertainties in Design Variables to Bolted Laminate End Displacement Before Damage Initiation

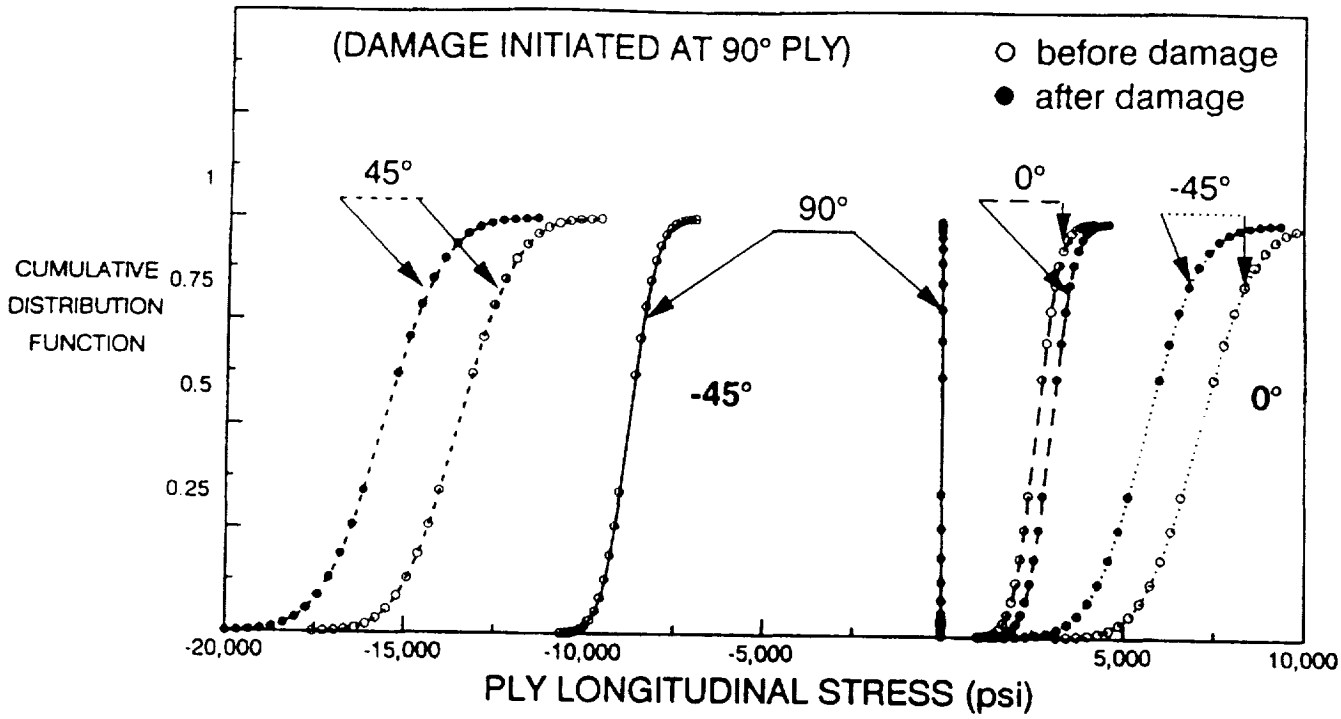

Figure 17.6: CDFs of Ply Longitudinal Stress Before and After Damage

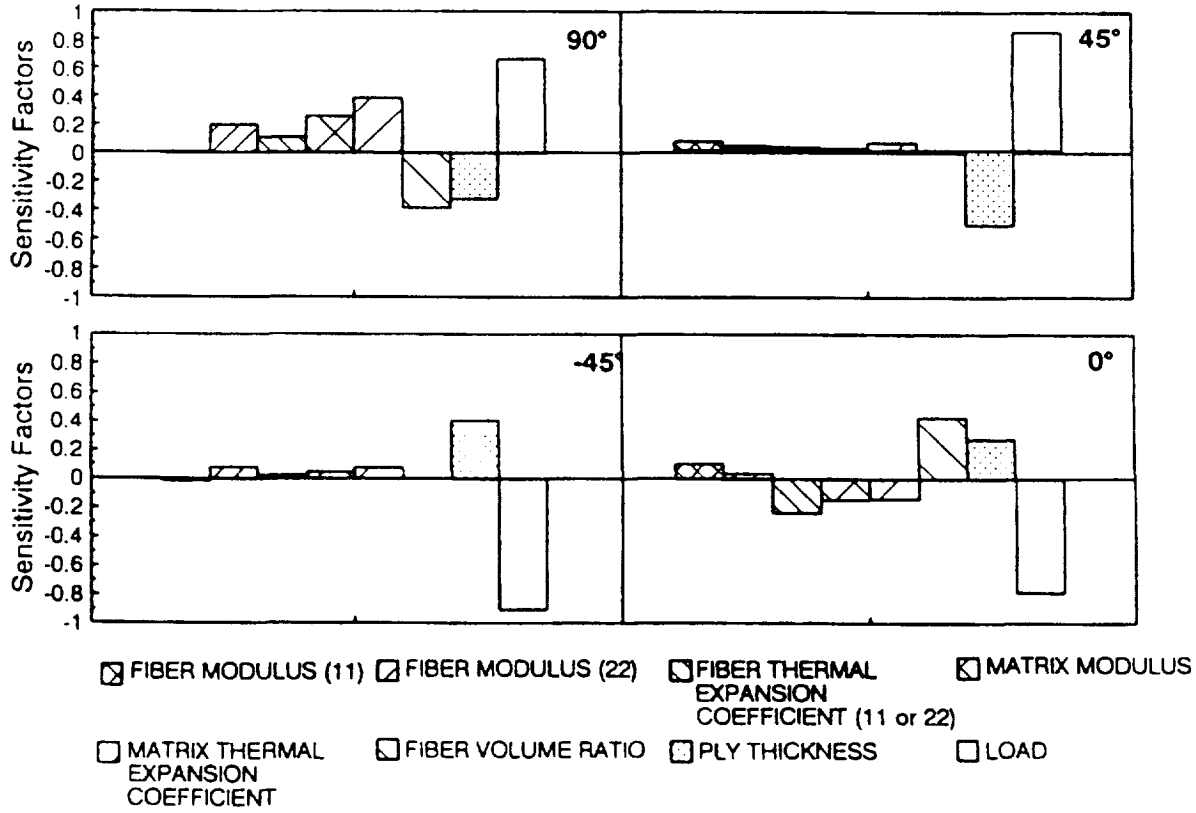

Figure 17.7: Sensitivity Factors for 0.001 Cumulative Probability of Ply Longitudinal Stresses Before Damage Initiation

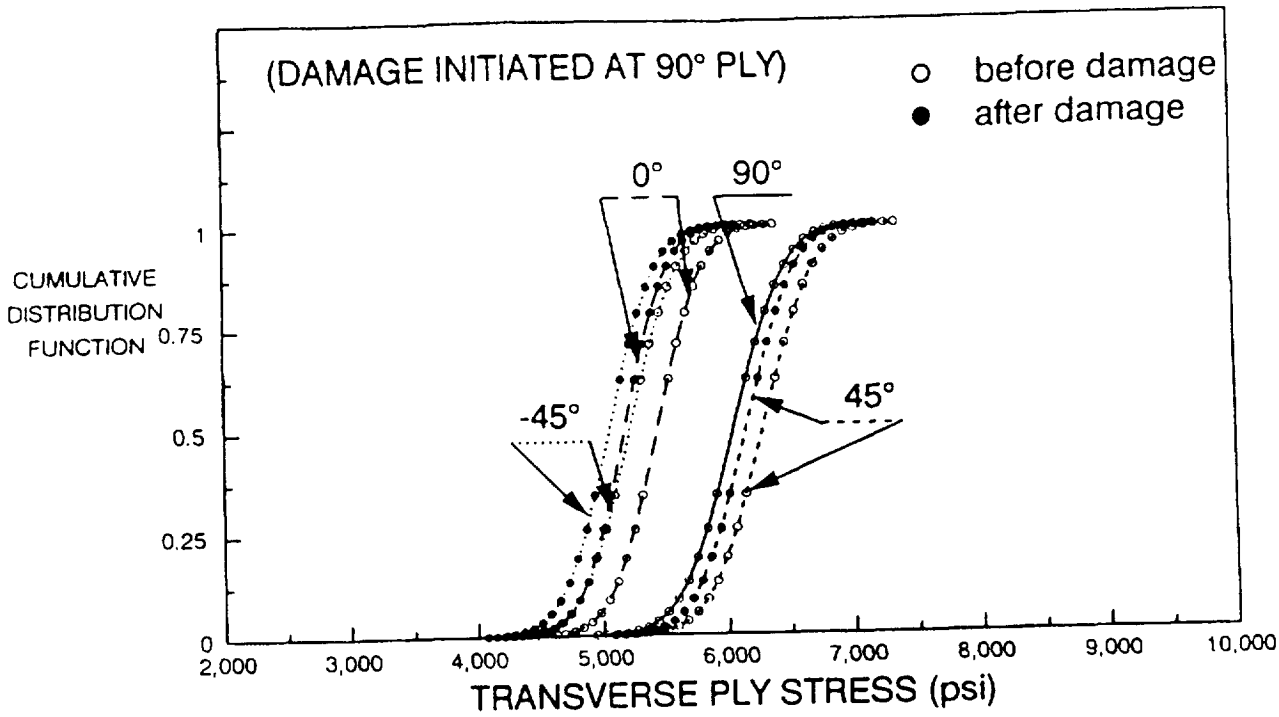

Figure 17.8: Ply Transverse Stress Before and After Damage

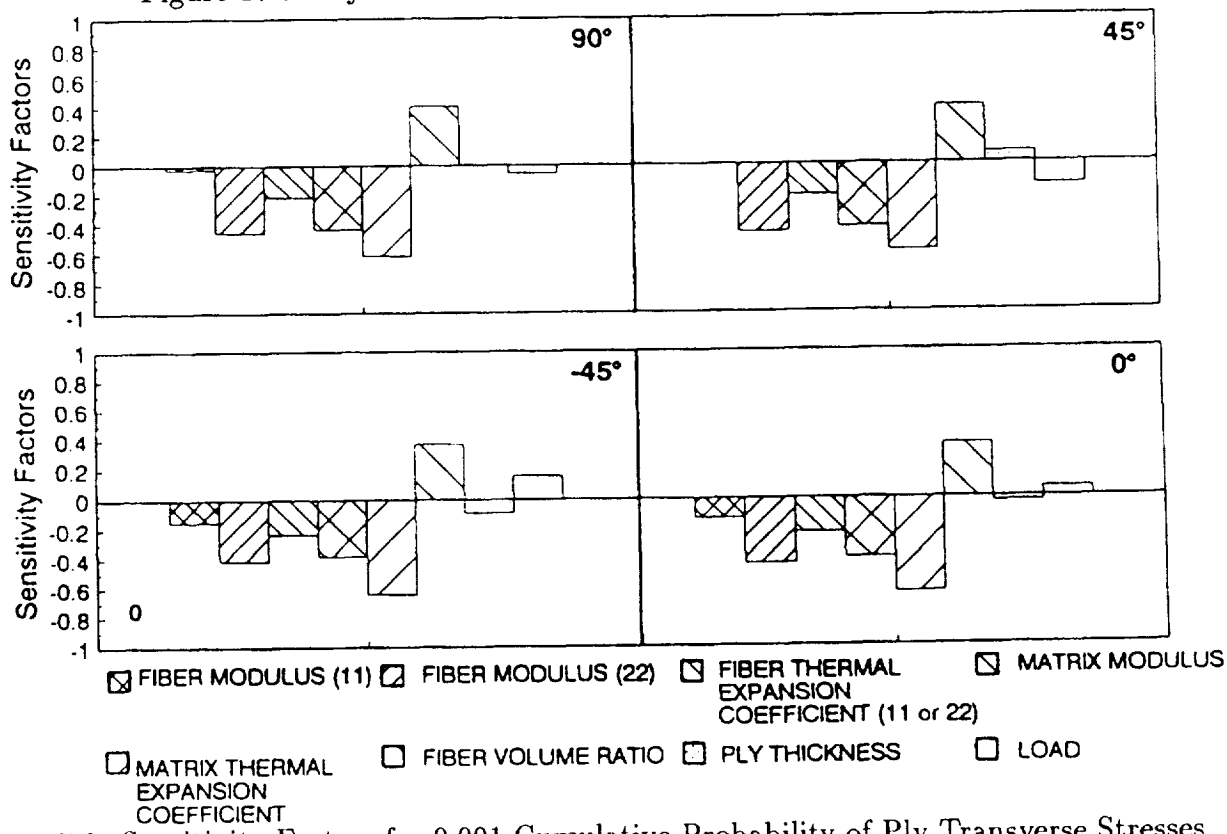

Figure 17.9: Sensitivity Factors for 0.001 Cumulative Probability of Ply Transverse Stresses Before Damage Initiation

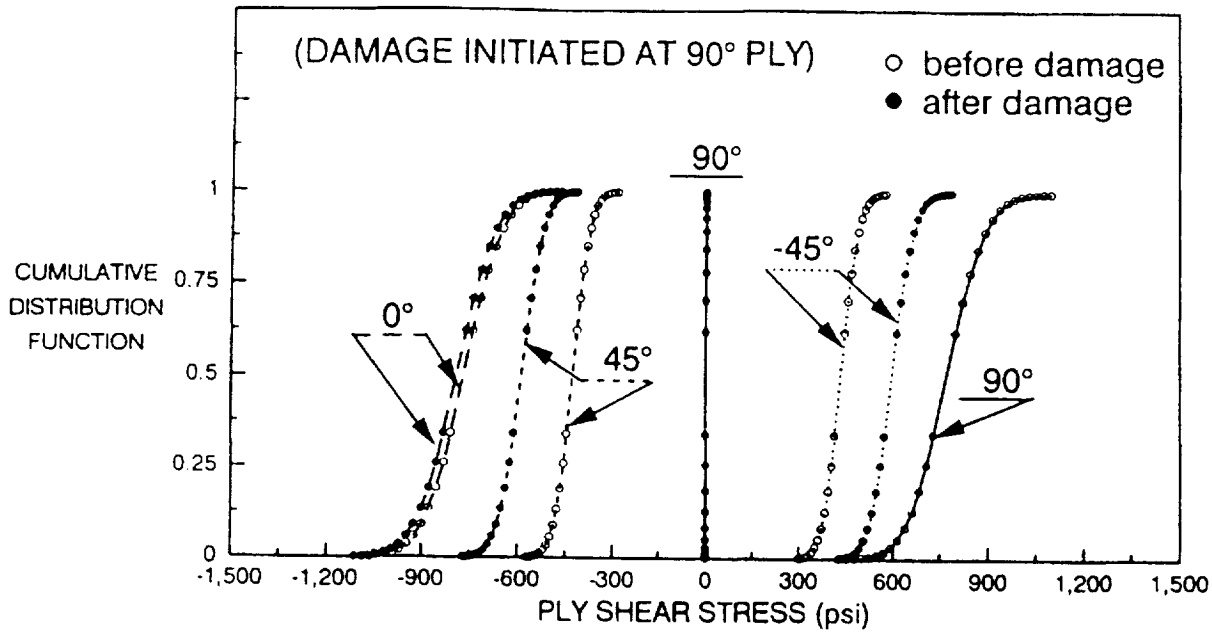

Figure 17.10: CDFs of Ply Shear Stress Before and After Damage

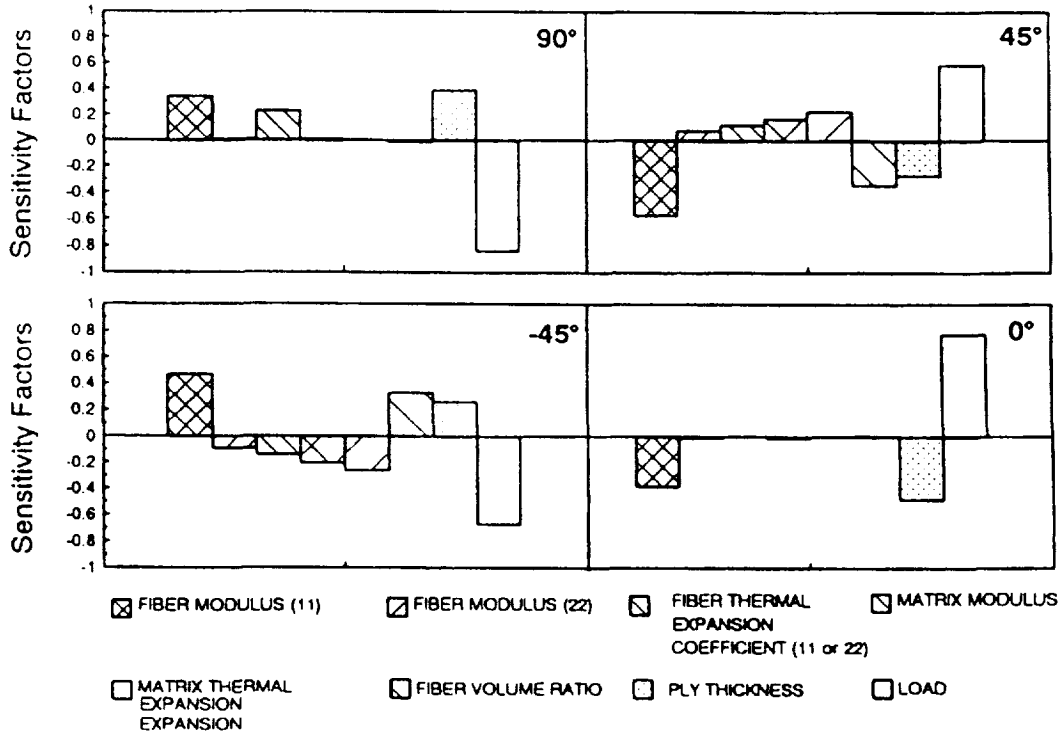

Figure 17.11: Sensitivity Factors for 0.001 Cumulative Probability of Ply Shear Stresses Before Damage Initiation

Chapter 18

Structural Durability of Damaged Metallic Panel Repaired with Composite Patches

Structural durability/damage tolerance characteristics of an aluminum tension specimen possessing a short crack and repaired by applying a fiber composite surface patch is investigated via computational simulation. The composite patch is made of graphite/epoxy plies with various layups. CODSTRAN is utilized for the simulation of combined fiber-composite/aluminum structural degradation under loading. Damage initiation, growth, accumulation, and propagation to structural fracture in both aluminum and composite patch are included in the simulation. Results show the structural degradation stages due to tensile loading and illustrate the use of computational simulation for the investigation of a composite patch repaired cracked metallic panel.

18.1 Introduction

In recent years laminated composite patches have been used for the repair of aging aluminum aircraft with potential fatigue cracks. Design considerations regarding the durability of a patch repaired aluminum panel require an a priori evaluation of damage initiation and propagation mechanisms under expected service loading and hygrothermal environments. In general, the controlling design load is tension perpendicular to the orientation of a crack. However, combined shear with tensile loading must also be taken into account when evaluating the performance of a composite patch repair. Concerns for safety and survivability of a patch-repaired aluminum panel require a quantification of the structural fracture resistance under loading.

Discussion in the current chapter is focussed on a composite patch repaired aluminum panel subject to tensile loading. Damage initiation, growth, accumulation, and propagation to fracture is simulated. Effect of the length of an existing crack is examined with regard to the damage progression and structural durability under applied loading. The damage initiation

load and the structural fracture load are quantified.

Fiber composite patches have tremendous advantages of light weight, high strength, durability, flexibility, and corrosion resistance. Inherent flexibilities in the design of a laminate configuration make composites more capable of fulfilling structural repair patch design requirements. However, for certain designs structural interaction between plies with different fiber orientations and the aluminum panel may adversely affect durability, especially in the presence of combined loading. The computational simulation approach presented in this chapter is well suited to investigate and identify the effects of structural interactions on damage and fracture propagation under design loads and overloads.

18.2 Composite Patch Repaired Aluminum

An aluminum tensile specimen of L=12 in. long, W=3.0 in wide, and t=0.12 in. thick is considered. The specimen has an initial defect/crack at its center. The central defect is oriented transverse to the tensile load direction. Defects of length 0.1, 0.3, and 0.5 in. are considered. The composite patch measures 2.0 in. wide, 3.0 in. long, and is bonded to the surface of the aluminum specimen, centered at the defect. Figure 18.1 shows a schematic of the patched aluminum tensile specimen. The patch laminate structure consists of twelve 0.00521 in. thick plies resulting in a composite patch thickness of 0.063 in. The composite system is made of AS-4 graphite fibers in a high-modulus, high strength (HMHS) epoxy matrix. The fiber and matrix constituent properties, as well as properties of the aluminum, are obtained from a databank of material properties resident in CODSTRAN (2). The corresponding properties are listed in Appendix A.

The HMHS matrix properties are representative of the 3501-6 resin. The fiber volume ratio is 0.60 and the void volume ratio is 2 percent. The cure temperature is 96.1°C (205°F) and the loading temperature is 21°C (70°F). The adhesive bond is assumed to have the same properties as the HMHS epoxy matrix.

The finite element size at the vicinity of the defect is 0.1 in. Computed results are presented up to global fracture for each case. The defect is simulated by prescribing local failures in the aluminum prior to the application of the load.

The aluminum panel is subdivided into twelve 0.01 inch layers to enable the simulation of damage progression across the thickness. The type of damage growth and the sequence of damage progression depend on the composite patch structure, loading, material properties, and hygrothermal conditions.

Figure 18.2 shows damage progression for the aluminum specimen, with three different defect sizes and without a patch repair. As expected, the fracture load decreases with increasing defect size. Figure 18.3 shows damage progression for patch repaired specimens that have 0.1 in. defects. Four different patch laminate configurations are investigated. The best performance is shown by the $[0/90/\pm45/90/0]_S$ or $[\pm45/90_2/0_2]_S$ configuration and the worst performance is shown by $[90/0]_{3S}$ cross-ply laminate. Figure 18.4 shows the damage progression for $[\pm45/90_2/0_2]_S$ patch with three different defect sizes. Figure 18.5 indicates the

differences among different patch laminates for damage progression from a 0.5 in. defect.

Damage progression characteristics have the following general features:

1. Damage initiation is by matrix failure in the 90° plies of the composite patch adjacent to the defect in aluminum.
2. Damage growth is by further degradation of the patch with fiber fractures as well as new matrix failures in the angle plies.
3. In spite of composite damage growth, the patch is effective as a crack arrestor, inhibiting growth of the initial defect in aluminum.
4. Damage/fracture propagation characteristics depend on the patch laminate configuration.

Figure 18.6 shows damage energy release rates for $[\pm 45/90_2/0_2]_S$ and $[90/0]_{3S}$ patches. The $[90/0]_{3S}$ cross-ply patch shows a very low resistance to initial damage growth from the 0.5 in. aluminum defect. On the other hand, the $[\pm 45/90_2/0_2]_S$ patch shows a very high initial resistance to damage growth. The directions of damage growth and progression for the two patches are distinctly different as seen in Figure 18.7.

Figure 18.8 shows the effect of combined shear and tension loading on damage progression for a $[\pm 45/90_2/0_2]_S$ patch. Very low levels of shear loading do not have a significant effect. However, when the magnitude of the shear loading becomes comparable to the tensile loading, the shear load becomes a very significant factor for damage propagation. Also, ultimate fracture propagation becomes more sudden when the shear load is larger.

Figure 18.9 shows the strength recovery due to a $[\pm 45/90_2/0_2]_S$ patch repair on the original aluminum specimen with 0.5 in. defect. Practically the full strength of defect-free aluminum is regained by the patch repair. Additionally, the composite patch repaired specimen is more damage tolerant compared to the original defect-free aluminum. The demonstrated quantification of defect and damage tolerance for a given patch repair is fundamental in the process of identifying the optimal laminate configuration for each application.

18.3 Conclusions

1. Computational simulation, with the use of established composite mechanics and finite element modules, can be used to predict the influence of an existing defect as well as loading, on the safety and durability of a composite patch repaired aluminum panel.
2. CODSTRAN adequately tracks the damage growth and subsequent propagation to fracture for a patch repaired aluminum specimen with an initial defect.
3. Damage initiation, growth, and accumulation stages involve matrix cracking as well as fiber fractures in the composite patch area that is contiguous to the initial defect in aluminum.

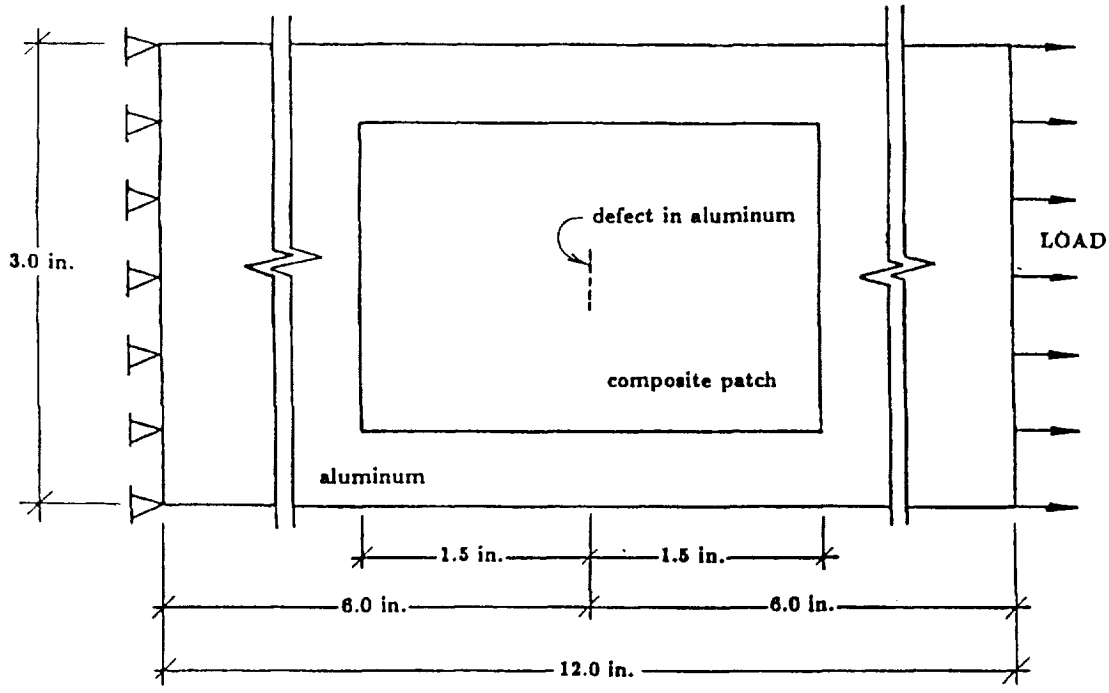

Figure 18.1: Composite Patch Repaired Aluminum

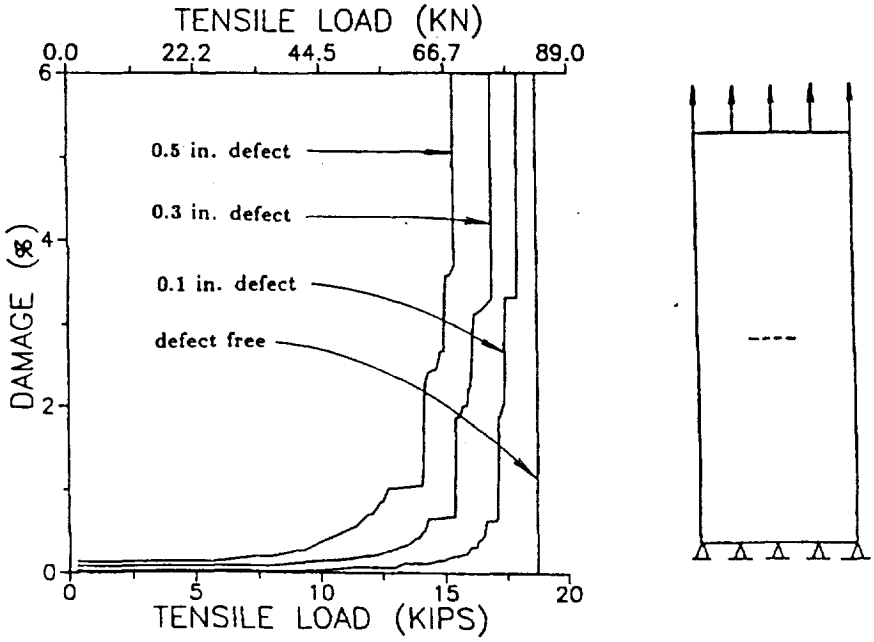

Figure 18.2: Damage Progression for Aluminum Specimen Without Patch

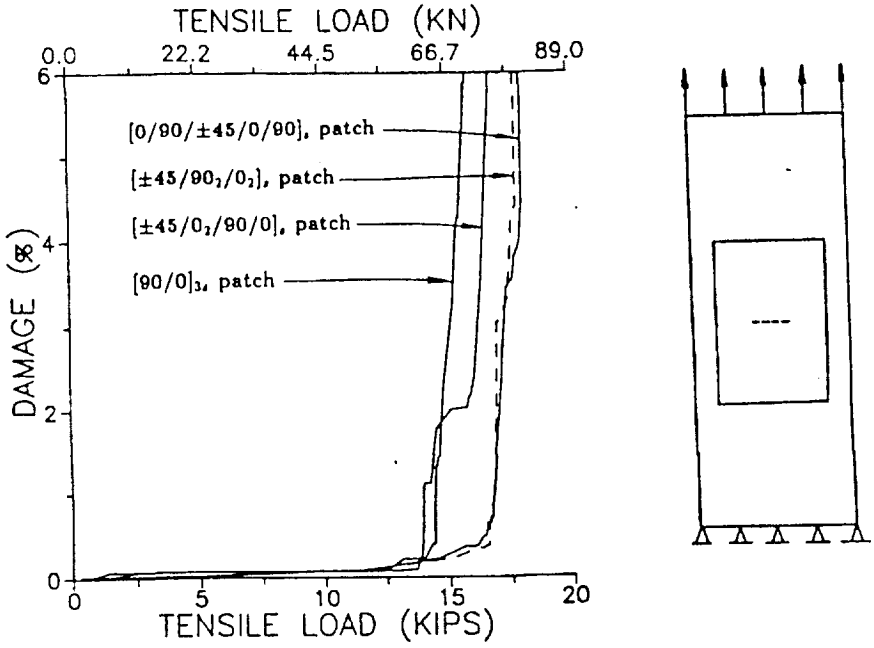

Figure 18.3: Patch Laminate Configuration Effect On Damage Progression from 0.1 in. long defect

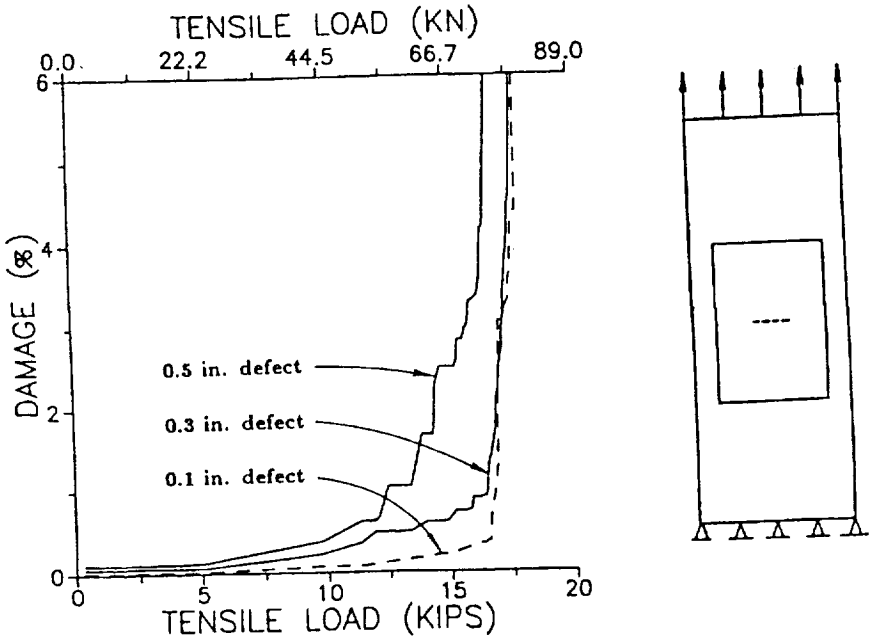

Figure 18.4: Defect Size Effect On Damage Progression

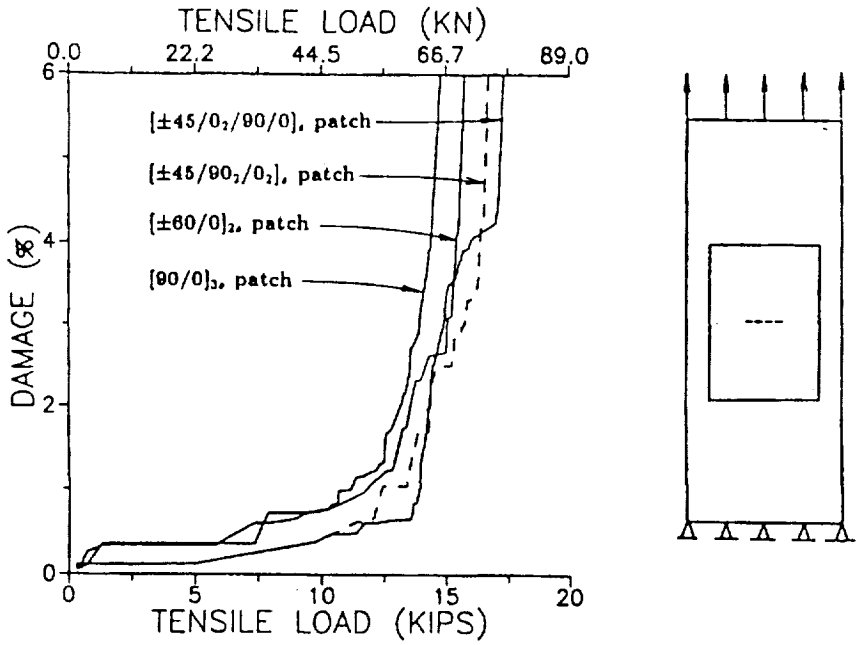

Figure 18.5: Patch Laminate Configuration Effect On Damage Progression from 0.5 in. long defect

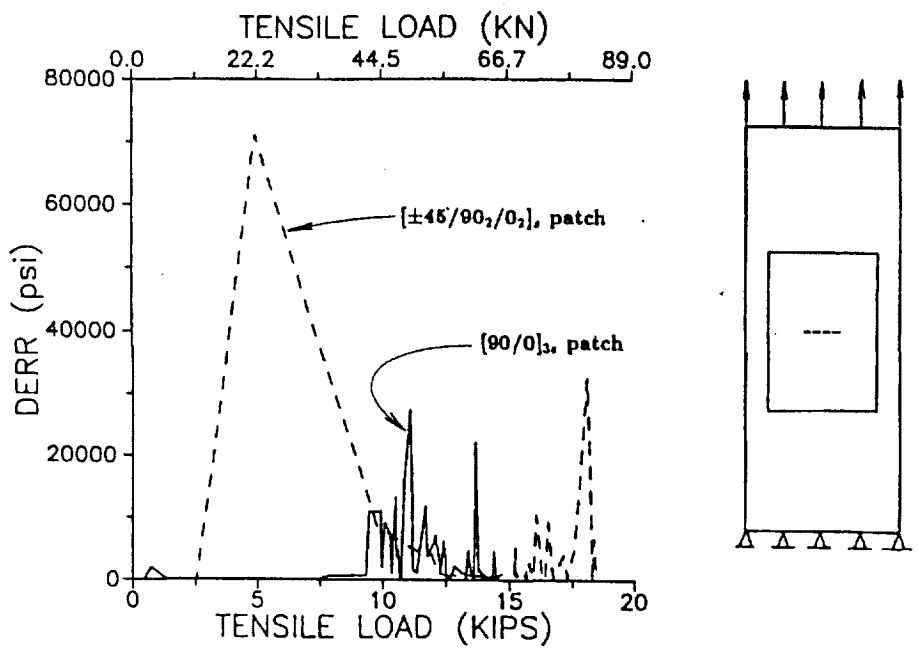

Figure 18.6: Laminate Configuration Effect On Damage Energy Release Rates

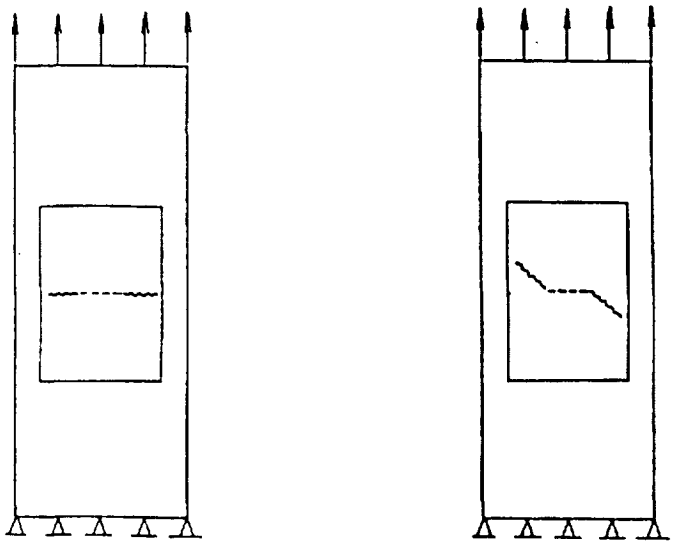

$[\pm 45/90_2/0_2]_S$ patch
self-similar crack growth

$[90/0]_{3S}$ patch
$\pm 45°$ crack growth

Figure 18.7: Effect of Patch Laminate On Damage/Fracture Orientation

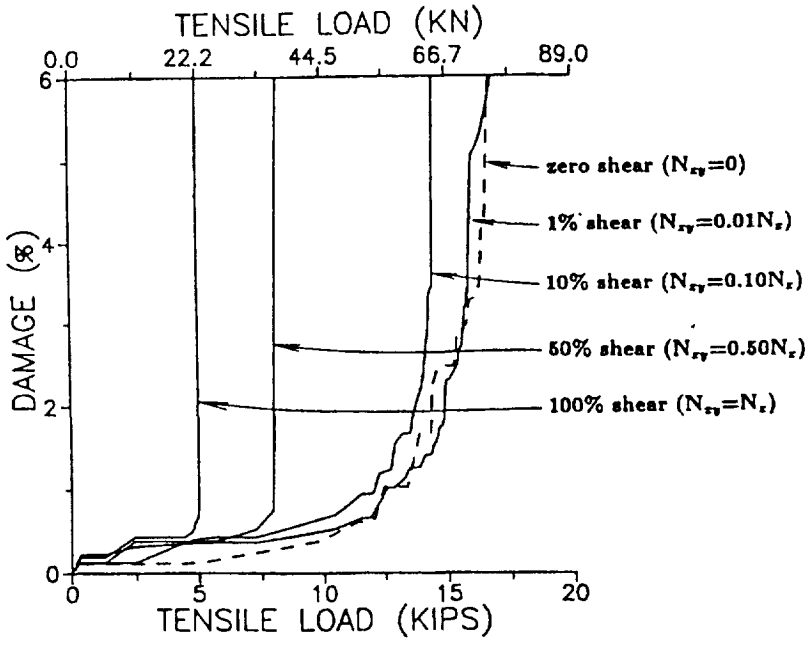

defect length=0.5 in., graphite/epoxy $[\pm 45/90_2/0_2]_S$ patch

Figure 18.8: Damage Progression Under Combined Loading

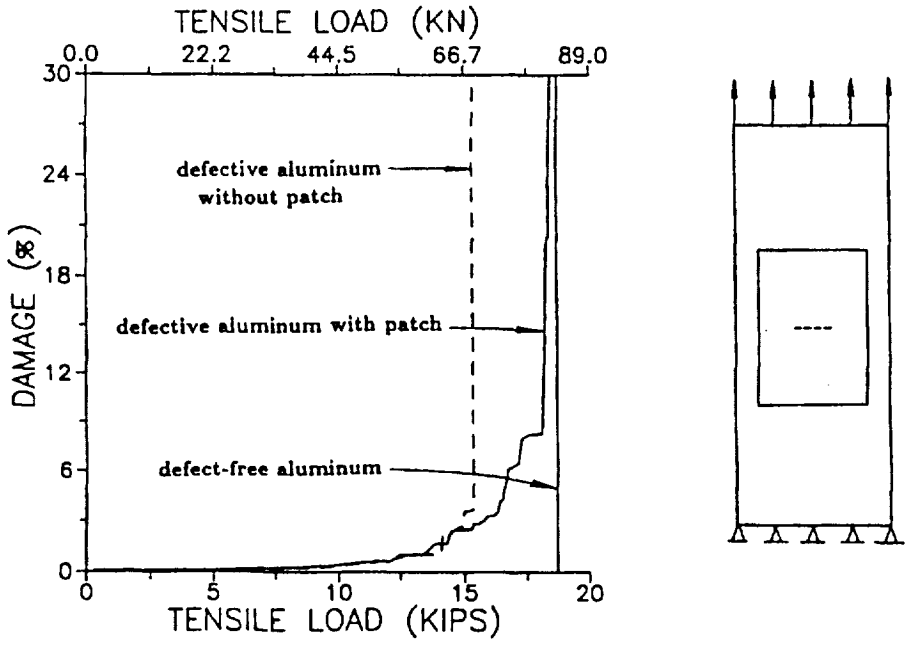

defect length=0.5 in., graphite/epoxy $[\pm 45/90_2/0_2]_S$ patch

Figure 18.9: Strength Recovery Due To Patch Repair

Chapter 19

Progressive Fracture of Composite Offshore Risers

Structural durability/damage tolerance characteristics of a pressurized fiber composite tube designed as an offshore oil production riser is investigated via computational simulation. The composite structure is made of graphite/epoxy angle plies and S-glass/epoxy hoop plies. CODSTRAN is utilized for the simulation of composite structural degradation under loading. Damage initiation, growth, accumulation, and propagation to structural fracture are included in the simulation. Results show the structural degredation stages due to pressurization of a composite riser and illustrate the use of computational simulation for the investigation of a composite tube.

19.1 Introduction

In recent years laminated composite tubes have been proposed, designed, and qualified as offshore oil production and injection/pressurization risers. Riser tubes are subject to internal/external pressures, tension, and bending loads. Design considerations with regard to the durability of a composite riser tube require an evaluation of damage initiation and propagation mechanisms under expected service loading and hygrothermal environments. In general, the controlling design load is internal pressurization. Concerns for safety and survivability of a riser tube require a quantification of the composite structural fracture resistance under loading.

Discussion in the current chapter is focussed on a composite riser tube subject to internal pressure. Damage initiation, growth, accumulation, and propagation to fracture is simulated. The influence of an existing defect due to inadvertent damage is examined with regard to the damage progression and structural durability under applied loading. The damage initiation load and the structural fracture load are quantified.

Composite riser tubes have tremendous advantages of light weight, high strength, durability, flexibility, and corrosion resistance. However, for certain designs structural interaction between plies with different fiber orientations may adversely affect durability, especially in the

presence of defects. The CODSTRAN computational simulation code is well suited to investigate and identify the effects of structural interactions on damage and fracture propagation under design loads and overloads. Any inadvertent ply damage such as transverse cracks, accidental ply cuts during fabrication or service, and defect induced fiber fractures could weaken the overall structural strength and durability. Defects may or may not have a significant effect on durability for a particular application. It is therefore useful to quantify the reduction in the overall strength and durability of a composite structure due to preexisting defects.

19.2 Simulation of a Composite Riser

A composite system made of graphite/epoxy angle plies that are sandwiched between glass/epoxy hoop plies [?] is used to illustrate CODSTRAN durability analysis of a representative riser tube structure.

The laminate structure consists of one hundred and sixteen plies resulting in a composite shell thickness of 15.6 mm (0.614 in.). The laminate configuration is $[90_{36}/\pm 20_{22}]_s$. The 90° plies are in the hoop/circumferential direction of the tube and the helically wound angle plies are oriented 20° with respect to the axial direction as depicted in Figure 19.1. Constituent material in-situ properties for the S-glass fibers, T300 graphite fibers, and the EPOX epoxy matrix are given in Appendix A.

The in-situ fiber volume ratios are 0.60 for the graphite/epoxy angle plies and 0.66 for the S-glass/epoxy hoop plies. The riser tube has a mean diameter of 229 mm (9.0 in.). The finite element model contains 544 nodes and 512 quadrilateral shell elements as shown in Figure 19.2. An axial length of 457 mm (18.0 in.) is considered for the computational model. The composite tube is simulated as a closed-end cylindrical pressure vessel by applying a uniformly distributed axial tension such that the generalized axial stresses in the shell wall are half those developed in the hoop direction. The tube is subjected to an internal pressure that is gradually increased until fracture.

Computed results are presented up to global fracture for a tube with a partial-thickness defect. The defect is simulated by prescribing fiber failures in the outermost eighteen plies of the tube prior to the application of internal pressure. The defect extends 28.6 mm (1.125 in.) along the axial direction of the tube. The defect is associated with one node of the finite element model and size of the defect is derived from the tributary length of the node along the tube axis. The CODSTRAN simulation process takes into account the nonlinearities due to material and structural effects and shows the reduction in the ultimate internal pressure because of local defects in the outer plies of the composite structure.

CODSTRAN gives a damage initiation pressure of approximately 50 MPa (7.2 ksi). Initial damage is in the form of matrix cracking in the 90° glass/epoxy circumferential plies that are contiguous to the defective plies. When the pressure is increased to 57 MPa (8.3 ksi) all plies at the defective node fail in transverse tension. The laminate configuration is well balanced with regard to the hoop and angle ply transverse strengths when the tube is

subjected to internal pressure loading. Matrix failure occurs first in the hoop plies as the angle plies are subjected to a small relative rotation due to axial stresses, allowing the pipe to stretch axially. At locations other than the defective node, matrix failure starts at the inner hoop plies and spreads to the outer hoop plies. After the hoop plies are degraded in their transverse stiffnesses, angle plies are also damaged due to transverse tension. At 60 MPa (8.7 ksi) pressure, matrix cracking spreads to all hoop and angle plies at the vicinity of the defect, causing a slight bulge. However, through-the-thickness extension of the defect/cut does not occur. Instead, damage near the defect becomes stable and damage progression continues by matrix cracking of all hoop and angle plies at remote locations. The damage stabilization phenomenon for composite cylindrical shells subjected to internal pressure has been shown previously.[9]

After the completion of the matrix failure phase, the simulated pressure may be increased up to 103 MPa (15.0 ksi) without any additional damage. Ultimate fracture of the pipe occurs at 107 MPa (15.5 ksi) due to fiber fractures precipitating a structural fracture.

The simulated fracture pressure of 107 MPa is 2 to 14 percent higher than experimental measurements of the bursting pressure (94 to 105 MPa) for similar composite riser tubes with small defects [?]. It may be noted that the difference of computational simulation results from test data is within the variability limits of fiber tensile strength.

Figure 19.3 shows an overall summary of damage progression for the riser tube with increasing pressure. The initial defect acts as a point of nucleation for damage initiation by matrix cracking in the hoop plies adjacent to the short longitudinal cut. However, the defect does not induce fiber fractures. After the growth and accumulation of ply transverse failures by matrix cracking the damage becomes stable and the internal pressure may be increased by over 200 percent above the damage initiation pressure prior to the ultimate fracture of the tube. It should be noted that damage/fracture progression characteristics would be different for a different laminate configuration. The demonstrated quantification of defect and damage tolerance for a given riser tube is fundamental in the process of identifying the optimal structural configuration for each application.

19.3 Conclusions

The significant results from this investigation in which CODSTRAN (COmposite Durability STRuctural ANalysis) is used to evaluate damage growth and propagation to fracture of a composite riser tube are as follows:

1. Computational simulation, with the use of established composite mechanics and finite element modules, can be used to predict the influence of an existing defect as well as loading, on the safety and durability of a pressurized composite tube.

2. CODSTRAN adequately tracks the damage growth and subsequent propagation to fracture for a composite riser tube with a partial-thickness defect.

3. Minor defects do not have a significant effect on the structural fracture pressure for the

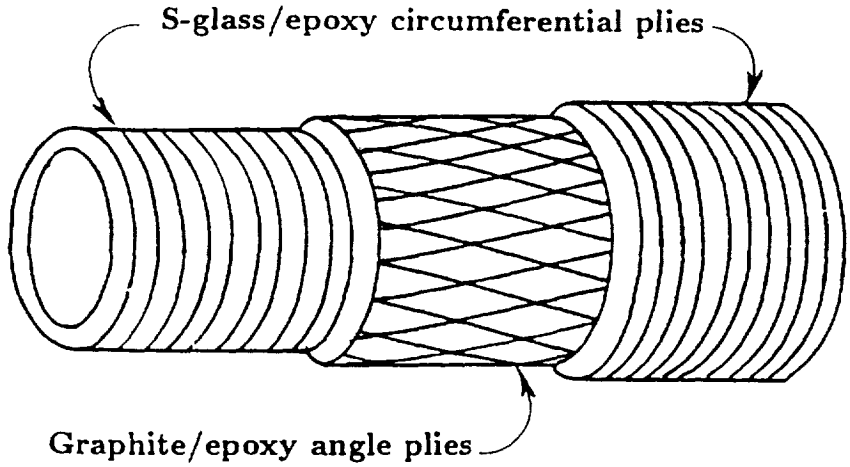

Figure 19.1: Composite Structure of Riser Tube: Wall thickness = 15.6 mm (0.614 in.); tube diameter = 229 mm (9.0 in); Hybrid Laminate: $[90_{36}/\pm 20_{22}]_s$

tube considered. Damage initiation, growth, and accumulation stages involve matrix cracking only. Ply fiber fractures occur immediately preceeding structural fracture.

4. The demonstrated procedure is flexible and applicable to all types of constituent materials, structural geometry, and loading. Homogeneous materials as well as composites can be simulated.

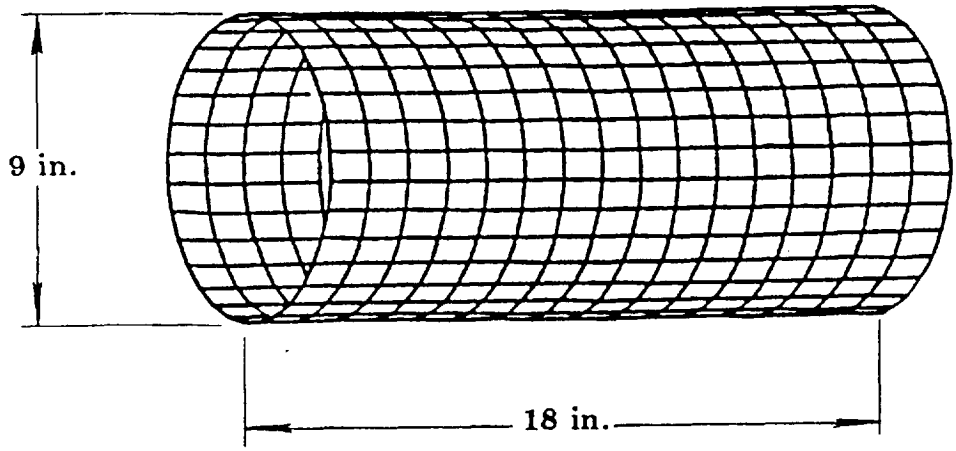

Figure 19.2: Finite Element Model: 544 Nodes, 512 Quadrilateral Elements; S-glass/epoxy circumferential plies, graphite/epoxy angle plies; Wall thickness = 15.6 mm (0.614 in.); tube diameter = 229 mm (9.0 in); Model Length = 457 mm (18 in), hybrid Laminate: $[90_{36}/\pm 20_{22}]_s$

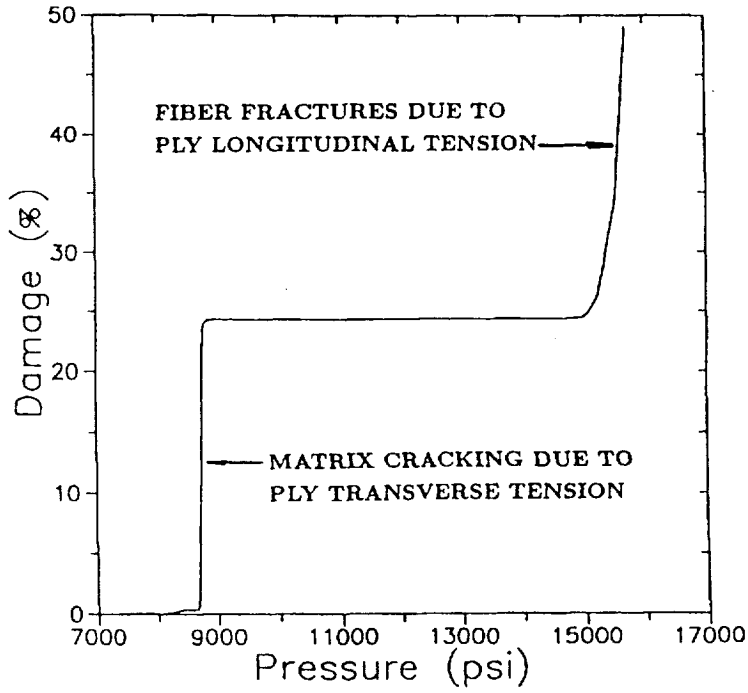

Figure 19.3: Damage Progression with Pressure; S-glass/epoxy circumferential plies, Graphite/epoxy angle plies; Wall thickness = 15.6 mm (0.614 in.); tube diameter = 229 mm (9.0 in); Hybrid Laminate: $[90_{36}/\pm 20_{22}]_s$; Initial defect of 28.6 mm (1.125 in) length

Chapter 20

Discontinuously Stiffened Composite Panel under Compressive Loading

An application of CODSTRAN is presented to examine the response of stiffened composite panels via the simulation of damage initiation, growth, accumulation, progression, and propagation to structural fracture or collapse. The structural durability of a composite panel with a discontinuous stiffener is investigated under compressive loading induced by the gradual displacement of an end support. Results indicate damage initiation and progression to have significant effects on structural behavior under loading.

20.1 Introduction

Stiffened composite panels are used in many structural components to satisfy requirements of reduced weight, increased stiffness, and stability. The present chapter demonstrates the capability of CODSTRAN to evaluate the response and degradation of a discontinuously stiffened composite panel under a displacement controlled loading.

20.2 Stiffened Composite Panel

The demonstration example for this chapter consists of a stiffened composite panel, depicted in Figures 20.1 and 20.2, subjected to axial compression. The finite element model shown in Figure 20.1 uses thick shell elements with duplicate nodes where there are sudden changes in composite properties. The use of duplicate nodes to achieve accurate structural representation at locations of abrupt change in the laminate was discussed in a previous chapter. The composite system for this example is made of AS-4 graphite fibers in a high-modulus, high-strength epoxy matrix (AS-4/HMHS). The corresponding fiber and matrix properties are obtained from a databank of composite constituent material properties resident in CODSTRAN.

The properties used for the AS-4 graphite fibers and HMHS epoxy matrix are given in Appendix A. The HMHS matrix properties are representative of the 3501-6 resin. The skin laminate consists of forty-eight 0.132 mm. (0.00521 in.) plies resulting in a composite thickness of 6.35 mm. (0.25 in.). The fiber volume ratio is 0.60. The laminate configuration is $[[0/\pm 45/90]_s]_6$. The 0° plies are in the axial direction of the stiffener, along the x axis indicated in Figure 20.2a. The width of the stiffened panel is 991 mm (39 in.) and it has a length of 559 mm (22 in.). The stiffener hat sections are made from the same AS-4/HMHS composite structure as the outer skin. The stiffeners are perfectly bonded to the skin at all surfaces of contact. This example is physically very similar to the stiffened composite panel analyzed in [?]. Similar to [?], large displacements are taken into account. The novelty in the present chapter is that composite constituent level progressive damage simulation is integrated into the structural analysis of the stiffened panel.

Axially compressive loading is applied by imposing a gradually increasing uniform axial displacement at the clamped edge of the panel. A displacement controlled CODSTRAN simulation is employed to monitor damage initiation and progression as the panel is loaded. Figure 20.3 shows the relationship between induced loading due to the imposed displacement of the clamped edge and the produced damage during damage initiation and growth stages. First ply failure is in the surface ply of the skin near the end of the stiffener.

With reference to Figure 20.3, damage initiation is under a 635 kN (143 kip) loading by compressive failures in the 0° first ply at approximately 6.4 mm from the stiffener web ends toward the clamped edge of the panel. As loading increases, damage grows contiguously in the plane of the skin. Across the laminate thickness, damage growth is first into the zero degree plies. When loading reaches 737 kN, the ±45° angle plies also begin to participate in damage progression. After the 737 kN loading level, damage growth is accompanied with negligible increase in loading. After a 737.4 kN ultimate load, corresponding to a cumulative damage level of approximately 0.14 percent, the induced compressive load decreases as a through-the-thickness damage propagation stage is entered with increasing global strain. The damage propagation mode is highly localized to the unstiffened composite skin areas immediately adjacent to the ends of the stiffener toe elements.

Figures 20.4a and 20.4b show the Ply 1 longitudinal stress contours under a 689 kN load during damage growth. Composite properties are degraded according to the accumulated damage, resulting in the lowering of ply stresses in the damaged regions. Damage is localized to the skin, adjacent to the ends of the stringer toe elements bonded to the skin. Due to the localized nature of damage, the overall pattern of stress contours shown in Figure 20.4a is not significantly affected during the initial stages of damage. The significant local effects at the damaged region are indicated in Figure 20.4b by the detailed stress relief contours.

Figure 20.5 shows the overall relationship between the applied global strain and the corresponding total axial compressive force in the panel. The CODSTRAN simulation indicated in Figure 20.5, takes into account geometric nonlinearities caused by large displacements as well as the effects of structural degradation with damage. Linear analysis and geometrically nonlinear analysis results, not taking into account the effects of structural damage, are also shown in Figure 20.5 for comparison with CODSTRAN simulation. Before the damage

initiation stage, CODSTRAN simulation is identical to geometrically nonlinear structural analysis. However, the information provided by CODSTRAN with regard to damage progression and damage tolerance during the various degradation stages cannot be obtained from any traditional linear or nonlinear structural analysis result.

Figure 20.6 shows the direct relationship between the applied global strain and the volume of damage produced in the composite structure. After the damage initiation stage, overall damage volume increases precipitously yet steadily with the applied global strain through the maximum loading stage and beyond.

A measure of composite structural damage tolerance is obtained by defining the Strain Energy Release Rate (SERR) as the amount of incremental work done on the structure per unit volume of the created damage during degradation [?], [?]. Figure 20.7 shows the SERR as a function of the applied global strain on the panel. The peak SERR level occurs at damage initiation, corresponding to a global deformation of approximately 4000 microstrains. SERR falls to a much lower level after damage initiation, indicating the lack of damage tolerance of this structure after initial damage. Fluctuations in the SERR indicate changes in the structural resistance against damage under progressive end displacement. The maximum loading level of 737.4 kN (166 kips), corresponding to an applied global deformation of approximately $5100\mu\epsilon$, is marked by a small but sharp local peak in the SERR.

Figure 20.8 shows the z components of displacements under a $4500\mu\epsilon$ global strain during damage growth. The overall displacement contours depicted in Figure 20.8 are not affected by the localized damage. Figure 20.8 indicates that the apparent global response of the stiffened panel, as may be observed during a physical test, does not show any significant signs of the damage progression that is taking place in the plies of the laminate.

Figure 20.9 shows the x components of displacements under the same $4500\mu\epsilon$ global strain as in Figure 20.8. Axial displacement contours shown in Figure 20.9 are only slightly affected near the local damage. Figure 20.9 indicates that in order to detect damage growth in a laboratory test it is necessary to measure accurately the local strains in the damaged zone.

Figure 20.10 shows Ply 1 longitudinal stress contours immediately after through-the-thickness laminate fractures occur under a 737.4 kN (166 kip) ultimate loading. The stress relief contours near the stringer toe edges shown in Figure 20.10 are indicative of laminate failure locations.

20.3 Concluding Remarks

The significant results and overtones from this investigation in which CODSTRAN (COmposite Durability STRuctural ANalysis) is used to evaluate structural response of a stiffened composite panel, considering damage initiation and progression effects, are as follows:

1. Computational simulation, with the use of established composite mechanics and finite element modules, can be used to predict the damage tolerance, safety, and durability of built-up composite structures such as composite skin panels with integrated stiffeners.

2. CODSTRAN adequately tracks the damage initiation, growth, and subsequent propagation to fracture for any composite structure.

3. Non-destructive evaluation of in-service structural integrity is facilitated by the prediction of damage initiation/progression locations and mechanisms.

4. CODSTRAN simulations may be carried out under either load controlled or displacement controlled conditions.

5. The demonstrated procedure is flexible and applicable to all types of constituent materials, structural geometry, and loading. Hybrid composite structures, composite laminates containing homogeneous materials such as metallic foils, as well as binary composites can be simulated. The hygrothermal environment, residual stresses induced by the curing process, local defects due to fabrication error and/or accidental damage may be included in a CODSTRAN simulation.

6. Fracture toughness parameters such as the structural fracture load and the ultimate load are identifiable for any structure by the demonstrated method. It is also useful to carry out CODSTRAN simulations prior to physical testing to guide the data acquisition strategy and to enable the detailed interpretation of experimental results with regard to damage initiation/progression mechanisms and damage tolerance.

7. The availability of CODSTRAN facilitates composite structural design and certification by allowing the efficient and effective evaluation of design options and by providing early design loads.

8. Computational simulation by CODSTRAN represents a new global approach to structural integrity assessment.

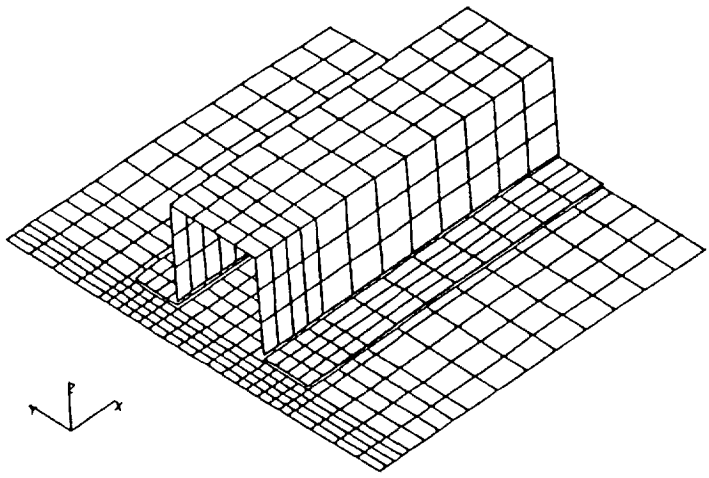

Figure 20.1: Stiffened Composite Panel Finite Element Model: AS-4/HMHS$[[0/\pm 45/90]_s]_6$

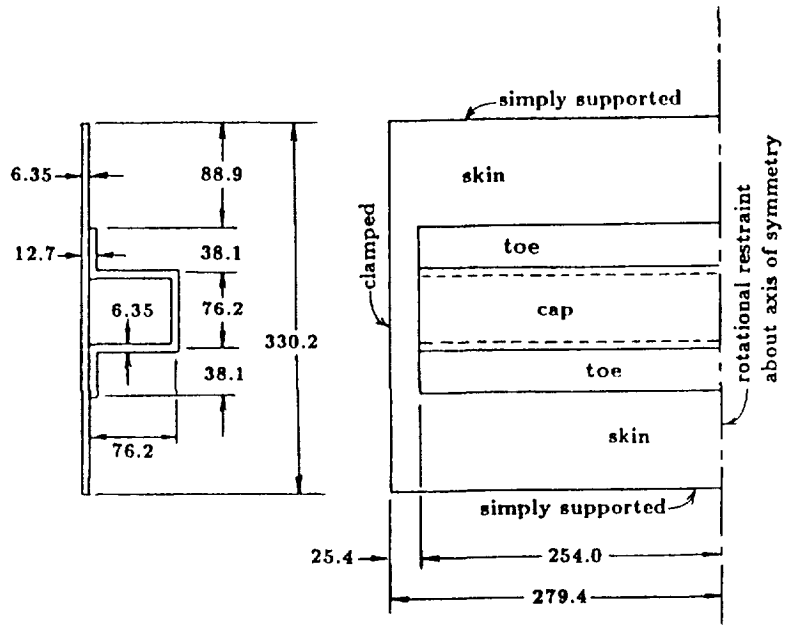

Figure 20.2: Stiffened Composite Panel AS-4/HMHS$[[0/\pm 45/90]_s]_6$; Cross Section and Plan (All dimensions are in mm)

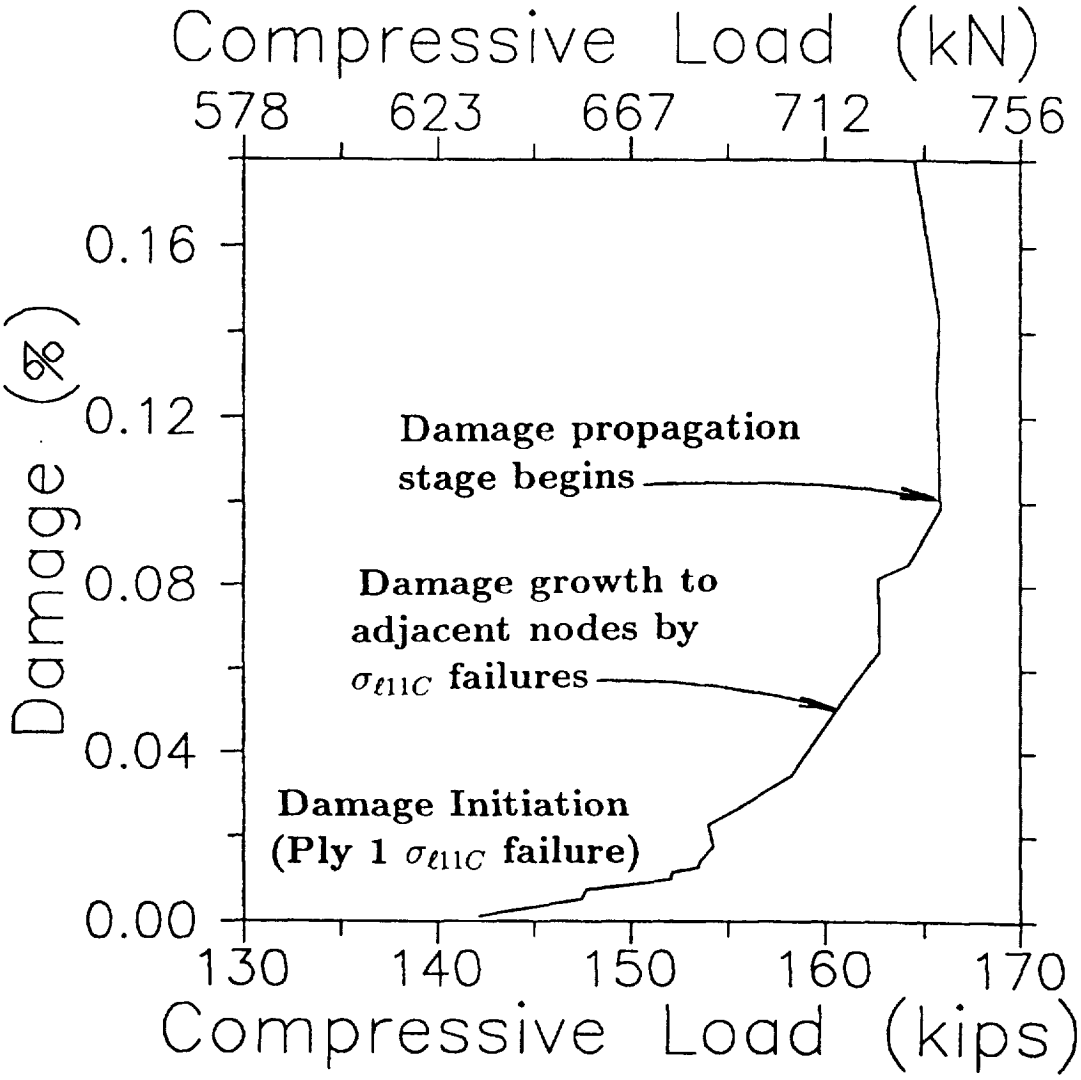

Figure 20.3: Damage Initiation and Growth under Compressive Load; AS-4/HMHS$[[0/\pm 45/90]_s]_6$

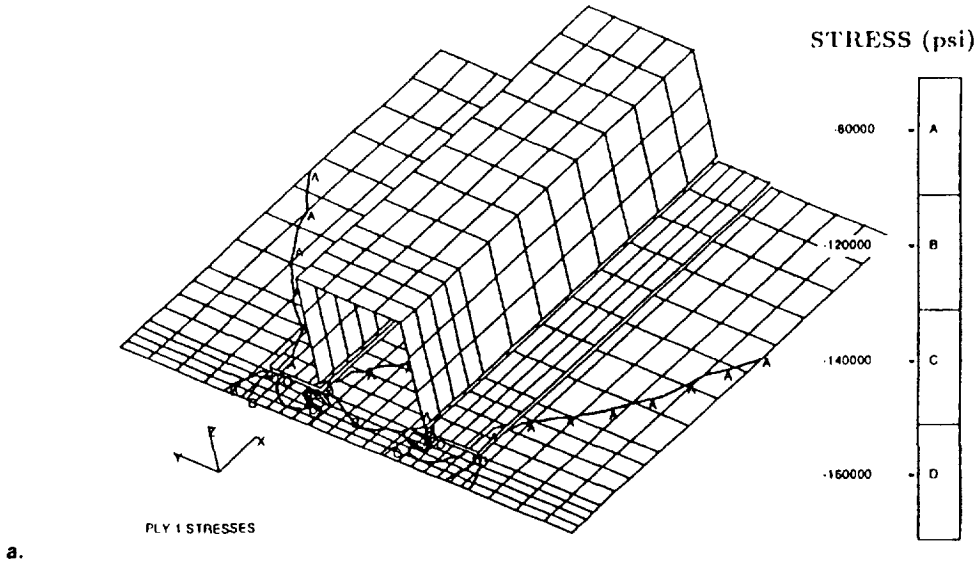

a.

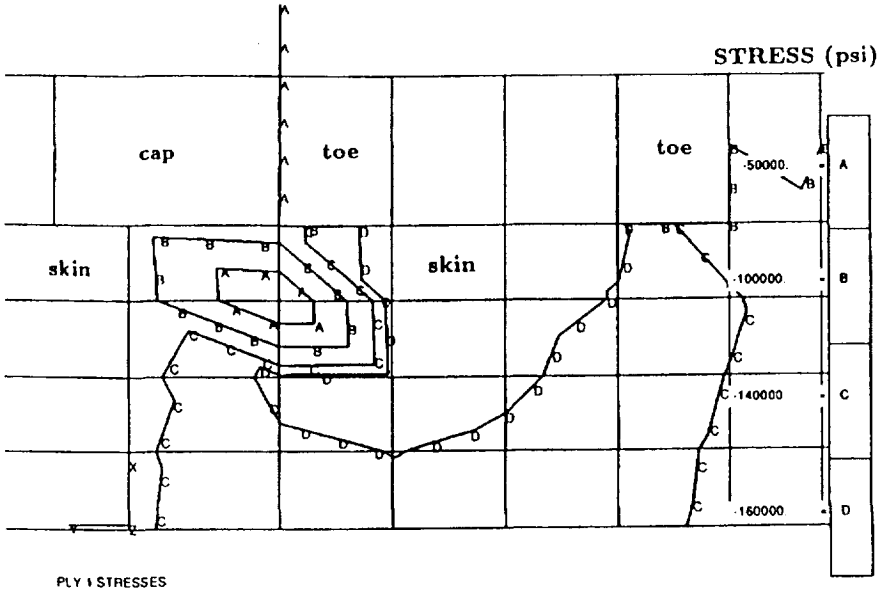

b.

Figure 20.4: a) Ply 1 Global Longitudinal Stress Contours after Initial Damage Growth; b) Ply 1 Stress Relief Details in Critical Region after Initial Damage Growth; AS-4/HMHS$[[0/\pm 45/90]_s]_6$

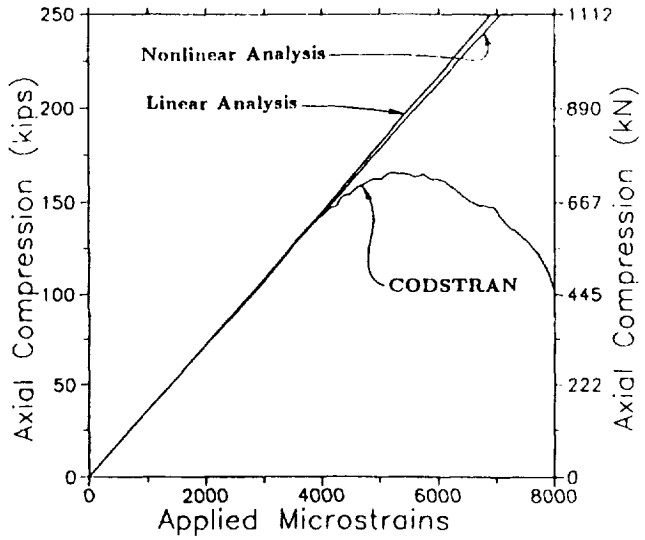

Figure 20.5: Induced Compressive Load with End Displacement AS-4/HMHS$[[0/\pm 45/90]_s]_6$

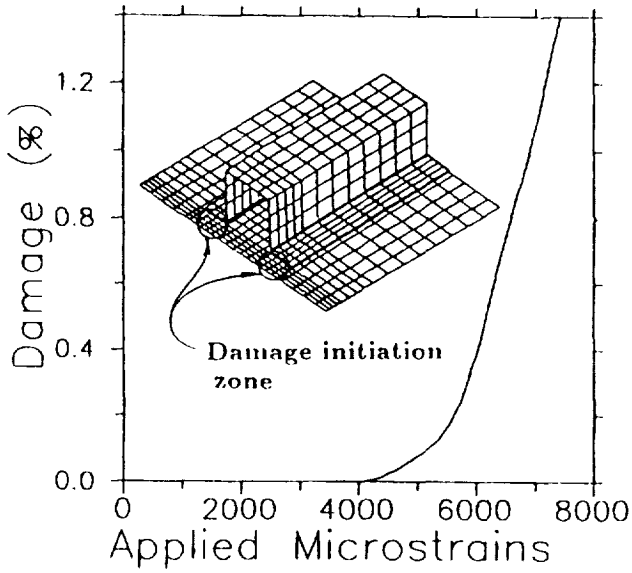

Figure 20.6: Damage Propagation with End Displacement AS-4/HMHS$[[0/\pm 45/90]_s]_6$

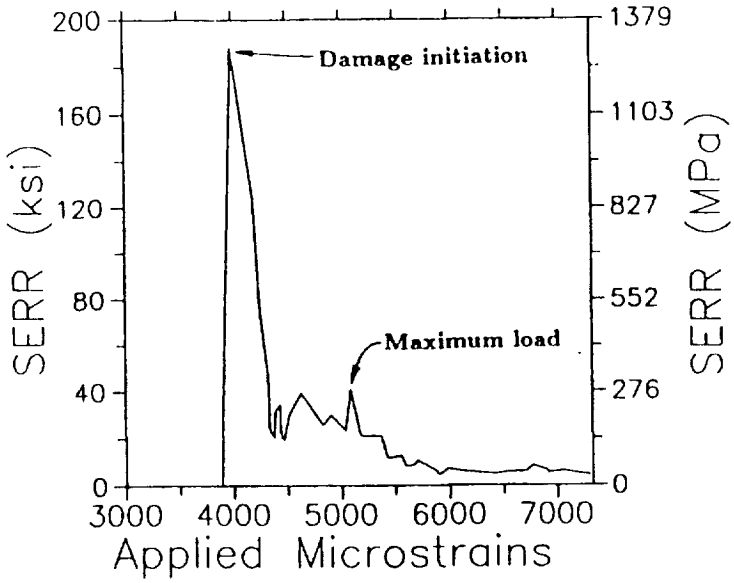

Figure 20.7: Strain Energy Release Rate with End Displacement; AS-4/HMHS$[[0/\pm 45/90]_s]_6$

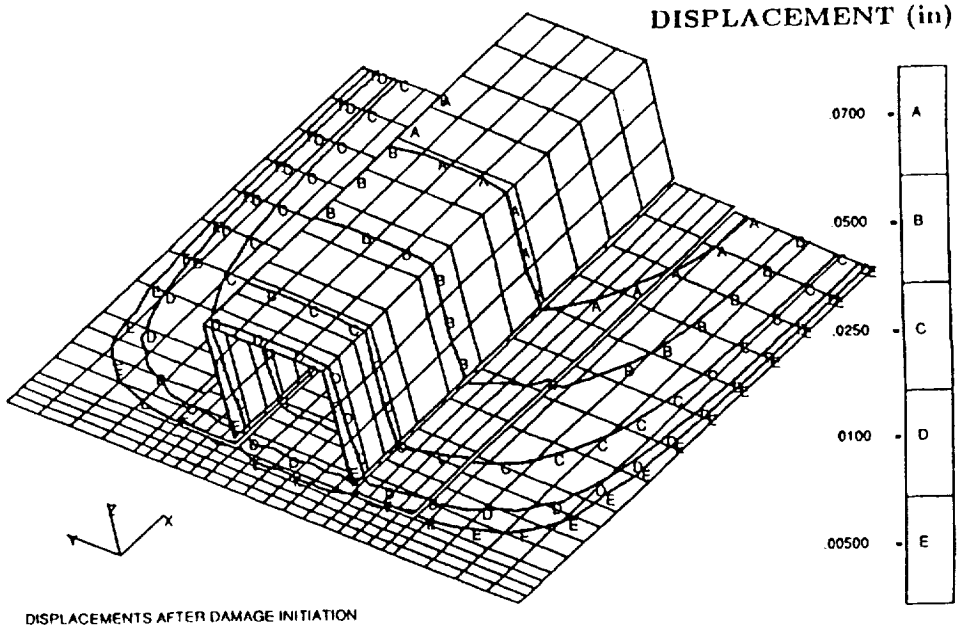

Figure 20.8: Displacements (z components) after Damage Initiation; AS-4/HMHS$[[0/\pm 45/90]_s]_6$

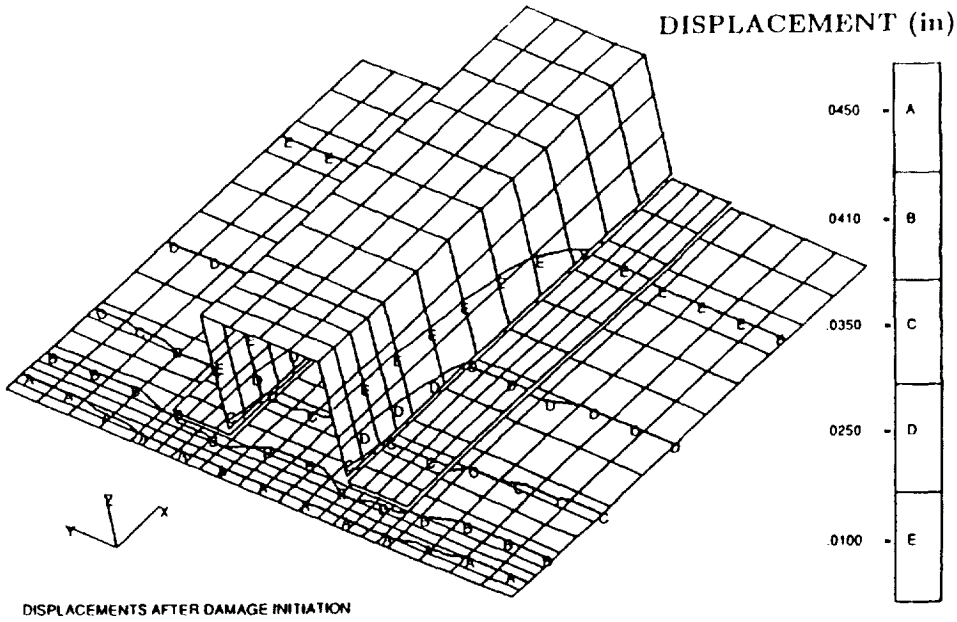

Figure 20.9: Axial Displacements after Damage Initiation; AS-4/HMHS$[[0/\pm 45/90]_s]_6$

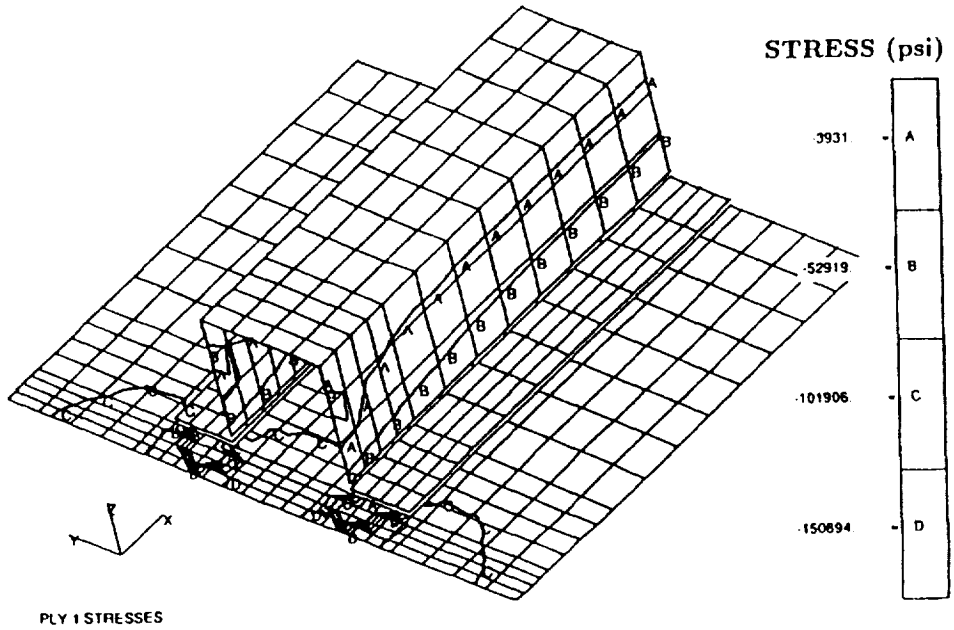

Figure 20.10: Ply 1 Longitudinal Stresses after through-the-thickness Damage Propagation; AS-4/HMHS$[[0/\pm 45/90]_s]_6$

Chapter 21

Effect of Combined Loads on the Durability of a Stiffened Adhesively Bonded Composite Structure

Progressive fracture and damage tolerance characteristics of a stiffened graphite/epoxy panel is investigated via computational simulation. An integrated computer code is utilized for the simulation of composite structural degradation under loading. Damage initiation, growth, accumulation, and propagation to structural fracture are included in the simulation. Results indicate damage initiation and progression to have significant effects on structural behavior under loading.

21.1 Introduction

Stiffened panels are used in many composite aerospace structural components to satisfy requirements of reduced weight, increased stiffness, and stability. In these applications stiffened composite panels are required to withstand significant bending and twisting loads. Design considerations with regard to the durability of stiffened panels require an a priori evaluation of damage initiation and propagation mechanisms under expected service loading. Concerns for safety and survivability of critical components require a quantification of the composite structural damage tolerance during overloads.

21.2 Stiffened Panel

The structural example for this paper consists of a stiffened composite panel, depicted in Figures 21.1 and 21.2, subjected to bending and torsion. The finite element model shown in Figure 21.1 uses thick shell elements with duplicate nodes where there are sudden changes in composite properties. The use of duplicate nodes to achieve accurate structural representation at locations of abrupt change in the laminate was discussed in a previous paper [?].

The composite system is made of AS-4 graphite fibers in a high-modulus, high strength (HMHS) epoxy matrix. The fiber and matrix properties are obtained from the databank of composite constituent material properties resident in CODSTRAN. The corresponding fiber and matrix properties are given in Appendix A. The HMHS matrix properties are representative of the 3501-6 resin. The skin laminate consists of forty-eight 0.132 mm. (0.00521 in.) plies resulting in a composite thickness of 6.35 mm. (0.25 in.). The fiber volume ratio is 0.60 and the void volume ratio is 1 percent. The laminate configuration is $[[0/\pm 45/90]_s]_6$. The adhesive bond at the joint between the skin and the stiffener has the same properties as the HMHS epoxy matrix. The 0° plies are in the axial direction of the stiffener, along the x axis indicated in Figure 21.1. The width of the stiffened panel is 991 mm (39 in.) and it has a length of 559 mm (22 in.). The stiffener hat sections are made from the same AS-4/HMHS composite structure as the outer skin. The stiffeners are adhesively bonded to the skin at all surfaces of contact. Composite constituent level progressive damage simulation is integrated into the structural analysis of the stiffened panel.

21.2.1 Bending load

Bending is applied by imposing a gradually increasing uniformly distributed bending moment at the unstiffened edge of the panel. The damage initiation, progression, and failure of the composite structure is monitored. The outcome of the computational simulation of the composite panel is summarized in Figure 21.3 with a plot of the damage progression as a function of the load. The values of the load are normalized with respect to a maximum load (failure load) of 10,050 lb-in.

The scalar damage variable, shown on the ordinate of the graph in Figure 21.3, is derived from the total volume of the composite material affected by the various damage mechanisms.[5,7] Computation of the shown scalar damage variable has no interactive feedback on the detailed simulation of composite degradation.

Damage initiation of the composite panel started when the normalized load reached 0.672. The damaged nodes were those at the skin-stiffener junction at the beginning of the stiffener. First ply failure was at the surface ply of the skin at the end of the stiffener. Ply damage, shown in Table 21.1, took place in the following plies of skin: The first 0° ply was damaged due to compressive failure, indicating a debonding from the stiffener. On the tension side, the 90° and ±45° plies failed in transverse tension. The 0° plies on the tension side failed in longitudinal tension.

When the normalized load reached 0.88 the composite structure weakened and became unstable due to accumulation of ply damage and the fracture of a number of nodes. The final damage propagation stage was entered when the load was increased to 10,050 lb.

The displacements in the z direction of the center of the unstiffened free edge are plotted as a function of the bending load in Figure 21.4. The displacements are normalized with respect to the maximum displacement of 0.1188 in., corresponding to the maximum load of 10,050 lb-in.

Figure 21.5 shows a plot of the first ply longitudinal $\sigma_{\ell 11}$ stresses corresponding to a nor-

Table 21.1: **Damage Initiation: Normalized bending load = 0.67**

PLY NO.	FIBER ANGLE	FAILURE MODE
1	0°	$\sigma_{\ell 11C}$
44	90°	$\sigma_{\ell 22T}$
45	90°	$\sigma_{\ell 22T}$
46	-45°	$\sigma_{\ell 22T}$
47	+45°	$\sigma_{\ell 22T}$
48	0°	$\sigma_{\ell 11T}$

malized load of 0.8 that corresponds to a stable damage growth stage prior to structural fracture.

21.2.2 Torsional load

Torsional load was uniformly applied along the free edge of the composite panel and was increased gradually. Damage initiation and progression of the panel structure were monitored. The outcome of computational simulation indicated that damage progression increases with the applied load as shown in Figure 21.6. Structural behavior of the composite panel was stable and it tolerated local ply damage until the normalized applied load reached 0.852 (The load was normalized with respect to the failure load of 9,772 lb-in). When the load was increased further, the damage progression and fracture accelerated and the panel failed at the maximum load of 9,772 lb-in.

Normalized displacements in the z direction, at the middle node of the free edge, are plotted in Figure 21.7. The "knee" in the displacement curve of Figure 21.7 corresponds to the normalized damage initiation load of 0.43. At the damage initiation stage the following observations may be made with regard to ply failures of the skin laminate: 1) The -45° third ply failed by $\sigma_{\ell 22T}$ transverse tension. 2) The +45° forty-seventh ply failed by $\sigma_{\ell 11C}$ longitudinal compression.

When the normalized torsional load reached 0.86, the damage of the composite panel became severe and the structure weakened. This stage was followed by less stable damage propagation that failed the structure when the maximum load was reached.

Figure 21.8 shows the first ply longitudinal $\sigma_{\ell 11}$ stresses corresponding to a normalized load of 0.86 corresponding to the significant damage growth stage prior to structural fracture.

21.3 Conclusions

The significant conclusions from this investigation in which CODSTRAN (COmposite Durability STRuctural ANalysis) is used to evaluate structural response of a stiffened composite panel, considering damage initiation and progression effects, are as follows:

1. Computational simulation, with the use of established composite mechanics and finite element modules, can be used to predict the damage tolerance, safety, and durability of built-up composite structures such as composite skin panels with integrated stiffeners.

2. CODSTRAN adequately tracks the damage initiation, growth, and subsequent propagation to fracture for any composite structure.

3. Non-destructive evaluation of in-service structural integrity is facilitated by the prediction of damage initiation/progression locations and mechanisms.

4. The demonstrated procedure is flexible and applicable to all types of constituent materials, structural geometry, and loading. Hybrid composite structures, composite laminates containing homogeneous materials such as metallic foils, as well as binary composites can be simulated. The hygrothermal environment, residual stresses induced by the curing process, local defects due to fabrication error and/or accidental damage may be included in a CODSTRAN simulation.

5. Fracture toughness parameters such as the structural fracture load and the ultimate load are identifiable for any structure by the demonstrated method. It is also useful to carry out CODSTRAN simulations prior to physical testing to guide the data acquisition strategy and to enable the detailed interpretation of experimental results with regard to damage initiation/progression mechanisms and damage tolerance.

6. The availability of CODSTRAN facilitates composite structural design and certification by allowing the efficient and effective evaluation of design options.

7. Computational simulation by CODSTRAN represents a new global approach to progressive damage and fracture assessment for any structure.

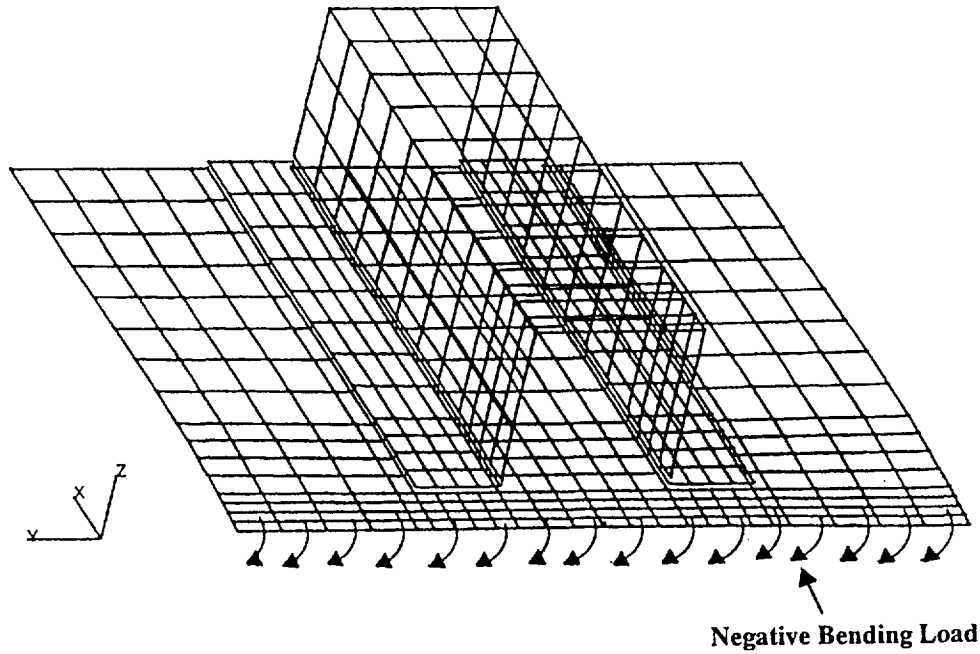

Figure 21.1: Stiffened Composite Panel Finite Element Model; AS-4/HMHS$[[0/\pm 45/90]_s]_6$

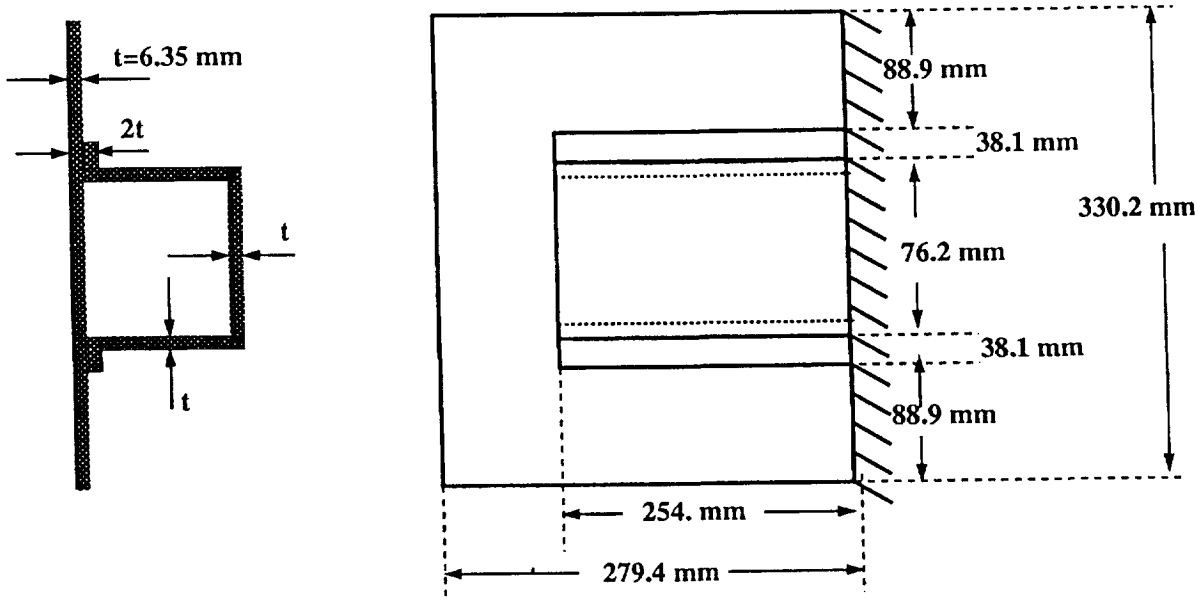

Figure 21.2: Stiffened Composite Panel; AS-4/HMHS$[[0/\pm 45/90]_s]_6$; Cross Section and Plan (All dimensions are in mm)

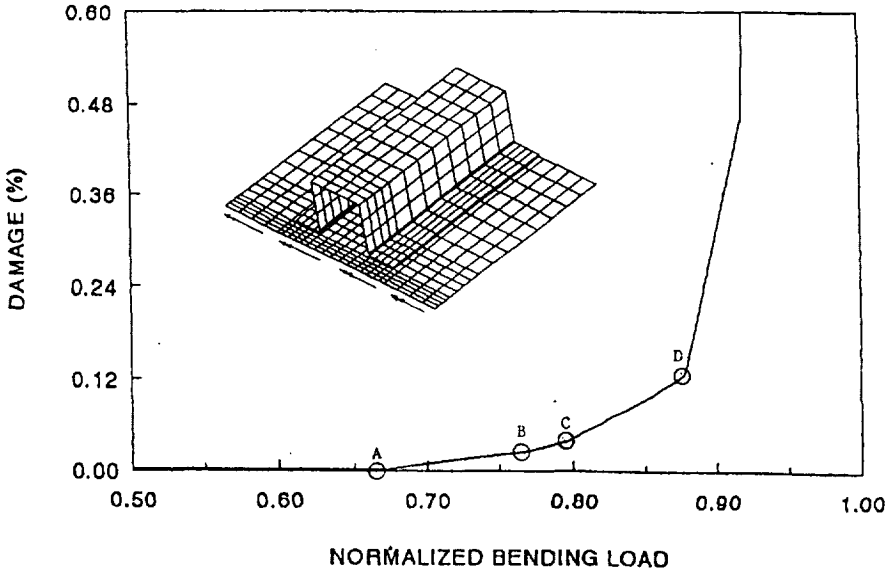

Figure 21.3: Damage Initiation and Growth under Bending Load; AS-4/HMHS$[[0/\pm 45/90]_s]_6$

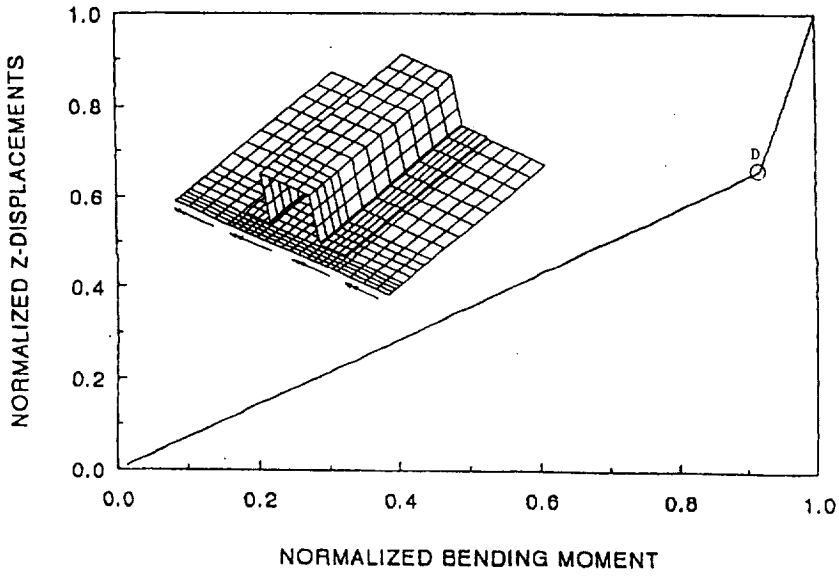

Figure 21.4: Displacements due to Bending; AS-4/HMHS$[[0/\pm 45/90]_s]_6$

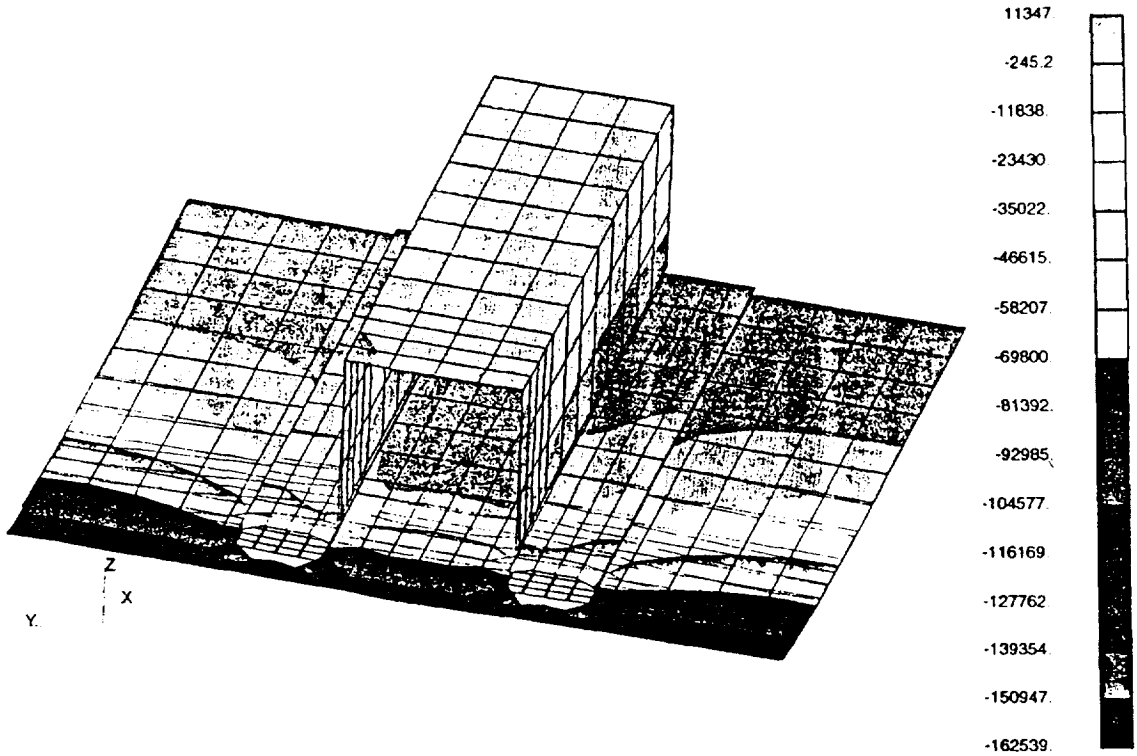

Figure 21.5: Ply 1 Longitudinal Stress Contours (psi) after Initial Damage Growth; AS-4/HMHS$[[0/\pm 45/90]_s]_6$

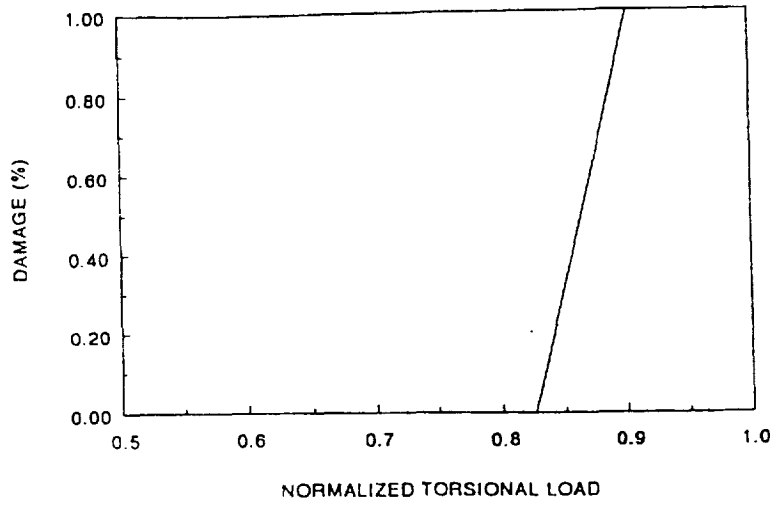

Figure 21.6: Damage Progression under Torsional Load; AS-4/HMHS$[[0/\pm 45/90]_s]_6$

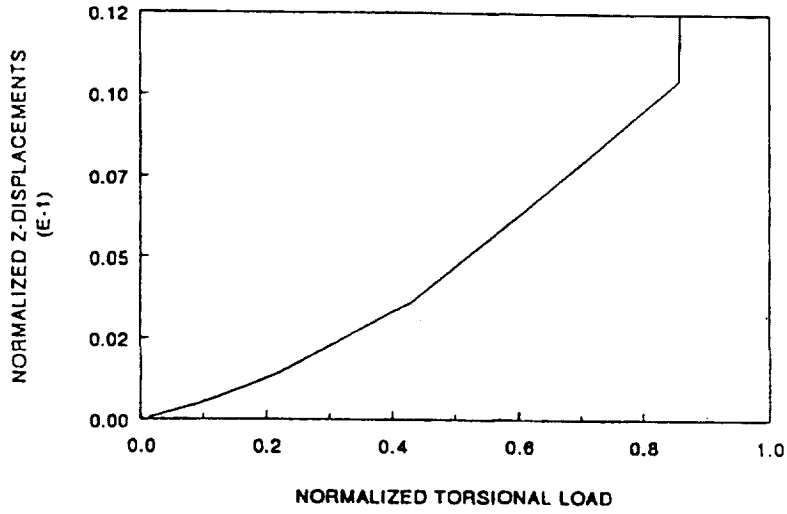

Figure 21.7: Displacements due to Torsion; AS-4/HMHS$[[0/\pm 45/90]_s]_6$

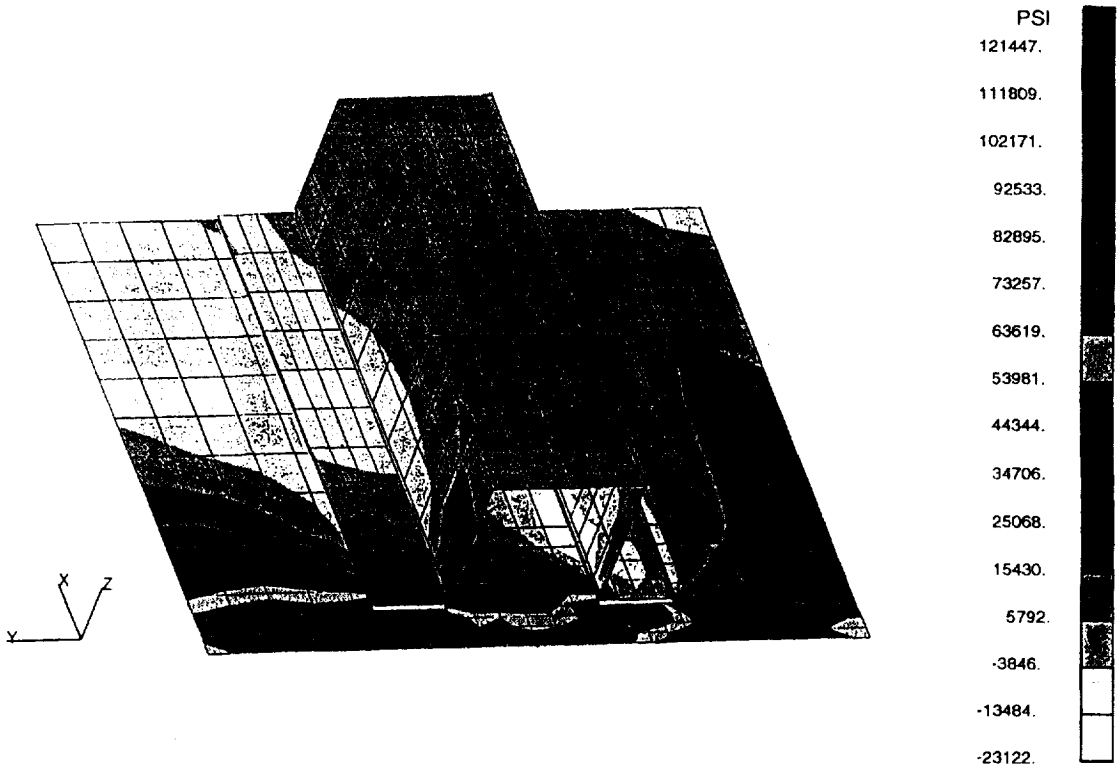

Figure 21.8: Ply 1 Longitudinal Stress Contours (psi) under Torsion; AS-4/HMHS$[[0/\pm 45/90]_s]_6$

Chapter 22

Progressive Fracture in Adhesively Bonded Concentric Cylinders

Progressive damage and fracture of an adhesively bonded graphite/epoxy thin composite shell is evaluated via computational simulation. CODSTRAN is used for the simulation of composite degradation under loading. Damage initiation, growth, accumulation, and propagation to fracture are included in the simulation. Results show the damage progression sequence and structural fracture resistance during different degradation stages. Design implications with regard to damage tolerance of thin walled composite cylindrical shell joints are examined. Influence of the type of loading as well as ply layup and local geometry on damage initiation and progression is investigated.

22.1 Introduction

Thin composite shells have tremendous advantages of light weight, high strength, durability, and corrosion resistance. However, in many cases structural interaction between plies with different fiber orientations adversely affects durability, especially at a joint. Concerns for safety and survivability of a pipe joint require a quantification of the composite structural fracture resistance under loading. The current chapter is focussed on a thin composite pipe joint subject to internal pressure. Damage initiation, growth, accumulation, and propagation to fracture is simulated.

Graphite/epoxy composite shells have found extensive use as pipes and pressure vessels. Composite shells may be subject to internal/external pressures, tension, and flexure loads. In general, the controlling design load is pressurization. However, for thin composite shells, combined bending with pressure becomes important. The objective of this chapter is to present an integrated computational method that evaluates the effects of loading, load combinations, local geometry, and laminate configuration on the durability of a jointed thin composite cylindrical shell.

22.2 Cylindrical Shell Joint

A graphite/epoxy laminated thin composite shell with a circumferential lap joint is considered. The composite system is made of AS-4 graphite fibers in a high-modulus, high strength (HMHS) epoxy matrix. The fiber and matrix properties are obtained from a databank of composite constituent material properties resident in CODSTRAN (11). The corresponding fiber and matrix properties are given in Appendix A. The HMHS matrix properties are representative of the 3501-6 resin. The fiber volume ratio is 0.60 and the void volume ratio is 1 percent. The cure temperature is 177°C (350°F) and the use temperature is 21°C (70°F). The adhesive bond at the joint is assumed to have the same properties as the HMHS epoxy matrix.

The specimen is built by joining two cylinders where one of the cylinders fits exactly inside the other cylinder concentrically at the joint. Each segment of the shell has a length of 305 mm (12 in.). The inside diameter of the inner shell is 254 mm (10 in.). The length of axial overlap at the joint is 51 mm (2 in.). Figure 22.1 shows a schematic of the specimen considered. The specimen has an overall length of 559 mm (22 in.) as shown in Figure 22.1. To evaluate possible local effects on structural degradation, edges of the joint are tapered axially as shown in Figure 22.2. Two values of the slope s at the taper are considered in this investigation. At first a relatively steep taper slope of s=2 is assumed. Five closely spaced nodes are taken in the axial direction at the taper to enable accurate assessment of stress concentration effects. The number of circumferential nodes is 32. The overall finite element model of the specimen contains 704 nodes and 672 quadrilateral elements.

The jointed specimen is first investigated under internal pressure. The composite shell is simulated as a closed-end cylindrical pressure vessel by applying a uniformly distributed axial tension such that the generalized axial stresses in the shell wall are half those developed in the hoop direction. The tube is subjected to an internal pressure that is gradually increased through different stages of degradation. Damage progression is computationally simulated as the loading is increased.

For the first specimen the laminate consists of 12 plies that are configured as $[90/\pm 20]_4$ with a total thickness of 1.68 mm (0.066 in). The $\pm 20°$ angle plies are helically wound around the cylinder and their orientation is given with respect to the axial direction. The 90° plies are oriented in the circumferential direction.

Damage initiation occurs by matrix cracking of the innermost $\pm 20°$ plies due to transverse tensile failures. The location of initial damage is within the smaller diameter shell near the overlapping joint. The internal pressure at damage initiation is 1.32 MPa (192 psi). After damage initiation, damage growth is due to spreading of the transverse tensile failures to other $\pm 20°$ plies on both sides of the shell joint. At a pressure of 2.03 MPa (295 psi) damage begins progression to the 90° or circumferential plies. Through-the thickness fracture occurs at a pressure of 3.94 MPa (571 psi).

To investigate the effects of combined pressurization and bending, the same specimen is subjected to a flexural load that increases in proportion to internal pressure. The ratio of bending load to pressure is taken to be 0.328 N-mm/Pa (20 in-lbs/psi). The results indicate

the presence of flexural load to have a detrimental effect on durability and damage tolerance.

In general, overall structural damage may include individual ply damage and also through-the-thickness fracture of the composite laminate. CODSTRAN is able to simulate varied and complex composite damage mechanisms via evaluation of the individual ply failure modes and associated degradation of laminate properties. The type of damage growth and the sequence of damage progression depend on the composite structure, loading, material properties, and hygrothermal conditions. A scalar damage variable, derived from the total volume of the composite material affected by the various damage mechanisms is also evaluated as an indicator of the level of overall damage induced by loading. This scalar damage variable is useful for assessing the overall degradation of a given structure under a prescribed loading condition. The rate of increase in the overall damage during composite degradation may be used as a measure of structural propensity for fracture. Computation of the overall damage variable has no interactive feedback on the detailed simulation of composite degradation. The procedure by which the overall damage variable is computed is given in Reference 7. In this paper, the composite structure is defined to be 100 percent damaged when all plies of all nodes develop some damage. Usually, structural fracture will occur near a stress concentration before the 100 percent damage level is reached.

Figure 22.3 shows the damage progressions with increasing internal pressure, with and without bending. When bending is present, the damage initiation stage moves to a very early loading stage and the fracture pressure is approximately one third of that for pressurization without bending. More detailed examination would indicate that bending induces local buckling of the thin shell adjacent to the lap joint.

Next, the same specimen is considered to have a less steep taper of s=0.5 to assess the possible effects of local stress concentrations. Figure 22.4 shows a comparison of results for taper slopes of s=2 and s=0.5. In Figure 22.4 the solid lines correspond to s=2 and the dashed lines correspond to s=0.5. Results indicate that the general characteristics of structural damage initiation and progression stages are not changed much by softening the slope at the taper. The overall structural effects have a much more significant influence on damage progression as compared to local stress concentrations.

A closer investigation of the stress state in the tapered end of the joint is of interest. Figure 22.5 shows the hoop stress variations of the inner and outer hoop plies at an internal pressure of 1.14 MPa (165 psi) prior to damage initiation. Distance along the taper is measured from the base reference toward the thicker part of the joint. The taper length is 3.353 mm (0.132 in.). Figure 22.5 indicates that hoop stresses are lower in the taper but high in the single thickness shell adjacent to the joint. The inner ply stresses are considerably higher compared to the outer ply stresses. Figure 22.6 shows the axial stresses that are the transverse stresses for the hoop plies. These stresses are raised within the taper. Another raised stress at the taper is the shear stress in the $\pm 20^{\circ}$ angle plies as shown in Figure 22.7. However the shear stress levels are too low to affect durability. Figure 22.8 shows the hoop stresses at the taper under combined bending and pressure loading prior to damage. The internal pressure for Figure 22.8 is 68.9 KPa (10 psi) and the corresponding bending load is 22.6 N-m (200 in-lbs). In this case the hoop stresses within the taper are raised. Fig-

ure 22.9 shows the corresponding axial stresses that are approaching the critical levels of ply transverse strength.

To investigate the effect of laminate configuration on durability, a specimen with the same geometry but made of a cross-ply laminate is subjected to internal pressure. The ply layup is $[0/90]_4$. The overall damage progression is shown in Figure 22.10 in comparison with the $\pm 20°$ angle ply laminate. For the cross ply laminate the damage initiation stage is delayed, yet the final structural fracture stage is quickened, indicating a lower damage tolerance for the cross-ply laminate.

22.3 Conclusions

In the light of the durability investigation of the example jointed composite shell specimen and from the general perspective of the available CODSTRAN (COmposite Durability STRuctural ANalysis) computer code, the following conclusions are drawn:

1. Computational simulation, with the use of established composite mechanics and finite element modules, can be used to predict the influence of local joint geometry as well as loading, on the safety and durability of thin composite cylindrical shells.

2. Damage initiation, growth, and accumulation stages involve matrix cracking as well as fiber fractures in the thin composite shell contiguous to the joint region.

3. Under flexural loading, a much lower internal pressurization hastenes the damage initiation and fracture of the shell.

4. Changes in the local geometry such as the taper slope have only a minor effect on the structural durability characteristics.

5. Cross-ply laminates have better performance with regard to damage initiation but are not damage tolerant when compared to angle ply laminates.

6. The demonstrated procedure is flexible and applicable to all types of constituent materials, structural geometry, and loading. Hybrid composites and homogeneous materials, as well as binary composites can be simulated.

7. Fracture toughness parameters such as the structural fracture load and damage progression characteristics are identifiable for any structure by the demonstrated method.

8. Computational simulation by CODSTRAN represents a new global approach to progressive damage and fracture assessment for any structure.

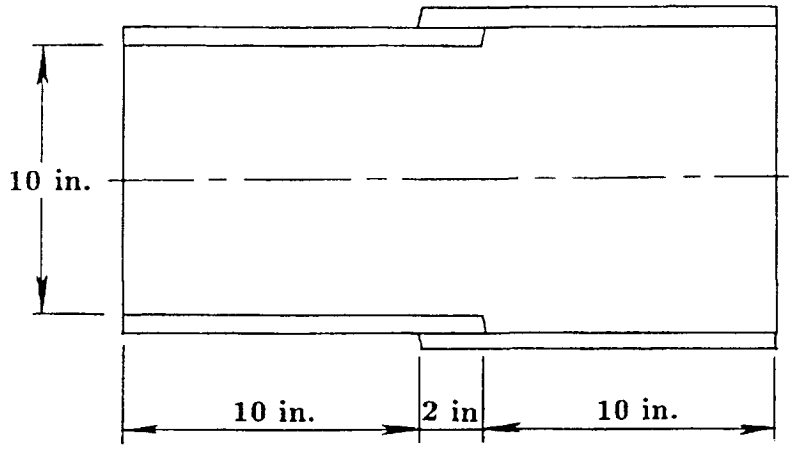

Figure 22.1: Concentrically Bonded Thin Composite Shells; Graphite/Epoxy:$[90/\pm 20]_4$

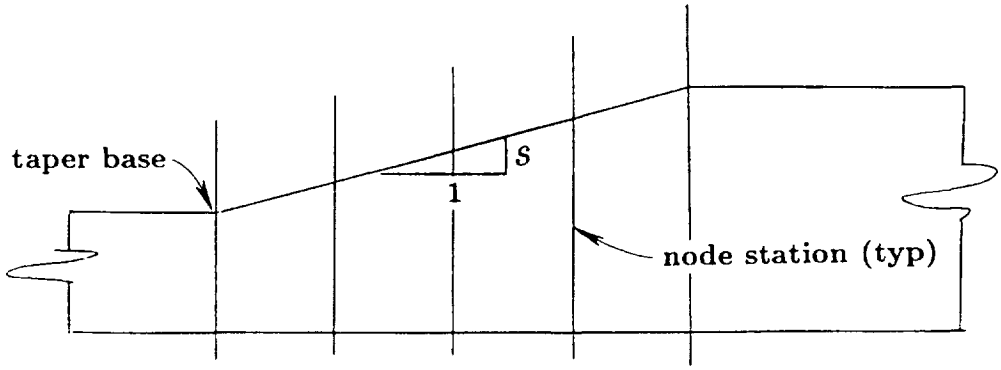

Figure 22.2: Geometry of Taper; Graphite/Epoxy:$[90/\pm 20]_4$

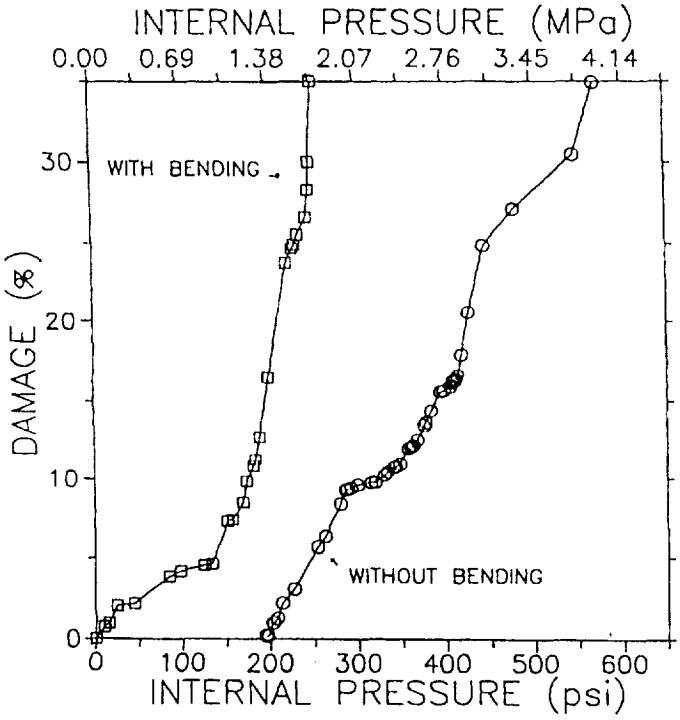

Figure 22.3: Damage Progression with Pressure; Graphite/Epoxy:$[90/\pm 20]_4$

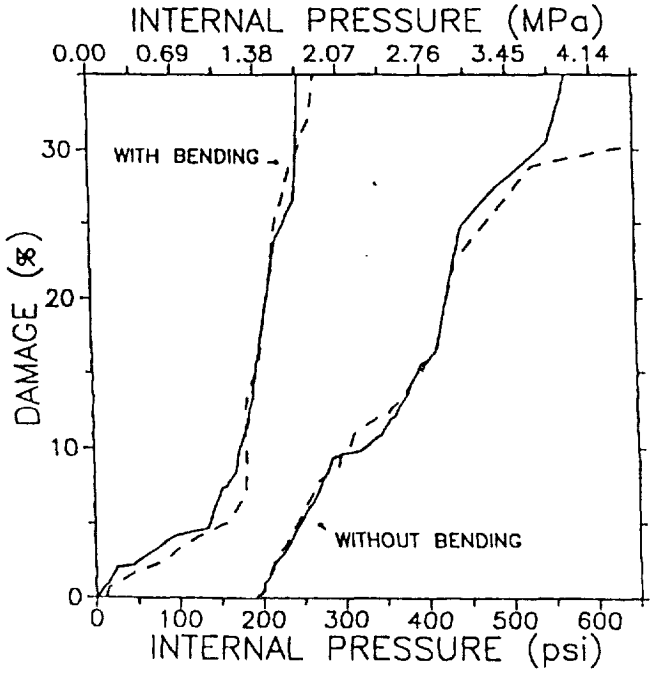

Figure 22.4: Effect of Taper Angle on Damage Progression; Graphite/Epoxy:$[90/\pm 20]_4$

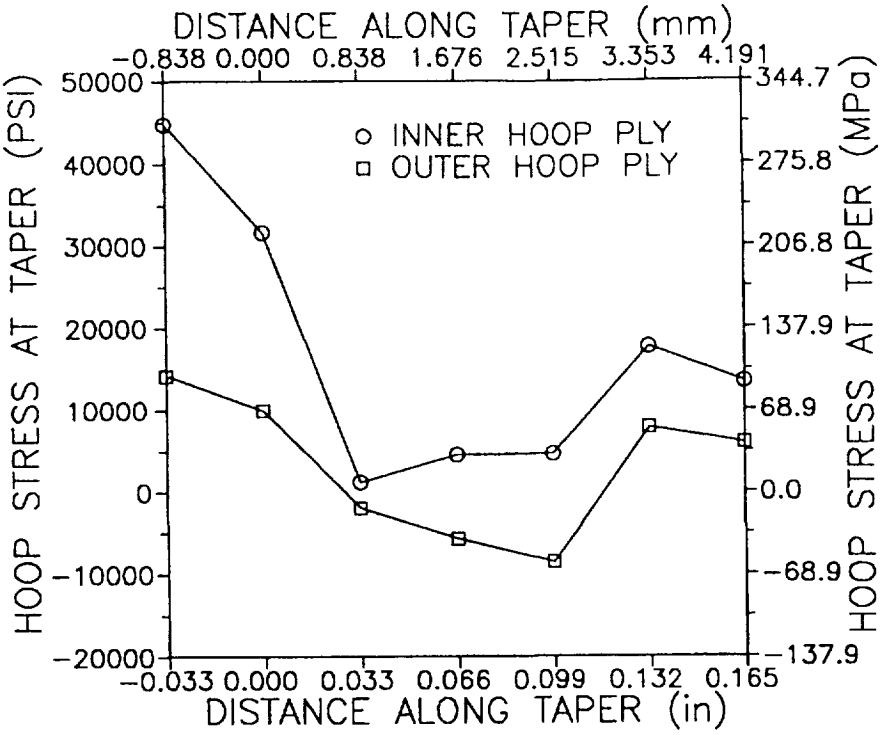

Figure 22.5: $\sigma_{\ell 11}$ Hoop Stresses in 90° Plies; Graphite/Epoxy:$[90/\pm 20]_4$ Pressure Only

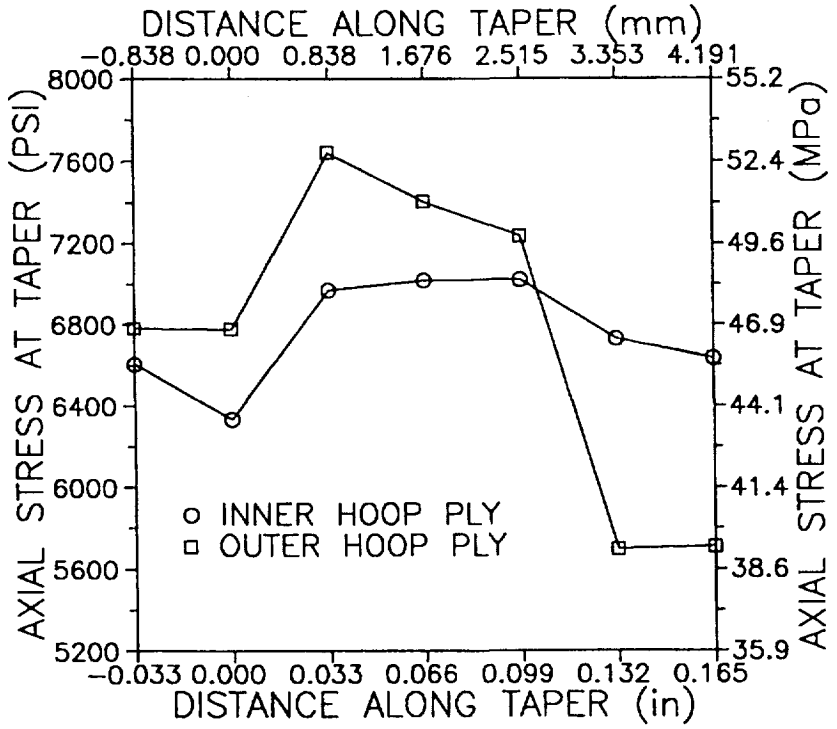

Figure 22.6: $\sigma_{\ell 22}$ Axial Stresses in 90° Plies; Graphite/Epoxy:$[90/\pm 20]_4$ Pressure Only

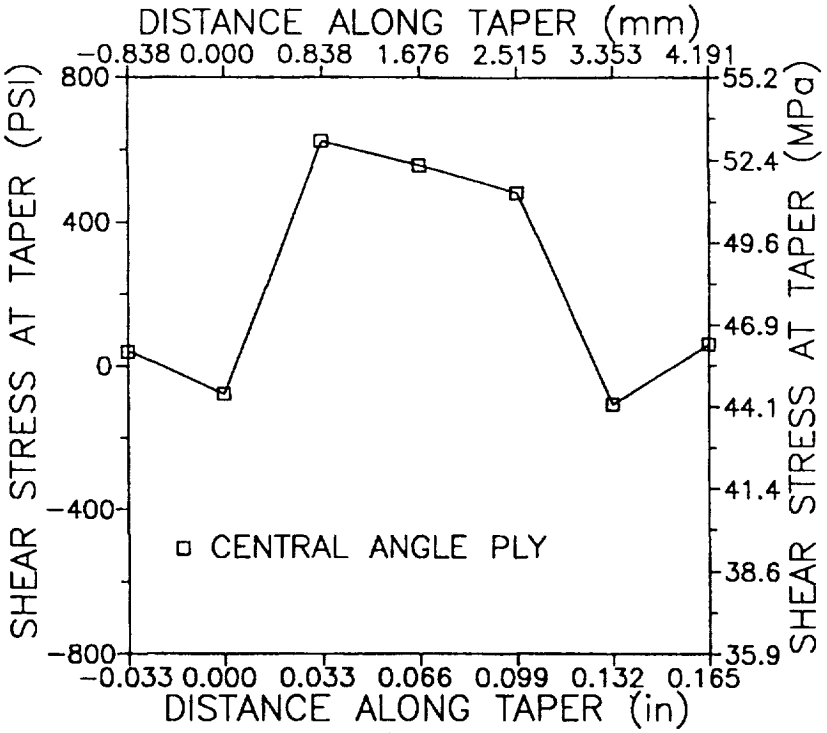

Figure 22.7: $\sigma_{\ell 13}$ Shear Stresses in $\pm 20°$ Center Ply Graphite/Epoxy:$[90/\pm 20]_4$ Pressure Only

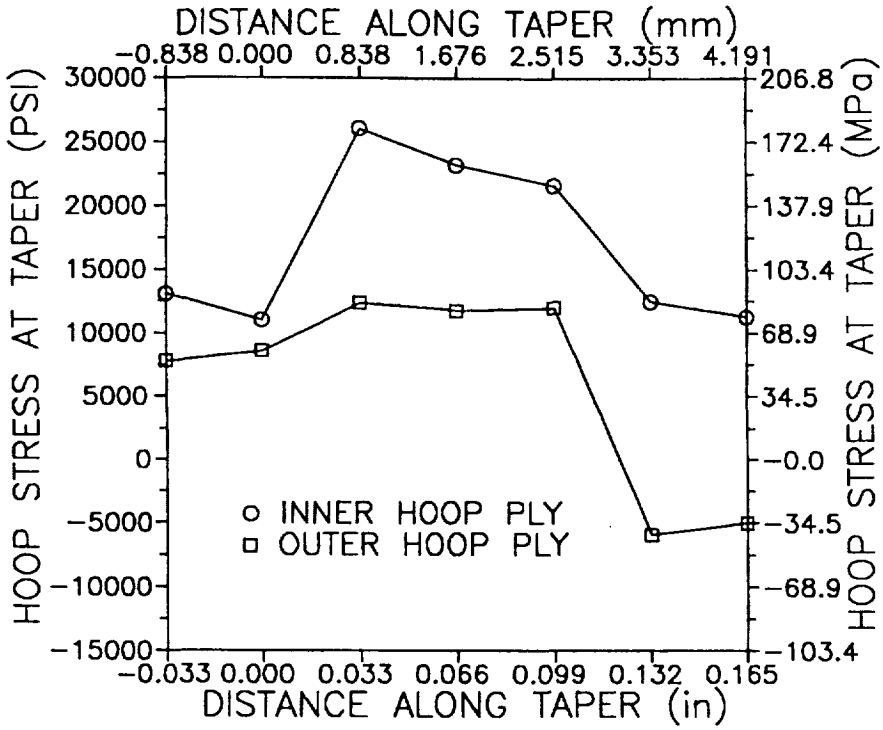

Figure 22.8: $\sigma_{\ell 11}$ Hoop Stresses in 90° Plies; Graphite/Epoxy:$[90/\pm 20]_4$ Pressure and Bending

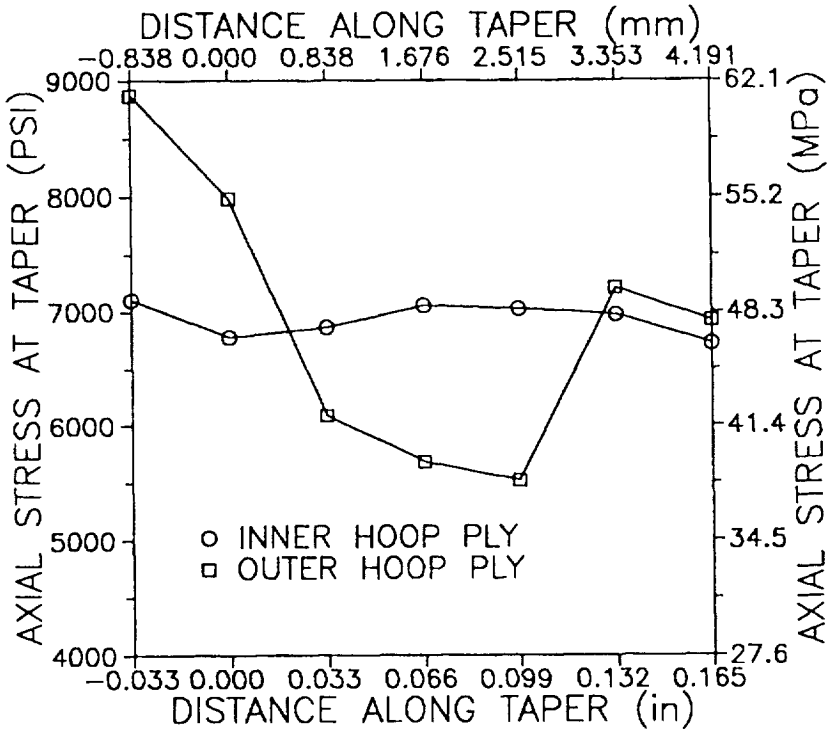

Figure 22.9: $\sigma_{\ell 22}$ Axial Stresses in 90° Plies; Graphite/Epoxy:$[90/\pm 20]_4$ Pressure and Bending

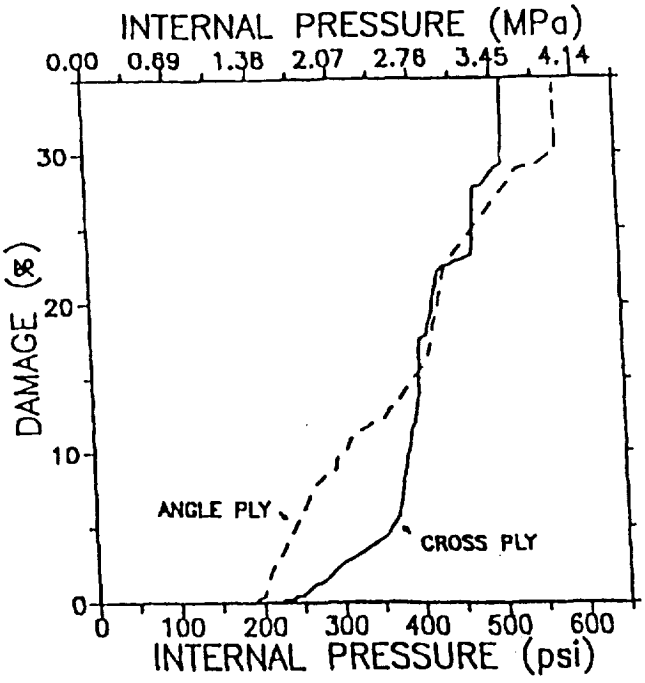

Figure 22.10: Damage Progression with Pressure; Graphite/Epoxy:$[90/\pm 20]_4$ and $[0/90]_4$

Chapter 23

The C(T) Specimen in Laminated Composites Testing

Use of the compact tension C(T) specimen in laminated composites testing is investigated by considering two examples. CODSTRAN is used to evaluate damage propagation stages as well as the structural fracture load. Damage initiation, growth, accumulation, progressive fracture, and ultimate fracture modes are identified. Specific dependences of C(T) specimen test characteristics on laminate configuration and composite constituent properties are quantified.

23.1 Nomenclature

$E_{\ell ii}$ - composite modulus in direction i
$K_{\ell 12\alpha\beta}$ - directional interaction factor
$S_{\ell ij\alpha}$ - composite stress limit corresponding to sign of stress α
$\sigma_{\ell ij}$ - ply stress in material directions ij
$\nu_{\ell ij}$ - Poisson's ratio with respect to directions ij

23.2 Introduction

Design considerations with regard to the durability of fiber composite structures require an a priori evaluation of damage initiation and fracture propagation mechanisms under expected loading and service environments. Concerns for safety and survivability of critical components require a quantification of the structural fracture resistance under loading.

Inherent flexibilities in the selection of constituent materials and the laminate configuration make composites more capable of fulfilling structural design requirements. However, those same design flexibilities render the assessment of composite structural response and durability more elaborate, prolonging the design process. It is difficult to design and certify a composite structure because of the complexities in predicting the overall congruity and performance of

fibrous composites under various loading and hygrothermal conditions.

Laminated composite design practice has been based on extensive testing with attempts to apply formal fracture mechanics concepts to interpret test results. In certain cases interpretation of laminated composite test data via fracture mechanics has been satisfactory. However, in most cases fracture mechanics methods have significantly underpredicted the strength of fiber composites. Reconciliation of test results with fracture mechanics has required significant modifications of effective fracture toughness and specific laminate configuration dependent effective stress concentration field parameters. Additionally, required adjustments of fracture mechanics parameters have had to be reassessed with every change in constituent and laminate characteristics.

The proposed ASTM standard E24.07.02 on the translaminar fracture of composites includes C(T) specimen testing to generate experimental data with regard to crack propagation, similar to E399 standard for metals. However, even when C(T) test data were available for a given laminate, many questions on the damage progression characteristics would not be easily answered and sensitive material parameters would be difficult to identify. The complete evaluation of laminated composite fracture requires an assesment of ply and subply level damage/fracture processes.

The present approach by-passes traditional fracture mechanics to provide an alternative evaluation method, conveying to the design engineer a detailed description of damage initiation, growth, accumulation, and propagation that would take place in the process of ultimate fracture of a fiber composite structure. Results show in detail the damage progression sequence and structural fracture resistance during different degradation stages. This chapter demonstrates that computational simulation, with the use of established material modeling and finite element modules, adequately tracks the damage growth and subsequent propagation to fracture for fiber composite C(T) specimens.

23.3 Graphite/Epoxy Specimen

The structural example for this case consists of a C(T) specimen made of AS-4 graphite fibers in a low modulus high strength (LMHS) toughened epoxy matrix. The fiber and matrix properties are obtained from a databank [11] of composite constituent material properties resident in CODSTRAN. The corresponding fiber and matrix properties are given in Appendix A. The LMHS matrix properties were representative of the 977-2 resin. The 977-2 toughened epoxy resin matrix has been designed for space applications since it does not become brittle at low temperatures. At room temperatures the stress limits are comparable to those of usual epoxy resin. However, the straining capability is considerably higher and the material is less stiff than standard epoxy resin.

The fiber volume ratio was 60 percent. The laminate structure consisted of thirty-six 0.133 mm (0.00525 in.) plies, resulting in a composite thickness of 4.80 mm (0.189 in.). The laminate configuration was $[0_2/90]_{6s}$. The 0° plies were in the direction of loading and the 90° plies were perpendicular to the load direction. The C(T) specimen, as shown in Figure 23.1, had a height of 2H=30 mm (1.18 in), an effective width (distance between load line and

back face) of W=25.0 mm (0.984 in), a notch slot height of 2h=0.3 mm (0.012 in), and a distance between load line and notch tip of a=12.5 mm (0.492 in). A computational model of the specimen was prepared using 420 rectangular thick shell elements with 467 nodes as shown in Figure 23.2. Pin holes were not modeled in the finite element representation of the specimen to enable nodal support and loading. The finite element model was configured to have a nodal point at the center of each pin hole. One of the load points was restrained in all degrees of freedom except for θ_z. The other load point was restrained only in the D_y, D_z, θ_x, θ_y directions but allowed freedom in D_x, and θ_z directions. A concentrated tensile load was applied in the D_x direction. The load was increased gradually.

Figure 23.3 shows N_x generalized stress contours under a 1,779 N (400 lbs) loading, prior to damage initiation. The generalized stresses are defined as the through-the-thickness stress resultants per unit width of the laminate. The maximum tensile stresses were concentrated at the tip of the preexisting notch. These generalized N_x tensile stresses produce longitudinal tension in the 0° plies and transverse tension in the 90° plies. There was a distinct compression zone at the back of the specimen opposite the notch due to compressive N_x stresses.

Figure 23.4 shows N_y generalized stress contours under the 1,779 N (400 lbs) loading. The maximum tensile stresses were concentrated at the tip of the preexisting notch. The tensile N_y stresses produce longitudinal tension in the 90° plies and transverse tension in the 0° plies. There were also distinct compression zones at the top and bottom of the specimen above and below the notch tip due to compressive N_y stresses.

Figure 23.5 shows N_{xy} generalized shear stress contours under the 1,779 N (400 lbs) loading. The maximum shear stresses were concentrated at half-way between the notch tip and back corners of the specimen. The N_{xy} shear stresses produce in-plane shear stresses in both the 0° plies and the 90° plies.

Generalized stress contours with stress concentrations shown in Figures 23.3, 23.4, and, 23.5 indicate possible locations of damage initiation and progression. In a traditional fracture mechanics approach the stress concentrations at the notch tip would be modeled as singularities to calibrate the fracture toughness. In the present computational simulation approach effects of the through-the-thickness generalized stresses were assessed by evaluating ply local stresses and stress limits in a composite mechanics module via laminate theory and ply micromechanics equations. Modeling the degradation of composite properties at the notch tip and elsewhere via computational simulation enabled the assessment of damage progression modes, without the assumption of a through-the-thickness stress singularity based on original material properties. Computational simulation showed damage initiation at 2,091 N (470 lbs) due to transverse tensile failures in the 90° plies at the notch tip. Damage growth continued gradually at the vicinity of the notch tip by transverse tensile failures of both the 90° plies as well as the 0° plies until a load of 3,114 N (700 lbs) was reached. It should be noted that transverse tensile failures in the 90° plies were caused by N_x generalized stresses whereas transverse tensile failures in the 0° plies were caused by the N_y generalized stresses. Above 3114 N (700 lbs) new damage zones were formed due to compressive failures of 0° plies at the back face and in-plane shear failures half way between the notch tip and back corners of the specimen.

Compressive failures of the 0° plies at the back face began at the surface of the specimen. The ply compressive failures were in the compressive shear mode, mainly controlled by matrix shear strength and shear modulus. This mode of failure is also called delamination failure [11] as it is typically followed by delamination of the failed plies. As plies were failed at critical nodes the corresponding stiffness associated with the failure modes were reduced to zero in the computational model; thereby accounting for stress redistributions through the thickness of the laminate. At 3,745 N (842 lbs) additional damage zones were formed due to new compressive failures of 0° plies at the back face, compressive failures of the 90° plies at the top and bottom, and enlargement of matrix shear failure zones half way between the notch tip and back corners of the specimen. The notch tip remained at its original position as there were no fiber failures at the notch tip. When loading was increased to 3,767 N (847 lbs), damage increased significantly with through-the-thickness fracture of the compression and shear failure zones, but still without notch extension. The simulated ultimate load was reached at 3,870 N (870 lbs) due to the coalescence of shear and compressive damage zones into the notch tip and disintegration of the specimen.

Figure 23.6 shows the physical locations of 1) damage initiation at the notch tip by matrix cracking due to ply transverse tensile $\sigma_{\ell 22T}$ failures, 2) $\sigma_{\ell 12S}$ in-plane shear failures , 3) $\sigma_{\ell 11C}$ longitudinal compression failures in 0° plies at the back face, and 4) $\sigma_{\ell 11C}$ longitudinal compression failures in 90° plies at the sides of the specimen. In-plane shear failures at locations 2 in Figure 23.6, were the most significant factor affecting the overall damage progression characteristics and the ultimate load for this specimen. As the in-plane shear failures caused by the $\sigma_{\ell 12}$ stresses occurred, the matrix stiffness of the failed plies was reduced to zero and the computational simulation cycle was repeated. The diminished shear capacity of the plies with matrix failures caused the stress redistributions that resulted in the longitudinal compressive failures of the 0° plies at the back face of the specimen.

Figure 23.7 shows the damage progression with applied loading, indicating that the rate of damage progression increases considerably after the 3,114 N (700 lbs) loading is exceeded. The scalar damage variable shown in Figure 23.7 is derived from the total volume of the composite material affected by the various damage mechanisms. This scalar damage variable is useful for assessing the overall degradation of a given structure under a prescribed loading condition. The rate of increase in the overall damage during composite degradation may be used as a measure of structural propensity for fracture. Computation of the overall damage variable has no interactive feedback on the detailed simulation of composite degradation. In this paper the overall damage variable is defined simply as the ratio of the volume of damaged plies to the total volume of the composite specimen. The procedure by which the overall damage variable is computed is given in Reference [5].

The global Damage Energy Release Rate (DERR) is defined as the rate of work done by external forces during structural degradation, with respect to the produced damage [5]. DERR can be used to evaluate structural resistance against damage propagation at different stages of loading. Low DERR levels indicate that degradation takes place without a significant resistance by the structure. On the other hand, high DERR levels are due to well defined stages of overall structural resistance to damage propagation. Figure 23.8 shows the DERR as a function of loading, indicating significant DERR levels at damage initiation, at the beginning of the damage propagation phase, and at the ultimate load. The first DERR peak

occurs at damage initiation under a 2,091 N (470 lbs) loading, indicating a well defined damage initiation load. The second peak occurs at a 3,114 N (700 lbs) load, immediately prior to ply longitudinal compressive failures at the back face of the specimen. After this load DERR is reduced to very low levels indicating the specimen exerts no significant resistance against further degradation. The third and final peak occurs at the ultimate load when a significant DERR level is experienced indicating the sudden energy release at the ultimate load.

Figure 23.9 shows load versus the COD displacement, indicating that the damage initiation and growth stages prior to the 3114 N (700 lbs) loading are not discernable from the load-COD relationship for this case. Above the 3114 N (700 lbs) loading, softening of the load-displacement relation is due to extensive damage accumulation, including longitudinal compressive failures of the 0° plies in the back face of the specimen.

A displacement controlled laboratory test reached 3,959 N (890 lbs) at the peak load for this specimen and overall test response was consistent with computational simulations. However, the damage initiation and growth stages were not discernable during test observations. Computational simulation was able to fill in the degradation details that were needed to completely assess fracture characteristics. Computer simulation also indicated that the ultimate load was most sensitive to the matrix shear strength for this specimen.

23.4 Ceramic Matrix Composite Specimen

Progressive fracture of a ceramic matrix fiber composite compact tension C(T) specimen was computationally simulated. The composite system consisted of SiC (Nicalon) fibers in an aluminosilicate glass (1723) matrix. The fiber volume ratio was 45 percent. The laminate structure consisted of twelve 0.213 mm (0.00837 in.) thick plies, resulting in a composite thickness of 2.55 mm (0.100 in.). The laminate configuration was $[0/90]_{3s}$. The C(T) specimen, as shown in Figure 23.10, had a half-height of H=23.95 mm (0.943 in), a width (distance between load line and back face) of W=40.13 mm (1.58 in), a half-height of notch slot of h=1.68 mm (0.066 in), and a distance between load line and notch tip of a=18.12 mm (0.713 in). The specimen complied with ASTM E399 specifications.

The finite element model was made containing 161 nodes and 130 quadrilateral thick shell elements, as shown in Figure 23.11, with 0° plies oriented in the loading direction. As in the previous example, pin holes were not modeled in the finite element representation of the specimen to enable nodal support and loading. The finite element model was configured to have a nodal point at the center of each pin hole. One of the load points was restrained in all degrees of freedom except for θ_z. The other load point was restrained only in the D_y, D_z, θ_x, θ_y directions but allowed free movement in D_x, and θ_z directions. A concentrated tensile load was applied in the D_x direction. The load was increased gradually. Figure 23.12 shows ply 1 (0° ply) longitudinal stress contours under a 445 N (100 lbs) loading, prior to damage initiation. The maximum tensile stresses were concentrated at the tip of the preexisting notch. There was a distinct compression zone at the back face of the specimen opposite the notch.

Test data on the SiC/glass C(T) specimen with the same geometry, composite ply constituents, and symmetric cross-ply laminate configuration was presented in reference [13]. The simulated specimen, with an a/W ratio of 0.452, was modeled after specimen 88C23-6 in reference [13]. Reported observations during experiments indicated the specimen response to loading was in the brittle mode.

Fiber and matrix elastic properties used in the computational simulation were taken from reference [13]. However, reference [13] did not report the constituent material strengths. To enable assessment of damage progression characteristics for the specimen and to evaluate the sensitivity of specimen fracture to fiber strength, an effective in-situ fiber strength of 276 MPa (40 ksi) was calibrated. Calibration of material strength via parametric mapping to enable computational simulation of brittle fracture with a reasonably sized finite element model is detailed in reference [15]. As noted in reference [15], the effective strength σ_e depends on the ratio of the finite element size to the size of the inelastic process zone at the notch tip. The effective strength is obtained by calibrating the specific finite element model with the experimental data. The compressive strength of SiC fibers is expected to be significantly higher than the tensile strength. However, since the fracture of the SiC/glass C(T) specimen was controlled by fiber tensile strength at the notch tip, and no specific compressive strength data was available, fiber compressive strength was assumed to be the same as tensile strength in the computational simulation. Also, since the stress-free temperature was not reported in reference [13], residual stresses were not explicitely modeled in the computational simulation. Therefore, the calibrated strengths used for the simulation of this specimen included the effects of residual stresses due to fabrication temperatures.

The constituent properties used in the computational simulation of progressive fracture were as follows:

SiC (Nicalon) Fiber Properties:

Number of fibers per end = 1
Fiber diameter = 0.012 mm (0.472E-3 in)
Fiber Density = 2.07E-6 Kg/m^3 (0.278 lb/in^3)
Longitudinal normal modulus = 200 GPa (29.0E+6 psi)
Transverse normal modulus = 200 GPa (29.0E+6 psi)
Poisson's ratio (ν_{12}) = 0.30
Poisson's ratio (ν_{23}) = 0.30
Shear modulus (G_{12}) = 77.2 GPa (11.2E+6 psi)
Shear modulus (G_{23}) = 77.2 GPa (11.2E+6 psi)
Longitudinal thermal expansion coefficient = 4.57E-6/°C (2.54E-6 /°F)
Transverse thermal expansion coefficient = 4.57E-6/°C (2.54E-6 /°F)
Longitudinal heat conductivity = 8.08 J-m/hr/m^2/°C (108 BTU-in/hr/in^2/°F)
Transverse heat conductivity = 8.08 J-m/hr/m^2/°C (108 BTU-in/hr/in^2/°F)
Heat capacity = 503 J/Kg/°C (0.12 BTU/lb/°F)
Tensile strength = 276 MPa (40 ksi)
Compressive strength = 276 MPa (40 ksi)

Glass (1723) Matrix Properties:

Matrix density = 6.70E-7 Kg/m^3 (0.090 lb/in^3)
Normal modulus = 85.5 GPa (12,400 ksi)
Poisson's ratio = 0.22
Coefficient of thermal expansion = 6.70E-6/°C (1.21E-5 /°F)
Heat conductivity = 7.5 BTU-in/hr/in^2/°F
Heat capacity = 0.17 BTU/lb/°F
Tensile strength = 207 MPa (30.0 ksi)
Compressive strength = 2.07 GPa (300 ksi)
Shear strength = 207 MPa (30.0 ksi)
Allowable tensile strain = 0.0073
Allowable compressive strain = 0.0073
Allowable shear strain = 0.0124
Allowable torsional strain = 0.0124
Void conductivity = 16.8 J-m/hr/m^2/°C (0.225 BTU-in/hr/in^2/°F)
Glass transition temperature = 816°C (1500°F)

CODSTRAN simulation of the SiC/Glass C(T) specimen indicated a damage initiation load of 667 N (150 lbs). Initial damage was in the form of fiber fractures by longitudinal failure of the 0° plies at the notch tip. When the load was further increased, fiber fractures and matrix cracking due to excessive transverse ply stresses spread to all plies at the notch tip and immediately ahead of it. Computational simulation was carried out to show the details of progressive damage and fracture propagation in the composite structure up to the global fracture of the C(T) specimen. Global fracture was simulated at 1,320 N (297 lbs), breaking the C(T) specimen into two pieces.

Figure 23.13 shows the simulated relationship between structural damage and the applied loading. The damage initiation stage corresponds to the development of a damage zone at the notch tip by longitudinal tensile fractures of the 0° plies. Fiber fractures in the 0° plies were immediately followed by the fracture of the 90° plies. The damage initiation stage was concluded at a 890 N (200 lbs) load by the formation of a damage/fracture zone at the tip of the original notch. After the damage initiation stage, the loading was increased to 1.045 KN (235 lbs) without additional damage. When the load was increased beyond 1.045 KN, damage growth occurred by compressive fractures of the 0° plies at the back face of the specimen opposite the notch. Compressive failure at the back face of the specimen caused, in turn, tensile failures at the damage zone at the notch tip. The process of alternating compressive and tensile failures was continued until the final damage propagation stage was reached when compressive and tensile fracture zones coalesced and the C(T) specimen was broken into two pieces.

Figure 23.14 shows the simulated progression of fracture alternately from the tensile zone at the notch tip and from the compressive zone at the back face of the SiC/Glass specimen. The damage progression stages are labeled in Figure 23.14 in numerical order. Stage 1 corresponds to damage initiation by fiber fractures at the notch tip at 667 N (150 lbs) loading. Stage 2 corresponds to damage progression by fiber fractures and notch extension at 890 N (200 lbs). Stage 3 corresponds to compressive failures (σ_{f11C}) at the back face of specimen under 956-988 N (215-222 lbs). Stage 4 marks additional fiber tensile fractures and notch extension. Stage 5 corresponds to growth of compressive failures from the back of

the specimen. Stage 6 corresponds to additional compressive failure growth accompanied by fiber fractures at the tensile regions under 1,210-1,317 N (272-296 lbs) loading. Immediately following stage 6, global fracture occurs at 1,321 N (297 lbs) as the tensile and compressive failure regions are fully coalesced.

Figure 23.15 shows the DERR as a function of the applied tensile loading on the ceramic matrix fiber composite C(T) specimen. The DERR for damage initiation was relatively small, indicating low resistance to damage initiation under tensile loading. However, after the damage initiation stage, DERR reached considerably higher levels, indicating greater structural resistance against damage propagation prior to global fracture.

Figure 23.16 shows the load versus displacement relationship for the SiC/Glass C(T) specimen. The transition from damage initiation to damage growth is not easily discernible from the load-displacement relationship. However, as the damage propagation stage begins, the load-displacement behavior becomes highly nonlinear. At the structural fracture stage, the displacement increases without any increase in the loading. The global fracture load of 1,320 N (297 lbs) obtained by computational simulation was slightly under the 1,344 N (302 lbs) fracture load observed experimentally, as reported in Reference [13].

Computational simulation also indicated that damage initiation and progression is very sensitive to the fiber tensile strength for this specimen. Figure 23.17 shows the variation in the structural fracture load and the damage initiation load as functions of the fiber tensile strength. In particular, if the fiber strength increases above the 276 MPa (40 ksi) effective strength of SiC fibers, the fracture load increases at a very steep rate. Computational simulation results indicate that if effective fiber strength increases above 276 MPa (40 ksi), the in-plane shear failure mode begins to participate in the progressive fracture process. As the fracture progresses, matrix stiffness degradation due to in-plane shear failures allows a redistribution of fiber stresses ahead of the crack tip, causing a more ductile response. On the other hand, if the effective fiber strength is at or below 276 MPa (40 ksi), fracture progression is mainly controlled by the ply longitudinal fracture mode, accompanied by ply transverse tensile failures. When effective fiber strength was taken as 276 MPa (40 ksi), damage initiation at 150 lbs loading was controlled by Eq. (1), predicting longitudinal tensile failures in 0° plies at the notch tip. After damage initiation, damage growth was controlled by Eq. (7) in the 90° plies. On the other hand, if effective fiber strength were to be increased to 42 ksi, damage initiation and growth would occur at 167 lbs. Both the damage initiation as well as the damage growth modes were controlled by Eq (7). Sensitivity of the fracture progression mode and the resulting ultimate load to fiber strength explains some of the difficulty in fitting experimental data to a traditional fracture toughness parameter for the room temperature fracture of similar ceramic matrix C(T) specimens [13].

23.5 Concluding Remarks

The significant results from this investigation in which computational simulation was used to evaluate damage growth and propagation to fracture for graphite/epoxy and SiC/Glass fiber composite C(T) specimens are as follows:

1. Computational simulation, with the use of established composite mechanics and finite element modules, can be used to predict the influence of an existing notch, as well as loading, on the safety and durability of fiber composite structures.

2. Computational simulation adequately tracks the damage growth and subsequent propagation to fracture for fiber composite C(T) specimens.

3. Computational simulation can be used prior to testing to identify locations and modes of composite damage that need be monitored by proper instrumentation and inspection of the specimen during a laboratory experiment.

4. Interpretation of experimental data can be significantly facilitated by detailed results from a computational simulation.

5. Computational simulation provides detailed information on damage initiation and progression mechanisms, as well as identifying sensitive material parameters affecting structural fracture.

6. The demonstrated procedure is flexible and applicable to all types of constituent materials, structural geometry, and loading. Hybrid composite structures, composites containing homogeneous materials such as metallic layers, as well as binary composites can be simulated.

7. Fracture toughness parameters such as the structural fracture load are identifiable for any specimen or structure by the demonstrated method.

8. Computational simulation represents a new global approach that may be used for progressive damage and fracture assessment in design investigations.

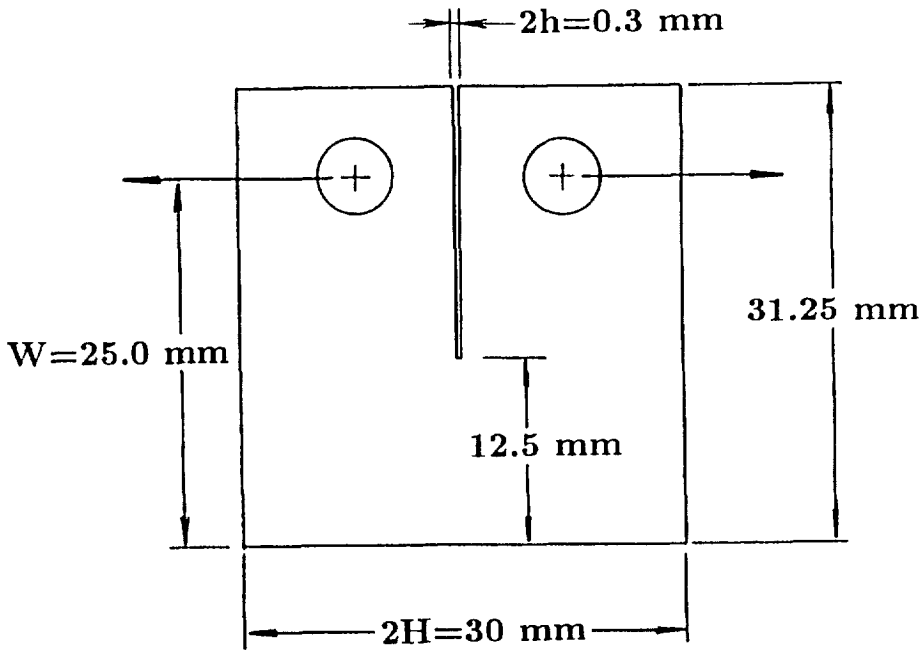

Figure 23.1: Graphite/Epoxy $[0_2/90]_{6s}$ C(T) Specimen: all dimensions are in millimeters; t=4.80 mm (0.189 in.), 2H=30 mm (1.18 in), W=25 mm (0.984 in), 2h=0.3 mm (0.012 in), a=12.5 mm (0.492 in)

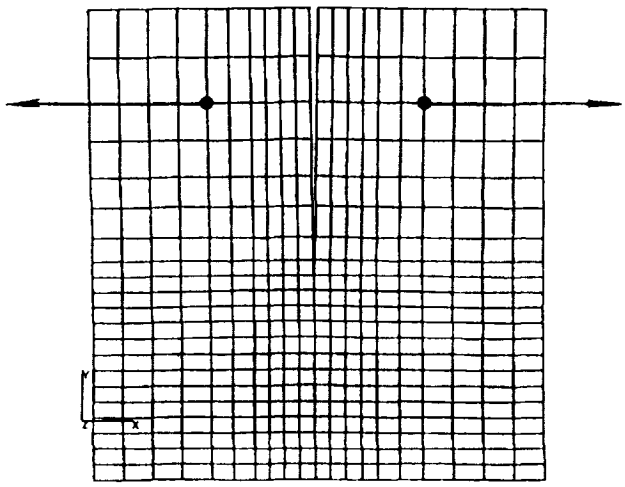

Figure 23.2: Graphite/Epoxy $[0_2/90]_{6s}$ C(T) Specimen Finite Element Model; 467 nodes, 420 quadrilateral elements

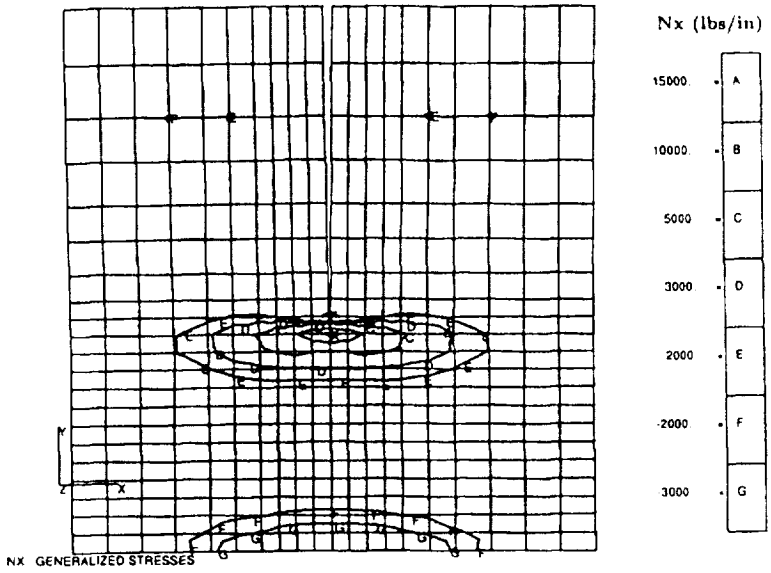

Figure 23.3: N_x Generalized Stresses under 1779 N (400 lbs) Load; Graphite/Epoxy $[0_2/90]_{6s}$ C(T) Specimen

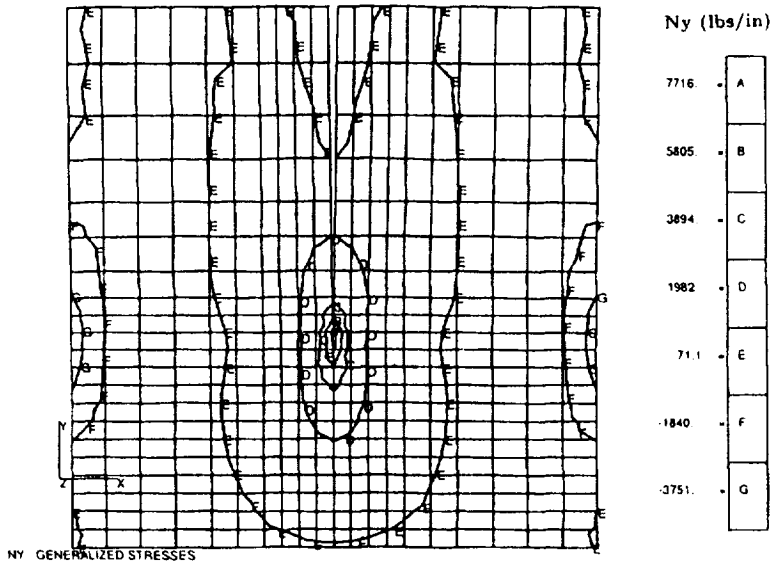

Figure 23.4: N_y Generalized Stresses under 1779 N (400 lbs) Load; Graphite/Epoxy $[0_2/90]_{6s}$ C(T) Specimen

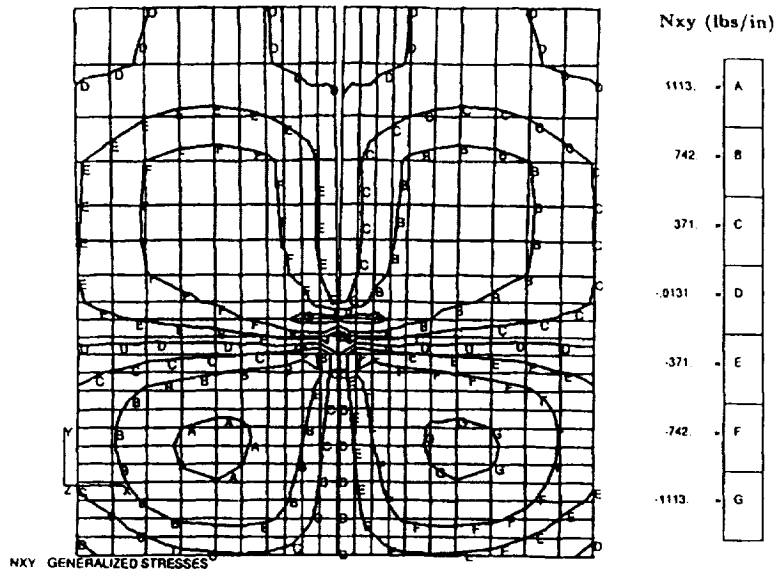

Figure 23.5: N_{xy} Generalized Stresses under 1779 N (400 lbs) Load; Graphite/Epoxy $[0_2/90]_{6s}$ C(T) Specimen

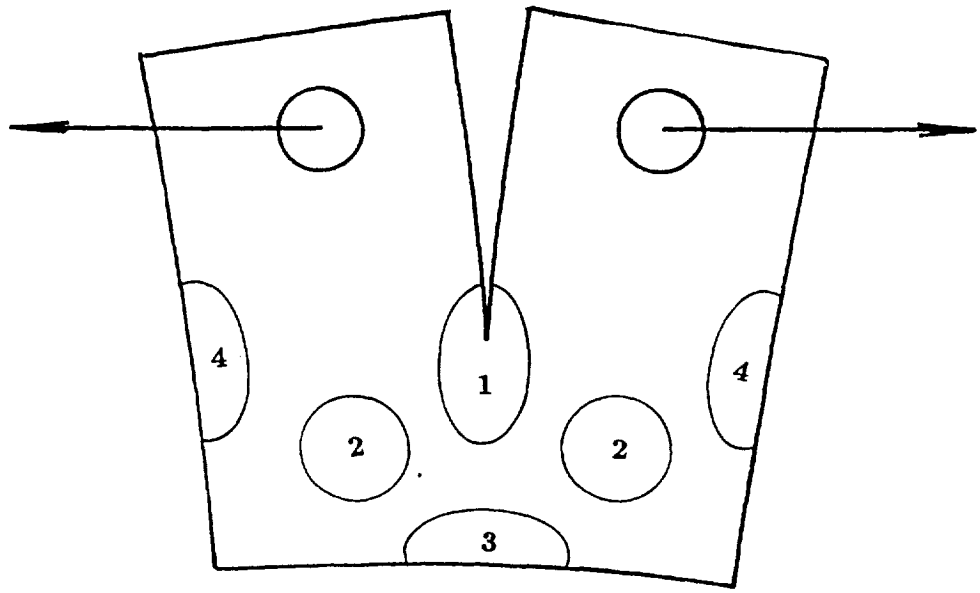

Figure 23.6: Damage Modes and Locations; Graphite/Epoxy $[0_2/90]_{6s}$ C(T) Specimen. 1) Matrix Cracking at the Notch tip; 2) Shear Failure Zones; 3) Compression Failure at the Back Face; 4) Compression Failures at the sides

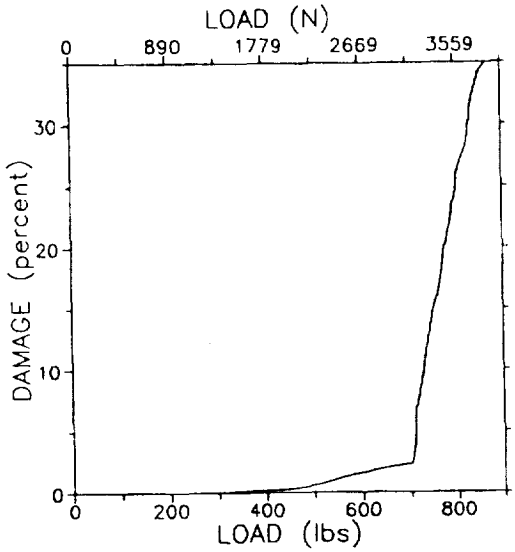

Figure 23.7: Damage Progression with Loading; Graphite/Epoxy $[0_2/90]_{6s}$ C(T) Specimen

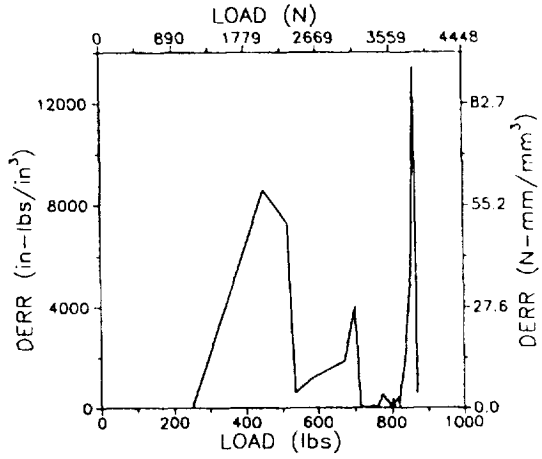

Figure 23.8: Damage Energy Release Rate with Loading; Graphite/Epoxy $[0_2/90]_{6s}$ C(T) Specimen

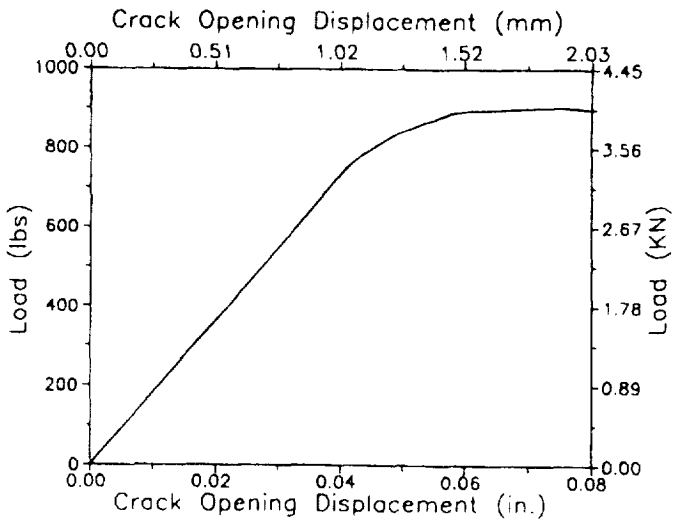

Figure 23.9: Load-Displacement Relationship; Graphite/Epoxy $[0_2/90]_{6s}$ C(T) Specimen

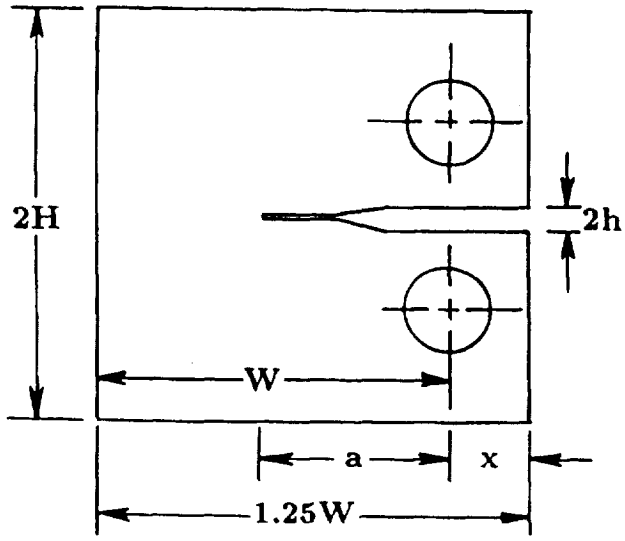

Figure 23.10: Ceramic Matrix Composite C(T) Specimen; t=2.55 mm (0.100 in.), H=23.95 mm (0.943 in), W=40.13 mm (1.58 in); h=1.68 mm (0.066 in), a=18.12 mm (0.713 in)

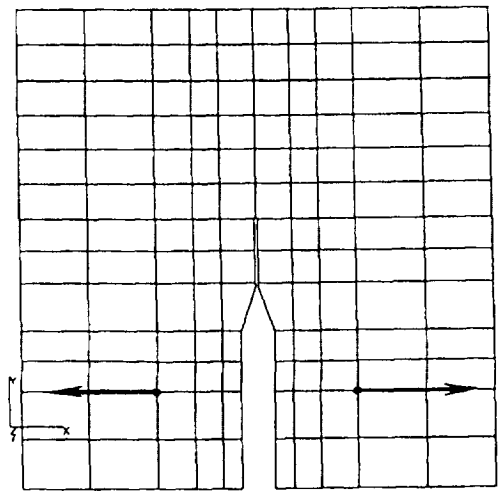

Figure 23.11: Ceramic Matrix Composite C(T) Specimen Finite Element Model; SiC/Glass$[0/90]_{3s}$ 161 nodes, 130 quadrilateral elements

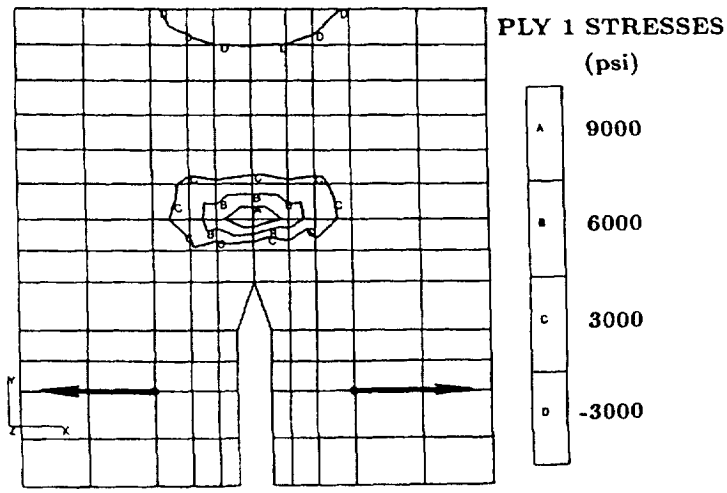

Figure 23.12: Ply 1 $\sigma_{\ell 11}$ Stresses under 445 N (100 lbs) Load; SiC/Glass$[0/90]_{3s}$ C(T) Specimen

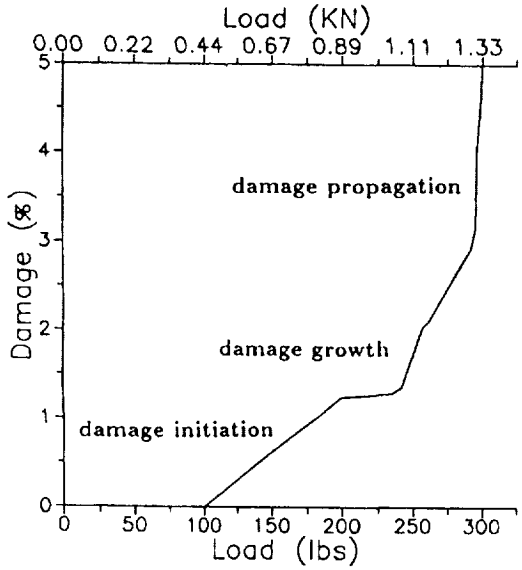

Figure 23.13: Damage Propagation with Loading; SiC/Glass$[0/90]_{3s}$ C(T) Specimen

1. **Damage initiation by fiber fractures at the notch tip (150 lbs)**
2. **Damage progression by fiber fractures and notch extension (200 lbs)**
3. **Compressive failures (σ_{11C}) at the back face of specimen (215-222 lbs)**
4. **Fiber fractures and notch extension (237 lbs)**
5. **Growth of compressive failures at the back of the specimen (237-242 lbs)**
6. **More compressive failure growth accompanied by additional fiber fractures at the crack tip (272-296 lbs)**
7. **Global fracture: specimen breaks (297 lbs)**

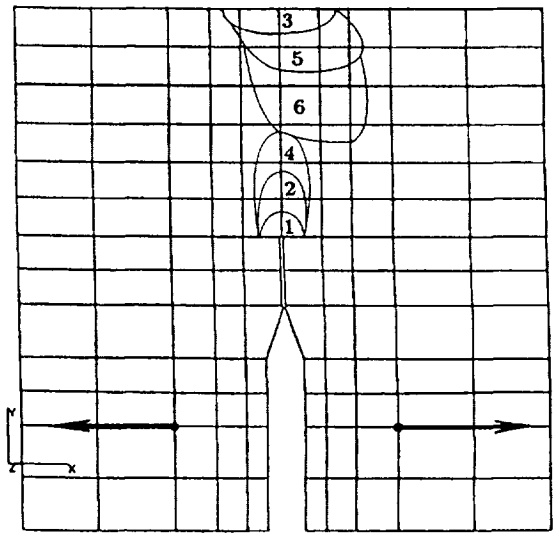

Figure 23.14: Damage Progression Sequence and Locations; SiC/Glass$[0/90]_{3s}$ C(T) Specimen

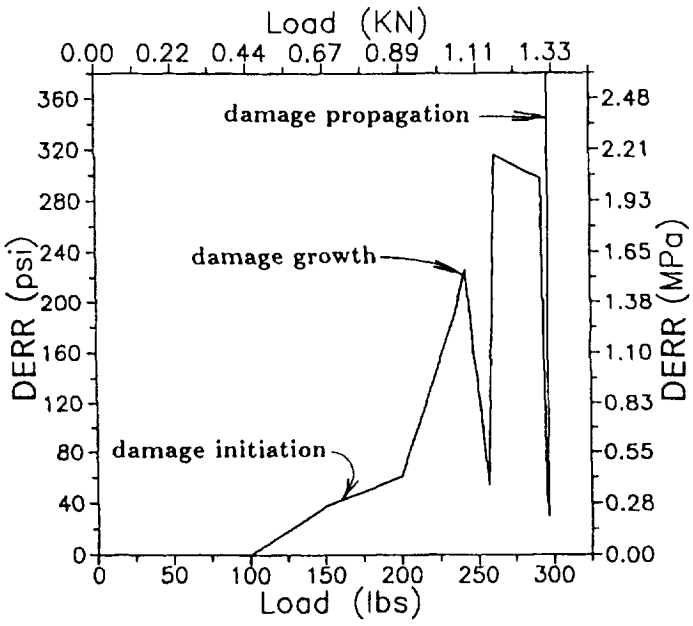

Figure 23.15: Damage Energy Release Rates with Loading; SiC/Glass$[0/90]_{3s}$ C(T) Specimen

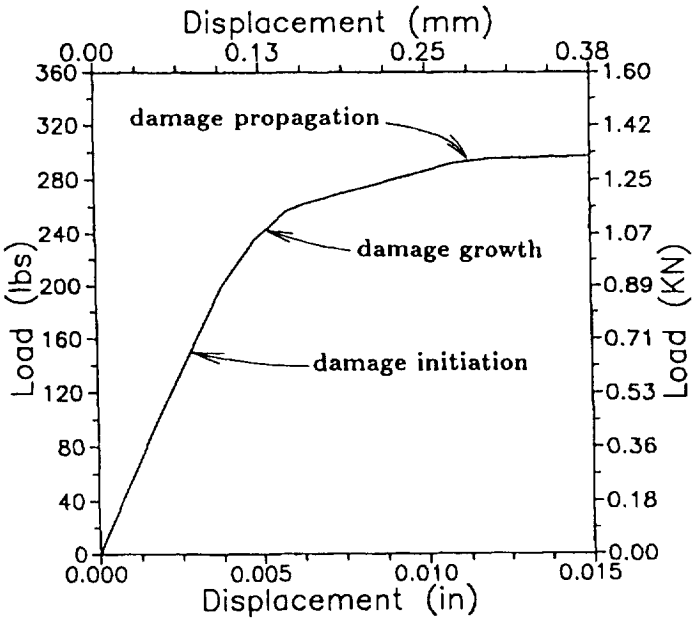

Figure 23.16: Load-Displacement Relationship; SiC/Glass$[0/90]_{3s}$ C(T) Specimen

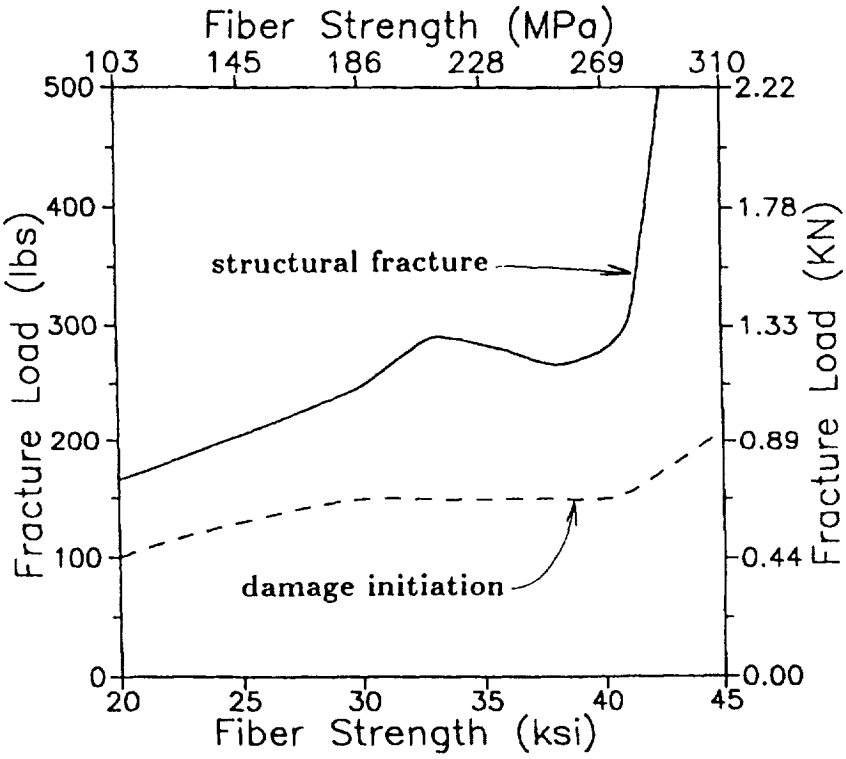

Figure 23.17: Effect of Fiber Strength on Fracture; SiC/Glass$[0/90]_{3s}$ C(T) Specimen

Chapter 24

Pressure Vessel Fracture Simulation

The influence of local defects or flaws and through the thickness cracks on the load carrying capability and structural behavior of steel cylindrical shells subject to internal pressure is investigated. The CODSTRAN computer code is used for the simulation of structural degradation under loading. Damage initiation, growth, accumulation, and propagation to structural fracture are included in the simulation. A mapping method is utilized to accurately simulate damage and fracture progression using a relatively coarse finite element mesh. A thick shell finite element model, subdivided across its thickness to a finite number of layers, is used to enable representation of gradual local damage growth across the shell thickness. Computational results are compared with traditional fracture mechanics for a design case, as well as with experimental data from the literature. The effect of local defects such as flaws and cracks on the durability of pressurized cylindrical shells is examined in detail.

24.1 Nomenclature

c - half length of crack
R - radius of cylindrical shell
s - finite element size at the crack tip
t - shell thickness
β - mapping ratio for computational model
σ_c - calibrated average effective strength for computational model
σ_y - uniaxial yield strength

24.2 Introduction

The design of cylindrical pressure vessels is based on many years of experience and analysis derived from fracture mechanics concepts. Design rules for pressure vessels are based on the experimentally evaluated fracture toughness to quantify the overall resistance against crack propagation for a particular material, crack length/orientation, structural geometry, and the state of stress. The methods of fracture mechanics have been successful in the quan-

tification of failure for pressure vessels due to the consistency of structural geometry. For a given structural geometry and crack size, fracture mechanics is an efficient predictor of the failure load based on an experimental calibration under similar conditions. However, when structural geometry and the state of stress are significantly different for the experimental calibration and for the structure to be designed, the use of fracture mechanics methodology for design purposes becomes questionable or uncertain, often requiring a new calibration. Also, traditional fracture mechanics does not convey to the design engineer a detailed description of damage initiation, accumulation, and propagation that would take place in the process of the ultimate fracture of a pressure vessel. In order to improve the design congruity and structural safety with regard to damage tolerance, it is helpful to have a quantitative account of the damage initiation and progression process that takes place prior to the global fracturing of a pressure vessel. The mechanisms of damage growth and propagation are important as precursors of ultimate structural fracture. Quantifications of the structural fracture resistance and damage tolerance are also useful in evaluating the safety of pressure vessels.

The COmposite Durability STRuctural ANalysis (CODSTRAN) computer code was originally developed for the simulation of damage initiation, growth, and progression to ultimate fracture for laminated composite structures. The CODSTRAN methodology can also be used for the durability analysis of structures that are made from traditional homogeneous materials such as steel.

24.3 Application to Steel Pressure Vessels

The structural fracture of a steel pressure vessel may be classified into two categories: *1)* ductile and *2)* brittle. Structural ductility is a measure of damage tolerance prior to ultimate fracture. Fracture propagation in a structure may be classified anywhere between the limits of perfectly ductile behavior to perfectly brittle. The ductility or brittleness of fracture as an observed phenomenon depends not only on material properties but also on many diverse factors such as geometry, boundary conditions, crack shape, extent, and orientation. The crack propagation phenomenon is by nature a geometric phenomenon as the existence of the crack itself changes the local deformations and geometry in the vicinity of the crack and influences the damage propagation process. In the traditional fracture mechanics approach, adjustment factors are often required to calibrate fracture predictions depending on structural scale, geometry, boundary conditions, and other effects. In many applications, fracture mechanics is exercised as an overall phenomenological quantifier, based on experimental results. In the present paper all geometric and scale factors are fully taken into account in the computational model. Material properties are the only factors that still require calibration depending on the brittleness of the material and the refinement of the computational model.

The generally accepted fundamental material property for steel is the yield strength under a uniaxial stress state. The local stress levels at the very tip of a crack usually exceed the yield strength during crack propagation for both brittle and ductile type failures. In the case of ductile failure a significant yielding zone develops at the tip of a crack before crack progression. On the other hand, in the case of brittle fracture the size of the yielding zone

is small compared to the size of the crack. Finite element analysis to simulate fracture progression on the basis of the actual yield strength of the material requires a finite element mesh size at the crack tip consistent with the size of the yielding zone. For brittle fracture the required finite element refinement becomes rather demanding on computational resources. To keep computational costs within reason, a coarser finite element mesh can be calibrated for the simulation of fracture progression using an average effective strength, σ_e, that depends on the relative size of the computational model. This effective strength is determined by a mapping parameter, β, that is related to the ratio of the finite element size to the size of the yielding zone at the crack tip. The justification of single parameter ratio mapping to enable accurate structural analysis using a coarse finite element mesh has been examined elsewhere [*14*]. In this paper, the mapping parameter β is defined for the computational model as the ratio of the uniaxial yield strength of the material, to the maximum average effective stress that can be developed in the tributary zone of the node located at the crack tip. The mapping ratio β is always a positive real number. A mapping ratio of less than or equal to unity indicates ductile behavior if the calibrated finite element simulation size s is taken to be equal to the half crack size c. A mapping ratio of zero is the lower limit on β, indicating infinite values of σ_e that would not be possible except in an unrealistic case of unlimited strain hardening and ductility. There is no formal upper limit to β. Calibration of the mapping ratio is carried out experimentally. In the computational simulation of progressive fracture, a common finite element model size s is selected to enable simulation of different size cracks of the same material using the same effective strength σ_e.

For better reliability of the simulation model it is desirable that as much of the damage progression history as possible, from the damage initiation stage to structural fracture, be taken into account in experimental calibration. In many cases, however, test data stops short of structural fracture, or a statistically representative set of test cases may not be available. Usually, computational simulation will also indicate the expected variability of the fracture load due to poorly defined structural fracture resistance.

The following initial defect cases are studied in this chapter to illustrate the methodology: *1)* partial thickness flaw ductile fracture, *2)* through the thickness crack ductile fracture, and *3)* through the thickness crack brittle fracture.

1) Partial thickness flaw ductile fracture

A high strength steel cylindrical shell pressure vessel is utilized to illustrate a typical durability analysis with a partial thickness flaw. The material is ductile maraging steel with a yield strength of 1,241 MPa (180 ksi) [*12*]. In the absence of experimental data, a unit mapping ratio of β=1.0 is assumed according to the expected ductile behavior of this material. The shell thickness is 21.8 mm (0.86 in.). The cylindrical shell has a diameter of 762 mm (30 in.), and a length of also 762 mm (30 in.). The finite element model contains 512 nodes and 480 elements. At one point along a generator line on the shell, at half-length of the cylinder, an initial surface flaw is prescribed. The depth of the flaw is 10.9 mm (0.43 in.) or half of the shell thickness. The flaw is 50.8 mm (2.0 in.) long, oriented parallel to the axis of the shell. The shell is subjected to an internal pressure that is gradually increased until ultimate fracture. To simulate the stresses in a closed-end cylindrical pressure vessel, a

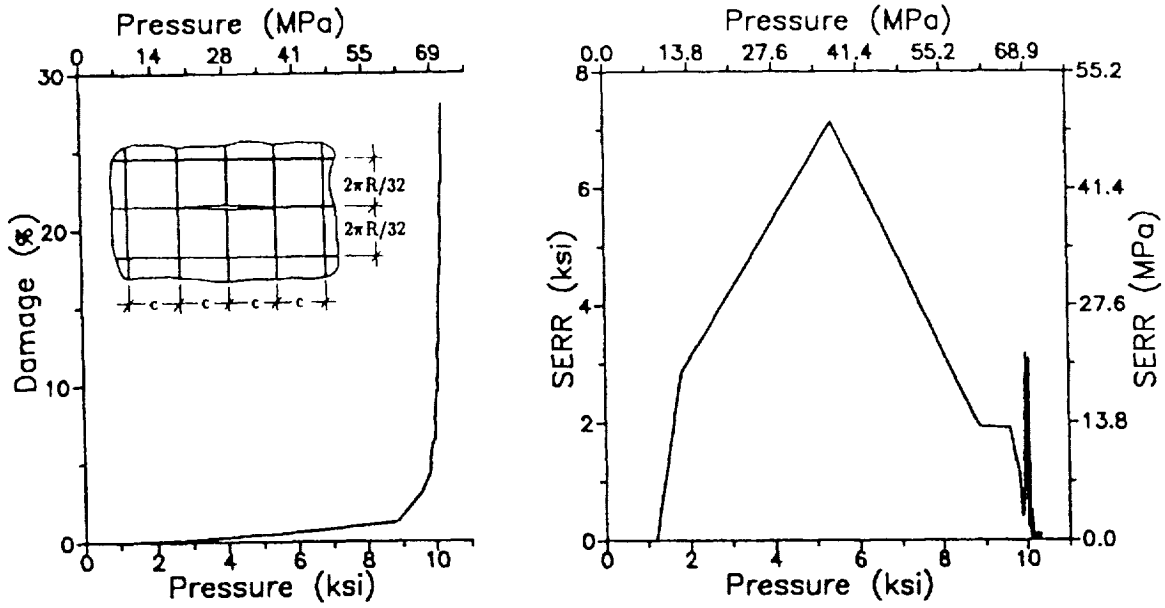

Figure 24.1: *Damage Propagation (left) and Strain Energy Release Rates (right) with Pressure for Maraging Steel Shell with Partial Thickness Axial Flaw: R=381 mm (15 in.); t=21.8 mm (0.86 in.); s=25.4 mm (1.0 in.); β=1.0.*

uniformly distributed axial tension is applied to the cylinder such that axial stresses in the shell wall are half those developed in the hoop direction. To impose the axial loading, one of the end sections is restrained against axial translation and axial tension is applied uniformly at the opposite end of the shell. The ratio of the global axial load to internal pressure is kept constant at all load increments.

To simulate the gradual progression of damage across the thickness of the shell, the shell thickness is subdivided into 10 equal layers of 2.18 mm (0.086 in.) thickness each. An internal pressure of 8.27 MPa (1,200 psi) is applied for the first load increment. The initial flaw is prescribed in the form of a uniform depth surface crack at one node by imposing hoop stress failures in the finite layers 1 through 5.

Simulated damage progression highlights may be summarized as follows: Damage initiation occurs at the location of the initial flaw by yielding on the opposite surface from the original flaw side under a 12.4 MPa internal pressure. Damage growth is by yielding through the shell thickness at 37.2 MPa. At 61.1 MPa, damage progresses along the shell axis in both directions, and through the thickness yielding reaches a length three times the length of the original flaw. At 66.0 MPa, damage propagates in the hoop direction as well as further progressing in the axial direction. At 68.2 MPa, the damage region grows to be seven times the length of the original flaw. Damage also grows in the hoop direction with additional branches. Global structural fracture occurs at 71.1 MPa. It is interesting to note that damage initiation at 12.4 MPa is not contiguous to the original flaw as the relatively thin cylindrical shell readjusts its geometry so as to reduce stresses at the interior edge of the partial thickness crack.

Figure 1, *left* shows the relationship between structural damage and the applied internal

pressure. Damage propagation to ultimate structural fracture begins at approximately 69 MPa (10 ksi) internal pressure. After a 9.5 percent damage level is reached, additonal damage is propagated without significant increase of the internal pressure, indicating impending ultimate fracture. The strain energy released during damage growth is evaluated by computing the work done on the structure during damage. The Strain Energy Release Rate (SERR) is defined as the amount of released energy per unit damage volume produced. The SERR may be used as a measure of structural resistance to damage propagation. SERR is computed at structural degradation levels beginning with initial damage growth and progressing through the various damage stages up to structural fracture. Figure 1, *right* shows the SERR as a function of the internal pressure. It is interesting to note that the final two peaks in the SERR both occur very near the ultimate pressure of approximately 69 MPa (10 ksi). Figure 1, *right* also indicates that maximum structural resistance to damage propagation occurs at an internal pressure of approximately 37.9 MPa (5.5 ksi).

This case is similar to the design example given in reference [*12*] where fracture mechanics methods yield a permissible design pressure of 34.5 MPa (5 ksi) with a safety factor of 2. It is noteworthy that current results were obtained independent of traditional fracture mechanics.

2) Ductile Steel Vessel with Through the Thickness Crack

In this case simulations are made on cylindrical steel pressure vessels with through-the-thickness cracks and with ductile material properties. The examples are selected following the experimental data compiled in reference [*13*]. The material is plain carbon steel; C:0.36%,Mn:0.44-0.46%,Si:0.10-0.13%, with a yield strength of σ_y=238 MPa (34.5 ksi), and an ultimate tensile strength of σ_u=479 Mpa (69.5 ksi). The pressurization temperature range is 62-88^oC. For the first example in this category, the internal radius of the cylindrical shell is R=762 mm (30 in.) with a wall thickness of t=25.4 mm (1.0 in.), and a crack half length of c=76.2 mm (3.0 in.). The through-the-thickness crack is simulated by taking two originally coincident nodes at the center of the crack and assigning each one connectivities to finite elements on one side of the crack. As the shell is pressurized, the two nodes move away from one another simulating the crack opening.

At the crack tip the finite element axial size s is taken to be the same as the crack half length of c=76.2 mm (3.0 in.). The material is expected to develop or exceed its yield stress at the crack tip finite element node due to ductility and strain hardening. Calibration of the computational model is such that the experimentally observed crack extension pressure of P=7.58 MPa (1,100 psi) is approximately midway between the damage initiation and structural fracture pressures simulated. The average effective stress σ_e achieved in the finite element model at the crack tip is approximately 276 MPa (40 ksi), exceeding the yield strength of σ_y=238 MPa (34.5 ksi). Therefore, the mapping ratio for the computational model is $\beta=(\sigma_y/\sigma_e)$=0.86. Since β is less than 1.0 for a calibrated finite element size s that is equal to the characteristic size c of the crack, ductile fracture is indicated. Figure 2, *left* shows the simulated damage due to internal pressure using the calibrated effective strength of σ_e=276 MPa (40.0 ksi). The experimentally observed [*13*] average crack extension pressure of 7.58 MPa (1,100 psi) is also shown in Figure 2, *left* for comparison. The pressure levels that cause damage and the specific damage progression modes for this example can be summarized

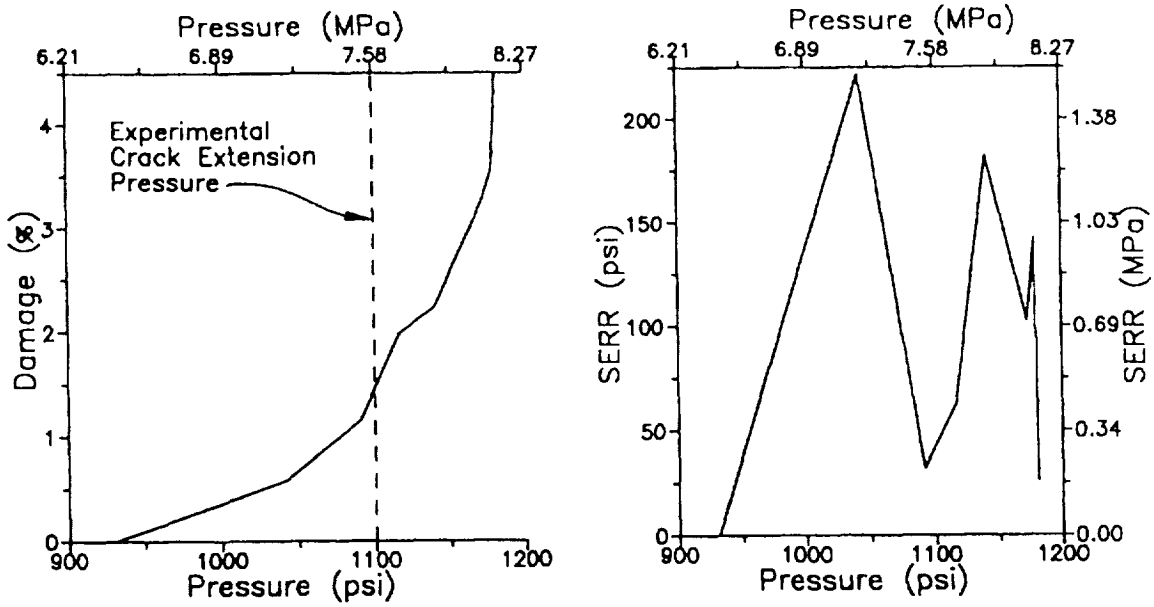

Figure 24.2: *Damage Propagation (left) and Strain Energy Release Rates (right) with Pressure for Ductile Plain Carbon Steel Shell with Full Thickness Axial Crack: R=762 mm (30 in.); t=25.4 mm (1.0 in.); c=76.2 mm (3.0 in.); s=76.2 mm (3.0 in.); β=0.86.*

as follows: Damage initiation starts at 7.18 MPa internal pressure by the formation of through-the-thickness yield zones at the tips of the existing crack. At 7.52 MPa, the length of damage zones at each end of the crack become as long as the original crack length 2c. At 7.69 MPa, the damage zones begin to bifurcate with branches in the hoop direction. At 8.09 MPa, damage zones furter extend and bifurcate with additional branches. The pressure vessel fractures at 8.14 MPa.

Figure 24.2, *right* shows SERR as a function of the applied internal pressure, indicating the two well defined structural resistance stages. The first peak in SERR corresponds to the damage initiation pressure. The second peak occurs immediately before final structural fracture. The significance of the high SERR at damage initiation is that a well defined fracture resistance predicts the consistency of test data on initial crack extension for this case. After damage initiation SERR drops to a much lower level, indicationg the lack of structural resistance to damage growth. Nevertheless, after approximately a 2 percent damage level is reached, a relatively higher SERR indicates structural resistance during the stage of damage bifurcation and the formation of hoop cracks emanating from the ends of the axial crack. At approximately 4 percent damage level, the SERR level is reduced as the pressure vessel enters the final structural fracture stage.

To test the calibration model with a different geometry, another example with the same material but with a smaller radius and a longer crack is simulated. The internal radius of the cylindrical shell is now 457 mm (18.0 in.) with the same wall thickness of t=25.4 mm (1.0 in.), and a crack half length of c=152 mm (6.0 in.). The finite element size at the crack tip is kept at s=76.2 mm (3.0 in.), as calibrated. Figure 24.3, *left* shows the simulated damage with internal pressure. Figure 24.3, *right* shows the SERR with pressure, indicating

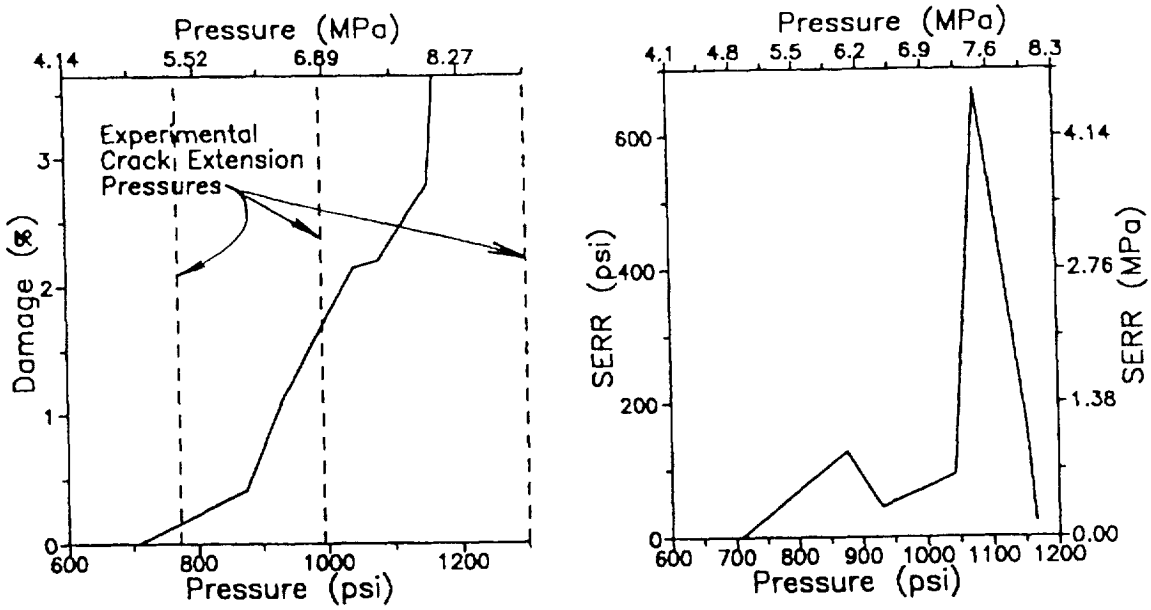

Figure 24.3: *Test Simulation of Fracture Progression for Smaller Radius Shell; Ductile Plain Carbon Steel with Full Thickness Axial Crack: R=457 mm (18 in.); t=25.4 mm (1.0 in.); c=152 mm (6.0 in.); s=76.2 mm (3.0 in.); β=0.86.*

a relatively low structural resistance to damage initiation, predicting the expected variability of experimental results and sensitivity to minor material defects and environmental factors. The low level of the initial SERR predicts the scatter of experimental observations and sensitivity to minor temperature variations affecting the ductility for initial crack progression. Nevertheless, the results show reasonable agreement with a collective interpretation of the three experimental observations from reference [*13*] on this example. The three experimental observations with this geometry indicate crack extension pressures of 5.32 and 6.86 MPa (772 and 994 psi) under laboratory temperatures in the range of 10-50°C and a crack extension pressure of 8.96 MPa (1,300 psi) at a temperature of $79°C$, as shown in Figure 24.3, *left*. Figure 24.3, *right* shows a peak level of structural resistance to fracture at a relatively late degradation stage, indicating the substantial damage tolerance of this pressure vessel. The emergence of maximum structural fracture resistance after significant damage growth can be used as a safety feature if the pressure vessel is instrumented for detecting damage induced distortions from normal structural response.

3) Brittle Steel Vessel with Through the Thickness Crack

The examples leading to brittle fracture of pressure vessels are also selected from experimental data compiled in reference [*13*]. The material for the brittle fracture examples is hot rolled steel; C:0.25%,Mn:0.85%,Si:0.02%, with a yield strength of σ_y= 793 MPa (115 ksi), and an ultimate tensile strength of σ_u= 862 MPa (125 ksi). The pressurization temperature is $-196°C$. For the calibration case in this category, the internal radius of the cylindrical shell is R=203 mm (8.0 in.); the wall thickness is t=6.35 mm (0.25 in.); and the crack half length is c=47.0 mm (1.85 in.).

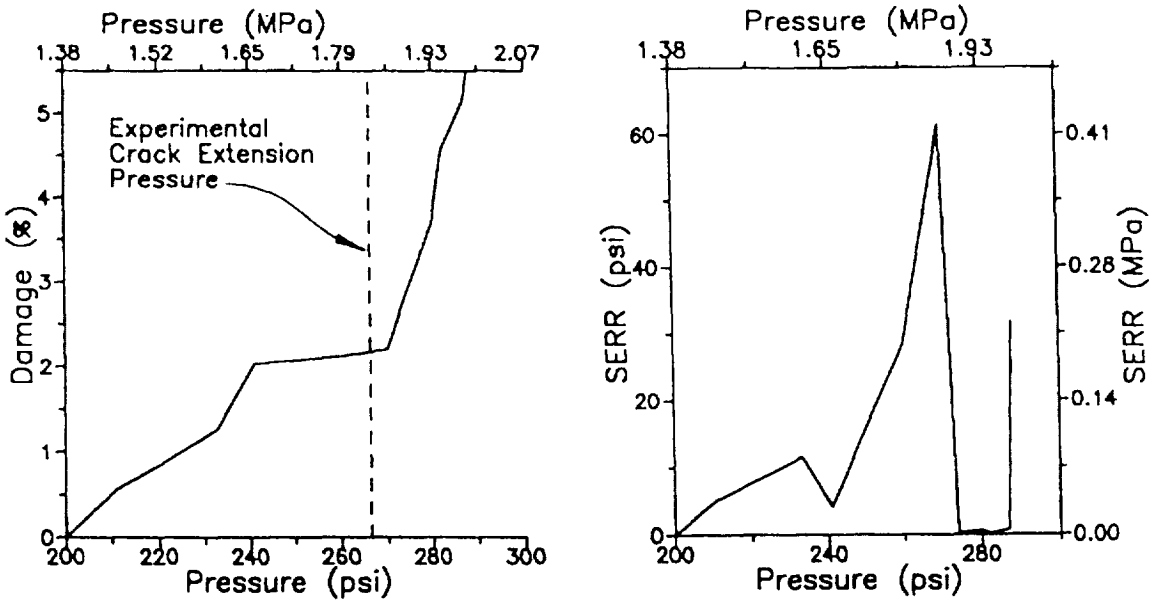

Figure 24.4: *Simulation of Damage Progression with Internal Pressure for Hot Rolled Brittle Steel Shell with Full Thickness Axial Crack: R=203 mm (8 in.); t=6.35 mm (0.25 in.); c=47 mm (1.85 in.); s=47 mm (1.85 in.); β=7.67.*

The finite element size s for model calibration is taken to be the same as the crack half length of c=47.0 mm. The material is not expected to be able to develop its yield stress in the characteristic zone due to brittle fracture. Calibration of the computational model results in an average effective strength of σ_e=103 MPa (15 ksi), which is 13 percent of the yield strength of σ_y=793 MPa (115 ksi), therefore, the mapping ratio is $\beta=(\sigma_y/\sigma_e)$=7.67. Since β is significantly greater than 1.0, and the finite element calibration size s is equal to the half crack size c, brittle fracture is indicated. Reducing the calibration finite element size to smaller than the crack characteristic size would reduce β and yield a more accurate model, but at a greater computational expense. Figure 24.4, *left* shows the simulated damage due to internal pressure using an effective strength of σ_e=103 MPa (15 ksi). The experimentally observed [*13*] crack extension pressure of 1.84 MPa (266 psi) is also indicated in Figure 24.4, *left* for reference. The pressure levels and damage progression modes for the simulation of this brittle example may be summarized as follows: Damage initation at the crack tip occurs when the internal pressure reaches 1.38 MPa. Later, damage zones begin to bifurcate under a 1.46 MPa pressure. New branches of damage emanate from the crack tip at 1.66 MPa. Many additional small branches of damage are extended in the hoop direction at 1.77 MPa. Structural fracture occurs at 1.94 MPa.

Figure 24.4, *right* shows SERR as a function of the applied internal pressure. SERR is very low at damage initiation that occurs in the direction of the original crack along the axis of the shell. The initially low SERR level shown in Figure 24.4, *right* indicates the brittle nature of damage initiation. The maximum level of SERR is reached at a relatively late loading stage as damage bifurcates via branches emanating from the crack tips. The late onset of fracture resistance indicates structural damage tolerance in spite of brittle material properties.

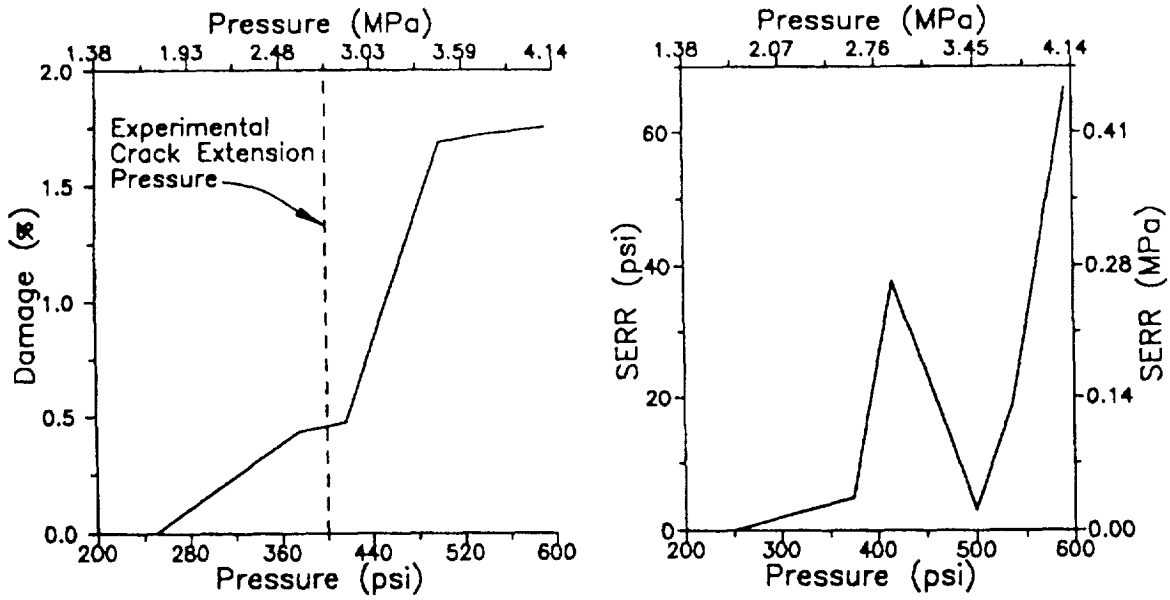

Figure 24.5: *Test Simulation of Fracture Progression for Smaller Radius and Thicker Shell with Longer Crack for Hot Rolled Brittle Steel Shell with Full Thickness Axial Crack: R=109 mm (4.3 in.); t=12.7 mm (0.5 in.); c=58.4 mm (2.3 in.); s=47 mm (1.85 in.); β=7.67.*

To test the calibration with a different geometry, another example with the same material, but with a longer crack, greater thickness, and smaller radius is simulated. The internal radius of the cylindrical shell is now R=109 mm (4.3 in.), with a wall thickness of t=12.7 mm (0.5 in.), and a crack half length of c=58.4 mm (2.30 in.). The finite element model axial size at the crack tip is kept at s=47.0 mm (1.85 in.) as calibrated. Figure 24.5, *left* shows simulated damage with pressure. The single experimental observation of initial crack extension at 2.76 MPa (400 psi) from reference [*13*] is also depicted for comparison. It must be noted that this experimental observation is subject to question because there is another test case in reference [*13*] with a 14 percent longer crack that has a 2 percent higher crack extension pressure. Therefore if more experimental data on this case were available, higher pressures would be expected for crack extension. Computational simulations are consistent with these experimental observations. Figure 24.5, *right* shows the SERR with pressure, indicating low structural resistance to damage initiation, but considerable resistance to secondary damage growth after initiation. The peak SERR is developed immediately before structural fracture.

24.4 General Remarks

The present investigation was limited to static internal pressure applied from within a cylindrical shell. CODSTRAN can be used to investigate other cases. These include: *1)* compression, *2)* bending, *3)* torsion, *4)* impact, *5)* blast pressure, and combinations of these loads. Applications of load combinations such as combined impact with pressure loading due to

pressurized tank drop can be investigated. Damage growth and fracture propagation in other types of structures such as variable thickness composites, hybrid composites, and thick composite shells, as well as steel pressure vessels and composite pressure vessels interlayered with steel or other metal alloys can be simulated. The relationship between internal damage and structural response properties such as displacements under loading, natural frequencies, vibration modes, buckling loads and buckling modes can be computed by CODSTRAN for any type of structure. The durability of multi-component structures such as cylindrical shells stiffened by integrated framework can also be investigated.

24.5 Summary of Results

The significant results from this investigation in which CODSTRAN (COmposite Durability STRuctural ANalysis) is used to evaluate damage growth and propagation to fracture of a cylindrical shell subjected to internal pressure are as follows:

1. CODSTRAN adequately tracks the damage growth and subsequent propagation to fracture for partial thickness defects and through-the-thickness cracks of pressurized cylindrical shells.

2. The definition and calibration of a mapping ratio enables accurate simulation of fracture propagation at a reasonable computational expense.

3. Brittleness or ductility of fracture propagation depends on structural geometry and crack length as well as on material behavior.

4. Thin cylindrical shells with a partial thickness flaw subjected to internal pressure readjust their geometry so as to reduce stresses at the crack tip.

5. The calibrated mapping ratio β may be used as an index of brittleness of fracture if the finite element model size s is selected consistent with the characteristic crack size c.

This chapter demonstrates that computational simulation, with the use of established material modelling and finite element modules, can be used to predict the effects of existing flaws, as well as loading, on the safety and durability of steel pressure vessels.

Bibliography

[1] Chamis, C. C. and Sinclair, J. H., "Dynamic Response of Damaged Angleplied Fiber Composites," NASA TM-79281, 1979.

[2] Chamis, C. C. and Williams, G. C., "Interply Layer Degradation Effects on Composite Structural Response," AIAA Paper No. 84-0849 CP, AIAA/ASM/ASCE/AHS 25th Structures, Structural Dynamics, and Materials Conference, May 14-16, 1984, Palm Springs, California.

[3] Chamis, C. C. and Smith, G. T., "Composite Durability Structural Analysis," NASA TM-79070, 1978.

[4] Irvine, T. B. and Ginty, C. A., "Progressive Fracture of Fiber Composites," NASA TM-83701, 1983.

[5] Murthy, P.L.N. and Chamis, C.C.,"ICAN: Integrated Composites Analyzer," *Composite Technology Review*, Spring 1986.

[6] Murthy, P.L.N. and Chamis, C.C.,"Integrated Composite Analyzer (ICAN): Users and Programmers Manual," NASA Technical Paper 2515, March 1986.

[7] Nakazawa, S., Dias, J.B., and Spiegel, M.S., *MHOST Users' Manual*, Prepared for NASA Lewis Research Center by MARC Analysis Research Corporation, April 1987.

[8] McCormick, C.W., ed.,"NASTRAN User's Manual (level 15)," NASA SP-222(01), 1972.

[9] Minnetyan, L., Murthy, P. L. N., and Chamis, C. C., "Progression of Damage and Fracture in Composites under Dynamic Loading," 31st SDM Conference, April 2 - 4, 1990, Long Beach, California; A Collection of Technical Papers, Part 2, pp. 941 - 949.

[10] Murthy, P. L. N., and Chamis, C. C.,"Composite Interlaminar Fracture Toughness: 3-D Finite Element Modeling for Mixed Mode I, II, and III Fracture," NASA TM-88872, 1986.

[11] Valisetty, R. R., and Chamis, C. C.,"Strain Energy Release Rates of Composite Interlaminar End-Notch and Mixed Mode Fracture: A Sublaminate/Ply Level Analysis and a Computer Code," NASA TM-89827, 1986.

[12] Murthy, P. L. N., and Chamis, C. C.,"Finite Element Substructuring Methods for Composite Mechanics," NASA TM-100297, 1988.

[13] Minnetyan, L., Murthy, P. L. N., and Chamis, C. C.,"Composite Structure Global Fracture Toughness via Computational Simulation," *Computers & Structures*, Vol. 37, No. 2, pp.175-180, 1990

[14] Chamis, C. C., "Simplified Composite Micromechanics Equations for Hygral, Thermal, and Mechanical Properties," NASA TM–83320, February 1983.

[15] Chamis, C. C. and Smith, G. T., "Environmental and High Strain Rate Effects on Composites for Engine Applications," *AIAA Journal*, V. 22, No. 1, January 1984, pp. 128-134

[16] Murthy, P. L. N. and Chamis, C. C., "Free-Edge Delamination: Laminate Width and Loading Conditions Effects," NASA TM–100238, December 1987, 27 pp.

[17] Rubenstein, R. and Chamis, C. C., "STAEBL/General Composites With Hygrothermal Effects (STAEBL/GENCOM)," NASA TM–100266, December 1987, 11 pp.

[18] Saravanos, D. A. and Chamis, C. C., "Mechanics of Damping for Fiber Composite Laminates Including Hygro-Thermal Effects," NASA TM–102329, April 1989.

[19] Murthy, P. L. N. and Chamis, C. C., "Simplified Design Procedures for Fiber Composite Structural Components/ Joints," NASA TM–103113, July 1990, 23 pp.

[20] Ginty, C. A. and Chamis, C. C. "Hygrothermomechanical Fiber Composite Fatigue: Computational Simulation," NASA TM–100840, 1988.

[21] Minnetyan, L., Chamis, C. C., and Murthy, P. L. N., "Structural Durability of a Composite Pressure Vessel," *Journal of Reinforced Plastics and Composites*, Vol. 11, No. 11, November 1992, pp. 1251-1269

[22] Minnetyan L., Chamis C.C., and Murthy P.L.N.,"Structural Behavior of Composites with Progressive Fracture," *Journal of Reinforced Plastics and Composites*, Vol. 11, No. 4, April 1992, pp. 413-442

[23] Minnetyan L., Murthy P.L.N., and Chamis C.C., "Progressive Fracture in Composites Subjected to Hygrothermal Environment," *International Journal of Damage Mechanics*, Vol. 1, No. 1, January 1992, pp. 60-79

[24] Minnetyan L., Chamis C.C., and Murthy P.L.N., "Damage Progression in Mechanically Fastened Composite Structural Joints," Proceedings of the American Society for Composites-Ninth Conference, September 20-22, 1994, University of Delaware, Newark, Delaware, pp. 397-404.

[25] Ranniger C.U., "Damage Tolerance and Arrest Characteristics of Pressurized Graphite/Epoxy Tape Cylinders," TELAC Report 91-11, Technology Laboratory for Advanced Composites, Department of Aeronautics and Astronautics, Massachusetts Institute of Technology, 77 Massachusetts Avenue, Cambridge, Massachusetts, June 1991.

[26] Spicola F., Dubois N., Tucker W., and Butts J., "Structural Failure in Filament Wound Right Circular Cylindrical Shells Subjected to Biaxial External Pressure," Proceedings of the ICCM-9 Conference, 12-16 July 1993, Madrid, Spain, Volume 5, pp. 209-216.

[27] Minnetyan, L., Rivers, J. M., Murthy, P. L. N., and Chamis, C. C., "Structural Durability of Stiffened Composite Shells," Proceedings of the 33rd SDM Conference, Dallas, Texas, April 13-15, 1992, Vol. 5, pp. 2879-2886

[28] Garala, H., Phyillaier, W., and Chaudhuri, R.,"Structural Response of Composite Cylinders to External Hydrostatic Pressure," Presented at the 16th Annual Mechanics of Composites Review, 12-13 November 1991, Stouffers Center Plaza Hotel, Dayton, Ohio.

[29] Chamis, C. C., Murthy, P. L. N., and Minnetyan, L., "Progressive Fracture of Polymer Matrix Composite Structures: A New Approach," NASA TM–105574, January 1992, 22 pp.

[30] Minnetyan, L., and Murthy, P. L. N.,"Design for Progressive Fracture in Composite Shell Structures," Proceedings of the 24th International SAMPE Technical Conference, Toronto, Canada, October 20-22, 1992, pp. T227-T240

[31] Jackson, W. C., and Martin, R. H.,"An Interlaminar Tension Strength Specimen," NASA–TM 107623, May 1992.

[32] Lekhnitskii, S. G., *Anisotropic Plates*, Gordon and Breach Science Publishers, 1968, pp. 95-98.

[33] Minnetyan, L., Chamis, C. C., and Murthy, P. L. N., "Effect of Adhesive Thickness on The Durability of a Stiffened Composite Panel," Proceedings of the 39th International SAMPE Symposium and Exhibition, April 11-14, 1994, Anaheim, California, Vol. 39, pp. 2044-2056.

[34] Sparks, C., Odru, P., Metivaud, G., and LeFloc'h, C., "Defect Tolerance Assessment and Non-Destructive Testing of Composite Riser Tubes," Proceedings of the 11th ASME International Conference on *Offshore Mechanics and Arctic Engineering*, Calgary, Alberta, Canada, June 7-12, 1992, Volume III, Part A-Materials Engineering, pp. 209-214

[35] Wang,J. T., Lotts, C. G., Davis, D. D., Jr., and Krishnamurthy, T., "Coupled 2D-3D Finite Element Method for Analysis of a Skin Panel with a Discontinuous Stiffener," Proceedings of the 33rd SDM Conference, Dallas, Texas, April 13-15, 1992, Vol. 2, pp. 818-827

[36] Coker, D., and Ashbaugh, N. E.,"Characterization of Fracture in $[0/90]_{3s}$ SiC/1723 Composites," Report No. WL-TR-91-4119, March 1992, Materials Directorate, Wright Laboratory, Air Force Systems Command, Wright-Patterson Air Force Base, Ohio.

[37] Chamis, C. C.,"Failure Criteria for Filamentary Composites," *Composite Materials Testing and Design: ASTM STP Publication 460*, American Society for Testing and Materials, Philadelphia, 1969, pp 336-351.

[38] Minnetyan, L., and Chamis, C. C.,"Pressure Vessel Fracture Simulation," *Fracture Mechanics: 25th Volume, ASTM STP 1220*, American Society for Testing and Materials, Philadelphia, 1995, pp 671-684.

[39] Barsom, J. M., and Rolfe, S. T.,*Fracture and Fatigue Control in Structures: Applications of Fracture Mechanics*, Second Edition, Prentice-Hall, 1987, pp. 208-212.

[40] Hahn, G. T., Sarrate, M., and Rosenfield, A. R., "Criteria for Crack Extension in Cylindrical Pressure Vessels," *International Journal of Fracture Mechanics*, Vol. 5, No. 3, September 1969, pp. 187-210.

[41] Shiao, M. C., and Chamis, C. C.,"Mapping Methods for Computationally Efficient and Accurate Structural Reliability," Proceedings of the 33rd SDM Conference, Dallas, Texas, April 13-15, 1992, pp. 433-443.

[42] Minnetyan, L. and Murthy, P. L. N.,"Progressive Fracture of Adhesively Bonded Joints," Proceedings of ASME 1994 Energy Technology Conference and Exhibition, January 23-26 1994, New Orleans, Louisiana, PD-Vol.62, pp. 351-356.

[43] Minnetyan, L., Rivers, J. M., Chamis, C. C., and Murthy, P. L. N., "Discontinuously Stiffened Composite Panel under Compressive Loading," *Journal of Reinforced Plastics and Composites*, Vol. 14, No. 1, January 1995, pp. 85-98.

[44] Chamis, C. C., and Shiao, M. C.,"IPACS - Integrated Probabilistic Assessment of Composite Structures: Code Development and Application," Third NASA Advanced Composites Technology Conference, Long Beach, CA, June, 1992.

APPENDIX A: Constituent Material Properties

AS-4 Graphite Fiber Properties:

Number of fibers per end = 10000
Fiber diameter = 0.00762 mm (0.300E-3 in)
Fiber Density = 4.04E-7 Kg/m^3 (0.063 lb/in^3)
Longitudinal normal modulus = 227 GPa (32.90E+6 psi)
Transverse normal modulus = 13.7 GPa (1.99E+6 psi)
Poisson's ratio (ν_{12}) = 0.20
Poisson's ratio (ν_{23}) = 0.25
Shear modulus (G_{12}) = 13.8 GPa (2.00E+6 psi)
Shear modulus (G_{23}) = 6.90 GPa (1.00E+6 psi)
Longitudinal thermal expansion coefficient = 1.0E-6/°C (-0.55E-6 /°F)
Transverse thermal expansion coefficient = 1.0E-6/°C (-0.56E-6 /°F)
Longitudinal heat conductivity = 43.4 J-m/hr/m^2/°C (580 BTU-in/hr/in^2/°F)
Transverse heat conductivity = 4.34 J-m/hr/m^2/°C (58 BTU-in/hr/in^2/°F)
Heat capacity = 712 J/Kg/°C (0.17 BTU/lb/°F)
Tensile strength = 3,723 MPa (540 ksi)
Compressive strength = 3,351 MPa (486 ksi)

HMHS Epoxy Matrix Properties:

Matrix density = 3.40E-7 Kg/m^3 (0.0457 lb/in^3)
Normal modulus = 4.27 GPa (620 ksi)
Poisson's ratio = 0.34
Coefficient of thermal expansion = 0.72/°C (0.4E-4 /°F)
Heat conductivity = 1.25 BTU-in/hr/in^2/°F
Heat capacity = 0.25 BTU/lb/°F
Tensile strength = 84.8 MPa (12.3 ksi)
Compressive strength = 423 MPa (61.3 ksi)
Shear strength = 148 MPa (21.4 ksi)
Allowable tensile strain = 0.02
Allowable compressive strain = 0.05
Allowable shear strain = 0.04
Allowable torsional strain = 0.04
Void conductivity = 16.8 J-m/hr/m^2/°C (0.225 BTU-in/hr/in^2/°F)
Glass transition temperature = 216°C (420°F)

LMHS Toughened Epoxy Matrix Properties:

Matrix density = 3.20E-7 Kg/m^3 (0.0430 lb/in^3)
Normal modulus = 2.41 GPa (350 ksi)
Poisson's ratio = 0.43
Coefficient of thermal expansion = 1.03/°C (0.57E-4 /°F)
Heat conductivity = 1.25 BTU-in/hr/in^2/°F
Heat capacity = 0.25 BTU/lb/°F

Tensile strength = 121 MPa (17.5 ksi)
Compressive strength = 242 MPa (35.0 ksi)
Shear strength = 93.4 MPa (13.5 ksi)
Allowable tensile strain = 0.08
Allowable compressive strain = 0.15
Allowable shear strain = 0.1
Allowable torsional strain = 0.1
Void conductivity = 16.8 J-m/hr/m^2/°C (0.225 BTU-in/hr/in^2/°F)
Glass transition temperature = 180°C (350°F)

ALT6 Aluminum Properties:

Density = 0.0443 lb/in^3
Normal modulus = 10000 ksi
Poisson's ratio = 0.33
Coefficient of thermal expansion = 1.29E-5 /°F
Heat conductivity = 104 BTU-in/hr/in^2/°F
Heat capacity = 0.23 BTU/lb/°F
Tensile strength = 52 ksi
Compressive strength = 52 ksi
Shear strength = 26 ksi
Allowable tensile strain = 0.0052
Allowable compressive strain = 0.0052
Allowable shear strain = 0.0905
Allowable torsional strain = 0.00905
Void conductivity = 0.225 BTU-in/hr/in^2/°F
Glass transition temperature = 1080°F

ER-2258 Matrix Properties:

Matrix density = 3.40E-7 Kg/m^3 (0.0457 lb/in^3)
Normal modulus = 3.79 GPa (550 ksi)
Poisson's ratio = 0.43
Coefficient of thermal expansion = 7.23E-3/°C (0.40E-4/°F)
Heat conductivity = 93,397 Joule-m/hr/m^2/°C (1.25 BTU-in/hr/in^2/°F)
Heat capacity = 1,046 Joules/Kg/°C (0.250 BTU/lb/°F)
Tensile strength = 91.1 MPa (13.2 ksi)
Compressive strength = 207 MPa (30.0 ksi)
Shear strength = 78.0 MPa (11.3 ksi)
Allowable tensile strain = 0.08
Allowable compressive strain = 0.08
Allowable shear strain = 0.04
Allowable torsional strain = 0.04
Void heat conductivity = 16,811 Joule-m/hr/m^2/°C (0.225 BTU-in/hr/in^2/°F)
Glass transition temperature 216°C (420°F)

Kevlar Aramid Fiber Properties:

Number of fibers per end = 580
Fiber diameter = 0.0117 mm (0.460E-3 in)
Fiber Density = 3.94E-7 Kg/m^3 (0.053 lb/in^3)
Longitudinal normal modulus = 152 GPa (22.00E+6 psi)
Transverse normal modulus = 4.14 GPa (0.60E+6 psi)
Poisson's ratio (ν_{12}) = 0.35
Poisson's ratio (ν_{23}) = 0.35
Shear modulus (G_{12}) = 2.90 GPa (0.42E+6 psi)
Shear modulus (G_{23}) = 1.52 GPa (0.22E+6 psi)
Longitudinal thermal expansion coefficient = -0.40E-5/°C (-0.22E-5 /°F)
Transverse thermal expansion coefficient = 0.54E-4/°C (0.30E-4 /°F)
Tensile strength = 2,758 MPa (400 ksi)
Compressive strength = 517 MPa (75 ksi)

GV6S Rubbery Polymer Matrix Properties:

Matrix density = 3.42E-7 Kg/m^3 (0.0460 lb/in^3)
Normal modulus = 68.9 MPa (10 ksi)
Poisson's ratio = 0.41
Coefficient of thermal expansion = 10.3E-3/°C (0.57E-4/°F)
Tensile strength = 48.3 MPa (7.0 ksi)
Compressive strength = 145 MPa (21.0 ksi)
Shear strength = 48.3 MPa (7.0 ksi)
Allowable tensile strain = 0.014
Allowable compressive strain = 0.042
Allowable shear strain = 0.032
Allowable torsional strain = 0.038

T300 Graphite Fiber Properties:

Number of fibers per end = 3000
Fiber diameter = 0.00762 mm (0.300E-3 in)
Fiber Density = 4.10E-7 Kg/m^3 (0.064 lb/in^3)
Longitudinal normal modulus = 221 GPa (32.0E+6 psi)
Transverse normal modulus = 13.8 GPa (2.00E+6 psi)
Poisson's ratio (ν_{12}) = 0.20
Poisson's ratio (ν_{23}) = 0.25
Shear modulus (G_{12}) = 8.96 GPa (1.30E+6 psi)
Shear modulus (G_{23}) = 4.83 GPa (0.70E+6 psi)
Longitudinal thermal expansion coefficient = -1.0E-6/°C (-0.55E-6 /°F)
Transverse thermal expansion coefficient = 1.0E-6/°C (-0.56E-6 /°F)
Longitudinal heat conductivity = 43.4 J-m/hr/m^2/°C (580 BTU-in/hr/in^2/°F)
Transverse heat conductivity = 4.34 J-m/hr/m^2/°C (58 BTU-in/hr/in^2/°F)
Heat capacity = 712 J/Kg/°C (0.17 BTU/lb/°F)
Tensile strength = 2,413 MPa (350 ksi)
Compressive strength = 2,068 MPa (300 ksi)

S-Glass Fiber Properties:

Number of fibers per end = 204
Fiber diameter = 0.00914 mm (0.360E-3 in)
Fiber Density = 5.77E-7 Kg/m^3 (0.090 lb/in^3)
Longitudinal normal modulus = 85.5 GPa (12.4E+6 psi)
Transverse normal modulus = 85.5 GPa (12.4E+6 psi)
Poisson's ratio (ν_{12}) = 0.20
Poisson's ratio (ν_{23}) = 0.20
Shear modulus (G_{12}) = 35.6 GPa (5.17E+6 psi)
Shear modulus (G_{23}) = 35.6 GPa (5.17E+6 psi)
Longitudinal thermal expansion coefficient = 5.1E-6/°C (2.8E-6 /°F)
Transverse thermal expansion coefficient = 5.1E-6/°C (2.8E-6 /°F)
Longitudinal heat conductivity = 0.56 J-m/hr/m^2/°C (7.5 BTU-in/hr/in^2/°F)
Transverse heat conductivity = 0.56 J-m/hr/m^2/°C (7.5 BTU-in/hr/in^2/°F)
Heat capacity = 712 J/Kg/°C (0.17 BTU/lb/°F)
Tensile strength = 2,482 MPa (360 ksi)
Compressive strength = 2,068 MPa (300 ksi)

EPOX Epoxy Matrix Properties:

Matrix density = 3.30E-7 Kg/m^3 (0.0443 lb/in^3)
Normal modulus = 4.14 GPa (500 ksi)
Poisson's ratio = 0.35
Coefficient of thermal expansion = 0.77/°C (0.428E-4 /°F)
Heat conductivity = 0.0933 J-m/hr/m^2/°C (1.25 BTU-in/hr/in^2/°F)
Heat capacity = 1,047 J/Kg/°C (0.25 BTU/lb/°F)
Tensile strength = 103 MPa (15 ksi)
Compressive strength = 241 MPa (35 ksi)
Shear strength = 89.6 MPa (13 ksi)
Allowable tensile strain = 0.02
Allowable compressive strain = 0.05
Allowable shear strain = 0.04
Allowable torsional strain = 0.04
Void conductivity = 16.8 J-m/hr/m^2/°C (0.225 BTU-in/hr/in^2/°F)
Glass transition temperature = 216°C (420°F)

REPORT DOCUMENTATION PAGE

Form Approved
OMB No. 0704-0188

1. AGENCY USE ONLY (Leave blank)	2. REPORT DATE	3. REPORT TYPE AND DATES COVERED
	July 2001	Final Contractor Report

4. TITLE AND SUBTITLE

Progressive Fracture of Composite Structures

5. FUNDING NUMBERS

WU–910–30–11–00
NAG3–1101

6. AUTHOR(S)

Levon Minnetyan

7. PERFORMING ORGANIZATION NAME(S) AND ADDRESS(ES)

Clarkson University
Department of Civil and Environmental Engineering
Potsdam, New York 13699–5710

8. PERFORMING ORGANIZATION REPORT NUMBER

E–12828

9. SPONSORING/MONITORING AGENCY NAME(S) AND ADDRESS(ES)

National Aeronautics and Space Administration
Washington, DC 20546–0001

10. SPONSORING/MONITORING AGENCY REPORT NUMBER

NASA CR—2001-210974

11. SUPPLEMENTARY NOTES

Contents were reproduced from the best available copy as provided by the author. Project Manager, Christos C. Chamis, Research and Technology Directorate, NASA Glenn Research Center, organization code 5000, 216–433–3252.

12a. DISTRIBUTION/AVAILABILITY STATEMENT

Unclassified - Unlimited
Subject Categories: 39, 24, and 15 Distribution: Nonstandard

Available electronically at http://gltrs.grc.nasa.gov/GLTRS

This publication is available from the NASA Center for AeroSpace Information, 301–621–0390.

12b. DISTRIBUTION CODE

13. ABSTRACT ***(Maximum 200 words)***

This report includes the results of a research in which the COmposite Durability STRuctural ANalysis (CODSTRAN) computational simulation capabilities were augmented and applied to various structures for demonstration of the new features and verification. The first chapter of this report provides an introduction to the computational simulation or virtual laboratory approach for the assessment of damage and fracture progression characteristics in composite structures. The second chapter outlines the details of the overall methodology used; including the failure criteria and the incremental/iterative loading procedure with the definitions of damage, fracture, and equilibrium states. The subsequent chapters each contain an augmented feature of the code and/or demonstration examples. All but one of the presented examples contains laminated composite structures with various fiber/matrix constituents. For each structure simulated, damage initiation and progression mechanisms are identified and the structural damage tolerance is quantified at various degradation stages. Many chapters contain the simulation of defective and defect free structures to evaluate the effects of existing defects on structural durability.

14. SUBJECT TERMS

Structural behavior; Damage tolerance; Buckling resistance;
Structural durability; Compressive loading; Adhesive thickness

15. NUMBER OF PAGES

263

16. PRICE CODE

17. SECURITY CLASSIFICATION OF REPORT	18. SECURITY CLASSIFICATION OF THIS PAGE	19. SECURITY CLASSIFICATION OF ABSTRACT	20. LIMITATION OF ABSTRACT
Unclassified	Unclassified	Unclassified	